

JAERI-Review
2005-013



JP0550283



PROGRESS REPORT ON NEUTRON SCIENCE
(APRIL 1, 2003-MARCH 31, 2004)

March 2005

(Eds.) Masaaki MATSUDA, Kazuo KURIHARA and Atsushi MORIAI

日本原子力研究所
Japan Atomic Energy Research Institute

本レポートは、日本原子力研究所が不定期に公刊している研究報告書です。

入手の問合わせは、日本原子力研究所研究情報部研究情報課(〒319-1195 茨城県那珂郡東海村)あて、お申し越し下さい。なお、このほかに財団法人原子力弘済会資料センター(〒319-1195 茨城県那珂郡東海村日本原子力研究所内)で複写による実費頒布を行っております。

This report is issued irregularly.

Inquiries about availability of the reports should be addressed to Research Information Division, Department of Intellectual Resources, Japan Atomic Energy Research Institute, Tokai-mura, Naka-gun, Ibaraki-ken 〒319-1195, Japan.

© Japan Atomic Energy Research Institute, 2005

編集兼発行 日本原子力研究所

Progress Report on Neutron Science
(April 1, 2003 - March 31, 2004)

Advanced Science Research Center[※]
and
Neutron Science Research Center, Tokai Research Establishment

Japan Atomic Energy Research Institute
Tokai-mura, Naka-gun, Ibaraki-ken

(Received February 17, 2005)

This issue summarizes research progress in neutron science at Japan Atomenery Research Institute (JAERI) by utilizing the research reactor JRR-3 during the period between April 1, 2003 and March 31, 2004. This report contains highlights in research from 10 neutron research groups at JAERI and summary reports of 82 papers.

Keywords : Neutron Science, JRR-3

※ Tokai Site
(Eds.) Masaaki MATSUDA, Kazuo KURIHARA and Atsushi MORIAI

中性子科学研究成果報告集
(2003 年度次報告)

日本原子力研究所
先端基礎研究センター※
東海研究所中性子利用研究センター

(2005 年 2 月 17 日 受理)

日本原子力研究所では、先端基礎研究センターおよび中性子利用研究センターに合わせて 12 の中性子研究・開発グループがあり、研究用原子炉 JRR-3 を利用した研究と開発を行っている。分野は中性子散乱（固体物性、高分子、生物、残留応力）、即発ガンマ線分析、中性子ラジオグラフィ、中性子光学、装置・検出器・デバイス開発と多岐にわたる。

本報告書は、これらのグループの活動報告に加えて、2003 年 4 月から 2004 年 3 月までの期間に行われたこれらのグループの中性子科学研究、所外との協力研究および共同研究、黎明研究の成果として 82 編の研究報告を収録する。

東海研究所：〒319-1195 茨城県那珂郡東海村白方白根 2-4

※ 東海駐在

(編) 松田 雅昌・栗原 和男・盛合 敦

Contents

Organization of JAERI (Neutron Science Relation in Tokai)	1
List of JAERI Instruments	2
1. Highlights in Research at JAERI	5
1.1 Neutron Diffraction Study of Biological Macromolecules Using BIX-type Neutron Diffractometers	7
1.2 Neutron Scattering Studies of Structure Functionality of Soft Matters	9
1.3 Neutron Scattering Research on Spin-lattice Correlations	11
1.4 Neutron Scattering Studies on the <i>f</i>-electron Systems	13
1.5 Neutron Scattering Studies of Functional Materials	15
1.6 Neutron Diffraction Studies of Industrial Materials	17
1.7 Diverse Studies on Neutron Imaging	19
1.8 Novel Approaches for Neutron Induced Prompt γ -ray Using	21
1.9 Development and Application of Neutron Optics	23
1.10 R&D of Neutron Instruments for J-PARC	25
1.11 International Collaborations	29
2. Research Reports	31
2.1 Biology	33
- Structure and Mechanism -	
2.1.1 Neutron Crystallographic Analysis of Endopolygalacturonase I from <i>Stereum Purpureum</i> at Atomic Resolution	33
M. Sato, T. Shimizu, T. Nakatsu and H. Kato	

2.1.2	Complicated Water Network in the Minor Groove of B-DNA Decamer d(CCATTAATGG) ₂ Observed by Neutron Diffraction Measurements.....	34
	S. Arai, T. Chatake, T. Ohhara, K. Kurihara, I. Tanaka, N. Suzuki, Z. Fujimoto, H. Mizuno and N. Niimura	
2.1.3	Neutron Diffraction Experiments of Insulin Crystal	36
	M. Maeda, T. Chatake, I. Tanaka, K. Kurihara and N. Niimura	
2.1.4	Neutron Fiber Diffraction of Troponin C within the Muscle Thin Filaments.....	37
	S. Fujiwara, F. Matsumoto and S. Deshimaru	
2.1.5	Small-angle Neutron Scattering of Smooth Muscle Heavy Meromyosin	38
	S. Deshimaru, S. Maruta, F. Matsumoto, T. Arata, K. Wakabayashi and S. Fujiwara	
2.1.6	Neutron Scattering Study on Self-assembly of Tau Molecules in Water	39
	S. Naito, M. Furusaka, S. Fujiwara, J. Suzuki, Y. Kobayashi and N. Niimura	
2.2	Soft Matter	41
	- Polymer Glasses, Gel and Phase Separation -	
2.2.1	<i>In-situ</i> SANS Observation of Enzymatic Polymerization of Artificial Cellulose	43
	H. Tanaka, T. Hashimoto, K. Kurosaki, M. Ohmae, S. Kobayashi and S. Koizumi	
2.2.2	Direct In-situ Observations in Living Anionic Polymerization by Small Angle Neutron Scattering	44
	K. Yamauchi, H. Hasegawa, T. Hashimoto, H. Tanaka, R. Motokawa and S. Koizumi	
2.2.3	Small-angle Neutron Scattering Observation on Soap-free Emulsion Polymerization of Poly (<i>N</i> -isopropylacrylamide)- <i>block</i> -poly (Ethylene Glycol).....	45
	R. Motokawa, T. Nakahira, M. Annaka, T. Hashimoto and S. Koizumi	
2.2.4	Small-angle Neutron Scattering Study on Living Radical Polymerization with Reversible-addition-fragmentation-chain-transfer (RAFT Polymerization) Process of Styrene... ..	46
	N. Mukawa, R. Motokawa, M. Takenaka, T. Hashimoto and S. Koizumi	
2.2.5	Viscoelastic Effects on the Nucleation and Growth in Semi-dilute Polymer Solution.....	47
	M. Takenaka, N. Iwase, T. Hashimoto and S. Koizumi	

2.2.6	Crystal Structure of Deuterated Polyethylene	48
	Y. Takahashi and T. Kumano	
2.2.7	The First Success in Direct Extraction of Hydrogen Atoms in Polyethylene Crystal	49
	K. Tashiro, I. Tanaka, T. Oohara, N. Niimura, S. Fujiwara, K. Kurihara and T. Kamae	
2.2.8	Observation of Niobates Nanosheets in Aqueous Solutions by Neutron Scattering	50
	D. Yamaguchi, N. Miyamoto, S. Koizumi, T. Nakato and T. Hashimoto	
2.2.9	Preparation of Palladium Nanoparticles with Dendrimers as Observed by SANS	51
	H. Tanaka, T. Hashimoto, H. Ito, K. Naka, Y. Chujo and S. Koizumi	
2.2.10	Structural Analysis of Polymer Electrolyte Membranes Based on Crosslinked Polytetrafluoroethylene by Small-angle Neutron Scattering	52
	T. Yamaki, M. Asano, R. Motokawa, S. Koizumi and M. Yoshida	
2.3	Strongly Correlated Electron Systems and Superconductivity	53
	-U-compounds, Ce- compounds, Transition-metal Oxides-	
2.3.1	Spin State Transition of $\text{Pr}_{1-x}\text{Ca}_x\text{CoO}_3$	55
	T. Fujita, Y. Yasui, T. Miyashita, Y. Kobayashi, M. Sato, Y. Shimojo, N. Igawa, Y. Ishii and K. Kakurai	
2.3.2	Two Magnetic Transitions of $\text{NdBaCo}_2\text{O}_5$	56
	M. Soda, Y. Yasui, M. Ito, S. Iikubo, M. Sato and K. Kakurai	
2.3.3	Structures and Spin States of $\text{NdBaCo}_2\text{O}_{5.5}$	57
	M. Soda, Y. Yasui, M. Ito, S. Iikubo, M. Sato and K. Kakurai	
2.3.4	Ni Impurity Effects on the Antiferromagnetic State in the Lightly Hole-doped $\text{La}_{2-x}\text{Sr}_x\text{CuO}_4$	58
	H. Hiraka, T. Machi, N. Watanabe, Y. Itoh, M. Matsuda and K. Yamada	
2.3.5	Magnetic Structure and Low Energy Excitation in a Non-centrosymmetric Heavy Fermion Superconductor CePt_3Si	59
	N. Metoki, K. Kaneko, T. D. Matsuda, A. Galatanu, T. Takeuchi, S. Hashimoto, T. Ueda, R. Settai, Y. Onuki and N. Bernhoeft	

2.3.6	Magnetic Structure of NpFeGa_5	61
	E. Yamamoto, N. Metoki, K. Kaneko, D. Aoki, Y. Homma, Y. Shiokawa and Y. Onuki	
2.3.7	Magnetic Structure, Phase Diagram, and Metamagnetic Transition in NpCoGa_5	62
	N. Metoki, K. Kaneko, E. Colineau, N. Bernhoeft, D. Aoki, Y. Homma, Y. Shiokawa, E. Yamamoto and Y. Onuki	
2.3.8	Magnetic Properties of $5f$ Itinerant Antiferromagnet UPdGa_5	64
	S. Ikeda, N. Metoki, Y. Haga, K. Kaneko, T. D. Matsuda and Y. Onuki	
2.3.9	Magnetic Excitations in Heavy-fermion Superconductor $\text{PrOs}_4\text{Sb}_{12}$	66
	K. Kuwahara, K. Iwasa, M. Kohgi, K. Kaneko, S. Araki, N. Metoki, H. Sugawara, Y. Aoki and H. Sato	
2.3.10	Effect of Magnetic Field on Static Spin Correlation in Electron-doped System	67
	M. Fujita, M. Matsuda, S. Katano and K. Yamada	
2.4	Magnetism and Low Temperature Physics	69
	- Low Dimension, Frustration, Magnetic Transitions and Quantum Liquids -	
2.4.1	Phonon Measurements in the Spin Gap System TlCuCl_3	71
	A. Oosawa, K. Kakurai and H. Tanaka	
2.4.2	Magnetic Excitations from the Linear Heisenberg Antiferromagnetic Spin Trimer System	72
	$\text{A}_3\text{Cu}_3(\text{PO}_4)_4$ with $\text{A}=\text{Ca}$, Sr , and Pb M. Matsuda, K. Kakurai, A. A. Belik, M. Azuma, M. Takano and M. Fujita	
2.4.3	Crystal and Magnetic Structures of Triple Perovskite $\text{Ba}_3\text{Fe}_2\text{ReO}_9$	73
	M. Wakeshima, K. Yamamura, Y. Hinatsu, N. Igawa and Y. Ishii	
2.4.4	Neutron Powder Diffraction Study for $S = 1/2$ Quantum Antiferromagnet NH_4CuCl_3	74
	M. Fujisawa, A. Oosawa, Y. Ishii, H. Tanaka and K. Kakurai	
2.4.5	Estimation of Temperature Dependence of Magnetic Structure of Z-type Barium Ferrite	75
	$\text{Ba}_3\text{Co}_{18}\text{Fe}_{242}\text{O}_{41}$ by Powder Neutron Diffraction Y. Takada, T. Nakagawa, Y. Fukuta, T. A. Yamamoto, T. Tachibana, T. Shimada, Y. Ishii and N. Igawa	

2.4.6	Crystal Structure of the Spin Gap System TiCuCl_3	76
	A. Oosawa, Y. Ishii, K. Kakurai and H. Tanaka	
2.4.7	Study of Ferromagnetism of CeP under High Pressure	77
	D. Kawana, T. Osakabe, A. Hannan and M. Kohgi	
2.4.8	Neutron Powder Diffraction Study of RB_{12}	78
	T. Osakabe and F. Iga	
2.4.9	Magnetic Field Effects on the Diffuse Scattering of a Spin-frustrated Spinel Ferrite ZnFe_2O_4 Single Crystal	79
	K. Kamazawa, K. Katano and Y. Tsunoda	
2.4.10	Antiferromagnetic Ordering in a Ternary Uranium Compound $\text{U}_3\text{Ni}_5\text{Al}_{19}$	81
	Y. Haga, N. Metoki, K. Kaneko and Y. Onuki	
2.5	Structural Physics	83
	- Ionic Conductivity, Phase Transition, Dynamics -	
2.5.1	Momentum Dependence of Low Energy Modes of Methane Hydrate	85
	T. Kamiyama, S. Ohonuma, D. Nio, Y. Kiyonagi, T. Uchida, T. Ebinuma, H. Narita, N. Igawa and Y. Ishii	
2.5.2	Thermal Vibration of Superionic Conducting Glass $(\text{AgI})_{0.8}-(\text{Ag}_2\text{MoO}_4)_{0.2}$	86
	D. Hosaka, A. Thazin, T. Shimoyama, T. Sakuma, H. Takahashi, M. Arai and Y. Ishii	
2.5.3	Phonon Study on High Performance Thermoelectric Material "Skutterudite"	87
	C. H. Lee, M. Matsuda and H. Sugawara	
2.5.4	Origin of FSDP for Superionic Silver Vanadate Glasses	88
	H. Takahashi, Y. Sanao, T. Sakuma and Y. Ishii	
2.5.5	Lattice Dynamics of PbTiO_3	89
	I. Tomeno, Y. Ishii, Y. Tsunoda, K. Oka and H. Unoki	
2.5.6	Structural Study of $\text{Ca}_3\text{Ru}_2\text{O}_7$ by Powder Neutron Diffraction	90
	Y. Yoshida, S. I. Ikeda, N. Shirakawa, N. Aso, M. Nishi, Y. Uwatoko and S. Katano	

2.5.7	Defect Structure of Oxygen-excess Pyrochlore-type $\text{Ce}_2\text{Zr}_2\text{O}_8$ Elucidated Using Neutron Powder Diffraction	91
	H. Otake, N. Igawa and Y. Ishii	
2.5.8	Modulated Structure of Bi-substituted Misfit Layered Cobaltite $[\text{Ca}_2\text{CoO}_3]_p\text{CoO}_2$	92
	Y. Miyazaki, Y. Suzuki, M. Onoda, N. Igawa, Y. Ishii, Y. Morii and T. Kajitani	
2.5.9	Direct Observation of the Hydrogen Transfer in the Solid-state Organic Photoreaction by Neutron Diffraction Method	93
	T. Hosoya, H. Uekusa, T. Ozeki, Y. Ohashi, T. Ohhara, I. Tanaka and N. Niimura	
2.5.10	Small-angle Neutron Scattering Study on the Precipitation of 6000 Al Alloys	94
	M. Ohnuma, J. Suzuki, T. Honma and K. Hono	
2.6	Materials Science and Industrial Applications	97
	- Microstructure and Residual Stress -	
2.6.1	Elastic Constants Measurement of NCF600 by Neutron Diffraction -Evaluation on Residual Stress of Weld Joint in Nuclear Core Internal Structure-	99
	R. Mizuno, A. Moriai, H. Suzuki and Y. Morii	
2.6.2	Development of New Stress Measurement Method Using Neutron Diffraction	100
	H. Suzuki, A. Moriai, N. Minakawa and Y. Morii	
2.6.3	Strain Measurement of $\text{Al}_2\text{O}_3/\text{YAG}$ Binary MGC by Neutron Diffraction	101
	H. Suzuki, Y. Waku, A. Moriai, N. Minakawa and Y. Morii	
2.6.4	Phase Transformation at Crack Tip of Shape Memory Alloy TiNi	102
	Y. Akiniwa, H. Kimura, K. Tanaka, N. Minakawa and Y. Morii	
2.6.5	Estimation of Change in Texture by Restoration of a Ferrite Steel after Large Strain Deformation	103
	T. Suzuki, Y. Tomota, M. Uno, A. Moriai, T. Kamiyama and H. Tashiro	
2.6.6	Residual Stress Measurement Using Neutron Diffraction for a Quenched Steel Bar with Induction Heating	104
	H. Tokuda, Y. Tomota, T. Suzuki, K. Kawasaki, A. Moriai, N. Minakawa and Y. Morii	

2.6.7	Distribution of the Martensite of Induction Hardened S45C Round Bar Observed by Small Angle Neutron Scattering	105
	K. Inoue, K. Aizawa, A. Moriai and F. Ikuta	
2.6.8	A Challenge to d_0 -Disused Neutron Stress Measurement Using Area Detector	106
	T. Sasaki, Y. Morii, N. Minakawa, N. Niimura and Y. Hirose	
2.6.9	Evaluation of Strength in Overlaid Materials by Neutron Diffraction	107
	T. Ishikawa, K. Miyata, H. Yano, R. Ishikawa, Y. Morii, A. Moriai and N. Minakawa	
2.6.10	Residual Strain Measurements in 3-axial Directions for 2-dimensional Cylindrical Carbon-carbon Composite by Neutron Diffraction Method	108
	S. Baba, N. Minakawa, A. Moriai, M. Yamaji and M. Ishihara	
2.6.11	Distribution of the Martensite of Induction Hardened S45C Round Bar Observed by Very Small Angle Neutron Scattering Apparatus PNO	109
	K. Inoue, T. Hirayama, K. Aizawa, A. Moriai and F. Ikuta	
2.6.12	Non-destructive Measurement of Residual Stress Beneath the Surface of Laser Peened Steel	110
	K. Akita, Y. Sano, T. Kubo, S. Ohya, H. Suzuki and A. Moriai	
2.6.13	Residual Stress Analysis of Metal/Ceramic Functionally Graded Materials	111
	M. Hataya, M. Nakagawa, T. Hanabusa, K. Kusaka, T. Matsubara, Y. Morii, N. Minakawa, A. Moriai and H. Suzuki	
2.6.14	Quality Estimation of Aluminum Die-casting by Neutron Diffraction	112
	M. Hataya, A. Moriai, H. Suzuki, Y. Morii, T. Hanabusa and N. Minakawa	
2.6.15	Investigation of the Residual Stress Measurement by the Neutron Scattering of an Amorphous Metal	113
	N. Minakawa, A. Moriai, H. Suzuki and Y. Morii	

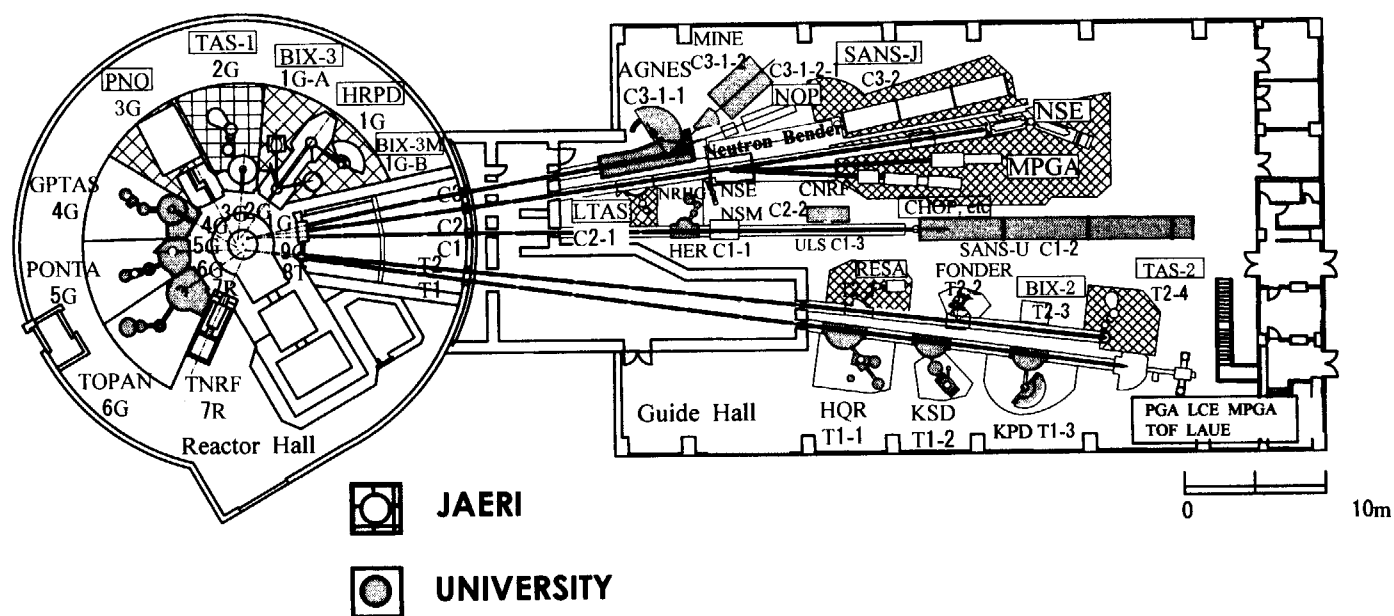
2.7 Fundamental Physics	115
- Interferometry -	
2.7.1 Development of High Intensity Ultracold Neutron Production with Ortho-deuterium	117
M. Utsuro, M. Tanaka, K. Mishima, Y. Nagai, T. Shima, Y. Fukuda, T. Kohmoto, T. Momose, A. Moriai, K. Okumura and H. Yoshino	
2.8 Instrumentation and Methods	119
- Extreme Conditions, Beam Handling, Detectors and Data Treatments -	
2.8.1 Development of the Thermal Neutron Focusing Device	121
T. Osakabe and K. Soyama	
2.8.2 Development of Electrostatic Levitation Furnace for Neutron Scattering Experiments of High Temperature Liquids	122
T. Masaki, T. Ishikawa, P. -F Paradis, Y. Arai, N. Igawa, Y. Ishii and S. Yoda	
2.8.3 Neutron Imaging Characteristics of CaBPO ₃ : Ce ³⁺ Based Photostimulable Phosphors	123
K. Sakasai, M. Katagiri, M. Matsubayashi, T. Nakamura and Y. Kondo	
2.8.4 CRYOPAD on the Triple-axis Spectrometer TAS-1 for Spherical Polarimetry	124
M. Takeda, M. Nakamura, Y. Shimojo, K. Kakurai, E. Lelievre-berna, F. Tasset and L. -P. Regnault	
2.8.5 Development of Cold Neutron Imaging Detector	125
H. Sakurai, F. Tokanai, S. Gunji, S. Motegi, M. Kaneko, S. Kikuchi, J. Suzuki and T. Oku	
2.8.6 A Study on Application of a Magnetic Neutron Lens to Focusing Geometry SANS Experiments	126
T. Oku, J. Suzuki, H. Sasao, T. Adachi, T. Shinohara, K. Ikeda, T. Morishima, K. Sakai and H. M. Shimizu	
2.8.7 Development of Optical Devices and Detectors for Cold Neutrons	128
H. M. Shimizu, T. Adachi, K. Ikeda, T. Shinohara, K. Hirota, H. Sato, Y. Takizawa, S. Morita, H. Ohmori, K. Sakai, T. Oku, J. Suzuki, S. Satoh and M. Furusaka	

2.8.8	Development of a High-performance Microstrip Gas Chamber with a Capability of Track Discrimination for Neutron Detection	129
	T. Nakamura, S. Masaoka, H. Yamagishi, K. Soyama and K. Aizawa	
2.9	Neutron Radiography	131
2.9.1	Neutron Irradiation Characteristics of CaBPO_5 : Ce^{3+} Based Photostimulable Phosphors	133
	K. Sakasai, M. Katagiri, M. Matsubayashi, T. Nakamura and Y. Kondo	
2.9.2	Development and Application of Neutron Radiography Techniques with High Temporal Resolution	134
	K. Mishima, Y. Saito and M. Matsubayashi	
2.9.3	Very Low Energy Neutron Radiography with Neutron Energy Selection System for Variable Image Contrast	135
	Y. Kawabata, T. Nakano, M. Hino, T. Oku, J. Suzuki and U. Matsushima	
2.9.4	Preliminary Bone Imaging Study Using Neutron Computed Tomography	136
	T. Takeda, Y. Tsuchiya, M. Matsubayashi, J. Wu, T. T. Lwin and A. Yoneyama	
2.9.5	3D Measurement of Void Distribution of Boiling Flow in a Tight-lattice Rod Bundle by Neutron Tomography	137
	M. Kureta and H. Tamai	
2.9.6	Experimental Study on Void Fraction in Tight-lattice Rod Bundles	138
	M. Kureta, H. Yoshida, A. Ohnuki and H. Akimoto	
2.9.7	Measurement of Vapor Behavior in Tight-lattice Bundles by Neutron Radiography	139
	M. Kureta and H. Akimoto	
2.9.8	Observation of Simulated Mixed OXide Fuel Rod by Neutron Radiography	140
	R. Yasuda, M. Nakata, M. Matsubayashi, A. Harada, K. Harada and Y. Nishino	
2.9.9	Observation of Hydrogen Distribution in Hydrogen-absorbing-alloys by Using Neutron-radiography Technique	141
	M. Matsubayashi, T. Ebisawa, K. Kubo, H. Arashima and H. Itoh	

2.10 Prompt γ -ray Analysis	143
2.10.1 Cadmium Analysis in Rice by Multiple Gamma-ray Detection Method	145
Y. Toh, M. Oshima, M. Koizumi, A. Osa, A. Kimura, J. Goto and Y. Hatsukawa	
2.10.2 Development of Neutron In-beam Mossbauer Spectrometer	146
M. K. Kubo, Y. Kobayashi, Y. Yamada, Y. Sakai, H. Shoji, C. Yonezawa and H. Matsue	
2.10.3 A Research on Boron in Soybean Plants Using Doppler Broadening of Prompt γ -ray	147
Y. Sakai, M. K. Kubo, H. Matsue and C. Yonezawa	
 Appendix	149
 Appendix A	151
Program Committee for Neutron Beam Utilization in the JFY 2003 of the Advisory Council for JAERI's Research Facilities	
 Appendix B	152
Themes of Cooperative Research Projects with Universities in the JFY 2003	
 Appendix C	155
Themes of Cooperative Research Projects with Private Enterprises and National Laboratories in the JFY 2003	
 Appendix D	156
Publication List in the Period of the JFY 2003	

Reactor Building



Experimental Building



JRR-3 Beam Experimental Facilities

This is a blank page.

Organization of JAERI (Neutron Science Relation in TOKAI)

Organization Name	Director Name	Group Name	Group Leader (Guest Scientist)
Department of Research Reactor	Director, F. Sakurai	Research Reactor Utilization Division	General Manager, H. Sagawa
Office of Planning	Director, S. Okada	Division of Collaborative Activities	Head, T. Inabe
Neutron Science Research Center 	Director, Y. Fujii Y. Morii ^{※1} S.K.Sinha ^{※2} (UCSD)	Research Group for Neutron Structural Biology	R. Kuroki
		Research Group for Neutron Scattering from Functional Materials	Y. Ishii
		R&D Group for Industrial Application of Neutron	T. Nakanishi (Tokyo Univ.)
		Research Group for Industrial Applica-tion of Neutron Structural analysis	Y. Morii
		R&D Group for Neutron Instrument	M. Arai (KEK)
		Research Group for Neutron Detector and Optical Device	K. Soyama
		Research Group for Nanostructure	S. Shamoto
		Research Group for Analysis of Biomacromolecular Function	N. Go
Advanced Science Research Center 	Director, H. Yasuoka T. Yamashita ^{※1} G. H. Lander ^{※2} (ITU)	Research Group for Neutron Scattering Study on Spin-Lattice Correlations	K. Kakurai
		Research Group for Neutron Scattering on Uranium System	N. Metoki
		Research Group for Soft Matter & Neutron Scattering	T. Hashimoto (Kyoto Univ.)
		Research Group for Neutron Optics	H. M. Shimizu (RIKEN)
Department of Materials Science	Director, Z. Yoshida	Research Group for Actinides Science	K. Minato

※1: Deputy Director, ※2: Invited Researcher

List of JAERI Instruments

A. Neutron Scattering Instruments

Beam Port	Instrument	Moderator	Instrument Staff
1G	High Resolution Powder Diffractometer (HRPD)	Thermal (H ₂ O)	Yoshinobu Ishii, Naoki Igawa, Yutaka Shimojo
1G-A	Diffractometer for Biological Crystallography-III (BIX-3)	Thermal (H ₂ O)	Taro Tamada
1G-B	Single Crystal Diffractometer for Biological Macromolecules(BIX-3M)	Thermal (H ₂ O)	Kazuo Kurihara
2G	Triple-Axis Spectrometer (TAS-1)	Thermal (H ₂ O)	Kazuhisa Kakurai, Susumu Katano
3G	Apparatus for Precise Neutron Optics and Neutron Diffraction Topography (PNO)	Thermal (H ₂ O)	Satoshi Koizumi, Kazuya Aizawa
T2-1	Diffractometer for the Residual Stress Analysis (RESA)	Thermal (H ₂ O)	Atsushi Moriai
T2-3	Diffractometer for Biological Crystallography-II (BIX-2)	Thermal (H ₂ O)	Takashi Ohhara
T2-4	Triple-Axis Spectrometer (TAS-2)	Thermal (H ₂ O)	Masaaki Matsuda
C2-1	Low energy Triple-Axis Spectrometer (LTAS)	Cold (Liquid H ₂)	Naoto Metoki
C2-2	New Reflectometer (C2-2)	Cold (Liquid H ₂)	Kazuhiko Soyama
C2-3-2-1 T-1-4-2	Multiple Prompt Gamma-ray Analysis (MPGA)	Cold (Liquid H ₂)	Masumi Ohshima
C2-3-3	(CHOP)	Cold (Liquid H ₂)	Kazuya Aizawa
C3-1-2-1	Neutron Optics (NOP)	Cold (Liquid H ₂)	Jun-ichi Suzuki, Takayuki Oku
C3-2	Small-Angle Neutron Scattering Instrument (SANS-J)	Cold (Liquid H ₂)	Satoshi Koizumi, Jun-ichi Suzuki
T1-4-1 C2-3-2-2	Prompt Gamma – ray Analysis System (PGA)	Cold (Liquid H ₂)	Hideki Matsue
T1-4-1A	Low Temperature Chemical Experiment Equipment (LCE)	Cold (Liquid H ₂)	Yasuyuki Aratono
T1-4-4 C2-3-3-4	Neutron Laue Diffractometer for Biology (LAUE)	Cold (Liquid H ₂)	Atsushi Moriai

B. Special Accessories

B-1. Cryostats, Magnets and Furnaces

Accessory	Number	Performance	Instrument Staff
Dilution Refrigerator	1	$T_{\min} = 10\text{mK}, H_{\max} = 5\text{T}$ (Vertical)	N. Metoki
Dilution Refrigerator (Liquid- ^4He -Free)	2	$T_{\min} = 50\text{mK}$	Y. Morii
10T Magnet (Liquid- ^4He -Free)	1	$T_{\min} = 100\text{mK}, H_{\max} = 10\text{T}$ (Vertical)	S. Katano
^3He Cryostat	1	$T_{\min} = 0.3\text{K}, H_{\max} = 6\text{T}$ (Vertical)	N. Metoki
Orange Cryostat	1	$T_{\min} = 1.5\text{K}$	T. Osakabe
Horizontal Magnet	1	$T_{\min} = 1.5\text{K}, H_{\max} = 5\text{T}$ (Horizontal)	J. Suzuki
4K Cryostat	2	$T_{\min} = 4\text{K}$	Y. Shimojo
10K Cryostat	6	$T_{\min} = 10\text{K}$	Y. Shimojo
Furnace for Soft Matter	1	$T = 0 - 300^\circ\text{C}$	S. Koizumi
800K Displex	1	$T = 5 - 800\text{K}$	M. Matsuda
Furnace	2	$T_{\max} = 1100\text{K}$	Y. Shimojo
Furnace	1	$T_{\max} = 1600\text{K}$	Y. Ishii

B-2. Pressure Devices

McWhan Cell	3	$P_{\max} = 2.5\text{GPa}$	T. Osakabe S. Katano
Sapphire Anvil Cell (under development)	several	$P_{\max} = 6\text{GPa}$	T. Osakabe
Oscillatory Shear Machine	1	$T = \text{RT} - 200^\circ\text{C}$, Amplitude = 0.01 - 2mm, Frequency = 0.1 - 100Hz	S. Koizumi
Tension Testing Machine	1	Tensile Speed = 0 - 0.01mm/sec, Range of Load = 50 - 1000kgf $\pm 1\%$	A. Moriai

B-3. Detectors

Neutron Imaging Plate	several	Resolution = 100 μm	R. Kuroki
-----------------------	---------	--------------------------------	-----------

This is a blank page.

1. Highlights in Research at JAERI

This is a blank page.

1.1 Neutron Diffraction Study of Biological Macromolecules Using BIX-type Neutron Diffractometers

R. Kuroki

Research Group for Neutron Structural Biology

Hydrogen atoms and water hydration surrounding biological macromolecules play important roles in many physiological functions. The neutron diffraction study of biological macromolecules using the neutron diffractometer equipped with an imaging plate system has become a powerful method of identifying the positions of hydrogen (deuterium) atoms and bound waters of biological macromolecules. Here, we describe three topics of the neutron crystallography of biological macromolecules, namely, B-DNA, porcine insulin and endopolygalacturonase I using neutron diffractometers (BIX-3 and 4) installed at JRR-3.

Neutron Diffraction Study of B-DNA

In the previous X-ray studies of DNA duplex, the hydration network structure around DNA was predicted using the oxygen positions of water molecules. To fully understand the role of hydrogen on the structure of B-DNA duplex, we determined the hydration patterns and hydrogen positions of B-DNA by both X-ray and neutron crystallographic analyses.

The neutron diffraction experiments were carried out using the BIX-4 diffractometer. The DNA sequence d(CCATTAAATGG)₂ was selected as a sample. To avoid the high background coming from the incoherent neutron scattering of hydrogen atoms, the crystallization experiments were carried out in

D₂O solutions. We used our refined result of X-ray structural analysis as the initial model of DNA structure for neutron analysis since the unit cell parameters of the X-ray data and the neutron data were almost the same (space group P3₂21, unit cell dimensions $a=b=32.9$ Å and $c=96.1$ Å).

It was determined that the spine of hydration in the minor groove of AT-tract DNA is built by the combination of many water bridges. In particular, previous X-ray studies showed that the hydration pattern in the minor groove has a simple hexagonal shape determined by the oxygen positions of water molecules. On the other hand, by determining H and D atoms, we succeeded in observing the complex water network in the minor groove. Figure 1 shows the schematic diagram of the hydrogen bond network in the minor groove of d(CCATTAAATGG)₂, which was obtained from our measurements. In Fig. 1, the oxygen atoms of D₂O observed by X-ray analysis were superimposed on the results obtained by neutron structural analysis. In this figure, the hexagonal hydration pattern is shown by lines colored in red. As shown in Fig. 1, we found that the observed hydration network in the minor groove exhibits both a simple hexagonal pattern and many water bridges bonded to the DNA molecules. These results suggest that many hydrogen bonds between the spine of hydration and DNA strands support the B-DNA helical structure.

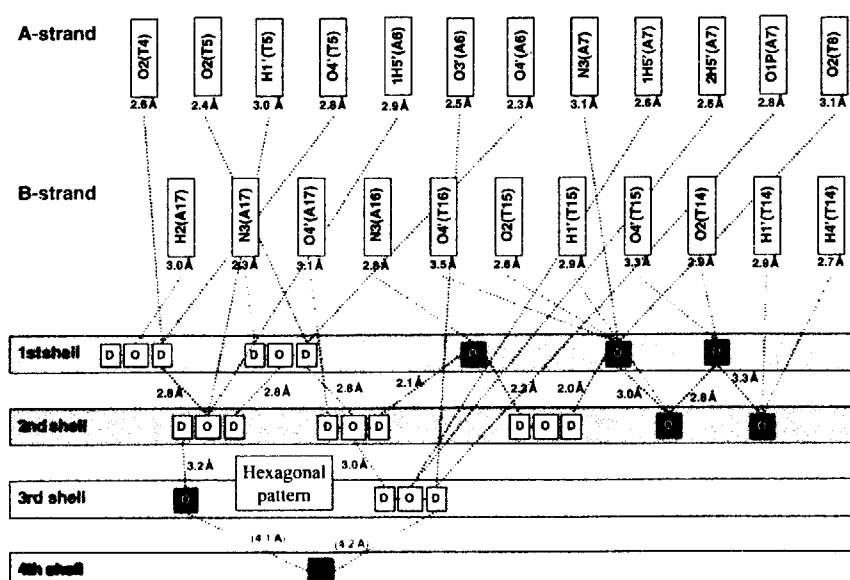


Figure 1:
The schematic diagram of the hydrogen bonds network in the minor groove of d(CCATTAAATGG)₂. The oxygen atoms of water observed by X-ray diffraction are colored in blue. The hexagonal hydration pattern is shown in the lines colored in red.

Neutron Diffraction Study of Porcine Insulin

The cubic insulin crystal (space group $I213$, $a=b=c=78.9$ Å) contains a solvent volume of 65% and has multiple hydration layers. To elucidate hydrogen and hydration in cubic insulin crystals, a large single crystal of cubic insulin ($4.0 \times 4.0 \times 1.3$ mm³ in volume) for neutron protein crystallography was grown in D₂O by a phase diagram technique. The neutron diffraction experiments were carried out at room temperature with the BIX-type neutron single-crystal diffractometer installed at JRR-3.

The crystal was sealed in a quartz capillary for the measurement. The step scanning method was used for the data collection. The collection time per frame was controlled to be 55 minutes on the basis of the monitor counts of the direct beam in front of the crystal.

The protonation and deprotonation of two nitrogen atoms (N_π and N_τ) in the imidazole ring of histidine provide very important information for discussing protein crystallography. This information can be given by neutron diffraction. Figure 2 shows the $2Fo-Fc$ positive nuclear density map for His5 in the B-chain (B5 His) and His10 in the B-chain (B10 His). In His5 in the B-chain, N_π is protonated and N_τ is deprotonated. In contrast, in B10 His, both N_π and N_τ are protonated. This indicates that B5 His is electrically neutral and B10 His is positively charged.

Reference M.Maeda *et al.*: J.Synchrotron Radiat.11 (2004) 41.

Neutron Structure Analysis of Endo-polygalacturonase I from *Stereum Purpureum*

Endopolygalacturonases (endoPGs, EC 3.2.1.15) catalyze the hydrolysis of the α -1,4-glycosidic linkages between adjacent α -D-galacturonic acid residues within the pectin main chain. The X-ray crystal structure analyses of endoPG I from *Stereum purpureum* identified catalytic residues and accounted for the general acid-base catalysis of the enzyme. However, it was impossible to specify experimentally which catalytic residue is a general base or acid because no significant electron density for hydrogen atoms is observed around catalytic residues. In view of this, we prepared single-crystals suitable for high-resolution neutron crystal structure analysis with hanging-drop vapor diffusion, followed by macroseeding in sitting-drop (drop: 0.5 ml, reservoir: 4 ml) vapor diffusion. The typical dimensions of the crystals grown were $3.0 \times 1.9 \times 0.8$ mm. The crystals were soaked for 40 days in a reservoir solution containing 25% PEG4000, which was prepared with D₂O, and then used in the neutron experiments.

Neutron diffraction data were collected up to 1.5 Å resolution, with a completeness of 81% and $R_{\text{merge}} = 0.12$, using a single-crystal diffractometer (BIX-4). The initial structure, obtained by X-ray analysis, was refined using the program CNS, and manually modified using the program O. Further refinement by simulated annealing and energy minimization is in progress.

Reference T.Shimizu *et al.*: Biochemistry 41 (2002) 6651.

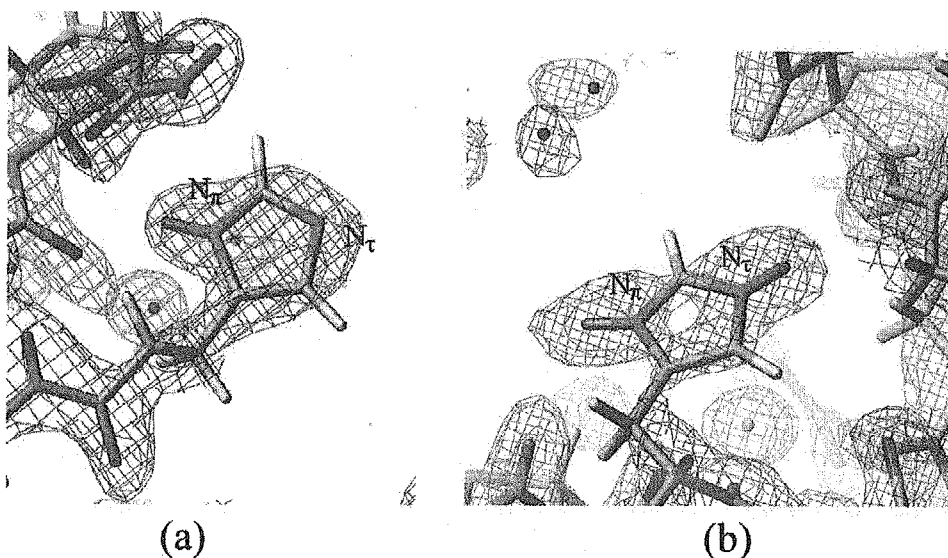


Figure 2:
2Fo-Fc positive nuclear density map of (a) His5 in the B-chain and (b) His10 in the B-chain of cubic insulin.

1.2 Neutron Scattering Studies of Structure Functionality of Soft Matters

T. Hashimoto

Research Group for Soft Matter & Neutron Scattering

Soft matters (or complex liquids) comprise various systems such as polymers, membranes, micelles, liquid crystals, gels, colloids, supercooled liquids, and multicomponent liquids. They are an assembly of molecules and/or supramolecules, and have a hierarchical structure composed of various levels of structural units with a spatial scale ranging from nanometers to microns, and a time scale ranging from picoseconds to hours. Their hierarchical structure is easily reorganized in response to environmental changes such as temperature and pressure and to various external stimuli, such as flow, deformation, chemical reactions, and electromagnetic radiation. Fundamental studies of these phenomena, and the self-organization and reorganization of the hierarchical structure of soft matters, would make an important contribution to the physics of "open" nonequilibrium systems, i.e., systems open to various external energy flows as described above.

In the research on soft matter and neutron scattering, we aim to explore "the mechanics" of molecular assemblies. By an advanced small-angle scattering technique, we will explore in-situ and real-time processes of the formation or

organization of structural units and processes of structural units that change their size and shape. Special emphasis will be focused on elucidating the role of chemical reactions in the mechanics of various molecular assemblies or their hierarchical structures.

For this purpose, our research group will upgrade two existing spectrometers for small-angle neutron scattering, SANS-J and PNO (Fig. 1: SANS-J and PNO). The focusing lenses of MgF₂ and sextupole permanent magnet are planned to be installed on SANS-J (a pin-hole small-angle scattering spectrometer) in collaboration with the neutron optics research group (NOP). With these focusing devices, we aim to access up to a smaller limit of $q \sim 10^{-4} \text{ \AA}^{-1}$ and to achieve a higher gain of intensity, both of which will be improved by an order of magnitude compared with the current spectrometer. The lowest $q \sim 10^{-5} \text{ \AA}^{-1}$, which is inaccessible by pin-hole SANS, should be covered using PNO with a Bonse-Hart-type double-crystal setup. Effort to improve PNO is now focused on reducing measurement time and noise level. As for the former objective, we will construct a tandem countersystem, which will be reported elsewhere.

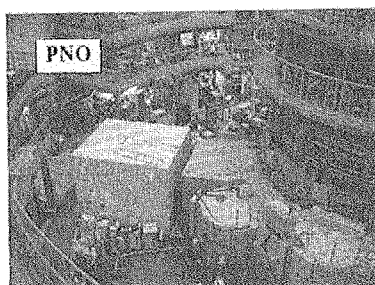
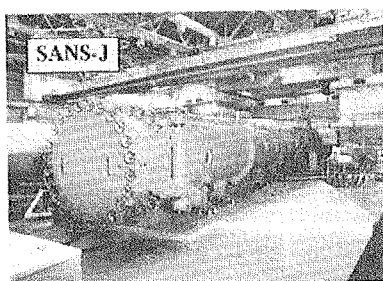


Figure 1:
Pin-hole SANS spectrometer (SANS-J) and
double crystal ultra SANS spectrometer (PNO).

In vivo biosynthesis of cellulose

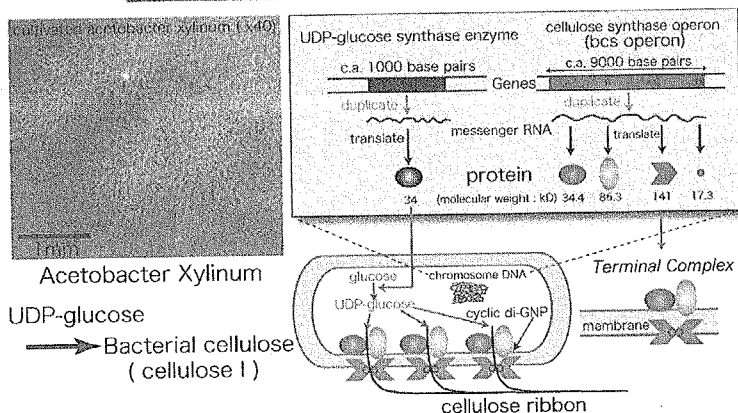


Figure 2

We present one example of our current activities, exploring the molecular assemblies in chemically reacting systems, that is in situ and real-time observations in the in vitro synthesis of cellulose via enzymatic polymerization. The bi-macromolecule "cellulose" is generally synthesized in vivo via a biosynthetic pathway. Figure 2 shows the schematic diagram of "*Acetobacter xylinum*" (at the lower right corner), which forms a cloud of crystallized cellulose fibrils outside its body via the in vivo synthesis of cellulose. The in vitro synthesis of cellulose, which has been hardly achieved since its first attempt in 1941, was successful, starting with a mixture of β -cellobiosyl fluoride (substrate monomer) and the enzyme "cellulase" (polymerization catalyst) dissolved in an aqueous organic solvent (acetonitrile/acetate buffer) (Fig. 3: Kobayashi *et al.*, J. Am. Chem. Soc., 113, 3079 (1991)). The cellulose of about 22 glucose units thus successfully obtained is highly regio- and stereo-controlled so as to have a primary structure exactly identical to that of native cellulose.

We performed in situ SANS and USANS during the in vitro synthesis of cellulose. Before starting polymerization, SANS shows a power law behavior of $q^{-\alpha}$ ($\alpha=4$, Porod's law)

originating from a sharp and smooth interface of enzyme aggregates with several hundreds of nanometers in the polymerization medium. After starting polymerization, the power law changes; as polymerization proceeds, α starts to decrease and finally reaches $\alpha=3.7$ (Fig. 4).

This power law behavior of $\alpha=3.7$ can be recognized between the upper cut-off length scale covered by USANS ($\sim 10\mu\text{m}$) and the lower cut-off length scale covered by SANS (10nm). Thus, we confirmed that the synthesized cellulose form a crystalline aggregate on the surface of enzyme aggregates with a self-similar surface having the surface fractal dimension $D_s=2.3$, where $D_s=6-\alpha$, extending over such a strikingly large length scale over 3 orders of magnitude, which has hardly been reported so far. The diffusion-limited aggregation of an enormous number of cellulose macromolecules will inevitably end up forming such a unique surface fractal structure on the surface of nearly spherical enzyme aggregates, as described above (Fig. 5).

In vitro synthesis of cellulose via enzymatic polymerization

Kobayashi *et al.* J. Am. Chem. Soc., 113, 3079 (1991), *Macromolecules*, 25, 3237 (1992),
Chem. Lett., p.393 (1992)

- enzyme : cellulase (normally used as enzyme for hydrolysis reaction of cellulose)
- substrate (monomer) : β -D-cellobiosyl fluoride (minimum unit recognized by cellulase)

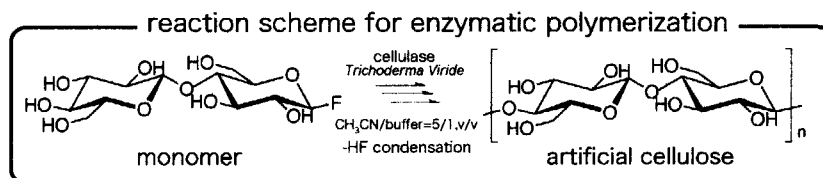


Figure 3

In-situ SANS observation of enzymatic polymerization

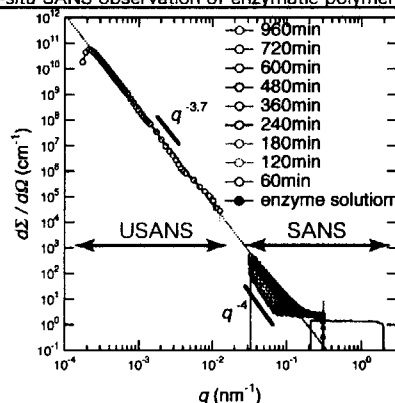


Figure 4

Possible mechanism of enzymatic polymerization

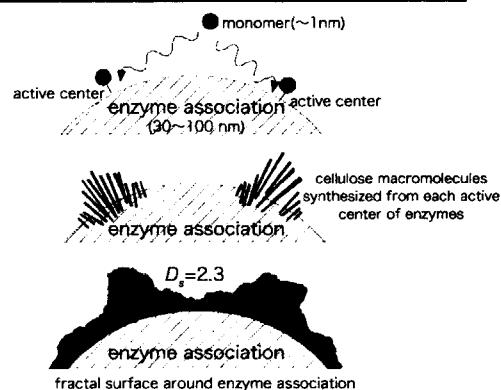


Figure 5

1.3 Neutron Scattering Research on Spin-lattice Correlations

K. Kakurai

Research Group for Neutron Scattering Study on Spin-Lattice Correlations

The aim of the research project on spin-lattice correlations using neutron scattering is to determine the role of the correlation between spin degrees of freedom and other degrees of freedom as charge and orbital degrees of freedom respectively, which are closely associated with the lattice. These spin-lattice correlations may play important roles in explaining novel phenomena in condensed matters as in high- T_c superconductors, CMR materials, and magnetically low-dimensional and frustrated systems. In this project, emphasis is given on the utilization of polarized neutron scattering for this purpose.

Installation of the Cryogenic Polarization Analysis Device (CRYOPAD) on TAS-1

CRYOPAD is a novel polarization analysis device for measuring the spherical (3-dimensional) changes of neutron spin polarization in scattering. ILL and CEA-Grenoble, in the framework of EC/ENPI, and JAERI, in the framework of the MoU between ILL and ASRC JAERI, have designed and assembled three third-generation CRYOPADs at ILL. One of these devices, optimized for both elastic and inelastic

scatterings, has been now successfully installed on the triple-axis spectrometer TAS-1 at JRR-3. As shown in Fig.1, the CRYOPAD consists of a couple of Nb Meissner screens and a hybrid precession torus (HPT) which has two independent precession coils for incident and outgoing neutrons. The inner and outer Meissner screens cooled to the superconducting state using liquid He serve to realize the zero-magnetic-field condition around the sample (residual magnetic field at sample position is less than 0.3nT) and to separate the precession field from the nutator field just outside the outer screen, respectively. As shown in the schematic in Fig.1, the combination of spin rotation in the nutator and HPT in the incident and outgoing beam independently enables the three-dimensional control of the incident polarization direction and outgoing analyzing direction (Fig.2). The instrument is currently being calibrated and tested. Figure 3 shows the result of spin rotation in the incident HPT.

First, the instrument will be primarily used in determining complex magnetic ground states in frustrated magnets and strongly correlated electron systems, where the ground states are expected to result from the subtle balance of magnetic and lattice couplings. Parallel to this, we will search for systems in which we could directly observe the nuclear-magnetic interference term in excitation spectra.

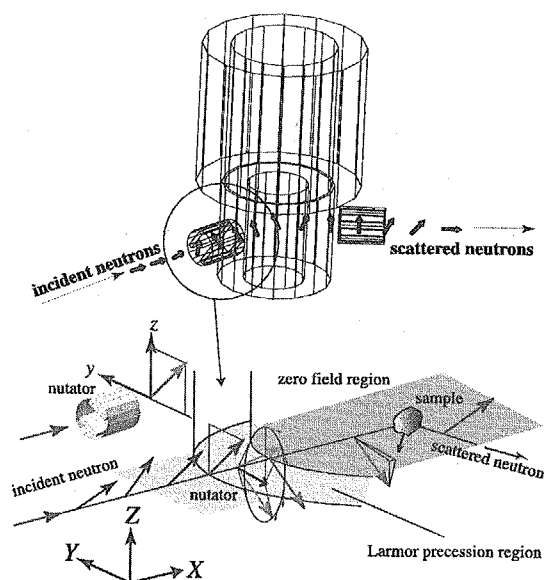


Figure 1: Schematic drawing showing the principal neutron spin rotations in the CRYOPAD.

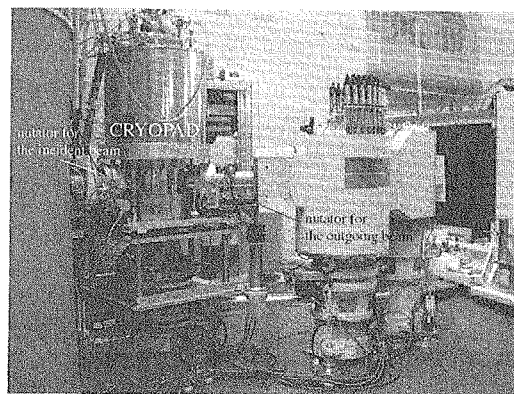


Figure 2: CRYOPAD installed on TAS-1.

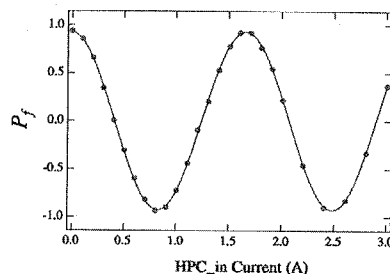


Figure 3: Neutron spin rotation using the incident HPC.

Spin-Lattice Correlation in Quantum Spin System

TiCuCl₃ is a spin singlet ground-state system with an excitation gap of $\Delta=7.5$ K. This system exhibits various quantum phase transitions such as field-induced, impurity-induced and pressure-induced magnetic orderings. Figure 5 shows the schematic of the pressure induced magnetic orderings. The system consists of three dimensionally weakly coupled spin ($S=1/2$) dimers. Upon the application of hydrostatic pressure, interdimer distance is reduced; hence, interdimer magnetic exchange interactions are increased. When interdimer correlation has developed sufficiently the system favors the magnetic ordered state. This is the quantum phase transition from the singlet ground-state phase to the magnetic ordered phase. This quantum phase transition can be directly observed by a neutron diffraction experiment, considering the development of the magnetic Bragg peak, as indicated in Fig.4. The polarized neutron scattering study of pressure-induced phase transition, however, revealed the successive nature of the phase transition at a relatively high pressure of 1.48 GPa. Using polarized neutron scattering, the spin components in and out of the scattering plane can be completely separated by measuring spin-flip and non-spin-flip

magnetic scatterings, respectively, when the polarization direction of the neutron spin at the sample position is perpendicular to the scattering plane. Figure 5 clearly shows that the spin component outside the scattering plane appears at the second magnetic phase transition at $T_{SR}=10$ K below $T_N=16.9$ K. Thus, the polarized neutron scattering experiment unambiguously demonstrates that this additional transition is associated with spin reorientation. This phenomenon can be regarded as a result of spin-phonon coupling in this system as has been already indicated by NMR and sound attenuation studies. To directly investigate spin-phonon coupling, phonon excitation in TiCuCl₃ has been studied over a wide temperature range from 4 K to R.T. Figure 6 depicts the temperature dependence of acoustic phonon excitation energy at $Q=(2.4,0,0)$. The excitation energy first gradually increases with decreasing temperature from $T=300$ K, but then shows a rapid increase below $T=50$ K. From the susceptibility measurement, the magnetic susceptibility has a broad maximum at around 38 K and decreases steeply towards zero with decreasing temperature to $T=0$ K, indicating the development of an antiferromagnetic short-range correlation below 38 K. Hence, it is tempting to infer that the rapid phonon excitation energy increase observed in the present experiment directly correlates to the development of an antiferromagnetic short-range correlation, i.e., the formation of spin singlet dimers.

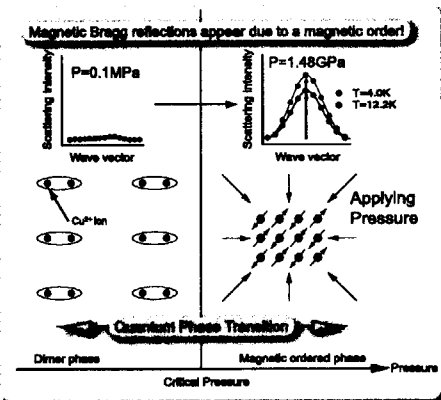


Figure 4: Pressure-induced quantum phase transition between the dimer phase and the magnetic ordered phase.

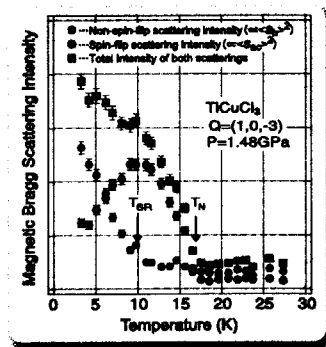


Figure 5: Temperature dependence of the magnetic Bragg scattering intensities in TiCuCl₃ at $P=1.48$ GPa.

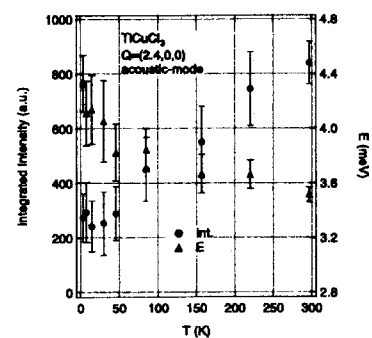


Figure 6: Temperature dependence of the integrated intensity I (solid points) and the excitation energy E (open points) of the acoustic mode at $Q=(2.4,0,0)$ in TiCuCl₃.

1.4 Neutron Scattering Studies on the f-electron Systems

N. Metoki

Research Group for Neutron Scattering on Uranium System

Superconductivity, discovered by Kamerlingh-Onnes in 1911, is a quantum mechanical phenomenon, in which materials show a zero electric resistivity at low temperatures as a result of the macroscopic phase coherence of conduction electrons propagating in solids. This phenomenon has been understood in terms of the phenomenological theory and the microscopic explanation, that is, the BCS theory, was presented 50 years after the discovery of superconductivity. In the past decades, many conventional BCS-type superconductors as well as exotic superconductors based on intermetallic compounds, organic materials, oxides such as high- T_c cuprates, and actinide compounds have been reported and have attracted strong interests from many scientists; this has been called the “*Renaissance of superconductivity*”. Superconductivity is also important for industrial applications such as high-field magnets, and electronic devices.

After the introduction of the BCS theory, it became known that two propagating electrons pair in the superconducting state, called the Cooper pair. The energy gain from the condensate pairing state to the normal metallic state is called the superconducting gap. The attractive force in the Cooper pair is mediated by the vibration of the crystallographic lattice, i.e., phonons, in BCS-type superconductors. On the other hand, it is believed that the pairing mechanism in unconventional superconductors such as high- T_c cuprate and

uranium superconductors, are not phonic ones, but magnetic fluctuations play an important role in such a mechanism. Superconductivity coexists with strongly suppressed magnetic ordering, or the superconducting phase exists in the vicinity of the quantum critical point, where there is strong magnetic fluctuation. In these systems, conduction electrons have a strong repulsion (strong correlation effect), thus pairing without an overlap of the wave function is energetically favorable. This can result in non- s -wave pairing, such as p -wave or d -wave non-BCS-type superconductivity with an anisotropic gap closing along the line node or on the point node.

Very recently, a new type of superconductor $\text{PrOs}_4\text{Sb}_{12}$ belonging to the family with the filled-skutterudite structure shown in Fig. 1 has been discovered [1]. This compound exhibits superconductivity below $T_c = 1.85$ K. Many experimental studies have shown an unconventional superconductivity in $\text{PrOs}_4\text{Sb}_{12}$, namely, there is a multiple superconducting phase involving internal degrees of freedom, anisotropic gap behavior, and the existence of an internal field in the superconducting state indicating broken time reversal symmetry in Cooper pairs. $\text{PrOs}_4\text{Sb}_{12}$ shows no magnetic ordering down to 50 mK, instead, a field-induced ordered phase has been reported in this compound with the application of a high magnetic field [2]. Neutron scattering experiments have been carried out to clarify this field-induced ordered phase on an

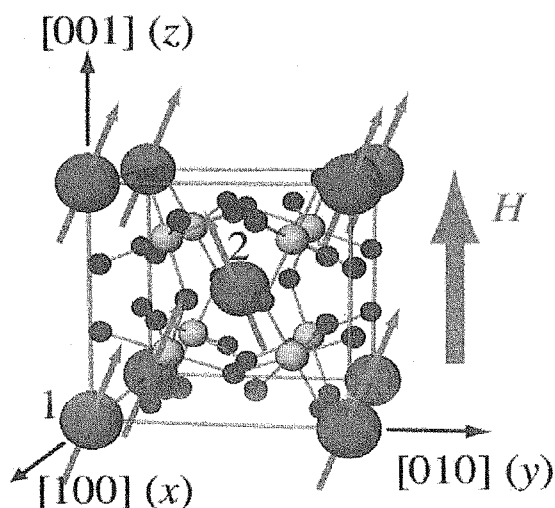


Figure 1(a):
The crystal structure of $\text{PrOs}_4\text{Sb}_{12}$ and the antiferromagnetic structure in the field induced antiferroquadrupolar ordered phase.

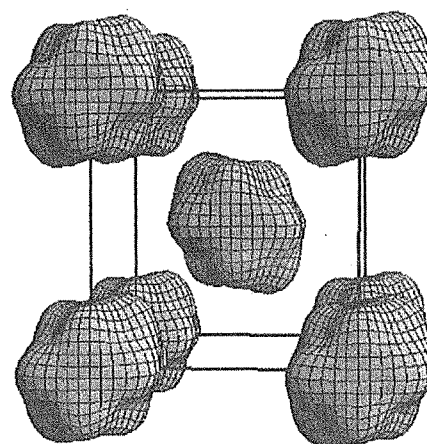


Figure 1(b):
The orbital structure of $\text{PrOs}_4\text{Sb}_{12}$ in the field induced antiferroquadrupolar ordered phase.

LTAS spectrometer using a liquid-He-free 10 T magnet and a ^3He - ^4He dilution refrigerator without liquid He as cryogen, both developed by JAERI [3,4].

We found antiferromagnetic superlattice reflections with $q=(100)$ observed in the field-induced ordered phase. Figure 2 shows the representative data measured in (210) reflection. A distinct antiferromagnetic peak was observed with the application of a field of 8 T at 0.25 K, while no trace of this peak was found for $H = 0$ T. From the integrated intensities of antiferromagnetic scattering on the $(hk0)$ scattering plane, we conclude that there is an antiferromagnetic component as large as $0.02 \mu_B$ along the $[010]$ direction. The magnetic structure is shown in Fig. 1. This antiferromagnetic structure and its temperature and field dependence have been explained by the field-induced antiferroquadrupolar ordering based on the f electron model with the singlet ground state and triplet excited state [3]. The ordering of the f electron orbital is schematically shown in Fig. 1 (b). The triplet excited state splits into three singlets and the level crossing of the two lowest singlets results in antiferroquadrupolar ordering. The field dependence of excitation level is also measured [4] and showed good agreement with that obtained using the model calculation, as shown in Fig. 3.

The phase diagram of $\text{PrOs}_4\text{Sb}_{12}$ is schematically shown in Fig. 4(a). The superconducting phase exists very close to the

antiferroquadrupolar phase. It should be noted that a strong magnetic and quadrupolar, namely, orbital fluctuation exists in the paramagnetic phase between the antiferroquadrupolar and superconducting phases. This f electron state with multiple degrees of freedom would be the origin of the heavy-fermion superconducting state, involving the possibility of realizing superconductivity mediated by orbital fluctuation which would play a dominant role in anisotropic superconducting pairing. This is suggested from the comparison of the phase diagram in high- T_c and uranium superconductors shown in Fig. 4(b), where superconductivity exists in the vicinity of the magnetically ordered phase with a strong magnetic fluctuation. Further studies are necessary to shed light on the microscopic mechanism of superconductivity in $\text{PrOs}_4\text{Sb}_{12}$.

References

- [1] E.D.Bauer, N.A.Frederick, P.-C. Ho, V.S.Zapf and M.B.Maple, Phys. Rev. B65 (2002) 100506(R).
- [2] Y.Aoki, T.Namiki, S.Ohsaki, S.R.Saha, H.Sugawara and H.Sato, J.Phys. Soc. Jpn. 71 (2002) 2098.
- [3] M.Kohgi, K.Iwasa, M.Nakajima, N.Metoki, S.Araki, N.Brnhoeft, J.-M. Mignot, A.Gukasov, H.Sato, Y.Aoki and H.Sugawara, J.Phys. Soc. Jpn. 72 (2003) 1002.
- [4] K.Kuwahara, K.Iwasa, M.Kohgi, K.Kaneko, S.Araki, N.Metoki, H.Sugawara, Y.Aoki and H.Sato, J.Phys. Soc. Jpn. 73 (2003) 1438.

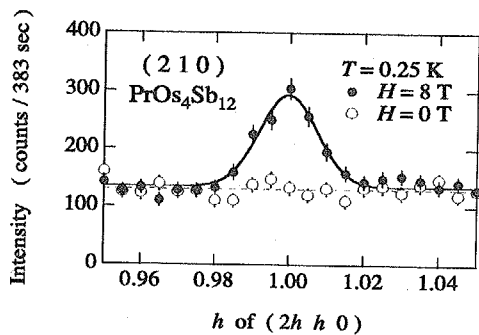


Figure 2: The (210) antiferromagnetic reflections induced by the antiferroquadrupolar ordering measured at 0.25 K with application of the magnetic field $H = 8$ T denoted by close circles, which disappeared for $H = 0$ T as indicated by open circles.

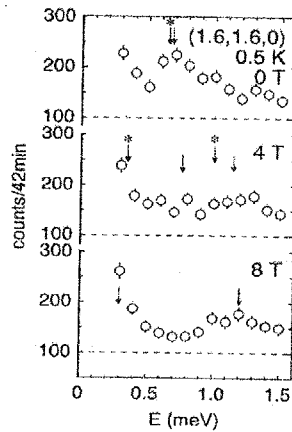


Figure 3: The inelastic scattering profiles under magnetic field. The arrows indicate the peak position expected from the model calculation based on the singlet ground state with triplet excited state. Meanwhile arrows with asterisk are the excited energy for doublet ground state with triplet excited state, which obviously disagree with experiments.

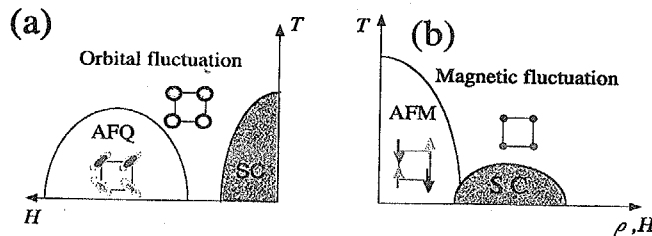


Figure 4: The schematic phase diagram of (a) $\text{PrOs}_4\text{Sb}_{12}$ and (b) High- T_c or uranium superconductors.

1.5 Neutron Scattering Studies of Functional Materials

Y. Ishii

Research Group for Neutron Scattering from Functional Materials

Studies of Methane Hydrate

Methane hydrate is an energy resource for the next generation. The energy from the accumulated methane hydrate on the sea floor near Japan is 100 times that from the consumed natural gas per year. Regarding its application, methane hydrate is used as the moderator material for a pulsed neutron source.

Study of Incoherent Inelastic Neutron Scattering of Methane Hydrate

The measurement of the inelastic neutron scattering of methane hydrate (D_2O+CH_4) was conducted using the low-energy triple-axis spectrometer (LTAS) installed in the JRR-3 guide hall. In Fig. 1, one can see a peak at a transfer energy of about 1.0 meV. This transfer energy is the energy required to excite from $J=0$ to $J=1$ levels in the rotation of methane molecules. Although the peak intensity measured at 10 K is large, the intensity decreases with increasing temperature, and at 100 K, this peak almost disappears. These results are almost the same as those for the natural methane hydrate examined by Gutt *et al.* using a pulsed neutron source.

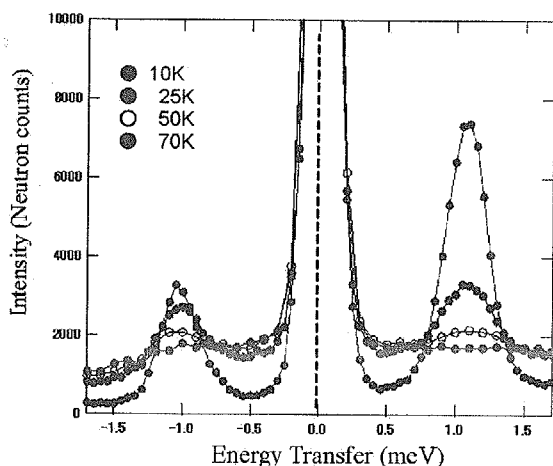
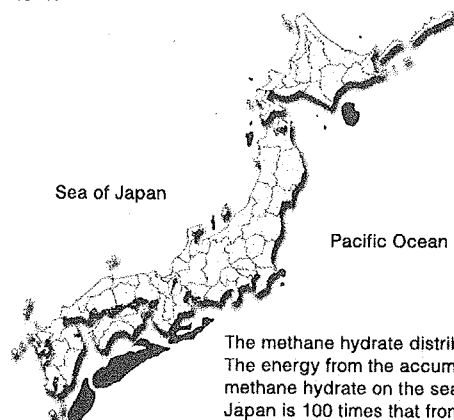


Figure 1:
Incoherent inelastic neutron scattering of synthesized methane hydrate (D_2O+CH_4).

Momentum Dependence of Diffraction Intensity of Low-energy Modes of Methane Hydrate

Methane hydrate is a good moderator material because it has a high hydrogen density and a large density of states around the thermal energy region (1-100 meV) for producing a well-defined Maxwellian. Figure 2 shows the E-constant spectra of $S(Q,E)$ around $E=6.5$ and 8 meV measured using TAS-1.



The methane hydrate distribution map. The energy from the accumulated methane hydrate on the sea floor near Japan is 100 times that from the consumed natural gas per year.

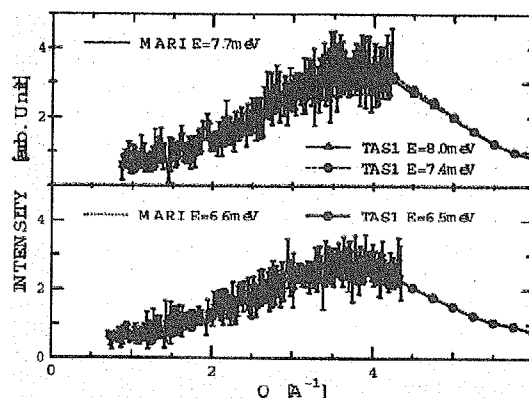


Figure 2:
Q-dependence of neutron diffraction intensities of methane hydrate.

Studies of Crystal Structure and Magnetic Structure of Functional Materials

The crystal and magnetic structures of the triple-perovskite-type compound $\text{BHf}_3\text{Fe}_2\text{ReO}_9$ were investigated because this compound showed a complex magnetic behavior below 50 K. The measurement was performed at 10 K and 300 K using a high-resolution neutron powder diffractometer (HRPD). The collected data were analyzed by the Rietveld method. The determined crystal and magnetic structures are shown in Fig. 3. The ordered magnetic moments was considerably smaller than the theoretical one of Fe^{3+} . From this experiment, the randomness of Fe and Re ions in the dimer sites led to the frustrations between magnetic couplings such as in the spin glass system.

The thermoelectric (TE) material $[\text{Ca}_2\text{Co}_3]\text{pCuO}_2$ has excellent TE properties at high temperatures. The modulated crystal structure of the Bi-substituted compounds was investigated to clarify the site performance of Bi and substitution effects. The fundamental crystal structure is shown in Fig. 4. The result structure formula is expressed as $[(\text{Ca}_{0.90}\text{Bi}_{0.10})_2(\text{Co}_{0.05}\text{Bi}_{0.05})\text{O}_3]_{0.618}\text{CoO}_2$. The observed increases in the Seebeck coefficient and electrical resistivity of the Bi-sub-

stituted phase can be explained in terms of the decrease in hole concentration in the CoO_2 sheet.

Development of Extremely High Temperature Furnace for Neutron Scattering Experiments

For very high temperature neutron scattering experiments, we developed an electrostatic levitation furnace. Figure 5 shows a levitated liquid Zr at 2100 K. The shape of the liquid Zr sample was almost spherical and its diameter was about 3 mm. This furnace was installed at the high-resolution neutron powder diffractometer (HRPD) in the JRR-3 reactor hall.

The experiment was successfully performed and the levitated molten Zr at the temperature 2100 K could be kept for twenty hours. The result of the neutron diffraction experiment of molten Zr is shown in Fig. 6. The shape of the scattering intensity is regarded as a typical diffraction pattern of liquid Zr. Since the volume of the sample is small, the diffraction intensity is insufficient. We are expecting to obtain an intense neutron beam from the J-PARC project in the near future, and extremely high temperature neutron experiments are expected to be performed using this furnace.

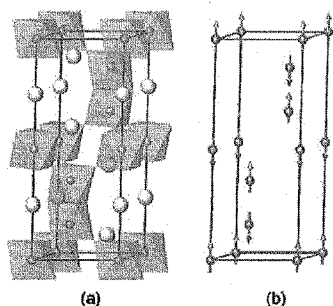


Figure 3:
Crystal and magnetic
structures of $\text{BHf}_3\text{Fe}_2\text{ReO}_9$.
a) crystal structure and
b) magnetic structure.

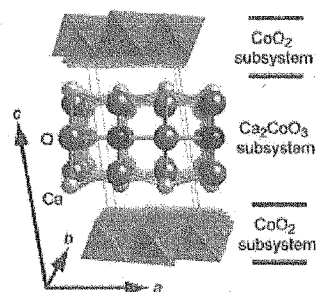


Figure 4:
Crystal structure of the
thermo-electric material.

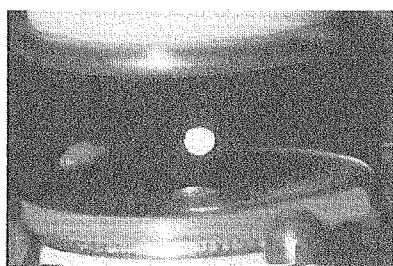


Figure 5:
Levitated liquid-Zr at 2100 K. A shape of
liquid-Zr sample was almost spherical and its
diameter was about 3 mm.

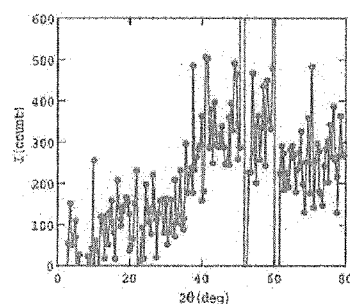


Figure 6:
Neutron diffraction pattern of liquid Zr
measured at 2100 K.

1.6 Neutron Diffraction Studies of Industrial Materials

Y. Morii

Research Group for Industrial Application of
Neutron Structural analysis

Residual Stress Analysis

For a detailed analysis of residual stress at any points in a sample, we should measure the spacing of diffraction planes along the three orthogonal directions by a conventional or general method. In this measurement, the sample will be replaced from a sample table of a diffractometer and reinstalled on the table. This reinstallation of the sample will cause measurement-positional error, and this positional error will become large with decreasing gage volume in precise measurements.

Development of New Method of Residual Stress Analysis and Measurement Technique

d_0 , which is defined the d-space of diffraction line under free stress, affects residual stress in calculation. For example, at a heat-affected zone near the welding part in steel, we do not determine d_0 by a destructive method, because of

martensite transformation.

Morii's group took the challenge of eliminating these problems, i.e., they developed a new residual stress measurement method without the reinstallation of the sample, and a new analysis method for the estimation of lattice constant. Figure 1 shows the lattice constant and stress versus the uniaxial applied stress for the Ni-base alloy NCF600 without measured d_0 . The stress-free lattice constant, a , takes almost a constant value and is independent of applied stress. This result was the same as that of another measurement. Therefore, this new method is quite useful for the measurement of the residual stress of industrial materials having a complex shape such as motor engines.

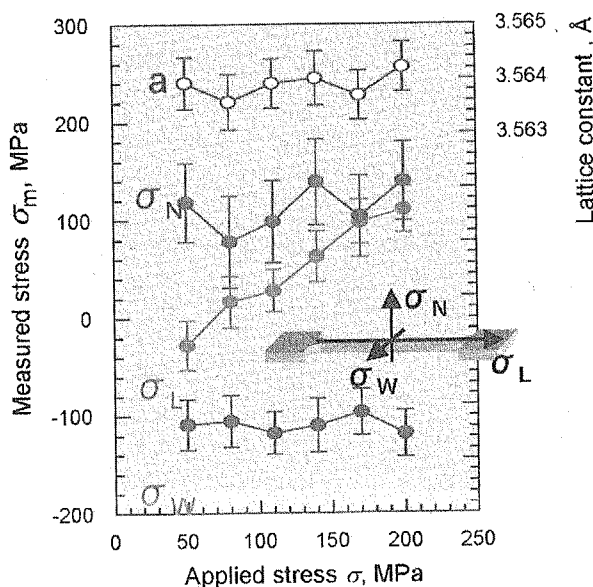


Figure 1:
Changes in each stress component and lattice constant without using measured d_0 . The lattice constant takes the constant value.

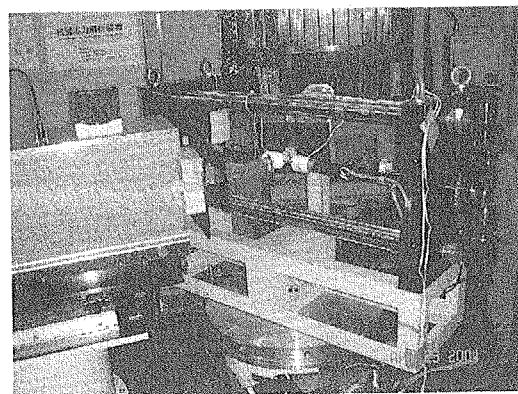


Figure 2:
Diffractometer for RESidual Stress Analysis (RESA)
installed in the JRR-3 guide hall.

Application of Neutron Diffraction for Industrial Materials

Strain Measurements of $\text{Al}_2\text{O}_3/\text{YAG}$ Binary MGC

$\text{Al}_2\text{O}_3\text{-Y}_3\text{Al}_5\text{O}_{12}$ (YAG) is a eutectic material and is used for motor engines and turbines that are operated at a high temperature of more than 1900 K, because of increase in thermal efficiency. This material consists of single crystals of both Al_2O_3 and YAG. Since thermal expansion coefficient differs between both phases, at high temperatures, residual stress is generated due to the mismatch of the thermal expansion between both phases. This is an important problem in industrial safety.

As a first step, powder diffraction measurement was conducted using a diffractometer for Residual Stress Analysis (RESA) installed in the guide hall of JRR-3 (Fig. 2). Figure 3 shows the diffraction pattern of $\text{Al}_2\text{O}_3/\text{YAG}$ and the result of Rietveld analysis. From this analysis, the lattice constants

of both phases were determined at room temperature.

The lattice strains were measured in each phase of the MGC sample. The sample was 4 mm wide, 3 mm thick and 40 mm long. Although in the YAG phase, both tensile and compressive residual strains were observed, in the Al_2O_3 -phase only compressive strain was observed.

Texture Change by Restoration of Ferrite after Large Deformation

When ferrite steel is subjected to heavy drawing, nanosized microstructures are grown. To clarify the texture change of the ferrite steel induced by annealing, texture was measured using RESA. The samples were annealed at several temperatures between 373 K and 1073 K for 3.6 Ks in vacuum. The pole figures of ferrite steel drawn by 0.2 mm are shown in Fig. 4. From this measurement, crystal orientation changes are observed in the sample.

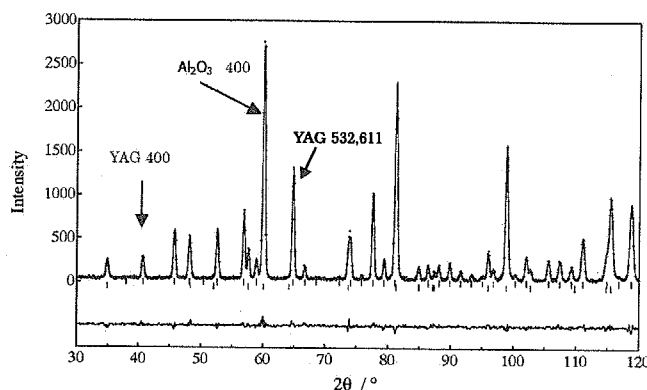


Figure 3:
Neutron diffraction pattern of $\text{Al}_2\text{O}_3\text{-Y}_3\text{Al}_5\text{O}_{12}$ (YAG).

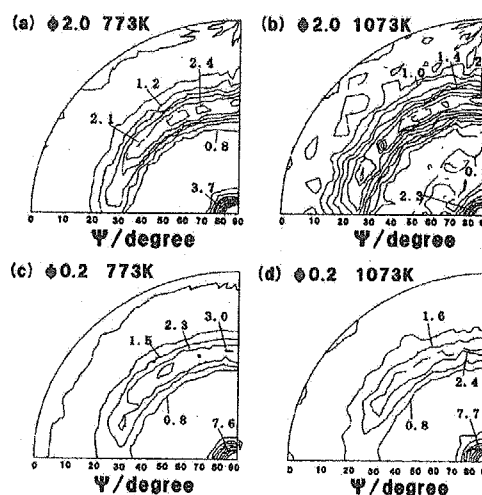


Figure 4:
The (110) pole figures of drawn ferrite steels annealed at 773 K ((a) and (c)) and 1073 K ((b) and (d)) for 3.6 Ks annealed, respectively.

1.7 Diverse Studies on Neutron Imaging

Department of Research Reactor

Nuclear Engineering

[M.Kureta *et al.*]

The Japan Atomic Energy Research Institute is carrying out a design study of the Reduced-Moderation Water Reactor (RMWR, Fig. 1) in cooperation with power companies, reactor makers and universities. The RMWR adopts a triangular tight-lattice fuel rod configuration with a gap width of about 1 mm between rods. The three-dimensional and instantaneous void fraction distribution in tight-lattice bundles was measured by neutron radiography (NR) to clarify the flow behavior and to verify advanced fine-mesh numerical analysis codes for the research and development of the RMWR.

Water lumps flow at the corner of the channel in the case of air/water two-phase flow, on the other hand, water lumps disappear at the corner when the void fraction is about \pm

0.1 under the RMWR simulation condition (= void fraction is about 0.8). Vapor accumulates in the central or wide space, and high-void-fraction spots appear between rods in the low-quality region (Fig. 2). Large vapor bubbles frequently flow upward not only in the central flow space but also in the peripheral space of the channel (Fig. 3).

Medical Application

[T.Takeda *et al.*]

Osteoporosis is a risk factor for fracture in the elderly persons. Since bone strength depends on the quantity and quality of the trabecular bone, the nondestructive inner observation of the bone provides useful information for the investigation of osteoporosis. The inner trabecular bone has been observed by micro-X-ray computed tomography (CT) using synchrotron

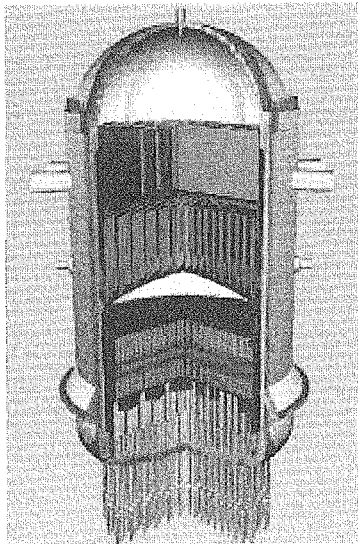


Figure 1:
Conceptual rendering of the
Reduced-Moderation Water Reactor.

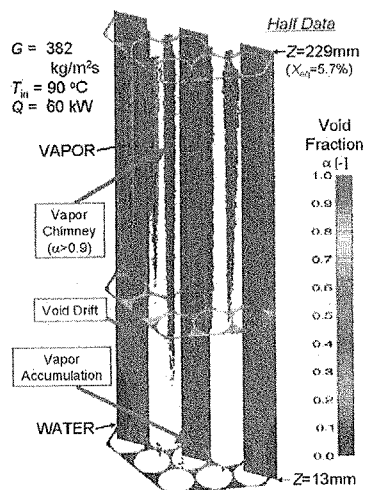


Figure 2:
Three-dimensional void distribution.

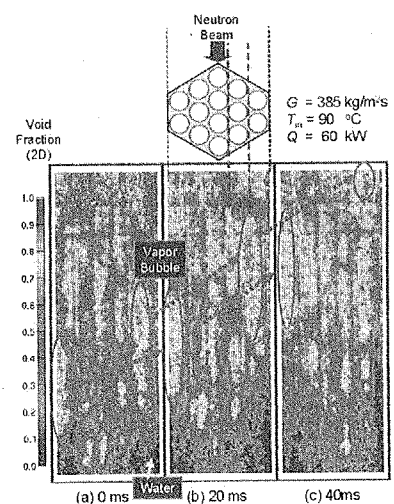


Figure 3:
Consecutive images of void fraction.

radiation, although the inner soft tissue was not visible. NR can sensitively detect minute changes in water content in tissues due to the large neutron attenuation coefficient of water. Therefore, there is a possibility of detecting the inner soft tissue structure of bone by NR. Neutron CT images showed different soft tissue densities, and gave an estimate of the amount of moisture in the bone. (Fig. 4)

Development of Imaging Devices

[K.Sakasai *et al.*, K.Mishima *et al.*]

The use of the neutron imaging plate (NIP) has made great success in the field of neutron scattering study; however, the NIP is sensitive to not only neutrons but also γ -rays. Therefore, it is difficult to discriminate neutron signals from γ -ray signals when the NIP is read. To overcome such a problem,

CaBPO₅:Ce³⁺-based materials were studied as a new neutron storage phosphor consisting of light materials. (Fig. 5)

An imaging system requires a high temporal resolution and a high spatial resolution to clarify rapid transient phenomena, such as boiling bubbles and molten metal-water interaction by high-frame-rate neutron radiography (HFR-NR). The limitation of the resolution of HFR-NR has restricted the application of this method. To overcome this limitation, it is important to search for the best combination of imaging devices such as fluorescent converters, high-speed video cameras, and image intensifiers. To achieve a high temporal resolution for HFR-NR, various combinations of imaging devices have been tested. Thus, fluorescent converters for realizing fast scintillation decay with killer materials have been developed.

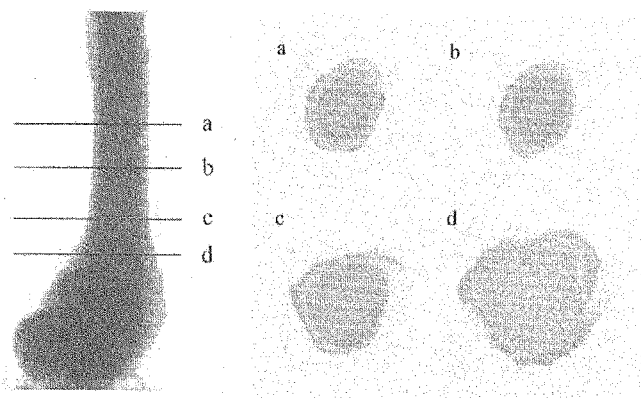


Figure 4:
Projection and CT images of rabbit's thighbone.

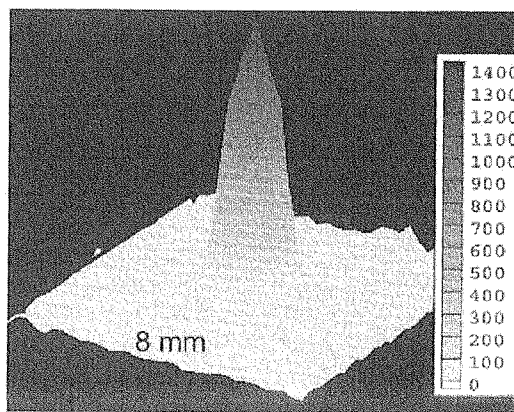


Figure 5:
A collimated neutron beam image obtained with the sample.

1.8 Novel Approaches for Neutron Induced Prompt γ -Ray Using

T. Nakanishi

R&D Group for Industrial Application of Neutron

Neutron In-Beam Mössbauer Spectrometer

[M.K.Kubo *et al.*]

An in-beam ^{57}Fe Mössbauer spectroscopy system using a parallel-plate avalanche counter (PPAC) has been developed for characterizing chemical species produced by neutron capture reaction of $^{56}\text{Fe}(n,\gamma)^{57}\text{Fe}$. A sample such as stainless foil sample of 25 μm thickness was placed at the target position of the JRR-3 PGA system facing the neutron beam at 45 degrees and the PPAC. The measurement was conducted at room temperature. The spectrum (Fig. 1) showed one singlet peak similar to the normal absorption peak, and no significant changes in physical or chemical state of iron in stainless steel caused by the nuclear reaction were observed. Metallic iron was also examined (Fig. 2). Although only four large peaks due to insufficient statistics were clearly observed, the spectrum consisted of a sextet

line as seen in normal absorption spectroscopy. In this study, the first step in the construction of a neutron in-beam Mössbauer spectrometer has been achieved. After recent improvements in the measurement system, the higher S/N ratio of the detector enabled us to obtain the first spectrum of semiconductor iron disulfide. New iron species different from the parent compound arising from the nuclear reaction were clearly observed.

Doppler Broadening of Prompt γ -Ray

[Y.Sakai *et al.*]

By probing Doppler-broadened line shapes of prompt γ -rays at 478 keV emitted from moving ^7Li produced via the $^{10}\text{B}(n,\alpha)^7\text{Li}$ reaction, matrix materials containing and/or surrounding boron species were nondestructively characterized for several stages of soybean growth. It was eluci-

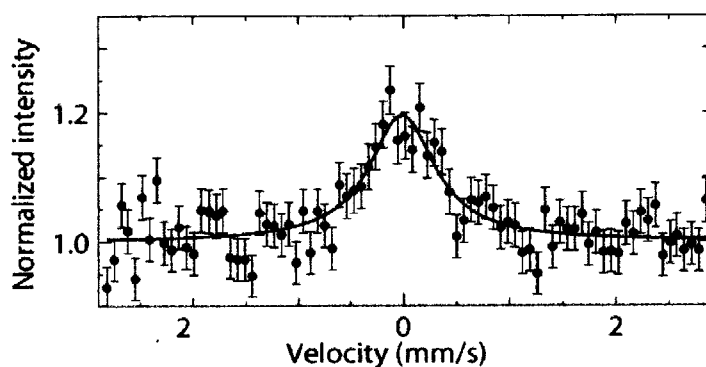


Figure 1: A neutron in-beam Mössbauer spectrum of stainless steel.

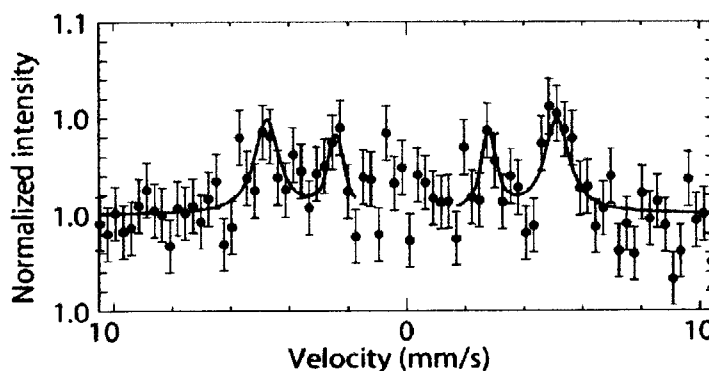


Figure 2: A neutron in beam Mössbauer spectrum of metallic iron.

dated that boron is in the form close to each other for dry seeds for planting and the dry seeds harvested, while it was revealed that boron exists in an aqueous solution for the two stages of growth; swelling seeds with a bourgeon and greenish sprout. This work is the first biological application of the Doppler broadening of prompt γ -rays. Each measurement was performed for several hours using the JRR-3 PGA system. The measured prompt γ -ray spectra at 478 keV of ^7Li for the soybean samples are shown in Fig. 3. It is safe to mention that the Doppler broadening method should be a new and powerful tool for the nondestructive characterization of boron species in biological samples.

Multiple γ -Ray Detection Method

[Y.Toh *et al.*]

PGA is suitable for the measurement of cadmium content.

When PGA is used to measure cadmium content, hydrogen is the disturbance element. Since the prompt γ -ray of hydrogen is 2223 keV, the prompt γ -ray of cadmium is covered by a low-energy tail due to Compton scattering and the detection limit is reduced. Cadmium mainly emits prompt γ -rays of 558 and 651 keV. By applying the multiple- γ -ray detection method to PGA, the influence of nuclei emitting only one prompt γ -ray can be coincidentally reduced. The detection limit of PGA in measuring cadmium in rice using the multiple- γ -ray detection method (MPGA) was estimated. Cd in rice was quantified by MPGA (see Fig.4) using the JRR-3 PGA system. Taking account of Compton γ -rays of hydrogen, it is presumed that one can quantify cadmium content in rice to 0.05 ppm or less by MPGA for 10 minutes if the detector system has about 10% absolute efficiency for prompt γ -rays of cadmium.

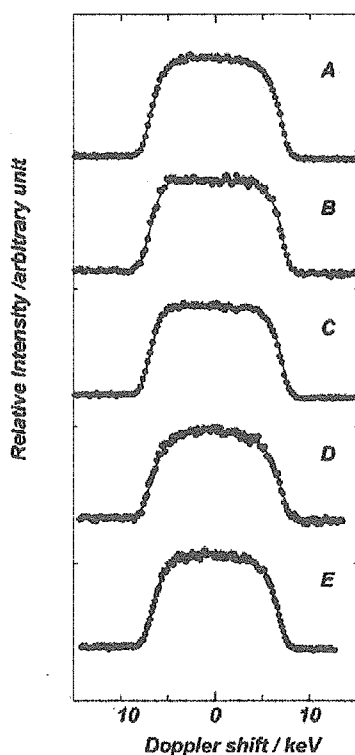


Figure 3:
Spectral Line-shapes of prompt γ -ray of 478 keV of ^7Li measured for the samples of soy-bean plant:
A; Dry seeds (0 day, i.e., before planting),
B; Swelling seeds with a small bourgeon (3 days),
C; Sprout (7 days),
D; Leaves of the young plant (40 days),
E; Dry seeds (153 days, harvested).
The abscissa refers to an energy shift from 478 keV.

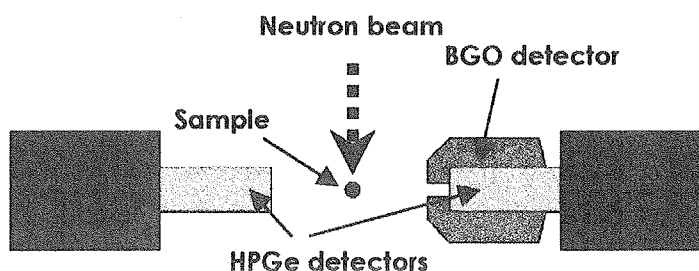


Figure 4:
A schematic drawing of γ -ray detectors used in the measurement for cadmium in rice.

1.9 Development and Application of Neutron Optics

H. M. Shimizu

Research Group for Neutron Optics

Neutron is a valuable probe in research in materials science and bioscience owing to its unique characteristics; it strongly penetrates material since it does not have an electric charge and it picks up information on light elements such as hydrogen atoms through nuclear interaction. An intense neutron beam for materials research is available at research reactors and accelerator-based facilities, but its research field is currently limited by its relatively low intensity.

We are developing a magnetic neutron lens for increasing effective beam intensity in collaboration with RIKEN within the research program “Development and Application of Neutron Optics” supported by the Special Coordination Fund for Promoting the Ministry of Education of the Japanese Government.

The magnetic neutron lens is a sextupole magnet in which six magnet poles are placed around an annular aperture. The neutrons are refracted along the gradient of magnetic field strength and focused onto the magnet axis according to the dipole interaction between a neutron magnetic dipole moment and a sextupole magnetic field. We have successfully developed a strong magnetic neutron lens with a length of 2 m and an aperture of 46.8 mm by employing a Ni-Ti superconducting sextupole magnet (Fig. 1) [1]. We have confirmed that the magnetic neutron lens has sufficient performance for focusing the cold neutron beam from the research reactor JRR-3, as shown in Figs. 2 and 3 [2, 3].

We have also successfully demonstrated that the magnetic

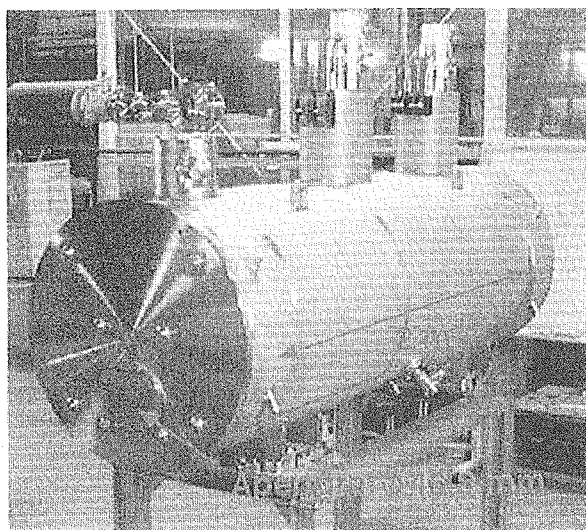


Figure 1:
A photograph of the Nb-Ti superconducting sextupole magnet for neutron beam focusing. Six poles of superconducting magnets are assembled in the cryostat.

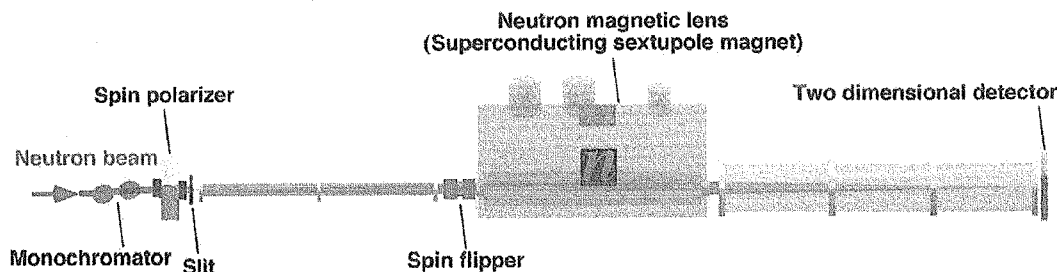


Figure 2:
Experimental apparatus to characterize the neutron magnetic lens. Monochromized and spin-polarized neutrons were delivered to the magnetic lens through a slit. The image of the focused neutrons was observed by the two dimensional detector placed on the focal plane.

neutron lens can be applied to a focusing geometry small-angle neutron scattering (F-SANS) experiment. In the demonstration, SiO₂ spherical particles packed in a quartz cell were mounted on the exit window of the magnetic neutron lens of the experimental apparatus shown in Fig. 2. The SANS from the sample was measured down to q of 10^{-3} \AA^{-1} using neutrons with a wavelength of 9.15 \AA and a two-dimensional detector placed at the focal plane, which is only 3.1 m from the sample (Fig. 4). The obtained SANS profile was well analyzed using the model of randomly packed spherical particles, taking account of the size distribution of the particles ($\sigma = 13 \text{ nm}$) and instrumental resolution, and then an interaction radius of 440 nm and a volume fraction of 0.52 were

determined [4].

References

- [1] J.Suzuki, T.Oku, T.Adachi, H.M.Shimizu, T.Hirumachi, T.Tsuchihashi and I.Watanabe, *J. Appl. Cryst.*, **36**, 795-799 (2003).
- [2] H.M.Shimizu, T.Adachi, M.Furusaka, Y.Kiyanagi, T.Oku, H.Sasao, T.Shinohara and J.Suzuki, *Nucl. Instr. and Methods*, **A529**, 5-9 (2004).
- [3] T.Oku, J.Suzuki, H.Sasao, T.Adachi, T.Shinohara, K.Ikeda, T.Morishima, K.Sakai, Y.Kiyanagi, M.Furusaka and H.M.Shimizu, *Nucl. Instr. and Methods*, **A529**, 116-119 (2004).
- [4] T.Oku, J.Suzuki, H.Sasao, S.Yamada, M.Furusaka, T.Adachi, T.Shinohara, K.Ikeda and H.M.Shimizu, *Physica B*, in press.

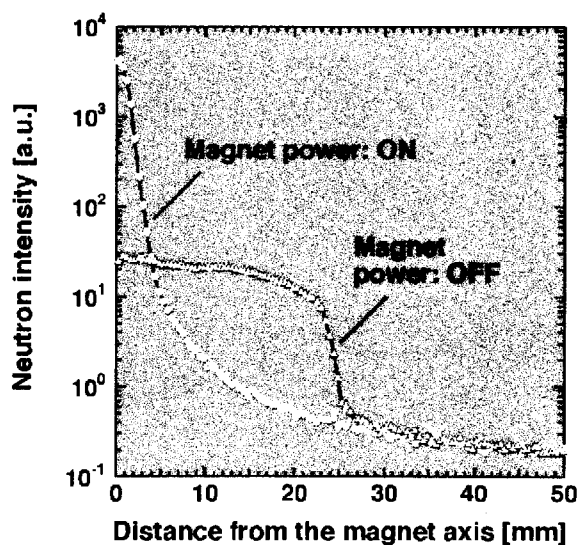


Figure 3:
Neutron beam profile observed by the two dimensional detector on the focal plane. The neutron beam density was clearly increased on the magnet axis.

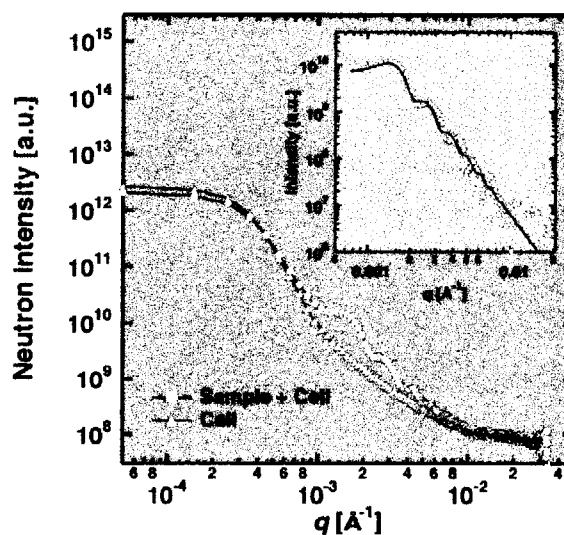


Figure 4:
SANS profiles of the SiO₂ spherical particles with the averaged diameter of 500 nm in the cell and the cell itself. The inset shows the profile of the sample in which the intensity of the cell is subtracted.

1.10 R&D of Neutron Instruments for J-PARC

M. Arai

R&D Group for Neutron Instrument

R&D Group for Neutron Instrument and Research Group for Neutron Detector and Optical Device have carried out the conceptual design and development of pulsed-neutron scattering instruments for the Japan Proton Accelerator Research Complex (J-PARC). The proposed instruments are as follows (Fig. 1).

(1) Engineering Diffractometer

This instrument will be installed at BL19 (decoupled-poisoned hydrogen moderator) and is designed to study various problems in material engineering, focusing on measurement of stresses within engineering components and understanding characteristics of materials behaviors during use, etc. This diffractometer can measure strain with an accuracy of $\pm 10^{-4}$ ~ $\pm 10^{-5}$ for 1mm^3 gauge volume.

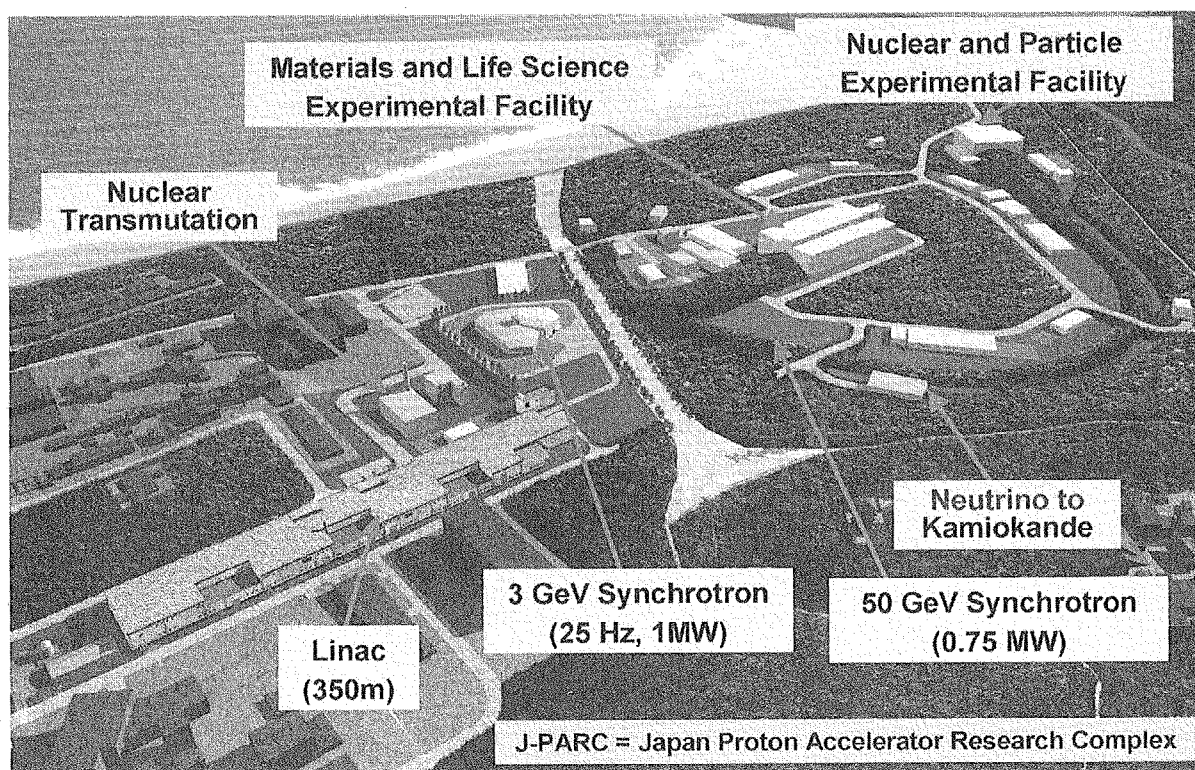
(2) Cold Neutron Disk-Chopper Spectrometer

This instrument will be installed at BL1 (coupled hydrogen moderator) and equipped with a primary (pulse-shaping)

disk-chopper in addition to a main (energy-selecting) disk-chopper. By optimizing the configuration, the spectrometer realizes both high-energy resolution ($\Delta E/E = 1\%$ at the best) and high-intensity (one order of magnitude higher than that of the present state-of-art chopper spectrometers) in the range of $E = 1 \sim 20$ meV. The spectrometer can cover up to $E < 80$ meV though with coarser resolutions. The spectrometer has large area detector banks, which cover large Q range with $\Delta Q/k_i \sim 0.5\%$.

(3) High Efficiency Indirect Geometry Crystal Analyzer Cold Neutron Spectrometer; DIANA

This instrument will be installed at BL11 (decoupled hydrogen moderator) and equips a primary supermirror guide path in addition to a crystal analyzer. By this configuration, the spectrometer realizes both high-energy resolution ($\Delta E/E = 0.5\%$ at the best) and high-intensity (2~3 order of magnitude higher than that of the state-of-arts indirect geometry spec-



Expected bird's-eye view of J-PARC.

trometers) in the range of $E=1\text{meV}\sim 45\text{meV}$. The spectrometer can use three types of crystal analyzers (PG (002), Ge ($\bar{3}11$) and Mica (00n) with $n=2$ and 4) to extend the measurable energy range. The spectrometer has large area crystal analyzer, which cover large Q range with $\Delta Q=0.5\text{ nm}^{-1}$.

(4) High-Intensity SANS

This instrument will be installed at BL15 (coupled hydrogen moderator). This SANS instrument achieves high intensity and wide Q range of $Q=0.001\sim 200\text{ nm}^{-1}$ measurements by wide wavelength-band use and focusing device such as magnetic neutron lens. The instrument has a small-angle detector bank, a medium-angle detector bank and a large-angle detector bank to realize above-mentioned characteristics.

(5) Ibaraki-Prefecture Industrial Material Diffractometer

Ibaraki Prefecture and J-PARC project team are planning to promote industrial application for material science. This instrument will be installed at BL20 (decoupled-poisoned

hydrogen moderator) and the main part is a versatile powder diffractometer with $\Delta d/d = 0.1\%$. This instrument is planned to be an immediate diffractometer so that industrial users can use it like chemical analyzers in their materials development process. The utilization system of the facility is quite important for promoting potential users to utilize the diffractometer by their side. Combination of several powder-diffraction softwares should be also developed for the materials structural studies.

(6) Ibaraki-Prefecture Biological Material Diffractometer

Ibaraki Prefecture and J-PARC project team are planning to promote industrial application for life science such as development of new drugs. This instrument is a single crystal diffractometer for structural analysis of biological macromolecules and organic compounds with unit cell dimensions less than 13.5 nm and will be installed at BL3 (coupled hydrogen moderator).

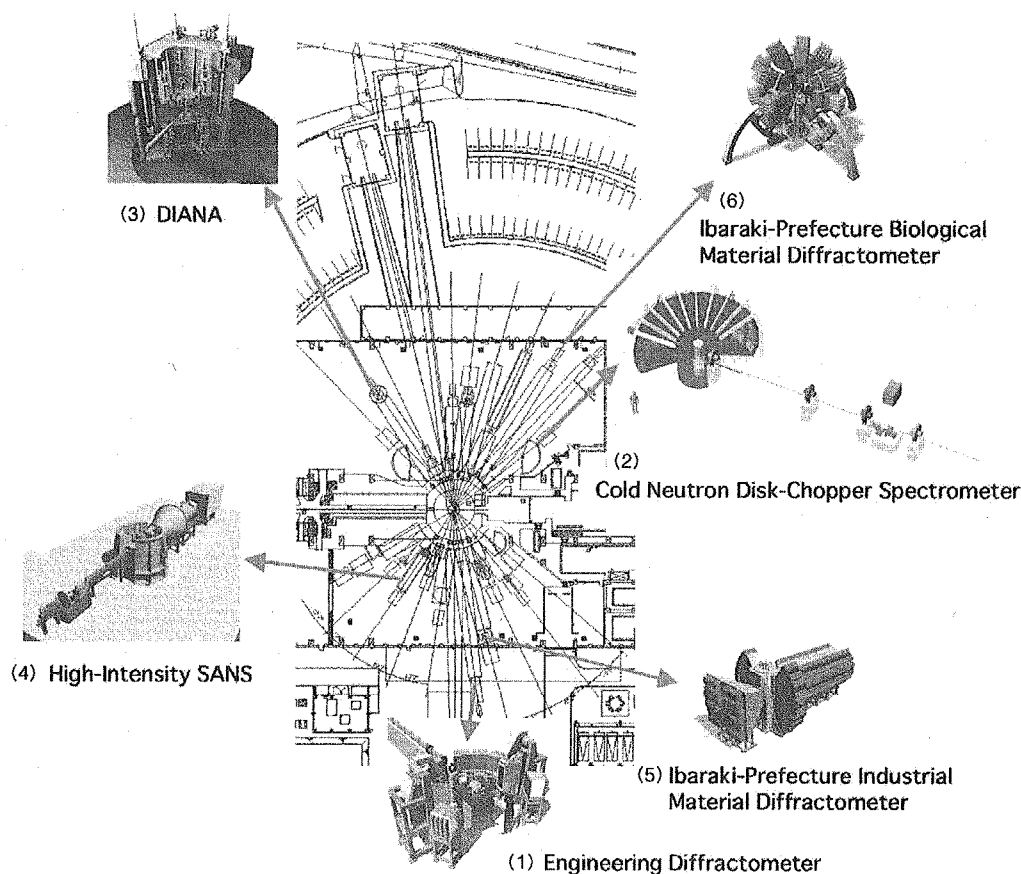
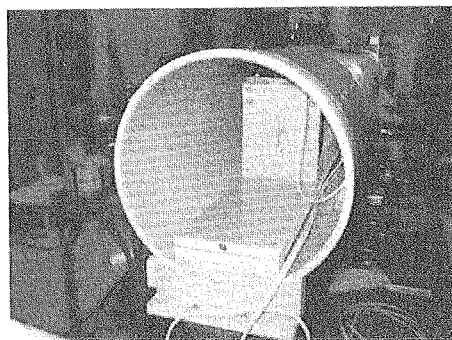


Figure 1: Proposed instruments by JAERI and Ibaraki prefecture.

Our group operates a test instrument with a disk-chopper (CHOP) on the C2-3 port, in the guide hall of JRR-3. The main purpose of using this instrument is to develop pulsed neutron scattering instruments and devices for the JSNS at J-PARC. We simulate a pulsed neutron source using the disk-chopper with a maximum rotation speed of 12000 rpm. We develop several devices such as an MSGC detector, a

Drabkin energy filter, a converging supermirror guide and a TOF-USANS instrument for the last few years. The highlight of our groups in this year is as follows.

The performance test of a high-resolution Drabkin energy filter was performed. The schematic layout of the experiment is shown in Fig. 2. In this test experiment, the Drabkin filter was driven statically to extract monochromatic neutrons from



Photograph of the Drabkin energy filter.

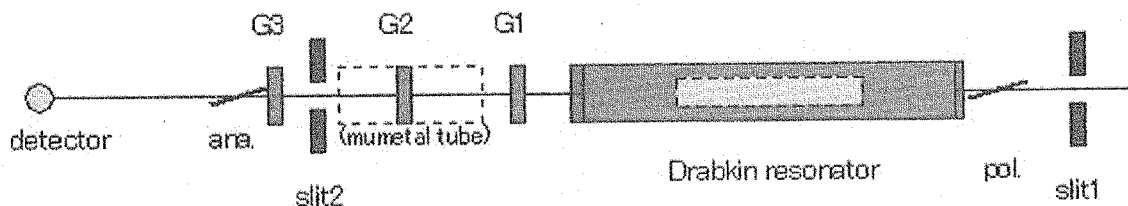


Figure 2: Schematic layout of a high-resolution Drabkin energy filter experiment.

pulsed beams from a disk-chopper. The close circle represents the data for incident neutrons and the purple close circle represents the data for extracted neutrons in Fig. 3. The peak width was 1.2% (FWHM) and the peak intensity was $88 \pm 7\%$. It should be noted that subpeaks at short wavelengths are reduced because of the nonuniformity of the guide field in the Drabkin filter, while those at long wave-

lengths are enhanced. This nonuniformity should be introduced when Drabkin filters are used for pulse shaping.

The downstream of the C2 cold neutron guide, which includes the C2-3 port, will be divided into 3 subports using a neutron bender next year, and we will continue the developments of instruments and devices on the subports.

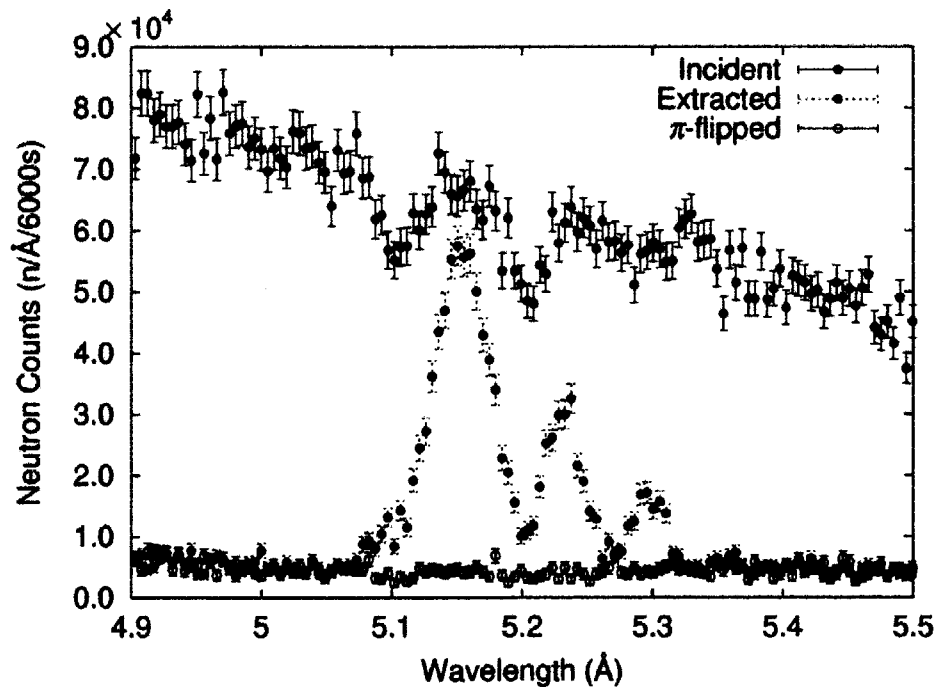


Figure 3: Extracted monochromatic neutrons from pulsed beam by the Drabkin energy filter.

1.11 International Collaborations

The JAERI-ILL collaborative effort on CRYOPAD project continued this fiscal year resulting into the successful installation of the CRYOPADUM on TAS-1. Dr. F. Tasset and Dr. E. Lelievre-Berna from ILL visited JAERI to help the hardware and software installation of CRYOPADUM. Dr. M. Takeda visited ILL to improve the HPT suspension in the CRYOPADUM and Dr. A. Oosawa visited ILL to participate at the start-up of D3 CRYOPADUM.

The cooperative researches with ORNL have been continued under the US-Japan cooperative program. The installation of the WAND instrument at the HB2 shielding tunnel has been completed (see Fig. 1). Efforts to develop computer control and data acquisition hard- and software for the new detector have been made by Drs. Y. Ishii, S. Katano, L. Robertson and J. Fernandez-Baca. When in operation at the new HB-2 port it is expected that the combination of a taller neutron beam and a new bent Ge monochromator system will result in a neutron flux gain factor of 5-10 at the sample position.

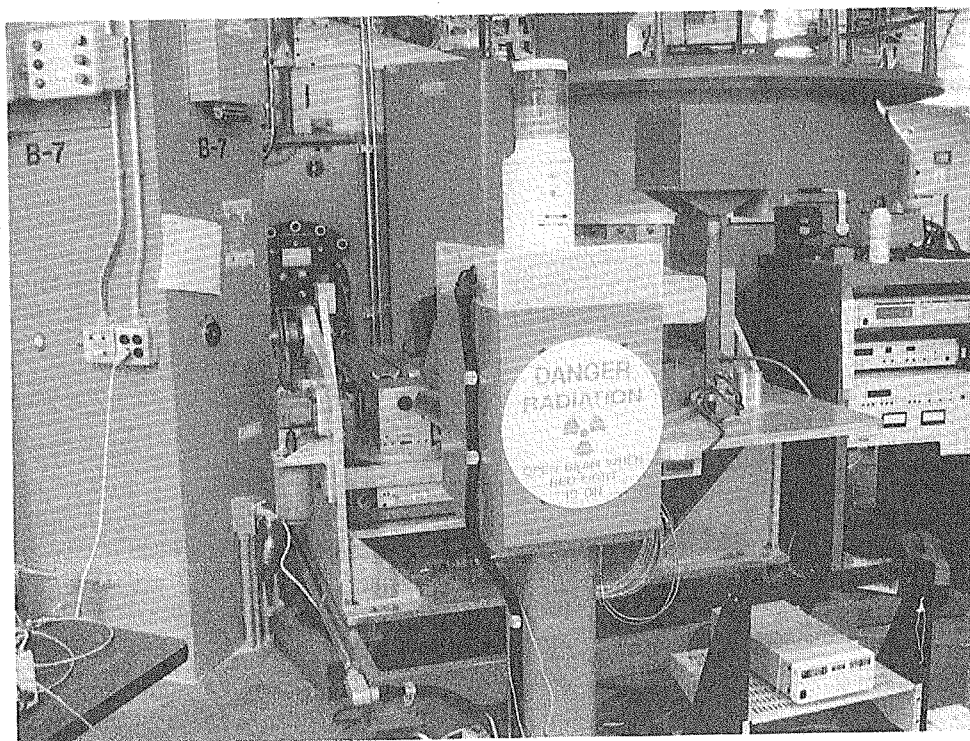


Figure 1: Relocated WAND at the HB-2 beam port.

This is a blank page.

2. Research Reports

2.1 Biology

- Structure and Mechanism -

This is a blank page.

2.1.1 Neutron crystallographic analysis of Endopolygalacturonase I from *Stereum purpureum* at atomic resolution

M. Sato¹, T. Shimizu², T. Nakatsu², and H. Kato²

¹Graduate School of Integrated Science, Yokohama City University,

²Graduate School of Pharmaceutical Sciences, Kyoto University

Endopolygalacturonases (endoPGs, EC 3.2.1.15) catalyze the hydrolysis of the α -1,4-glycosidic linkages between adjacent α -D-galacturonic acid residues within the pectin main chain. The X-ray crystal structure analyses of endoPG I from *Stereum purpureum* have identified catalytic residues and accounted for general acid-base catalysis of the enzyme. It was however impossible to specify experimentally which catalytic residue is a general base or acid because no significant electron density for hydrogen atom is observed around catalytic residues.

In view of this, we prepared single crystals suitable for high resolution neutron crystal structure analysis with hanging-drop vapor diffusion method, followed by macroseeding in a sitting-drop (drop: 0.5 ml, reservoir: 4 ml) vapor diffusion.

Typical size of the crystals grown was 3.0 x 1.9 x 0.8 mm (Fig. 1). The crystals were soaked for 40 days in a reservoir solution containing 25% PEG4000, which is prepared with D₂O, and then subjected to neutron experiment. Neutron diffraction data were collected up to 1.5 Å resolution, with a completeness of 81 % and Rmerge = 0.12, using a single-crystal diffractometer (BIX-4) at JAERI.

Figure 2 shows a typical still photograph recorded on Neutron Imaging Plate (45 cm x 100 cm) with a camera length of 200 mm and an exposure time of 30 min. The initial structure, obtained from X-ray analysis, was refined with CNS, and manual modification made with O. Further refinement by simulated annealing and energy minimization is in progress.

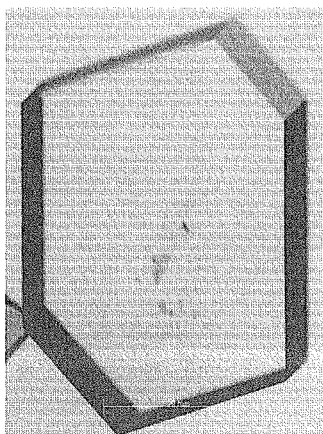


Figure 1: Typical size of the crystals grown.

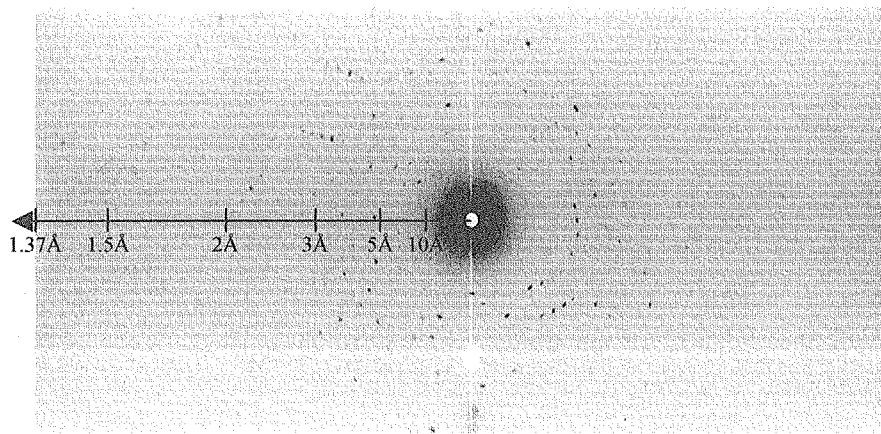


Figure 2: Typical still photograph recorded on Neutron Imaging Plate.

2.1.2 Complicated Water Network in the Minor Groove of B-DNA Decamer d(CCATTAATGG)₂ observed by Neutron Diffraction Measurements

S. Arai, T. Chatake¹, T. Ohhara, K. Kurihara, I. Tanaka², N. Suzuki³, Z. Fujimoto³, H. Mizuno³ and N. Niimura²

Neutron Science Research Center, Japan Atomic Energy Research Institute, 2-4 Tokai, Ibaraki 319-1195

¹Chiba institute of science, 3 Shiomi, Choshi, Chiba 288-0025

²Department of Technology, Ibaraki University, Naka-Narusawa, 4-12-1 Hitachi, Ibaraki 316-8511

³National Institute of Agrobiological Sciences, 2-1-2 Kannondai, Tsukuba, Ibaraki 305-8602

Specific hydration patterns around DNA duplex have long been recognized as one of the important determinants of nucleic acid structure (stability, polymorphism and flexibility) and nucleotide sequence recognition by proteins and drugs. In those previous studies, the observed hydration structure was obtained from the network of only the oxygen atoms of water molecules. In order to understand more fully the hydration patterns and hydrogen positions of B-DNA duplex, we have carried out both X-ray and neutron crystallographic analysis.

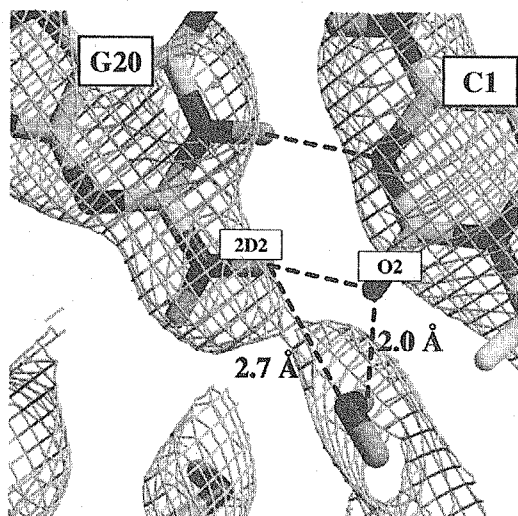


Figure 1: The inter-strand water bridge between CYT and GUA. The $2|F_o| - |F_c|$ nuclear density map contoured at 2.5 σ level.

The neutron diffraction experiments have been carried out by the BIX-4 neutron diffractometer installed at the JRR-3M reactor at the JAERI¹⁾. The DNA sequence d(CCATTAATGG)₂ was selected as a sample because the best condition of the crystal growth has been determined by using the crystallization phase diagram technique^{2,3)}. In order to avoid the high background coming from the incoherent neutron scattering of hydrogen atoms, the crystallization experiments have been carried out in D₂O solutions. The step scanning method (0.3°) was used for data collec-

tion. The exposure time of each frame was 3-6 hours and the total time for data collection was 31 days. The crystal was sealed in a quartz capillary for measurement. In this diffraction experiment, the quartz capillary was cooled at 279 K, which was the temperature condition of the crystal growth experiments. We used two crystals to collect the whole of neutron data sets because used DNA crystals were damaged by drying, which was accidentally occurred by the temperature gradient on the quartz capillary. Moreover, we have carried out the X-ray diffraction experiments of the crystal grown in D₂O by BL-41XU installed at SPring8 synchrotron radiation facility. The diffraction images obtained from X-ray and neutron diffraction experiments were processed and scaled using the program DENZO and SCALEPACK⁴⁾. Crystallographic refinement was performed using CNS⁵⁾. We used our refined result of X-ray structural analysis as the initial model of DNA structure for neutron analysis since the unit cell parameters of the X-ray data and the neutron data were almost the same. In both the neutron and X-ray analysis, the space group was P3₂21, with unit cell dimensions $a = b = 32.9$ Å and $c = 96.1$ Å.

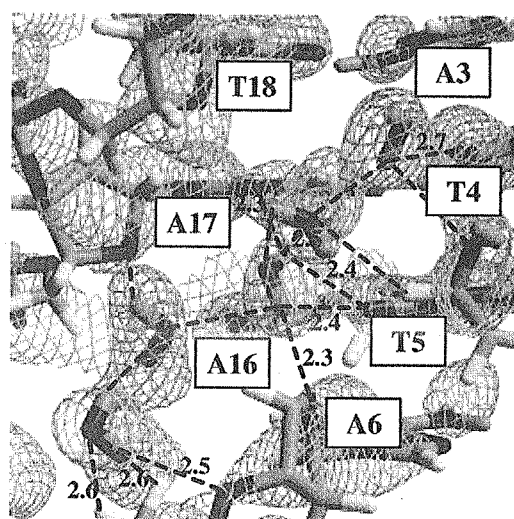


Figure 2: The spine of hydration in the minor groove determined by the neutron structural analysis.

To identify D_2O molecules, first the oxygen position of D_2O has been determined by X-ray analysis. Then the deuterium atoms of D_2O molecules were located by considering the direction of the hydrogen bond acceptor (N, O and P atoms) and the shape of $2|F_o| - |F_c|$ nuclear density map.

The Water Network in the Minor Groove

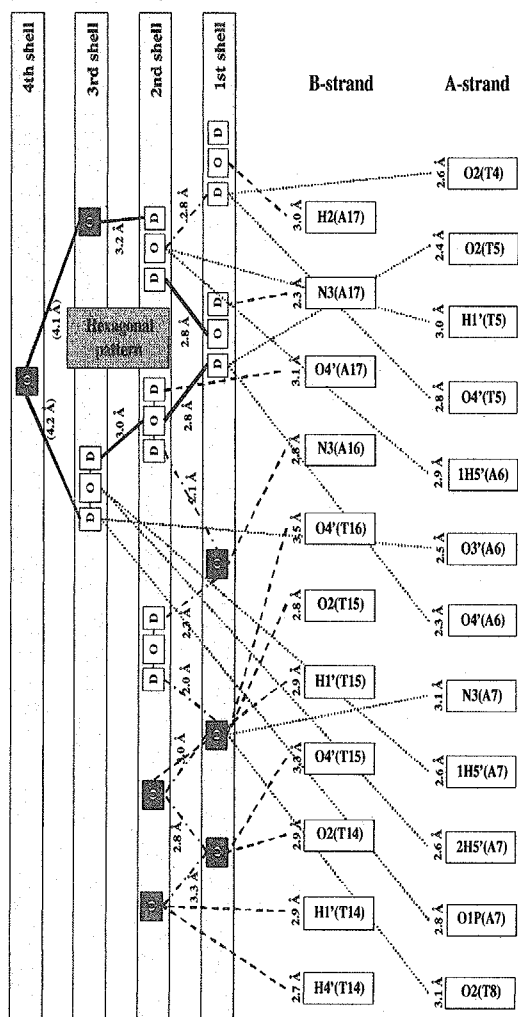


Figure 3: The schematic diagram of the hydrogen bonds network in the minor groove of $d(CCATTAAATGG)_2$. The oxygen atoms of water observed by X-ray diffraction are colored in black. The hexagonal hydration pattern is shown in the bold lines.

By the neutron crystallographic analysis, many H and D atoms have been located and 27 D_2O molecules including D atoms have been determined. Fig.1 shows an example of observed water bridge. It has been well known that the spine of hydration in the minor groove of A-T-tract DNA is built by the combination of many water bridges. Especially, the previous X-ray studies had shown that the hydration pattern in the minor groove is drawn as simple hexagonal shape determined

by the oxygen positions of water molecules⁶⁾. On the other hands, by determining H and D atoms, we have succeeded in observing the complicated water network in the minor groove (Fig.2). Fig.3 shows the schematic diagram of the hydrogen bonds network in the minor groove of $d(CCATTAAATGG)_2$, which has been observed by X-ray and neutron diffraction measurements. In Fig.3, the oxygen atoms of D_2O observed by X-ray analysis were superposed upon the results obtained by the neutron structural analysis. In this figure, the hexagonal hydration pattern is shown in the bold lines. It was difficult to observe the water molecules in the fourth hydration shell by the neutron diffraction measurements because the orientation of those water molecules is liable to become disorder and the maximum resolution limit in this study was not good (3.0 Å). However, as shown in Fig.3, we have found that the observed hydration network in the minor groove has shown not only the simple hexagonal pattern but also many water bridges bonded to the DNA molecules. It seems that this complexity of hydration pattern is derived from the extraordinary variety of an orientation of observed water molecules. These results suggest that many hydrogen bonds between the spine of hydration and DNA strands support the B-DNA helical structure.

This study has been carried out as a part of "Development of New Structural Biology Including Hydrogen and Hydration" in ORCS promoted by Ministry of Education, Culture, Sports, Science and Technology of Japan.

References

- 1) K. Kurihara, I. Tanaka, M. Refai Muslih, A. Ostermann, and N. Niimura : J. Synchrotron Radiat. **11** (2004) 68.
- 2) S. Arai, T. Chatake, and N. Niimura : Acta. Cryst. **D58** (2002) 151.
- 3) S. Arai, T. Chatake, N. Suzuki, H. Mizuno and N. Niimura : Acta. Cryst. **D60** (2004) 1032.
- 4) A.T. Brünger, P.D. Adams, G.M. Clore, W.L. DeLano, P. Gros, R.W. GrosseKunstleve, J.S. Jing, J. Kuszewski, M. Nilges, N.S. Pannu, R.J. Read, L.M. Rice, T. Simonson, G.L. Warren : Acta Cryst. **D54** (1998) 905.
- 5) Z. Otwinowski and W. Minor : Methods Enzymol. **276** (1997) 307-326.
- 6) G. Minasov, V. Tereshko and M. Egli : J. Mol. Biol. **291** (1999) 83.

2.1.3 Neutron diffraction experiments of insulin crystal

M. MAEDA¹, T. CHATAKE¹, I. TANAKA¹, K. KURIHARA¹ and N. NIIMURA^{1,2}¹Neutron Science Research Center, JAERI, Tokai, Ibaraki 319-1195.²Faculty of Technology, Ibaraki University, Naka-Narusawa, 4-12-1, Hitachi, Ibaraki 316-8511

Hydrogen atoms and hydration water molecules surrounding protein play important roles in many physiological functions. Neutron diffraction for protein crystallography using a neutron imaging plate system has become a powerful method for locating position of hydrogen (deuterium) atoms and bound waters of protein¹. The cubic insulin crystal (space group I2₁3, a=b=c=78.9Å) contains a solvent volume of 65 % and has multiple hydration layers². To elucidate hydrogen and hydration in cubic insulin crystals, a large single crystal of cubic insulin for neutron protein crystallography has been grown in D₂O by using a phase diagram technique. We have succeeded in growing a large single crystal (4.0 x 4.0 x 1.3 mm³ in volume) of cubic porcine insulin using the technique. The neutron diffraction experiments were carried out with the neutron single crystal diffractometer BIX-type installed at JRR-3M reactor in JAERI at room temperature. The crystal was sealed in quartz capillary for the measurement. The step scanning method was used for the data collection. The collection time per a frame was 55 minutes controlled by the monitor counts of direct beam in front of the crystal.

One of the results are shown as follows. The protonation and deprotonation of two nitrogen atoms (N π , N τ) in imidazole ring of histidine are very important information to discuss protein crystallography. This information can be given by neutron diffraction. Figure 1 shows the $2F_o - F_c$ positive neutron density map for His5 in the B-chain (B5 His) and His10 in the B-chain (B10 His). In His5 in B-chain, N π is protonated and N τ is deprotonated. On the contrary, in B10 His, both N π and N τ are protonated. This means that B5 His is electrically neutral and B10 His is positively charged³.

On the other hand, the structure of rhombohedral crystals of 2Zn insulin (space group R3, a=b=82.5Å, c=34.0Å) was initially solved at 2.8Å⁴. The structure of 2Zn insulin crystals has subsequently been refined and analyzed at 1.5Å⁵. Recently, the structure of 2Zn human insulin has been determined at 120 K and refined to 1.0Å⁶. The first neutron protein crystallography of 2Zn insulin has been reported at 2.2Å⁷, however, the definite structure of hydrogen and hydration could not be obtained. We have tested the neutron diffraction experiment of 2Zn insulin crystal. It was found that single crystals of 2Zn insulin larger than 2 mm³ were necessary for neutron diffraction ex-

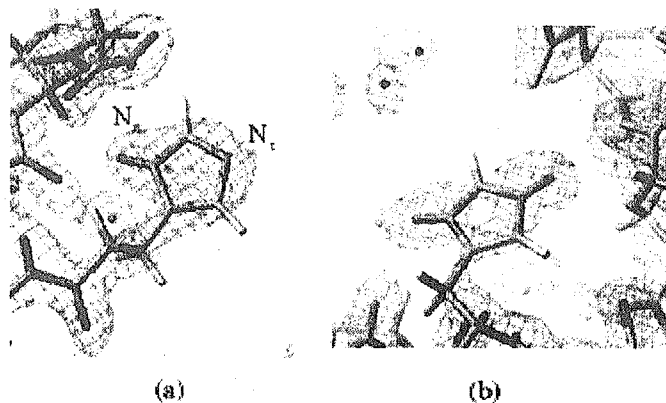


Figure 1: $2F_o - F_c$ positive nuclear density map of (a) His5 in the B-chain and (b) His 10 in the B-chain of cubic insulin

periments.

This work was supported in part by an Organized Research Combination System from the Ministry of Education, Culture, Sports, Science and Technology, Japan.

References

- 1) N. Niimura, Y. Minezak, T. Nonaka, J-C Castanga, F. Cipriani, P. Hoghoj, M. S. Lehmann and Wilkinson (1997). *Nat Struct Biol.* 4, 909-914.
- 2) J. Badger : *Biophys.* 61 (1993) 816.
- 3) M. Maeda, T. Chatake, I. Tanaka, A. Ostermann and N. Niimura: *J. Synchrotron Rad.* 11(2004) 41.
- 4) M. J. Adams, T. L. Blundell, E. J. Dodson, G. G. Dodson, M. Vijayan, E. N. Baker, M. M. Harding, D. C. Hodgkin, B. Rimmer and S. Sheat: *Nature* 224(1969) 491.
- 5) E. N. Baker, T. L. Blundell, J. F. Cutfield, S. M. Cutfield, E. J. Dodson, G. G. Dodson, D. C. Hodgkin, R. E. Hubbard, N. W. Isaacs, C. D. Reynolds., K. Sakabe, N. Sakabe and M. Vijayan: *Philos. Trans. R. Soc. London, Ser. B.* 319(1988) 369.
- 6) G. D. Smith, W. A. Pangborn and R. H. Blessing: *Acta. Cryst. D.* 59(2003) 474.
- 7) A. Wlodawer, H. Savage and G. Dodson: *Acta. Cryst. B.* 45(1989) 99.

2.1.4 Neutron Fiber Diffraction of Troponin C within the Muscle Thin Filaments

S. Fujiwara¹, F. Matsumoto^{1,2}, and S. Deshimaru^{1,2}

¹Neutron Science Research Center, JAERI, Tokai, Ibaraki 319-1195

²Laboratory for Structural Biochemistry, RIKEN Harima Institute, Hyogo 679-5148

Muscle contraction occurs by sliding of the two principal components in muscle cells, the “thin” filaments and the “thick” filaments, past each other. In skeletal and cardiac muscles, the regulation of the muscle contraction is conducted through interactions of the thin filament based proteins, troponin (Tn) C, TnI, TnT, tropomyosin, and actin. To understand the molecular mechanism of the regulation of muscle contraction, it is important to obtain information of the structures of these proteins within the thin filaments.

Since the muscle contraction is triggered by binding of Ca^{2+} to TnC, we have been studying, as a first step, the structure of TnC within the thin filament by small-angle neutron scattering¹⁾. It was found that TnC assumes a dumbbell-like structure, and moves toward the filament axis by binding of Ca^{2+} . It is thus important to obtain information on (possible) orientational change concomitant with this movement of TnC. Such information could be obtained from two-dimensional fiber diffraction patterns from the samples in which the filamentous axis is oriented. To explore the possibility of obtaining the orientational information of TnC within the thin filaments, we employed neutron fiber diffraction method. We prepared the native thin filaments (NTF) purified from bovine heart, and the reconstituted thin filaments containing deuterated TnC (dTnC-RTF). These samples were put into quartz capillaries of a diameter of 3 mm, and then oriented in magnetic field of 18 Tesla. Neutron fiber diffraction patterns of these oriented samples were measured with the Small-Angle Neutron Scattering Instrument (SANS-J) at the guide hall of the reactor JRR-3M in Japan Atomic Energy Research Institute. Neutrons with the wavelength of 6.5 Å ($\Delta\lambda/\lambda=12.98\%$) were employed, and the sample-to-detector distance was 2.0 m.

Figure 1 shows the neutron diffraction pattern of NTF. The background-subtracted pattern folded on the equator is shown. Exposure time of this pattern was 20 hours. This pattern clearly shows characteristics of the muscle thin filaments, including a strong intensity on the equator, actin-based layer lines at 59 Å, a weak cross-pattern across the equator due to tropomyosin, and at least up to 3rd layer lines of the meridional reflections due to troponin. Difference intensity of these meridional reflections between NTF and dTnC-RTF should in principle provide the reflections due only to TnC.

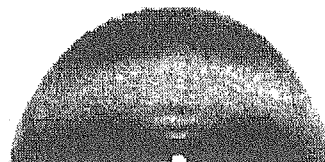


Figure 1: An example of neutron diffraction patterns of the oriented samples of the thin filaments.

Figure 2 shows the intensity distribution of these reflections. It is shown that there is a difference between the intensity distribution from NTF and those from dTnC-RTF, indicating that it is possible to extract the intensity distribution of TnC. The detailed analysis of these reflections is currently underway.

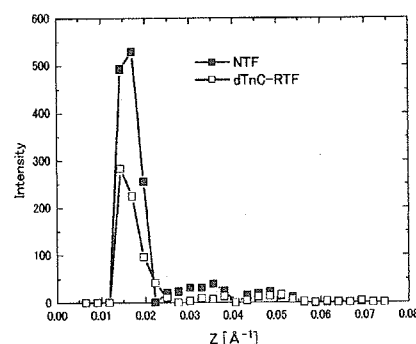


Figure 2: Intensity profiles of the meridional reflections of Tn within NTF and within dTnC-RTF.

Supported in part by the REIMEI Research Resources of Japan Atomic Energy Research Institute, and by Special Coordination Funds for Promoting Science and Technology from the Ministry of Education, Culture, Sports, Science and Technology, the Japanese Government.

References

- 1) F. Matsumoto *et al.*: J. Mol. Biol. (2004) in press.

2.1.5 Small-Angle Neutron Scattering of Smooth Muscle Heavy Meromyosin

S. Deshimaru^{1,2}, S. Maruta³, F. Matsumoto^{1,2}, T. Arata⁴, K. Wakabayashi⁵, and S. Fujiwara¹

¹Neutron Science Research Center, JAERI, Tokai, Ibaraki 319-1195

²Laboratory for Structural Biochemistry, RIKEN Harima Institute, Hyogo 679-5148

³Department of Bioengineering, Soka University, Tokyo 192-8577

⁴Department of Biology, Graduate School of Science, Osaka University, Osaka 560-0043

⁵Department of Mechanical Science and Bioengineering, Graduate School of Engineering Science, Osaka University, Osaka 560-8531

Muscles are composed of two kinds of filaments, actin-based “thin” filaments and myosin-based “thick” filaments. The interaction between actin and the “head” region of myosin, during which one ATP is hydrolyzed, makes these filaments slide past each other, thereby contracting muscles. The molecular mechanism of this muscle contraction and its regulation is one of the most important problems in biophysics, as it is a typical example of energy transduction mechanisms of living organisms. In vertebrate smooth muscles, the acto-myosin interaction is regulated by phosphorylation of myosin. One myosin molecule contains two heads, each of which hydrolyzes ATP, and an interaction between these two heads has been shown to be important in this myosin-linked regulatory mechanism. Knowledge of the structure of the two heads in the myosin molecule could therefore provide insight into the interaction between these two heads. In order to obtain structural information of the two heads in myosin in solution, we carried out neutron scattering experiments of smooth muscle heavy meromyosin (HMM), a proteolytic fragment of the myosin molecule which contains two heads.

Smooth muscle HMM was prepared by digestion of purified chicken gizzard myosin by V8 protease, followed by the purification with gel-filtration chromatography. To detect possible conformational changes of HMM under different structural states, we prepared four kinds of samples: unphosphorylated HMM, unphosphorylated HMM in the presence of ADP-BeF_x, an ATP-analogue which mimics ATP binding state, phosphorylated HMM (pHMM), and pHMM in the presence of ADP-BeF_x. A concentration series of HMM solution in D₂O was prepared for each state. Small-angle neutron scattering experiments were done on these samples. The measurements were done with the Small-Angle Neutron Scattering Instrument (SANS-J) at the guide hall of the reactor JRR-3M in Japan Atomic Energy Research Institute. Neutrons with a wavelength of 6.5 Å ($\Delta\lambda/\lambda=12.65\%$) were employed. The measurements were done at sample-to-detector distances of 6.0 m and 1.5 m.

Data taken at the two sample-to-detector distances were merged to obtain scattering curves covering Q -ranges ($Q=4\pi\sin\theta/\lambda$, where 2θ is the scattering angle

and λ the wavelength of neutrons) as wide as possible. Figure 1 shows the merged scattering curve extrapolated to zero protein concentration of each sample. Differences in the scattering curves are observed, particularly in the initial slopes of the curves and a bump in the region around $Q=0.07\text{Å}^{-1}$, indicating that the conformations of HMM under different states are different. Analysis by the Guinier plots of these curves showed that radii of gyration of HMM under these states were different, indicating again the conformational changes of HMM under the different states. A detailed analysis with model calculations is currently underway.

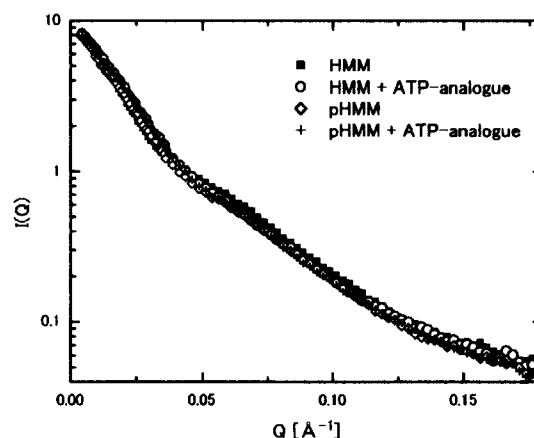


Figure 1: Scattering curves of HMM in the different states. The merged curves taken at the different sample-to-detector distances are shown. Filled squares denote the scattering curve of HMM, open circles denote that of HMM in the presence of ATP-analogue, open diamonds denote that of pHMM, and crosses denote that of pHMM in the presence of ATP-analogue.

This study was supported in part by Special Coordination Funds for Promoting Science and Technology from the Ministry of Education, Culture, Sports, Science and Technology, the Japanese Government.

2.1.6 Neutron scattering study on self-assembly of tau molecules in water

S. Naito¹, M. Furusaka¹, S. Fujiwara², J. Suzuki², Y. Kobayashi³, and N. Niimura²

¹High Energy Accelerator Research Organization, Tsukuba, Ibaraki 305-0801

²Japan Atomic Energy Research Institute, Ibaraki 319-1195

³College of Science and Technology, Nihon University, Tokyo 101-8308

An abnormal protein aggregation in cells causes cellular degeneration and death, and finally end up with grave disorders. Alzheimer's disease, an age-related dementia, is characterized by amyloid plaques and neurofibrillary tangles. Both are formed from abnormally aggregated protein; the plaques contain the AP peptide (a breakdown product of membrane protein) aggregated into fibers, the tangles contain tau protein aggregated into paired helical filaments (PHFs). In order to understand the origin of the disease it is important to understand the abnormal state of these proteins (resulting from proteolysis, phosphorylation, or other modifications including disulfide bond (SS) formation) and the subsequent aggregation. We have preliminarily studied the self-assembly of keratin proteins causing normal cell death of keratinocyte. The two types of keratin molecules form 8-mer consisting of 4 pieces of coiled-coil dimer in the early stage of cell death¹.

We synthesized gene-expressed tau (46Kda, consisting of 448a.a.). SANS were conducted at SANS-J [neutron wavelength (λ)=11.4 Å, sample distance (L)=10m] situated at the end of a cold-neutron guide tube from the JRR-3 reactor and at the SWAN, small and wide angle diffractometer at the KENS (Pulsed Neutron Scattering Facility in KEK). Figure 1 shows the SANS profile of tau solution in the buffer (12mg in 1 ml of 50 mM HEPES buffer, pH 7.8 containing 5mM DTT). Tau formed multimers without intermolecular disulfide bondings. Double logarithmic SANS plot profiles of tau in the buffer solution showed straight line that has a slope of -2 ($0.002 < q < 0.007$). This suggests that tau exists as bent rod-like molecules. In order to analyze the scattering intensity function in detail, a cross-section analysis was applied. For the medium scattering angle region, the scattering intensity of a rod-like particle of length L and the mean-square radius of cross section $\langle R_{cs}^2 \rangle$ were separated into the axial factor $I(q)_{\text{thin}}$ and the cross-sectional factor, $I(q)_{cs}$.

$$I(q) = I(q)_{\text{thin}} I(q)_{cs}$$

$\langle R_{cs}^2 \rangle^{1/2}$ measures the cross-sectional dimension.

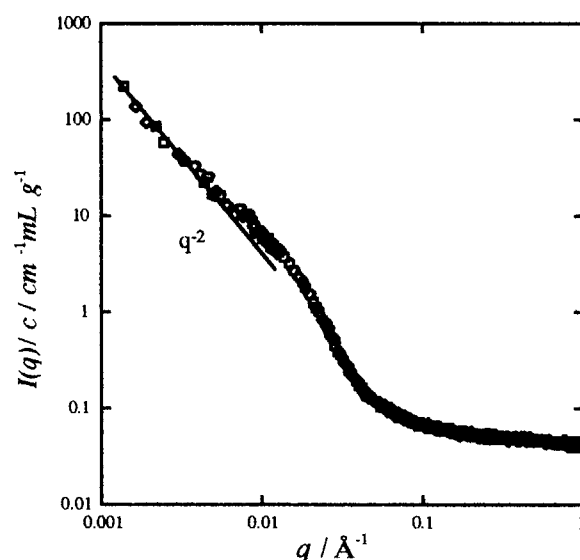


Figure 1: SANS profiles of tau aq. soln. at pH 7.8.

of the particle rather than the overall dimension. Here, q is the magnitude of scattering vector. $I(q)_{\text{thin}}$ is approximated by Lp/q and, in the scattering vector region of $q^2 \langle R_{cs}^2 \rangle < 1$, I_{cs} is proportional to $\exp\{-1/2 \langle R_{cs}^2 \rangle q^2\}$. In this q region, therefore,

$$\ln I(q)q = \ln I(0)q - 1/2 \langle R_{cs}^2 \rangle q^2,$$

and the plot of $\ln(I(q)q)$ vs. q^2 forms a straight line whose slope is $\langle R_{cs}^2 \rangle$. $I(0)$ is the zero-angle scattering intensity. R_{cs} is related to the radial distribution of scattering density. The real diameter (r) of rod-like tau was estimated by,

$$r = \sqrt{2} R_{csaq}$$

The diameter rod-like tau aggregate was estimated to be ca. 18Å. The diameter of the rod-like tau aggregate consisted of PHF's (cross-linked by SS bond) observed in neurocyte of Alzheimer's disease is 10 nm. Tau may recognize each other in a special way and aggregate easily if tau exists alone. The reason tau having less crystalline structure, such as α -helix and β -sheet, forms rod structure has been unknown, especially in neurocyte of Alzheimer's disease.

Reference

1) S.Naito *et al.*, JAERI-Review 2004-005, 17.

This is a blank page.

2.2 Soft Matter

- Polymer Glasses, Gel and Phase Separation -

This is a blank page.

2.2.1 *In-situ* SANS Observation of Enzymatic Polymerization of Artificial Cellulose

H. Tanaka, T. Hashimoto, K. Kurosaki¹, M. Ohmae¹, S. Kobayashi¹, and S. Koizumi²

Department of Polymer Chemistry, University of Kyoto, Kyoto 615-8510

¹Department of Materials Chemistry, Kyoto University, Kyoto 615-8510

²Advanced Science Research Center, JAERI, Tokai, Ibaraki 319-1195

Enzymatic polymerization was first reported by Kobayashi et al. in 1991, as the first successful way of synthesizing artificial cellulose *via* a nonbiosynthetic pathway¹⁾, utilizing β -cellobiosyl fluoride as an activated substrate monomer, and the cellulase, which had been generally used as an enzyme for hydrolysis reaction of cellulose, as rather polymerization catalyst, and an organic (acetonitrile) /aqueous (acetate buffer) solvent system (Figure 1). It was found that this method could provide highly regio- and stereo-controlled cellulose with a degree of polymerization of about 22 glucose units. However, detailed information about the mechanism of enzymatic polymerization has not been fully understood yet.

In this study, we have investigated the self-assembling process of cellulose synthesized *via* enzymatic polymerization *in situ* to elucidate the mechanism of this reaction, by means of time-resolved Small-Angle Neutron Scattering (SANS) measurement with SANS-J at JAERI, JRR-3M research reactor.

Figure 2 shows time-evolution of SANS profiles obtained in the course of polymerization process. Here the scattered intensity $I(q)$ is double logarithmically plotted as a function of the magnitude of the scattering vector q , defined by $q = (4\pi/\lambda)\sin(\theta/2)$, where λ and θ represent the wavelength and the scattering angle, respectively. The SANS profiles were corrected for the background scattering and the transmittance for the further analysis.

It should be noted that before polymerization the scattering profile for enzyme solution obeys Porod law or q^{-4} especially at lower q region, $q < 0.1 \text{ nm}^{-1}$ as indicated by the slope q^{-4} in the figure, which reflects a sharp interface composed of the enzyme associations with more than several hundreds of nanometers in size. On the other hand, once polymerization reaction has started, throughout the reaction process, the scattered intensity shows the power law of $q^{-\alpha}$ at almost all q range observed in this experiment, with α being between 3.0 and 4.0, indicating that cellulose synthesized form aggregated structure with self-similar surface having surface fractal dimension D_s given by $D_s = 6 - \alpha$.

It is also worth noting that, as polymerization proceeds, α tends to decrease from 4.0 to 3.7 and finally approach toward the finite value of 3.7 as shown in the figure, therefore, surface fractal dimension D_s in-

crease from 2.0 toward 2.3. This means that, just after polymerization has started, first aggregated structures with sharp interface are formed, and as polymerization proceeds, the surface become rougher due to the successive formation of cellulose around the structure.

These results suggest that the enzymatic polymerization is expected to occur on or near the surface of the self-assembled enzymes with a sharp interface, and cellulose thus synthesized maintain its position near the surface, and then, together with newly synthesized cellulose, formed the aggregated structure with rougher surface characterized by fractal dimension D_s around the enzyme associations.

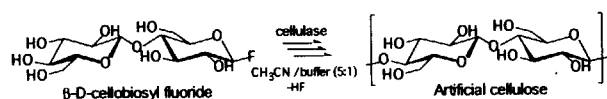


Figure 1: Scheme for enzymatic polymerization of cellulose

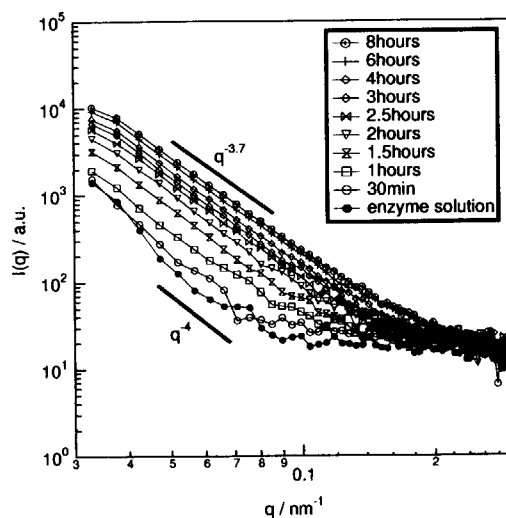


Figure 2: Time evolution of SANS profiles obtained during enzymatic polymerization.

References

- 1) S. Kobayashi, K. Kashiwa, T. Kawasaki, S. Shoda, *J. Am. Chem. Soc.*, **113**, 3079 (1991)

2.2.2 Direct In-situ Observations in Living Anionic Polymerization by Small Angle Neutron Scattering

K. Yamauchi¹, H. Hasegawa¹, T. Hashimoto^{1,2}, H. Tanaka^{1,2}, R. Motokawa², S. Koizumi²

¹Graduate School of Engineering Kyoto University, Nishikyo-ku, Kyoto, 615-8510

²Japan Atomic Energy Research Institute(JAERI), Tokai, Ibaraki, 319-1195

Small angle neutron scattering (SANS) has been a powerful technique to study dynamics of physical processes in polymer systems such as order-disorder transition of block copolymers, shear-induced phase transition of polymer blends, etc. SANS is also extremely useful to study chemical reactions in polymer systems such as polymerization, etc. We can look at not only concentration changes by chemical reactions but also structural changes (primary, secondary, and higher-order structures) by time-resolved SANS measurement.

In this study, we would like to present the preliminary results of our SANS study on the synthesis process of polyisoprene-*block*-poly(*d*₈-styrene) (PI-*block*-dPS). A mixture of isoprene, *d*₈-styrene, and *d*₆-benzene in the ratio of 1:1:2 by weight was introduced into a quartz cell under argon atmosphere. A solution of *sec*-butyllithium was added to the mixture via the syringe technique to give a little yellow color solution on isoprene anion. In the non-polar solvent it is known that the reactivity of isoprene is much larger than that of styrene resulting in the formation of PI-*block*-dPS block copolymer (Figure 1). As soon as *sec*-butyllithium was added to the mixture, time-resolved SANS measurement was started with the SANS-J instrument installed to JRR-3M research reactor with neutron wavelength of 0.7 nm at JAERI, Tokai, Japan. Time-resolved SANS intensity profiles were obtained with 5 min interval. The solution of living polymer in the quartz cell kept at 30 °C without stirring.

The resulting block copolymer was characterized by GPC (Gel Permeation Chromatography). The number-average molecular weight M_n and polydispersity index M_w/M_n values of polymers were calculated from GPC on the basis of polystyrene calibration. Characteristics data of PI-*block*-dPS was shown in Table 1.

Table 1: Characteristics of PI-*block*-dPS diblock copolymer

Sample	M_n	M_w/M_n
PI- <i>block</i> -dPS	1.41×10^5	1.03

The SANS profiles as shown in Figure 1 exhibited four different time region (Region 1-4) in terms of the number, position and intensity of scattering peaks. In

Region 1, only the intensity at low q increased with time suggesting the growth of PI chains. In Region 2, a peak appeared at $q = 0.2 \text{ nm}^{-1}$ and the intensity increased with time while the peak position remained constant. Moreover, GPC results suggested that the molecular weight was constant in Region 2. These results means block polymer chains are not grown in Region 2. In region 3, the peak position rapidly shifted toward smaller q and its intensity increased suggesting the growth of dPS blocks attached to the PI blocks. In this time region, the order-order transition (abrupt change in the width of the peak and appearance of the higher-order peaks at $3^{1/2}$ and $7^{1/2}$ positions of the first-order peak) was also observed. In Region 4, the order-order transition from cylinders to lamellae was observed induced by the further growth of the dPS blocks suggested by the positional changes of the higher order peaks to the integer multiples of the first-order peak. Time-resolved SANS results suggested that the stepwise growth of PI-*block*-dPS diblock copolymer chain and microphase separated structure.

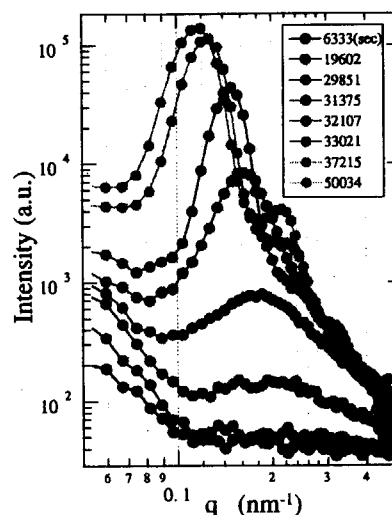


Figure 1: Time dependence of the SANS profiles in the living anionic polymerization of isoprene/styrene mixture in benzene.

2.2.3 Small-angle Neutron Scattering Observation on Soap-Free Emulsion polymerization of poly (*N*-isopropylacrylamide)-*block*-poly (ethylene glycol)

R. Motokawa, T. Nakahira, M. Annaka¹, T. Hashimoto² and S. Koizumi²

Department of Materials Technology, Chiba University, Inage-ku, Chiba 263-8522

¹Department of Chemistry, Kyushu University, Fukuoka 812-8581

²Advanced Science Research Center, JAERI, Tokai, Ibaraki 319-1195

A living ionic polymerization method ideally provides mono-dispersed and high molecular weight macromolecules. However it is difficult to obtain poly (*N*-isopropylacrylamide) (PNIPA) by the living anion polymerization method. This is because the amide group on *N*-isopropylacrylamide (NIPA) cannot be protected from anionic activation and from there a sub-polymerization process occurs to produce a branched polymer. To obtain the mono-dispersed linear polymer, there is a classical method of heterogeneous polymerization in a poor solvent, that is emulsion polymerization. It was reported that radical polymerization in the emulsion can provide the high molecular weight and mono-dispersed polymer. It is believed that the confined space of the emulsion strongly restricts bimolecular terminal reactions. Inclusion polymerization has a similar advantage to control radical.

We focus on the heterogeneous polymerization method as a nano-reaction vessel and aim to observe its polymerization process by small-angle neutron scattering (SANS) measurement. Along the interest, we designed a soap-free emulsion polymerization system to synthesize a new amphiphilic block copolymer of poly (*N*-isopropylacrylamide) - *block* - poly (ethylene glycol) (NE). PNIPA in water is famous for a distinct volume change due to dehydration at around 34°C. Utilizing the strong solvent-selectivity appearing above 34°C, the NE block copolymer forms a self-assembled micelle where radically activated PNIPA chains are packed in a core and the poly (ethylene glycol) (PEG) chains form corona.

We performed small-angle neutron scattering (SANS) measurements at research reactor JRR-3 of JAERI, at Tokai. We employed two SANS spectrometers of pinhole and double crystal Bonse-Hart types named SANS-J and PNO, respectively. SANS-J covers a q -range of $0.03 \leq q \leq 1 \text{ nm}^{-1}$ and the incident neutron of $\lambda = 0.65 \text{ nm}$ ($\Delta\lambda/\lambda = 13\%$). NIPA monomer and PEG were dissolved in D_2O , then $\text{Ce}(\text{NO}_3)_6(\text{NH}_4)_2$ was added to the solution as a redox initiator. The polymerization solutions were filled in a quartz cell of 2 mm thickness, which gives transmittance of 70%. The sample temperature was controlled for polymerization temperature at 25°C, 34°C, 40°C, 50°C and 60°C. Then, we polymerize the NE block

copolymer under the neutron beam. The double crystal spectrometer PNO is able to cover a q -region of ultra small-angle neutron scattering (USANS) of $10^{-4} \leq q \leq 10^{-2} \text{ nm}^{-1}$, $\lambda = 0.2 \text{ nm}$. The sample specimens were prepared the same as SANS-J.

Figure 1 shows the q -profiles for end polymerization products of different polymerization temperatures. In the temperature range above 34°C, we observed the asymptotic q -behavior, $I(q) \sim q^{-4}$, originating from the interfacial structure of aggregated emulsion. In the q -profiles, the crossovers of asymptotic q -behaviors are clearly seen as indicated by arrows of $q = 1/\xi$. These values of ξ reflect micelle size and become smaller as polymerization temperature increase. We consider that the PNIPA core strongly aggregates and dehydrates toward 60°C. As polymerization temperature increases, we obtain smaller molecular weight, M_n , of end products (NE) and molecular weight distribution, M_w/M_n , become relatively narrow distributions between 1.4 and 1.6. It seems quite probable that the value of M_n and M_w/M_n has a connection with micelle structure. On the other hand, we observed Ornstein-Zernike type scattering at 25°C, which indicates that polymerization proceeds in the homogeneous solution system and molecular weight distributions of end products (NE) are broader $M_w/M_n \sim 2.5$.

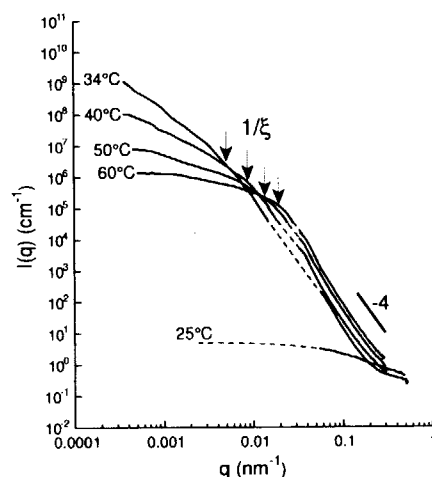


Figure 1: SANS profiles were obtained for end polymerization mixture at different polymerization temperature, 25°C, 34°C, 40°C, 50°C and 60°C.

2.2.4 Small-angle Neutron Scattering Study on Living Radical polymerization with Reversible-Addition-Fragmentation-chain-Transfer (RAFT polymerization) Process of Styrene

Naosuke Mukawa, Ryuhei Motokawa², Mikihiro Takenaka, Takeji Hashimoto and Satoshi Koizumi¹

Graduate School of Engineering, Kyoto University, Kyoto 615-8510, Japan

¹*Advanced Science Research Center, JAERI, Tokai-mura, Ibaraki 319-1195, Japan*

²*Department of Materials Technology, Chiba University, Inage-ku, Chiba 263-8522, Japan*

Living radical polymerization has recently emerged as one of the more effective technique for a preparation of well-defined polymer-structures by controlling molecular weight, molecular weight distribution and tailored architecture. There are several approaches have been reported and we particularly aim at a process of reversible addition-fragmentation chain transfer(RAFT process). The approach utilizes readily available thiocarbonylthio compounds as chain transfer agents (RAFT agents) to confer living character to the polymerization. We expected that there are any structures or behaviors controll the molecular weight and molecular weight distribution during RAFT polymerization. So we investigated polymerization process of polystyrene with RAFT by using time-resolved SANS measurement.

SANS-J instrument at Japan Atomic Energy Research Institute(JAERI) JRR-3M research reactor was used for this study with neutron wavelength of 0.65nm. The polymerization of d6-styrene monomer was performed with benzene as solvent and 2,2'-Azobis-isobutyronitrile (AIBN) as initiator and 1-phenylethyl phenyldithioacetate (1-PEPDTA;Figure 1) as RAFT reagent at 60 °C in quartz cell of 2mm thickness. The final polymer concentration was 50wt% and the molecular weight of the resulting polystyrene was about 20,000.

Figure 2 shows the time change in the scattering intensity after the onset of initiation. The polymerization process of styrene can be divided into the following two regions: (i) In region I or time $t \leq 600$ min, the scattering intensity increased with time at all observed q region, which reflects the progress of the polymerization. Moreover, the relatively steep slope appears at $q \leq 0.3 \text{ nm}^{-1}$ in the late stage of Region I, indicating that the heterogeneity is also formed due to the aggregation of the end functional group of RAFT in polymers. The fact of the formation of the heterogeneity agrees with the observation of the increases in turbidity of the samples at 420 min. (ii) In region II or $t \geq 600$ min, the intensity at $q \geq 0.3 \text{ nm}^{-1}$ hardly changed while the intensity decreases with time at $q \leq 0.3 \text{ nm}^{-1}$ and then the power law behaviors of q^{-4} , which reflects the domain structure with sharp interface appears at 1200min. This change indicating that the heterogeneity have coarsened with time and that

the sharp interface have developed in the later stage of the region II.

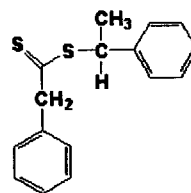


Figure 1: 1-PEPDTA.

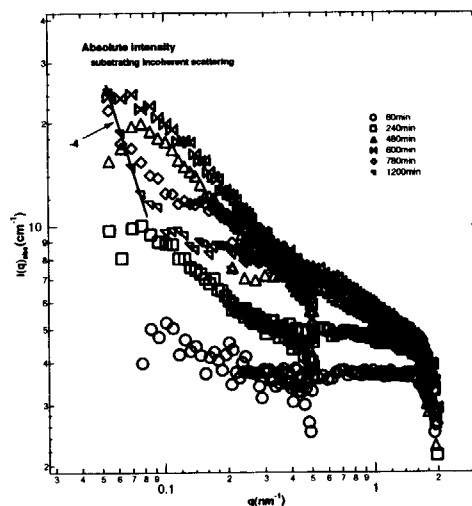


Figure 2: SANS profiles were obtained for in-situ observation of d6-polystyrene polymerization process at 60 °C.

2.2.5 Viscoelastic effects on the nucleation and growth in semi-dilute polymer solution

M.TAKENAKA, N.IWASE, T.HASHIMOTO and S.KOIZUMI¹

Department of Polymer Chemistry, Graduate School of Engineering, Kyoto University, Kyoto 606-8501

¹Advanced Science Research Center, JAERI, Tokai, Ibaraki 319-1195

Recently, it has been found that the dynamical asymmetry between constituent components in a mixture causes the coupling between stress and diffusion during phase separation processes of mixture due to the asymmetric stress division. This coupling is called "viscoelastic effects" and has been found to cause shear-induced phase separations in polymer solution and non exponential decay in dynamic scattering near equilibrium. The strength of the effects of viscoelasticity is characterized by the viscoelastic length ξ_{ve} defined by

$$\xi_{ve} = \left(\frac{D\eta_0}{3K_{os}} \right)^{0.5} \quad (1)$$

where D , η_0 , and K_{os} are, respectively, the inter-diffusion coefficient, the zero-shear viscosity, and the osmotic compressibility. In order to estimate ξ_{ve} , we need to obtain the value of K_{os} . Thus in this study we measured the scattering function of the polymer solution and estimated K_{os} . We used deuterated polystyrene (dPS, weight average molecular weight $= 5.0 \times 10^6$)/Diethyl Malonate (DEM) sample. We used three samples, dPS/DEM=2/96, 4/96, 6/94 (wt/wt). The SANS experiment were performed at SANS-J. Figure 1 shows the temperature dependence of the scattered intensity $I(q)$ of dPS/DEM=4/96. We fitted the scattered intensity, $I(q)$, with the structure factor calculated with random phase approximation, and estimated the interaction parameter χ and K_{os} of dPS/DEM polymer solutions. Figure 2 shows the temperature dependence of χ and K_{os} . χ decreased with temperature while K_{os} increased with temperature. The temperature dependence of χ can be expressed by ,

$$\chi = A(\phi) + \frac{B(\phi)}{T} \quad (2)$$

where T is absolute temperature and $A(\phi)$ and $B(\phi)$ depend on ϕ_{PS} . Next, we estimated spinodal temperature with the obtained T dependence of χ . The interaction parameter at Spinodal point, χ_s , can be calculated by ,

$$\chi_s = \frac{v_0}{2} (1\phi_{dPS}v_{dPS}\langle z_{dPS} \rangle + \frac{1}{\phi_{DEM}v_{DEM}}) \quad (3)$$

where ϕ_i is volume fraction, v_i is the molar volume, $\langle z_i \rangle$ is weight-average degrees of polymerization for i th components, and v_0 denote reference molar volume of the solution. We estimated the spinodal temperature by substituting χ_s into eq.(2). Figure 3 shows the spinodal curve of dPS/DEM, indicating that the dPS/DEM solution has an Upper Critical Solution Temperature type phase diagram.

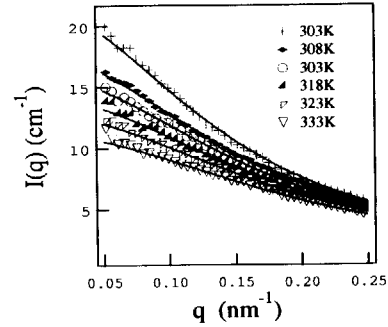


Figure 1: SANS profiles for dPS/DEM=4/96 (wt/wt).

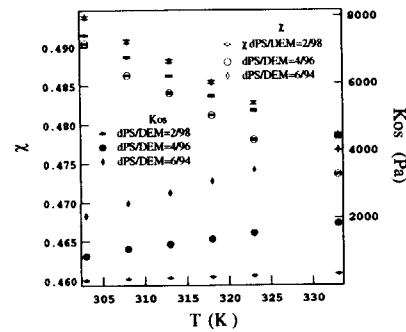


Figure 2: The temperature-dependence of χ and K_{os} of dPS/DEM solutions.

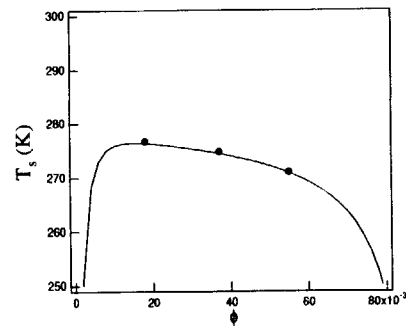


Figure 3: Spinodal Curve plot as a function of volume fraction of polystyrene ϕ .

2.2.6 Crystal Structure of Deuterated Polyethylene

Y. Takahashi and T. Kumano

*Department of Macromolecular Science, Graduate School of Science,
Osaka University Toyonaka, Osaka 560-0043, Japan*

Neutron diffraction has several advantages in comparison with X-ray diffraction for crystalline polymers.¹⁻³⁾ In the previous paper,³⁾ the crystal structure of deuterated polyethylene was determined in temperature range 10 - 300K by using the neutron diffraction on the equator measured for the fiber specimen by powder diffractometer, and the angle ϕ between the molecular plane and the b-axis and the rigid body temperature parameters were determined. On the other hand, the diffractometer BIX-3 and neutron imaging plate were developed by Niimura's group. In the present study, the neutron crystal structure analysis is carried out by using three-dimensional data measure by BIX-3 and neutron imaging plate.

The film of the commercially supplied deuterated polyethylene was made by a hot press and stretched in boiling water. The films were stacked and rolled up the cylinder with diameter 5mm.

The neutron diffraction was measured with BIX-3 and neutron imaging plates. The digital data of eight imaging plates were summed up in order to improve the signal to noise ratio. The integrated intensities were estimated according to the method developed for X-ray.⁴⁾ Digital data for one pixel of reflection arc are summed along the arc with constant 2θ and the summed intensities are plotted against a layer line. From the one-dimensional intensity curve thus obtained, the integrated intensity was estimated.

The structure refinement was made by the rigid body least-squares method.⁵⁾ The parameters to be refined are the azimuthal angle between the molecular plane and the a axis, θ , the translational temperature parameters, T_{11} , T_{12} , T_{22} , and T_{33} , and the librational temperature parameter, ω_{33} . Finally, the least-squares refinement converged to the discrepancy factor $R = 0.184$. The value θ is estimated to be 46.3° (standard deviation: 1.5°), which corresponds well to the value 45.1° (1.3°) determined in the previous paper.³⁾ Translational temperature parameters, T_{11} , T_{12} , and T_{22} , are 2.58 (0.67), 1.40 (0.66), and 2.54 (0.71), respectively, which correspond well to $T_{aa} = 2.49$ (0.42), $T_{ab} = 0.66$ (0.53), and $T_{bb} = 2.43$ (0.47) determined in the previous paper³⁾ within the accuracy of the standard deviations. The librational temperature parameter ω is 0.52 (0.52), which also corresponds to the value 1.04 (0.44) determined in the previous paper.³⁾

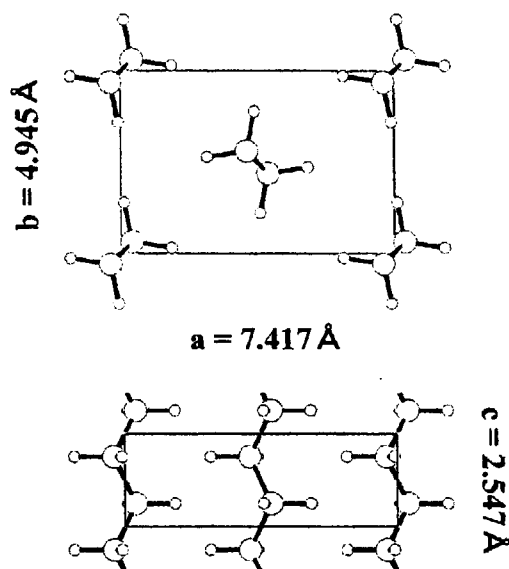


Figure 1: Crystal Structure of Polyethylene.

Acknowledgement

The authors express their thanks to Drs N. Niimura, I. Tanaka, and K. Kurihara of JAERI for neutron diffraction measurements.

References

- 1) Y. Takahashi: "Neutron Structure Analysis of Crystalline Polymers", *Recent Res. Devel. in Macromol. Res.*, **3** (1998) 265.
- 2) Y. Takahashi: "Neutron Diffraction by Crystalline Polymers", *ACS Symposium Series 739*, "Scattering from Polymers" edited by P. Cebe, B. S. Hsiao, and D. J. Lohse, Chapter 5, 74 (2000).
- 3) Y. Takahashi: *Macromolecules* **31** (1998) 3868.
- 4) Y. Takahashi and H. Imai, to be published.
- 5) Y. Takahashi, T. Sato, H. Tadokoro, and Y. Tanaka: *J. Polym. Sci. Polym. Phys. Ed.*, **11** (1973) 233.

2.2.7 The First Success in Direct Extraction of Hydrogen Atoms in Polyethylene Crystal

K.TASHIRO, I.TANAKA^{1,2}, T.OOHARA¹, N.NIIMURA^{1,2}, S.FUJIWARA¹,
K. KURIHARA¹, and T. KAMAE

Graduate School of Science, Osaka University, Osaka 560-0043

¹*Advanced Science Research Center, JAERI, Tokai, Ibaraki 319-1195*

²*Faculty of Engineering, Ibaraki University, Hitachi, Ibaraki 316-8511*

When we try to estimate the limiting physical properties of polymer crystals, we need to know the atomic positions in the crystal lattices, in particular the positions of hydrogen atoms as exactly as possible. However, even for the low-molecular-weight compounds, it has been difficult to extract the hydrogen atomic positions using an X-ray structure analysis technique. The situation is worse for polymer crystals, which show quite poor X-ray diffraction patterns because of small crystallite size. In a previous paper¹⁾ we succeeded in extracting the hydrogen atoms by calculating the Fo-Fc Fourier map based on the X-ray imaging-plate system. This success was based on the usefulness of 2-dimensional imaging plate detector. It may be possible to know the hydrogen atom positions in more exact and direct manner by taking the 2-dimensional neutron diffraction patterns of the uniaxially-oriented deuterated polymer materials using a neutron imaging plate system²⁾. As reported here, we have succeeded to pick up the hydrogen atom positions of orthorhombic polyethylene crystal by collecting the diffraction data for uniaxially-oriented fully-deuterated (D) and hydrogenous (H) polyethylene samples using a JAERI neutron imaging plate system BIX-3. The thus clarified hydrogen atom positions were refined and were compared with X-ray diffraction and electron diffraction results³⁾.

On the basis of the 2-dimensional neutron fiber diagrams taken for the uniaxially-oriented D and H polyethylene samples, the Fourier maps were calculated. As shown in Figure 1, the positive and negative density peaks of hydrogen atoms were detected clearly for the D and H polyethylene samples, respectively. In particular the Fo-Fc maps made the positions more clear. The structure parameters were refined on the basis of least-squares method. The reliability factors were 0.135 for 29 reflections of the D sample and 0.191 for 17 reflections of the H sample. Of course the X-ray structure analysis gave essentially the same crystal structure but the hydrogen atom positions could not be refined reasonably¹⁾. The refinement of both the hydrogen and carbon positions could be successfully made for the first time on the basis of neutron diffraction data. On the other hand, from the electron diffraction pattern measured for polyethylene single crystal grown from the solution, 45 reflections were

collected in total. The direct method allowed us to extract the hydrogen atoms and the final reliability factor was 0.176. However, the structure parameters were not as reasonable as those obtained by X-ray and neutron diffraction data. This is because of modification of relative intensities of diffraction spots due to the so-called multiple scattering effect in the single crystal.

In conclusion, we have succeeded in evaluating the hydrogen atomic positions as exactly as possible on the basis of 2-dimensional neutron diffraction patterns taken for D and H polyethylene samples. Although a fully deuterated sample is difficult to prepare the usefulness of combining this sample with neutron diffraction technique is clear as described here.

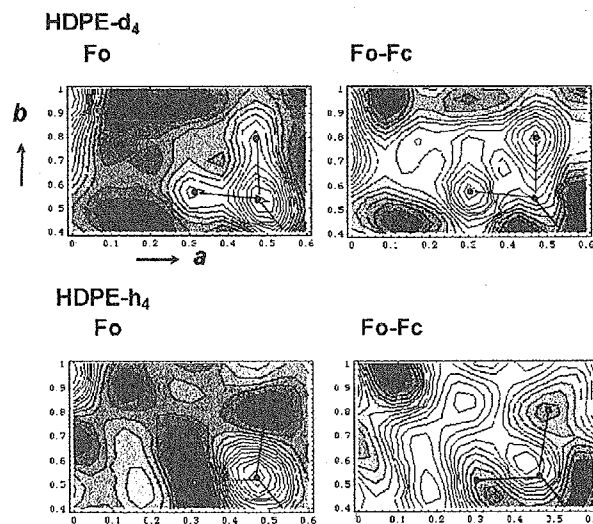


Figure 1: Fourier neutron density maps obtained for uniaxially-oriented (top) deuterated and (bottom) hydrogenous polyethylene samples.

References

- 1) K. Tashiro, H. Asanaga, K. Ishino, R. Tazaki, and M. Kobayashi, *J. Polym. Sci.: Part B: Polym. Phys.* **35** (1997) 1667.
- 2) N. Niimura, Y. Karasawa, I. Tanaka, J. Miyahara, K. Takahashi, H. Saito, S. Koizumi, and M. Hidaka, *Nucl. Instrum. Meth. Phys. Res. A* **349** (1994) 521.
- 3) K. Tashiro, I. Tanaka, T. Oohara, N. Niimura, S. Fujiwara, T. Kamae, *Macromolecules* **37** (2004) 4109.

2.2.8 Observation of Niobates Nanosheets in Aqueous Solutions by Neutron Scattering

D. Yamaguchi¹, N. Miyamoto², S. Koizumi¹, T. Nakato^{3,2}, and T. Hashimoto^{4,1}

¹Advanced Science Research Center, JAERI, Tokai, Ibaraki 319-1195

²PRESTO, Japan Science and Technology Corporation

³Graduate School of Bio-Applications and Systems Engineering (BASE), Tokyo University of Agriculture and Technology, 2-24-16 Naka-cho, Koganei-shi, Tokyo 184-8588

⁴Department of Polymer Chemistry, Graduate School of Engineering, Kyoto University, Katsura, Kyoto 615-8510

Exfoliation of inorganic layered materials into their unit layers has been paid attention because of their properties to form nanohybrids with other molecules. Among these layered materials, the layered niobates such as $\text{K}_4\text{Nb}_6\text{O}_{17}$ have high potential for application since they present excellent photoactive properties. Recently it is shown that the exfoliated nanosheets of $\text{K}_4\text{Nb}_6\text{O}_{17}$ exhibit peculiar liquid crystalline behavior^[1]. In this study the structure of exfoliated $\text{K}_4\text{Nb}_6\text{O}_{17}$ nanosheets in the aqueous solutions were investigated by small-angle and ultra-small-angle neutron scattering spectrometers (SANS-J and PNO).

An interesting feature of $\text{K}_4\text{Nb}_6\text{O}_{17}$ nanosheets is a variety of lateral sizes, which is controlled by breaking large single crystal of $\text{K}_4\text{Nb}_6\text{O}_{17}$ with using ultrasonication, while the fixed thickness of 1.8 nm^[1]. The liquid crystallinity is dependent on the lateral size and concentration of the nanosheets, that is, at higher concentration or larger lateral size of nanosheets, the solution exhibits liquid crystalline phase while at lower concentration or smaller lateral size, the solution is in the isotropic phase. However, a nonintuitive scattering behavior of lateral size dependence was observed on SANS measurement. That is, as the lateral size was decreased, the scattering peaks sharpened and the higher order scattering maxima came to appear, suggesting the degree of order increased.

Our speculation for this discrepant tendency between SANS observation and general phase behavior (above described) is following; The $\text{K}_4\text{Nb}_6\text{O}_{17}$ nanosheet has a specific bending modulus and the persistent length of the nanosheet is inversely proportional to the bending modulus. The nanosheets whose lateral sizes are bigger than the persistent length are naturally expected to be in bent (or crumpled) state. Therefore, in the case of nanosheets, whose lateral size is smaller than the persistent length and which are regarded as unbending and flat disk, they might form the liquid crystalline phase in which the distance between nanosheets are nearly constant at anywhere. While in the case of nanosheets which have extremely large lateral size compared to the persistent length, they might form the liquid crystalline phase where the intersheet distance is not constant but has a large distribution due to the crumple of each sheet.

To obtain further information about the structure

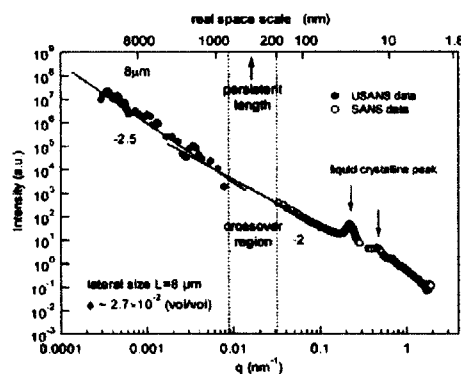


Figure 1: Combined SANS and USANS profiles for $\text{K}_4\text{Nb}_6\text{O}_{17}$ aqueous solution whose lateral size $L=8\mu\text{m}$ and concentration $\phi=2.7\times 10^{-2}$ (vol/vol).

of nanosheets the ultra-small-angle neutron scattering (USANS) measurement was performed. Figure 1 show the combined data of SANS and USANS for the nanosheet solution of which lateral size is $8\mu\text{m}$. As we can see in Figure 1, the USANS profile of nanosheet does not have any characteristic peaks but show a monotonic power law scattering of which index is slightly smaller than -2 (ca. -2.5). Supposing that the value of index, -2.5 obtained by the power law scattering of USANS, corresponds to the mass fractal dimension, it is suggested that the nanosheets take neither perfectly flat shape (of which mass fractal dimension is -2) nor perfectly collapsed shape (of which mass fractal dimension is -3) but partially bent and/or crumpled shape^[2]. Thus, the USANS data constructively support our speculation for nonintuitive lateral size dependence of SANS data. In the case of nanosheet whose lateral size is ca. $8\mu\text{m}$, the persistent length is estimated to be hundreds of nm from the crossover q region, where the power law index changes from -2.5 to -2. We can regard the niobate nanosheet, i.e., the elementary layer of $\text{K}_4\text{Nb}_6\text{O}_{17}$ crystal, as a softmatter, even though it is an inorganic crystal.

References

- 1) Miyamoto, N.; Nakato, T. *J. Phys. Chem. B*, **2004**, *108*, 6152.
- 2) Abraham, F. F.; Nelson, D. R. *J. Phys. (France)*, **1990**, *51*, 2653.

2.2.9 Preparation of Palladium Nanoparticles with Dendrimers As Observed by SANS

H. Tanaka, T. Hashimoto, H. Ito, K. Naka, Y. Chujo, and S. Koizumi¹

Department of Polymer Chemistry, University of Kyoto, Kyoto 615-8510

¹Advanced Science Research Center, JAERI, Tokai, Ibaraki 319-1195

It is well known that metal nanoparticles exhibit quantum mechanical properties, and which makes them promising materials for various kinds of applications in nanotechnology. The patterning of the metal nanoparticles into organized structures is quite essential to achieve useful properties for chemical, optical, magnetic, and electronic devices. One of the superior methodologies for controlling the organized structures involves the chemical cross-linking by organic ligands. Recently, Chujo et al. have found that by employing a cubic silsesquioxane¹⁾ or a polyamidoamine (PAMAM) dendrimer as such a cross-linker, it becomes attainable to organize palladium nanoparticles into spherical aggregates *via* self-organized templates in methanol solutions without any external force.

In this report, we focus on the structure formation mechanism of palladium nanoparticles prepared through alcoholic reduction of the mixture of palladium acetate in *N,N*-dimethylformamide and PAMAM dendrimer in methanol at 50 °C, by means of *in-situ* SANS and SAXS measurements. SANS measurements were performed with SANS-J at the guide hall of the reactor JRR-3M in JAERI.

Figure 1 shows SANS and SAXS profiles obtained during the reduction process. The scattered intensity $I(q)$ is plotted as a function of scattering vector q defined by $q = (4\pi/\lambda)\sin(\theta/2)$, with θ and λ being the scattering angle and the wavelength of incident beam, respectively. It should be noted that SANS measurements cover relatively lower q region, $q < 0.1 \text{ nm}^{-1}$, on the other hand, SAXS cover higher q region, $q > 0.1 \text{ nm}^{-1}$. The scattering vector q can be expressed with characteristic length ξ , $q = 2\pi/\xi$, therefore, SANS profiles can provide information on the structure with relatively larger size, $\xi > 60 \text{ nm}$, and SAXS profiles provide rather smaller structure, $\xi < 60 \text{ nm}$.

The time change of SANS and SAXS profiles show quite different features, that while SANS profiles show almost same tendency independent of the reaction time, where the form factor from assembly of dispersed spheres with average diameter of 80 nm as shown by solid curve are clearly observed even from 20 minutes after preparing the solutions, SAXS profiles exhibit distinct change as reaction proceeds, where the scattered intensity gradually increase with time, indicating the formation of palladium nanoparticles of 5 nm in average diameter as shown by dotted curve.

The experimental results described above are quite

indicative of the formation mechanism of spherical aggregates. It can be schematically depicted in Figure 2. First, palladium ions and PAMAM dendrimers associated to form spherical domains with average diameter 80 nm just after mixing of the two solutions due to attractive interactions between palladium ions and PAMAM dendrimers. Second, within such spherical domains, reductions of palladium ions were occurred, forming nanoparticles of 5 nm in average diameter, during the course of which the spherical domains of 80 nm diameter were maintained and served as templates for nanoparticle formation.

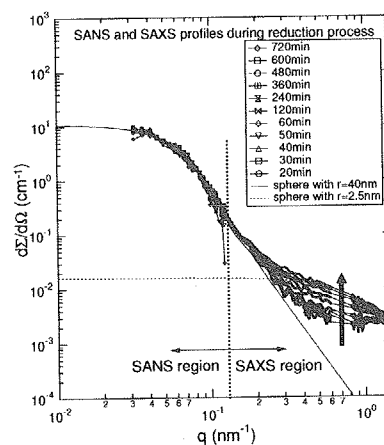


Figure 1: Time-resolved SANS and SAXS profiles during reduction process.

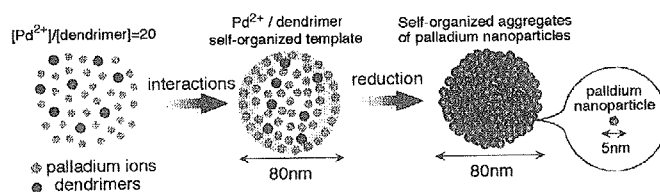


Figure 2: Schematic illustration of self-organizing process of palladium nanoparticles.

References

- 1) K. Naka, H. Ito, and Y. Chujo, *Nano. Lett.*, **2**, 1183 (2002)

2.2.10 Structural Analysis of Polymer Electrolyte Membranes Based on Crosslinked Polytetrafluoroethylene by Small-Angle Neutron Scattering

T. Yamaki, M. Asano, R. Motokawa¹, S. Koizumi¹ and M. Yoshida

Takasaki Radiation Chemistry Research Establishment, JAERI, Takasaki, Gunma 370-1292

¹Advanced Science Research Center, JAERI, Tokai, Ibaraki 319-1195

Polymer electrolyte fuel cells (PEFCs) have received much attention in the transportation and portable power fields. The proton exchange membrane (PEM) is a vital component in the PEFCs; this membrane acts as a separator to prevent mixing of the reactant gases and as an electrolyte for transporting protons from the anode to the cathode. The sulfonated fluorocarbon polymer membrane, *e.g.*, Nafion, is the PEM material widely used for this type of applications.

Our efforts have been independently focused on the development of novel PEM materials by radiation-induced graft polymerization of vinyl monomers (*e.g.*, styrene) into a fluorocarbon polymer film followed by sulfonation¹⁾. The use of radiation-crosslinked polytetrafluoroethylene (PTFE) films for the γ -ray-graft substrates enabled us to prepare the polymeric membranes with a much larger ion-exchange capacity (IEC) and moderate osmotic swelling property in water²⁾. Importantly, the crosslinking process of PTFE should be necessary for improving membrane performances.

The understanding and optimization of swelling and proton conductivity of our membranes require information on the microstructure and on its modification. Such information also leads to a deep insight into the dynamical properties inside the membrane from the molecular to macroscopic level. Therefore, the aim of this work is to clarify the structure of the crosslinked-PTFE based membranes under different external conditions using small-angle neutron scattering (SANS).

All the PEMs were prepared by our established procedure¹⁾. The vacuum-dried membranes in the acid form were stored in deuterated water before use. SANS experiments were carried out with the SANS-J instrument at the JRR-3M research reactor of JAERI. The scattering intensity was measured as a function of q , the magnitude of scattering vector. q is related to the scattering angle, θ , by the relationship $q = (4\pi/\lambda)\sin\theta$, where λ is the wavelength of the incident neutron beam (0.65 nm). The q range was varied from 0.03 to 2 nm⁻¹.

Figure 1 shows the SANS profile of the membrane based on 130-kGy crosslinked PTFE (IEC = 2.0 meq g⁻¹) together with that of Nafion for comparison. Nafion exhibited a characteristic scattering peak around $q = 1.4$ nm⁻¹, corresponding to a Bragg distance of 4.2 nm. This so-called "ionomer peak" is due

to a microphase separation between the hydrophilic ionic domains and hydrophobic polymer matrix. According to the previous SANS experiments, water in Nafion was found to be localized and form pools embedded in the matrix. In contrast, an entirely different profile was obtained for our membrane: an intense small-angle upturn in intensity and no well-defined peak. This demonstrates that the crosslinked-PTFE sulfonic acid membranes will possess the structural properties which cannot be rationalized by the so far presented models.

Based on the above preliminary results, more thorough investigation of the membranes prepared under different conditions is now in progress. A number of other studies including scattering at the smaller q range, investigation at various humidity levels, and quantitative interpretation of the data should be performed to understand the complex structure present in our hydrated membranes.

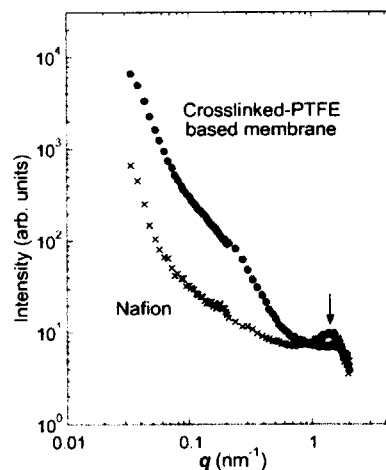


Figure 1: SANS profiles of the crosslinked-PTFE based electrolyte membrane and Nafion, both of which were swollen in deuterated water. The arrow indicates the "ionomer peak" on the pattern of Nafion.

References

- 1) T. Yamaki, M. Asano, Y. Maekawa, Y. Morita, T. Suwa, J. Chen, N. Tsubokawa, K. Kobayashi, H. Kubota and M. Yoshida : Radiat. Phys. Chem. **67** (2003) 403.
- 2) T. Yamaki, K. Kobayashi, M. Asano, H. Kubota and M. Yoshida : Submitted to Polymer.

2.3 Strongly Correlated Electron Systems and Superconductivity

- U-compounds, Ce-compounds,
Transition-metal Oxides -

This is a blank page.

2.3.1 Spin State Transition of $\text{Pr}_{1-x}\text{Ca}_x\text{CoO}_3$

T. Fujita, Y. Yasui, T. Miyashita, Y. Kobayashi, M. Sato, Y. Shimojo¹, N. Igawa¹, Y. Ishii¹ and K. Kakurai¹

Department of Physics, Nagoya University, Furo-cho, Chikusa-ku, Nagoya 464-8602

¹*Japan Atomic Energy Research Institute, Tokai, Ibaraki 319-1195*

Spin state change is a remarkable characteristic of Co oxides, which induces a variety of interesting physical behaviors. In perovskite Co oxides RCoO_3 ($\text{R}=\text{Y}$ and various rare earth elements), for example, the change is often found from the low spin (LS; spin $s=0$; t_{2g}^6) ground state to the intermediate spin (IS; $s=1$; $t_{2g}^5e_g^1$) or the high spin (HS; $s=2$; $t_{2g}^4e_g^2$) state with increasing temperature T .¹⁾ It indicates that the difference of the electronic energies, δE between these spin states is rather small. The value of δE is expected to increase with decreasing ionic radius r_R of R^{3+} , because the crystal field splitting Δ_c increases with decreasing r_R through the contraction of the volume (V_o) of the CoO_6 octahedra. However, it is not simple, in general, to understand the change of δE in detail only by considering Δ_c (and the Hund coupling J_H), because the Co-Co transfer energy t may also change δE mainly through the changes of Co-O-Co bond angle caused by the change of the ionic radius r_R of R^{3+} . For $\text{R}_{1-x}\text{A}_x\text{CoO}_3$ ($\text{A}=\text{Ba}$, Sr and Ca), we have to consider both effects of the hole doping and the δE (Δ_c)-change induced by the V_o -change.²⁾ External pressure can also change the value of δE . It is interesting to search for proper set of these parameters, r_R , carrier density, external pressure and so on, to obtain desired electronic state.

For $\text{Pr}_{1-x}\text{Ca}_x\text{CoO}_3$, a transition from the high temperature conducting phase to the low temperature less conducting (insulating) one has been reported by Tsubouchi *et al.*³⁾ in the very narrow region of $x \sim 0.5$. We have independently found a similar transition in the wide x region under the condition of high pressure $p > 5$ kbar.⁴⁾ The abrupt decrease of the magnetic susceptibility χ of $\text{Pr}_{0.6}\text{Ca}_{0.4}\text{CoO}_3$ at the transition temperature T_s with decreasing T under high pressure, can be seen as was reported at ambient pressure for $\text{Pr}_{0.5}\text{Ca}_{0.5}\text{CoO}_3$ in ref. 3. This result and those of ^{59}Co -NMR studies by the present authors' group, indicate that the transition is accom-

panied by the IS \rightarrow LS spin state change of Co^{3+} ions with decreasing T . We have carried out further studies by various methods to clarify details of the transition and to extract more information what factors determine the spin state of the system. Here, the results of the neutron diffraction studies for the samples of $\text{Pr}_{1-x}\text{Ca}_x\text{CoO}_3$ with x up to 0.5 are briefly presented.⁴⁾ The high resolution powder diffractometer (HRPD) of JRR-3M of JAERI in Tokai was used. Rietveld analyses were carried out by using the computer program Rietan 2000.⁵⁾

Because both the volumes V_u and V_o of the unit cell and the CoO_6 octahedra, respectively decrease significantly with increasing x in the region of the relatively large x , the value of Δ_c can be considered to increase with increasing x . However, detailed analyses of the magnetic susceptibilities χ and our NMR results indicate that δE decreases with increasing x . We think that the Co-Co transfer energy t acts an important role for the explanation of this behavior of δE . At the transition, the sudden increase of the tilting angle of the CoO_6 octahedra (or the sudden decrease of the angle α) takes place. This tilting stabilize the LS state through the reduction of t or the increase of δE in the low temperature phase.

References

- 1) for example, K. Asai, A. Yoneda, O. Yokokura, J. M. Tranquada, G. Shirane and K. Kohn: J. Phys. Soc. Jpn. **67** (1998) 290.
- 2) H. Masuda, T. Fujita, T. Miyashita, M. Soda, Y. Yasui, Y. Kobayashi and M. Sato: J. Phys. Soc. Jpn. **72** (2003) 873.
- 3) S. Tsubouchi, T. Kyomen, M. Itoh, P. Ganguly, M. Oguni, Y. Shimojo, Y. Morii and Y. Ishii: Phys. Rev. **B 66** (2002) 052418.
- 4) T. Fujita, T. Miyashita, Y. Yasui, Y. Kobayashi, M. Sato, E. Nishibori, M. Sakata, Y. Shimojo, N. Igawa, Y. Ishii, K. Kakurai, T. Adachi, Y. Ohishi and M. Sakata: J. Phys. Soc. Jpn. **73** (2004) No. 7.
- 5) F. Izumi and T. Ikeda: Mater. Sci. Forum **321-324** (2000) 198.

2.3.2 Two Magnetic Transitions of $\text{NdBaCo}_2\text{O}_5$

M. Soda, Y. Yasui, M. Ito, S. Iikubo, M. Sato and K. Kakurai¹

Department of Physics, Nagoya University, Chikusa-ku, Nagoya 464-8602

¹*Advanced Science Research Center, JAERI, Tokai, Ibaraki 319-1195*

Co-oxides often exhibit spin state change, which bring about a variety of physical behaviors.^{1,2)} RCoO_3 ($\text{R}=\text{Y}$ and rare earth elements) and $\text{RBaCo}_2\text{O}_{5+\delta}$ are examples of such systems. The latter systems are called oxygen deficient perovskites: RBaCo_2O_5 have the linkage of corner-sharing CoO_5 pyramids, while $\text{RBaCo}_2\text{O}_{5.5}$ have the linkage of alternating CoO_6 octahedra and CoO_5 pyramids. For these systems, various kinds of magnetic states and charge-ordered states have been reported.^{3,4)}

In the present work, neutron scattering studies have been carried out on a single crystal of $\text{NdBaCo}_2\text{O}_5$ to collect information on the spin state of Co ions in relation to the local structures. The average valence of Co ions is +2.5.

Neutron measurements were carried out by using the triple axis spectrometer TAS-2 installed at the thermal guide of JRR-3 of JAERI in Tokai. The crystal was first oriented with the $[010]$ (or $[100]$) axis vertical, where both $(h,0,l)$ and $(0,k,l)$ points in the reciprocal space could be reached due to the coexistence of the a^* - and b^* -domains. Measurements were also carried out for the crystal orientation with the $[110]$ axis vertical.

Integrated reflection intensities have been measured at various reciprocal points in the temperature (T) range of 7-370 K. (We use here the unit cell with the size of $\sim a_p \times 2a_p \times 2a_p$, where a_p is the lattice parameter of the cubic perovskite cell.) With decreasing T , the superlattice peaks appear at $T_N \sim 360$ K at $Q=(k'/2, k'/2, l)$ (k' :odd), which corresponds to the antiferromagnetic order. With further decreasing T , another set of superlattice peaks at $Q=(k'/2, 0, l)$ (k' :odd) appears at $T_{\text{CO}} \sim 250$ K. Detailed structure analyses have revealed that the set of superlattice peaks stems from the existence of two distinct Co-sites with different valences and different magnetic moments, indicating that the charge ordering exists below T_{CO} . When the temperature of the system is lowered through T_{CO} , the profile widths of all reflections which exist above T_{CO} , begin to increase at

$\sim T_{\text{CO}}$ and the peak intensities are reduced with the integrated intensities being kept unchanged. We think that large local lattice distortions caused by the charge ordering are the origin of the significant broadening of the reflections.

The magnetic structures have been determined at $T=300$ K (antiferromagnetic phase) and $T=7$ K (antiferromagnetic and charge ordered one). The magnetic structures at both temperatures have been found to be so-called G-type antiferromagnetic one (or NaCl-type). At 300 K, the aligned moments μ of Co ions, all of which have the average valence of +2.5, is $2.14 \pm 0.09 \mu_B$.

By analyzing the data at 7 K, we have found that all the apical oxygens of the pyramids and on the O-Co-O chains along the a -axis, are shifted in the way that the volumes of the pyramids expand or contract alternately from the positions above T_{CO} , which confirms that the charge ordering really takes place at T_{CO} . The magnitudes μ of the aligned moments of two crystallographically distinct Co sites are $2.68 \pm 0.04 \mu_B$ and $2.46 \pm 0.04 \mu_B$ at 7 K. (The moment directions are parallel or anti-parallel to $[100]$.) Because the magnetic reflection intensities do not exhibit anomalous T dependence, we think that Co ions are in the high spin state over the whole temperature range studied here ($T < T_N \sim 360$ K). The difference between the aligned moments of two Co sites is significantly smaller than that reported to be the ordering of Co^{3+} and Co^{2+} . The presently observed small difference of the moments between the crystallographically distinct sites indicates that the real charge difference between the sites may not be unity, that is, the time- or spatially-averaged valences of Co ions in the distinct sites cannot be considered to be +3 and +2.

References

- 1) H. Masuda *et al.*: J. Phys. Soc. Jpn. **72** (2003) 873.
- 2) T. Fujita *et al.*: J. Phys. Soc. Jpn. **73** (2004) No. 7
- 3) D. Akahoshi and Y. Ueda: J. Solid State Chem. **156** (2001) 355.
- 4) M. Soda *et al.*: J. Phys. Soc. Jpn. **72** (2003) 1729.

2.3.3 Structures and Spin States of NdBaCo₂O_{5.5}

M. Soda, Y. Yasui, M. Ito, S. Iikubo, M. Sato and K. Kakurai¹

Department of Physics, Nagoya University, Chikusa-ku, Nagoya 464-8602

¹*Advanced Science Research Center, JAERI, Tokai, Ibaraki 319-1195*

In Co-oxides, the spin state of Co ions is one of key elements to understand their physical properties. Because they often exhibit spin state change, a variety of physical behaviors are expected with the change of the difference of the electronic energies, δE between the spin states.^{1,2)} In $R_{1-x}A_x\text{CoO}_{3-\delta}$ ($A=\text{Sr, Ba and Ca}$), the substitution of R^{3+} with A^{2+} affects the effective value of δE through the introduction of hole-carriers and by changing the average ionic radius of $R_{1-x}A_x$. The electron transfer energy t seems to be also important to determine δE .²⁾ In $\text{RBaCo}_2\text{O}_{6-2\delta}$ ($x=0.5$) with relatively small size of R^{3+} , R and Ba are ordered and the oxygen-deficiency is also found to be in the ordered state.³⁻⁵⁾ The structure of $\text{RBaCo}_2\text{O}_{5.5}$ is formed by the linkage of alternating CoO_6 octahedra and CoO_5 pyramids along the b -axis. These systems provide a rather good opportunity to extract fundamental information how the magnetic state of Co ions within the pyramids and octahedra depend on such the local arrangements of the ligand atoms. In the present work, neutron scattering studies have been carried out on a single crystal of $\text{NdBaCo}_2\text{O}_{5.5}$ by using the spectrometer TAS-2 installed at the thermal guide of JRR-3 of JAERI in Tokai, to collect information on the spin state of Co ions in relation to the local structures.

Intensities of the neutron Bragg reflections with various indices have been measured on a single crystal of $\text{NdBaCo}_2\text{O}_{5.5}$ in the temperature range of 7-320 K, where several superlattice reflections as well as the fundamental reflections of the unit cell with the size of $\sim a_p \times 2a_p \times 2a_p$ have been found, where a_p is the lattice parameter of the cubic perovskite cell. With decreasing T from the temperature above 320 K, the intensities of several nuclear Bragg reflections change in the temperature region $T > 190$ K. At $T_c \sim 170$ K, additional intensity component appears at several nuclear Bragg points. Superlattice peaks corresponding to the G-type antiferromagnetic structure also appear ($Q=(k'/2, k', l)$; $k'=\text{odd}$) at this temperature. With further decreasing T , the intensity ratios among several reflections begin to change at $T^* \sim 30$ K. No additional reflections appear at this temperature.

At 40 K ($T^* < T < T_c$) and 7 K ($T < T^*$) the magnetic structures have been analyzed, where the spin states of Co ions within the CoO_6 and CoO_5 polyhe-

dra are basically clarified. One of characteristics of these magnetic structures is that there is the significant difference between the magnitudes of the aligned moments of Co^{3+} ions in CoO_6 and CoO_5 polyhedra. At 40 K the magnitude μ_1 and μ_2 of Co^{3+} in the octahedra and the pyramids are $1.28(\pm 0.04) \mu_B$ and $2.47(\pm 0.05) \mu_B$, respectively. These values indicate that Co^{3+} ions of the octahedra are in the intermediate spin (IS) state, while those of the pyramids are in the high spin (HS) state. The magnetic moments have the coplanar and canted structure, although the canting angles are different between the moments in the CoO_6 and CoO_5 polyhedra. In the region of $T < T^*$, μ_1 decreases gradually as T decreases, although the magnetic structure does not exhibit appreciable change. The electrical resistivity ρ begins to increase rapidly at T^* with decreasing T . These results suggest that the spin state of Co^{3+} ions in the octahedra approaches the low spin (LS) state below T^* . The direct evidence for the existence of the LS state of Co^{3+} ions in the octahedra has reported in $\text{TbBaCo}_2\text{O}_{5.5}$ ⁴⁾ by the present authors' group.

The present results and those reported in refs. 2, 4 and 5 indicate that the spin state of Co ions depends on their local arrangement of the ligand oxygens. The ionic radius r_R of R^{3+} is important for the determination of the spin state, too: For smaller r_R , Co^{3+} in the octahedra (pyramids) prefer the LS (IS) states more, and for large r_R , they prefer the IS (HS) states more. These relationships can be understood by considering the magnitude of the energy splitting between the t_{2g} and e_g orbitals created by the crystal field: With decreasing r_R , the volume of the polyhedra increases and the energy splitting decreases, resulting in the tendency to stabilize the higher spin state. The smaller energy splitting of Co ions of pyramids have higher spin states than in the octahedra.

References

- 1) H. Masuda *et al.*: J. Phys. Soc. Jpn. **72** (2003) 873.
- 2) T. Fujita *et al.*: J. Phys. Soc. Jpn. **73** (2004) No. 7
- 3) D. Akahoshi and Y. Ueda: J. Solid State Chem. **156** (2001) 355.
- 4) M. Soda *et al.*: J. Phys. Soc. Jpn. **72** (2003) 1729.
- 5) M. Soda *et al.*: J. Phys. Soc. Jpn. **73** (2004) 464.

2.3.4 Ni impurity effects on the antiferromagnetic state in the lightly hole-doped $\text{La}_{2-x}\text{Sr}_x\text{CuO}_4$ H. Hiraka, T. Machi¹, N. Watanabe¹, Y. Itoh¹, M. Matsuda² and K. Yamada*Institute for Materials Research, Tohoku University, Sendai 980-8577*¹*Superconductivity Research Laboratory, International Superconductivity Technology Center, Tokyo 135-0062*²*Advanced Science Research Center, JAERI, Tokai, Ibaraki 319-1195*

La_2CuO_4 , the parent material of the monolayer superconductor $\text{La}_{2-x}\text{Sr}_x\text{CuO}_4$ (LSCO), is one of the typical two-dimensional antiferromagnet. It is well known that the Néel temperature T_N (~ 320 K) is very sensitive to hole doping and the three-dimensional antiferromagnetic order disappears when doped by the amount of 2% Sr. Recent magnetization measurements^{1,2}, however, indicated that T_N increases by ~ 100 K with Zn- or Ni-substitution in the lightly hole-doped phase of LSCO ($x \sim 0.01$), suggesting strong correlation between the hole motion and the magnetic interaction. In order to clarify the interesting antiferromagnetic state directly, magnetic neutron study using single crystals is highly desirable.

Neutron diffraction measurements were carried out on the triple-axis spectrometer TAS-2, which is installed at the beam port T2-4 of JRR3M in JAERI (Tokai). Thermal neutron beam ($E_i = 13.5$ meV) was selected by the monochromator of PG(002) reflection. $\text{La}_{2-x}\text{Sr}_x\text{Cu}_{1-y}\text{Ni}_y\text{O}_4$ single crystals of $x = 0.01$ and $0.01 \leq y \leq 0.10$ were grown by the traveling-solvent-floating-zone method, and characterized by magnetization and electrical resistivity measurements. The cylindrical samples with dimensions of about $4\phi \times 20$ mm were set up in the $(h, k, 0)$ or $(h, 0, l)$ scattering plane (*Bmab* notation). We mainly measured magnetic Bragg reflections of $(1, 0, 2n)$, $(0, 1, 2n + 1)$ and $(1, 2n, 0)$, where n is integral.

Figure 1 shows the Ni-doping dependence of T_N in the antiferromagnetic phase of LSCO ($x = 0.01$). T_N drastically increases with y and it peaks at $y_{cr} = 0.03 \sim 0.04$, in agreement with magnetic susceptibility measurements. The highest T_N reaches up to ~ 310 K, which is comparable to T_N of La_2CuO_4 . Further, we observed that the magnetic-intensity pattern changes across the Ni concentration of y_{cr} . As shown in Fig. 1, it is regarded as a result of spin rotation by 90° in the CuO_2 planes, that is, from S/b -axis (realized in La_2CuO_4 , Cu-type) into S/a -axis (realized in La_2NiO_4 , Ni-type) with Ni substitution.

The striking recovery of T_N can be explained as a reduction of the magnetic frustration (or the magnetic instability) due to the hole-carrier localization near Ni impurities. This carrier-localization picture is consistent with the increased resistivity measured for the Ni doped compounds. In our conjecture, the hole carrier is supposed to occupy not the O-2p orbitals but

the Ni-3d orbitals in the CuO_2 planes over the low Ni doping. In other words, it results in Ni^{3+} states with $S = 1/2$ for small y . However, further Ni doping will provide Ni^{2+} states because of the finite hole numbers, and finally the magnetic anisotropy associated with $S = 1$ may trigger off the uniform spin rotation above y_{cr} .

Further investigation using neutron scattering techniques is now in progress to clarify this intriguing antiferromagnetic state.

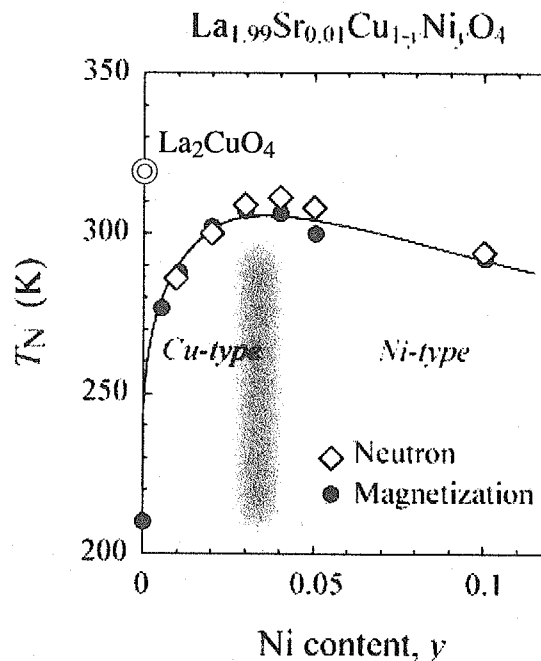


Figure 1: Magnetic phase diagram for Ni doped LSCO ($x = 0.01$). In the shadow region, a two phase mixture (Cu-type and Ni-type) or a uniform spin rotation ($0 < \phi < 90^\circ$) is expected.

References

- 1) M. Hückler, V. Kataev, J. Pommer, J. Harras, A. Hosni, C. Pflichtsch, R. Gross, and B. Büchner: Phys. Rev. B **59** (1999) R725.
- 2) T. Machi, I. Kato, R. Hareyama, N. Watanabe, Y. Itoh, N. Koshizuka, S. Arai, and M. Murakami: Physica C **388-389** (2003) 233.

2.3.5 Magnetic structure and low energy excitation in a non-centrosymmetric heavy fermion superconductor CePt₃Si

N. Metoki¹, K. Kaneko¹, T. D. Matsuda¹, A. Galatanu¹, T. Takeuchi², S. Hashimoto², T. Ueda², R. Settai², Y. Ōnuki^{1,2}, N. Bernhoeft³

¹ASRC-JAERI, Tokai, Naka, Ibaraki 319-1195

²Graduate School of Science, Osaka University, Toyonaka, Osaka 560-0043

³DRFMC, CEA/Grenoble, 38054 Grenoble Cedex 9, France

CePt₃Si is a heavy fermion superconductor with non-centrosymmetric structure (space group $P4mm$)¹⁾. This compound exhibits antiferromagnetic order at $T_N = 2.2$ K and enters into a heavy fermion superconducting state at $T_{SC} \approx 0.75$ K. We have carried out neutron scattering experiments in order to reveal the magnetic structure and the coexistence with superconductivity. We observed a low energy excitation which showed the heavy fermion quasi-elastic and inelastic nature based on the crystal field level splitting²⁾.

Neutron scattering experiments were carried out on thermal and cold triple-axis spectrometers TAS-1, TAS-2, and LTAS. Elastic scattering was measured with neutron beam at $E = 14.7$ meV monochromatized/analyzed with PG crystals, while inelastic scattering was measured with fixed final energy $E_f = 3.5, 14.7$ and 30.5 meV.

We observed clear antiferromagnetic peaks with the propagation vector $\mathbf{Q}_0 = (0 \ 0 \ 1/2)$

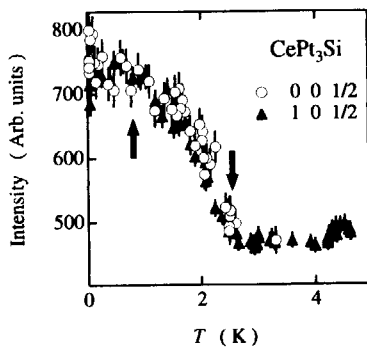


Figure 1: The intensity of (00 1/2) and (10 1/2) magnetic reflection as a function of temperature, shown by open circles and closed triangles, respectively.

below T_N with use of polycrystalline sample. The magnetic reflections were also clearly observed on a single crystalline sample. Figure 1 shows the temperature dependence of the (0 0 1/2) and (1 0 1/2) intensities with normalizing the signal intensity. It should be noted that the antiferromagnetic intensity remains almost constant below T_{SC} , indicating that the antiferromagnetic order coexists with the heavy fermion superconductivity. As shown in Fig. 2 the integrated intensity of the antiferromagnetic reflections can be explained with the model calculation based on the magnetic structure shown in the inset of Figure 2. The ferromagnetic sheets of Ce moments stacked antiferromagnetically along the c -axis. The obtained magnetic moment of

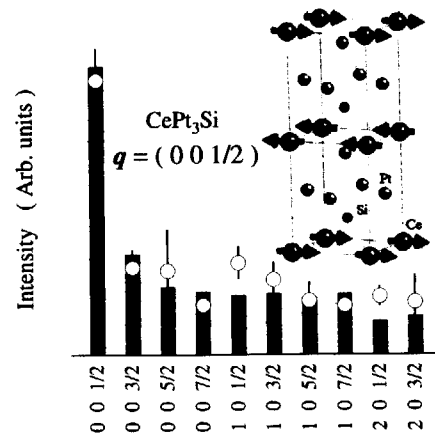


Figure 2: The integrated intensity of the antiferromagnetic reflections of CePt₃Si. The open circles are the experimental data, while bars are model calculation based on the magnetic structure shown in the inset. Note in-plane direction of the magnetic moment is unclear due to multi-domain structure.

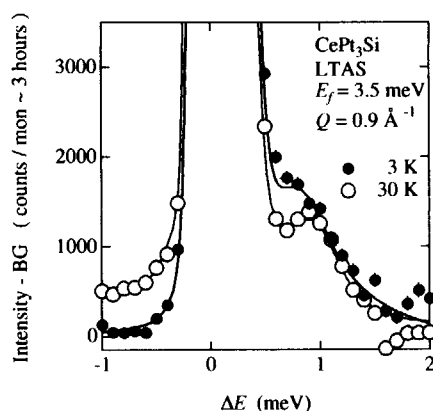


Figure 3: Low energy magnetic response of polycrystalline CePt_3Si . The solid and open circles represent data measured at 3 K and 30 K, respectively.

$0.16 \pm 0.01 \mu_B/\text{Ce}$ is strongly suppressed from the effective moment of Ce^{3+} ion $2.54 \mu_B/\text{Ce}$. This remarkable reduction is consistent with a presence of Kondo-like interaction¹⁾. The direction of the magnetic moment lying in the c -plane could not be determined because of the domain structure.

Inelastic scattering experiments have been carried out on a polycrystalline sample. The low energy excitation spectra at $Q = 0.9 \text{ \AA}^{-1}$ for $T = 3$ and 30 K with $E_f = 3.5 \text{ meV}$ are shown in Fig. 3. Note that the background has been subtracted. A clear inelastic peak at $\Delta E \approx 1 \text{ meV}$ at $T = 30 \text{ K}$ is found to co-exist with a quasi-elastic response, where the quasi-elastic response increases in intensity with decreasing temperature. The existence of the low-energy excitation $\approx 1 \text{ meV}$ is consistent with the broad specific heat anomaly around $T = 2 \text{ K}$ ¹⁾, which integrates to an entropy change of $R \ln 2$ at $\approx 25 \text{ K}$. The Schottky anomaly was observed in specific heat and thermal expansion on single crystal sample. Thus this low energy excitation can be concluded as the magnetic excitation based on low lying crystalline field level. We also observed a magnetic response at 24 meV in addition to some phonon scattering. This peak can be considered as the second crystal field level. The J multiplet of the Ce^{3+} ion splits into three doublets in a given point symmetry.

The excitation energies $\Delta E \approx 1 \text{ meV}$ and 24 meV are consistent with a step-like be-

havior observed in the electrical resistivity around 10 K and 100 K¹⁾. We found that the magnetic susceptibility is almost isotropic and well explained in terms of the mean field calculation based on the crystal field level scheme assuming $\Gamma_7(0 \text{ meV}) - \Gamma_6(1 \text{ meV}) - \Gamma_7(24 \text{ meV})$ ^{2,3)}. The almost isotropic magnetization curve and the metamagnetic behavior are also clearly reproduced by this level scheme³⁾.

The magnetic structure of the CePt_3Si may be relevant in connection with discussions of the pairing symmetry in this compound. The magnetic propagation vector $\mathbf{Q}_0 = (001/2)$ implies two interpenetrating, Néel magnetic sublattices which are ferromagnetic in the c -plane. Within a localized $4f$ model, on simultaneous space-time inversion a given magnetic sublattice is centrosymmetric and a pairing of spin-triplet character may be favorable. However, hybridization with Pt and Si breaks this degeneracy and a combination of these two competing effects may be relevant to the microscopic coexistence of the superconductivity and antiferromagnetic order.

Our low energy data showed the overlap of the quasi-elastic component with the width of $\approx 0.4 \text{ meV}$ and the first crystal field level at 1 meV , indicating that the kondo energy has the comparable energy scale to that of the first excited state with different orbital from the ground state. This is related to the strong reduction of the Ce magnetic moment. This result indicates that the magnetic as well as quadrupolar degree-of-freedom in the quasi-quartet ground state may play important role for the magnetism and the superconductivity. It is now highly interesting to establish the low lying modes relevant to the heavy quasiparticles and superconductivity as achieved in UPd_2Al_3 ⁴⁾.

References

- 1) E. Bauer *et al.*, Phys. Rev. Lett. 92 (2004) 027003.
- 2) N. Metoki *et al.*, J. Phys.: Condens. Matter 16 (2004) L207.
- 3) T. Takeuchi *et al.*, J. Phys.: Condens. Matter, 16 (2004) L333.
- 4) N. Metoki *et al.*, Phys. Rev. Lett. 80 (1998) 5417.

2.3.6 Magnetic structure of NpFeGa₅

E. Yamamoto¹, N. Metoki¹, K. Kaneko¹, D. Aoki², Y. Homma², Y. Shiokawa², Y. Ōnuki^{1,3}

¹ASRC-JAERI, Tokai, Naka, Ibaraki 319-1195

²IMR, Tohoku University, Oarai, Ibaraki 311-1313

³Graduate School of Science, Osaka University, Toyonaka, Osaka 560-0043

Actinide based '115' compounds have been attracted much attention, after the discovery of the high- T_C heavy fermion superconductivity in PuCoGa₅.¹⁾ So far no superconductivity has been reported in U- and Np-'115' compounds. Strong itinerant character of 5*f* bands in U-'115' would favor Pauli-paramagnetic or itinerant antiferromagnetic state, whereas the magnetism looks to be the most stable in Np system. The remarkable difference might be due to the character of 5*f* electrons. We have studied the magnetic structure of NpFeGa₅ on the thermal triple axis spectrometers TAS-1 and TAS-2.

The antiferromagnetic reflections were observed with the antiferromagnetic propagation vector $\mathbf{q}=(1/2\ 1/2\ 0)$ as shown in Fig. 1. The integrated intensities of the $(1/2\ 1/2\ l)$ peaks are plotted in Fig. 2. It is notable that the integrated intensity is strong for odd l and weak for even l . We found that this feature can be reproduced with assuming a ferrimagnetic structure due to Np and Fe magnetic sublattices as shown in the inset of Fig. 2. The in-plane moment direction cannot be determined because of the multi-domain structure. The magnetic moments were derived as $0.24\ \mu_B/\text{Fe}$ and $0.86\ \mu_B/\text{Np}$, respectively. The magnetic interactions of NpFeGa₅ are completely opposite to that of NpCoGa₅ with one more 3*d* electron. Furthermore Co has no magnetic moment, and the moment direction is also different.

The existence of Fe moment indicates that the 5*f*-3*d* hybridization is rather important in Np system. In U-'115' system, however, the U-5*f* and Ga-4*p* hybridization band plays dominant role for the transport and magnetic

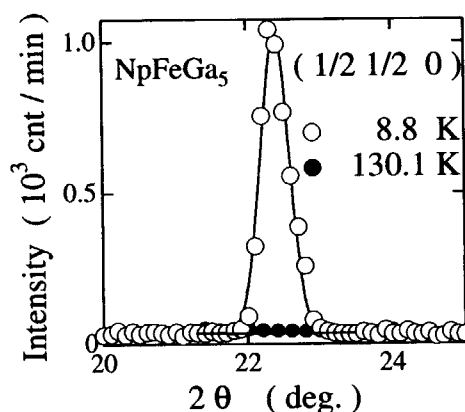


Figure 1: The radial scan at $(1/2\ 1/2\ 0)$ in NpFeGa₅.

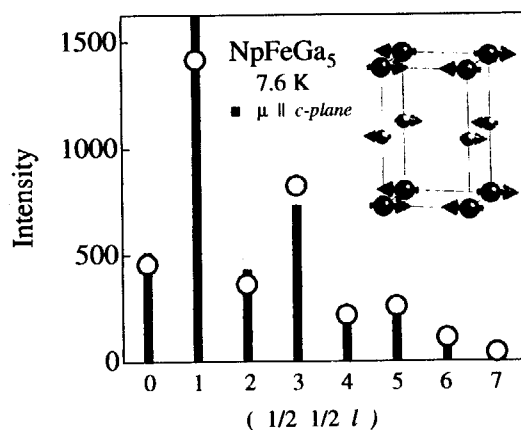


Figure 2: The Integrated intensity of AFM reflection of NpFeGa₅. Open circles denote the experimental data and the bars are the model calculation, assuming the magnetic structure shown in the inset.

properties. This difference is most likely due to the different 5*f* character in Np and U compounds.

References

- 1) J. L. Sarrao *et al.*, Nature **420**, 297 (2002).

2.3.7 Magnetic structure, phase diagram, and metamagnetic transition in NpCoGa_5

N. Metoki¹, K. Kaneko¹, E. Colineau², N. Bernhoeft³, D. Aoki⁴, Y. Homma⁴, Y. Shiokawa⁴,
E. Yamamoto¹, Y. Ōnuki^{1,5}

¹ASRC-JAERI, Tokai, Naka, Ibaraki 319-1195

²EC-JRC, Institute for Transuranium Elements, D-76125 Karlsruhe, Germany

³DRFMC, DEA/Grenoble, 38054 Grenoble Cedex 9, France

⁴IMR, Tohoku University, Oarai, Ibaraki 311-1313

⁵Graduate School of Science, Osaka University, Toyonaka, Osaka 560-0043

Actinide based '115' compounds have been attracted much attention, after the discovery of the heavy fermion superconductivity in PuCoGa_5 ¹⁾. The existence of the superconductivity in Ce and Pu compounds and the absence in U and Np ones are theoretically studied and discussed. Strong itinerant character of 5*f* bands in U-'115' would favor Pauli-paramagnetic or itinerant antiferromagnetic state, whereas the magnetism looks to be the most stable in Np system. We have studied the magnetic structure and the metamagnetic transition in NpCoGa_5 on the cold and thermal triple axis spectrometers LTAS and TAS-2.

We observed (110.5) antiferromagnetic reflection as shown in Figure 1(a), which disappears above T_N . The absence of the (000.5) antiferromagnetic reflection as shown in Fig. 1(b) indicates that magnetic moment of Np is parallel to the *c*-axis.

The deduced magnetic structure is shown in the inset of Fig. 2. The Np magnetic moment is directed along the tetragonal *c*-axis and exhibits ferromagnetic order in the basal plane. The ferromagnetic sheets are stacked antiferromagnetically along the *c*-axis. This magnetic structure is the same as the UPtGa_5 and UPdGa_5 ²⁻⁴⁾, which are iso-structural and iso-electronic compounds with the same number of valence electrons, assuming itinerant 5*f* electrons.

Figure 2 summarizes the integrated intensity of the antiferromagnetic reflections on the (*h h l*) scattering plane. The observed intensity can be well reproduced by the model cal-

culational, assuming magnetic form factor for Np^{3+} free ion. The magnetic moment of Np was estimated as $0.8(1)\mu_B$. It is in good agreement with a value obtained by a recent Mössbauer spectroscopy measurement⁵⁾.

High field neutron scattering experiments have been carried out in order to clarify the magnetic structure under magnetic field. We found that the (11-1.5) antiferromagnetic peak observed for $H=0$ T at $T=1.6$ K completely disappeared for $H=4.6$ T. It means that a simple ferromagnetic structure is stabilized in the high field phase.

Figure 3 indicates the field dependence of the (11-1.5) antiferromagnetic peak height.

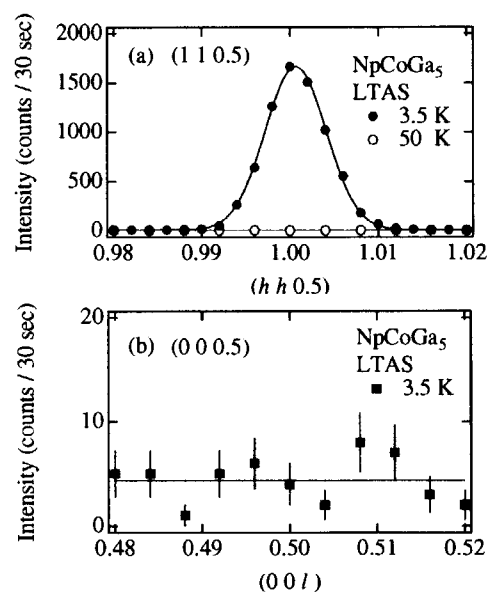


Figure 1: (a) The (110.5) antiferromagnetic peak of NpCoGa_5 . (b) The (00*l*) scattering profile at the (000.5) antiferromagnetic Bragg point.

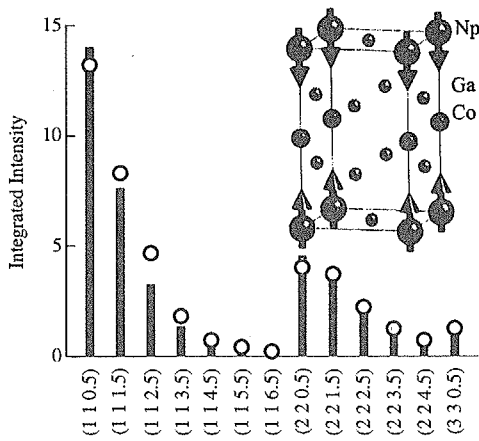


Figure 2: Integrated intensity of antiferromagnetic reflections of NpCoGa_5 . Open circles denote the experimental result and the bars are the model calculation for the magnetic structure shown in the inset.

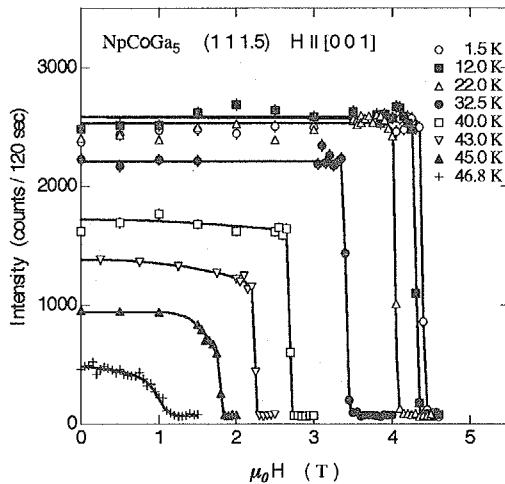


Figure 3: The field dependence of the (11-1.5) antiferromagnetic peak intensity of NpCoGa_5 . The field is applied parallel to the c -axis.

The antiferromagnetic Bragg intensity showed very little field dependence below $H_c(T)$ in the low temperature region for $T < 40$ K. The Bragg intensity dropped suddenly to the background level for $H > H_c(T)$, indicating a sharp transition from the antiferromagnetic to the ferromagnetic structure at $H_c(T)$.

When the temperature is close to the antiferromagnetic ordering temperature $T_N = 47$ K, the antiferromagnetic Bragg intensity decreases slightly with increasing $H < H_c(T)$. The jump remains sharp and the intensity is the same as the background level for $H > H_c(T)$. However for $T = 46.8$ K, just be-

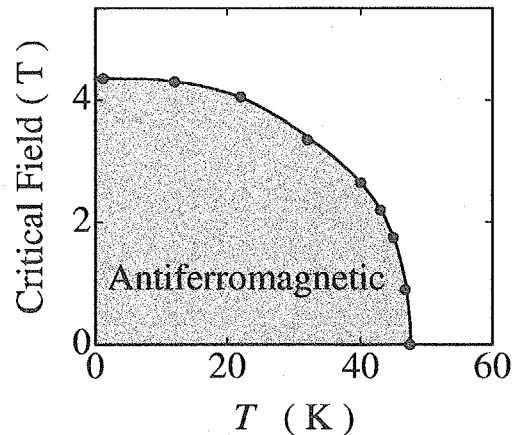


Figure 4: The H - T magnetic phase diagram of NpCoGa_5 . The hatched area indicates the antiferromagnetic phase. The paramagnetic phase with a field induced ferromagnetic component is realized in the other region.

low $T_N = 47$ K, the antiferromagnetic Bragg intensity exhibits a gradual field dependence around $H = 1$ T. The metamagnetic transition field was plotted as a function of temperature to reveal the magnetic phase diagram as shown in Fig. 4.

The metamagnetic transition of NpCoGa_5 is a spin flop of the Np magnetic moment. The weak spin flop field $H_c = 4.4$ T at 1.5 K in comparison with the magnetic ordering temperature $T_N = 47$ K can be understood in terms of the two dimensional magnetic interaction. We assume the strong in-plane ferromagnetic interaction between the nearest neighbor Np spin on the same plane, while the out-of-plane antiferromagnetic coupling is weak. The in-plane interaction plays dominant role for the magnetic ordering, where the ordered temperature has the energy scale of J . The ferromagnetic sheets can remain unchange, throughout the spin flop transition, that is why the spin flop field can be weak.

References

- 1) J. L. Sarrao *et al.*, Nature **420**, 297 (2002).
- 2) Y. Tokiwa *et al.*, J. Phys. Soc. Jpn **71** (2002) 725.
- 3) K. Kaneko *et al.*, Phys. Rev. B **68** (2004) 214419.
- 4) S. Ikeda, *et al.*, J. Phys. Soc. Jpn **72** (2003) 2622.
- 5) E. Colineau *et al.*, Phys. Rev. B **69** (2004) 184411.

2.3.8 Magnetic properties of 5f itinerant antiferromagnet UPdGa₅S. Ikeda^{1,2}, N. Metoki^{1,3}, Y. Haga², K. Kaneko², T. D. Matsuda² and Y. Ōnuki^{1,2}¹ Advanced Science Research Center, Japan Atomic Energy Research Institute, Tokai, Naka, Ibaraki 319-1195, Japan² Graduate School of Science, Osaka University, Toyonaka, Osaka 560-0043, Japan³ Department of Physics, Tohoku University, Sendai 980-8578, Japan

Actinide compounds incorporating 5f electrons have attracted much attention on account of their unusual magnetic and electronic properties such as heavy fermions and unconventional superconductivity. Especially, a recent discovery of high- T_c heavy fermion superconductors PuCoGa₅¹⁾ and PuRhGa₅²⁾ with the tetragonal HoCoGa₅-type crystal structure (space group $P4/mmm$) was a highly interesting topic in condensed matter physics. Prior to the Pu system, isostructural compounds UTGa₅ (T : transition metal) were studied from a viewpoint of electronic and magnetic properties. UTGa₅ with T =Fe, Ru, Os, Co, Rh and Ir shows Pauli-paramagnetic behavior, whereas T =Ni^{3,4)}, Pd^{5,6)} and Pt^{3,7,8)} exhibits itinerant antiferromagnetism below the Néel temperatures T_N =86 K, 31 K, and 26 K, respectively. In this paper we report the magnetic structure of UPdGa₅ studied by means of neutron scattering on a single-crystalline sample⁶⁾.

Figure 1 shows the temperature dependence of the magnetic susceptibility in UTGa₅ (T : Ni, Pd and Pt) for the field along the a - (the $[1,0,0]$ direction) and c - (the $[0,0,1]$ direction) axes, χ_a and χ_c , respectively. The magnetic susceptibility in UPdGa₅ is very small, less than 4×10^{-3} emu/mol. This susceptibility is much smaller than that of a U^{3+} free ion and/or a localized system UPd₃. Both χ_a and χ_c exhibit a weak temperature dependence, as shown in Fig. 1(b). The temperature dependence of the susceptibility above T_N can not be explained with the Curie-Weiss law. There exists a small magnetic anisotropy with $\chi_a > \chi_c$. We note that the small magnetic susceptibility with the weak temperature dependence would be understood based on an itinerant character of the 5f electrons. It should be also noted that the magnitude, temperature dependence, and anisotropy of the magnetic susceptibility in UPdGa₅ show intermediate behavior between UNiGa₅ and UPtGa₅. The susceptibility of UPdGa₅ exhibits a clear anomaly at the Néel temperature T_N =31 K. The susceptibility showed anisotropic behavior; χ_c decreases steeply below T_N while the decrease of χ_a is smaller than χ_c . Similar anisotropy in χ below T_N has been reported in UNiGa₅ and UPtGa₅, as shown in Fig. 1 (a) and (c), respectively. It indicates that the uranium moments orient parallel to the c -axis.

Figure 2 shows neutron diffraction profiles at

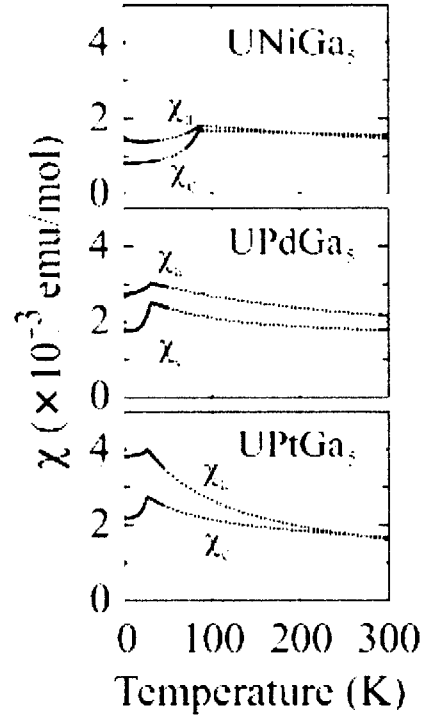


Figure 1: Temperature dependence of the magnetic susceptibility in (a) UNiGa₅, (b) UPdGa₅ and (c) UPtGa₅ for $H//[1,0,0]$ (a -axis) and $H//[0,0,1]$ (c -axis).

(1 1 0.5) and (0 0 1.5) measured below and above T_N . The antiferromagnetic reflections were observed at $(h\ 0\ l/2)$ and $(h\ h\ l/2)$ superlattice positions with integer h and l on the $(h\ 0\ l)$ and $(h\ h\ l)$ scattering planes. Therefore we conclude that the antiferromagnetic propagation vector is $q=(0\ 0\ 1/2)$; the magnetic moments couples ferromagnetically in the basal plane, and this ferromagnetic layer stacks antiferromagnetically along the c -axis. The absence of the magnetic peak at (0 0 1.5), as shown in Fig. 2(b), indicates that the direction of the magnetic moment is parallel to the c -axis. The integrated intensity of the antiferromagnetic peaks as denoted by open circles in Fig. 3 is well reproduced by the model calculation shown by bars, assuming this magnetic structure. The magnetic moment μ was determined to be $0.33\mu_B/U$ at 3.0 K. The magnetic structure in UPdGa₅ has been predicted by Kaneko *et al.* to be the same type as in UPtGa₅ from the temperature dependence of the

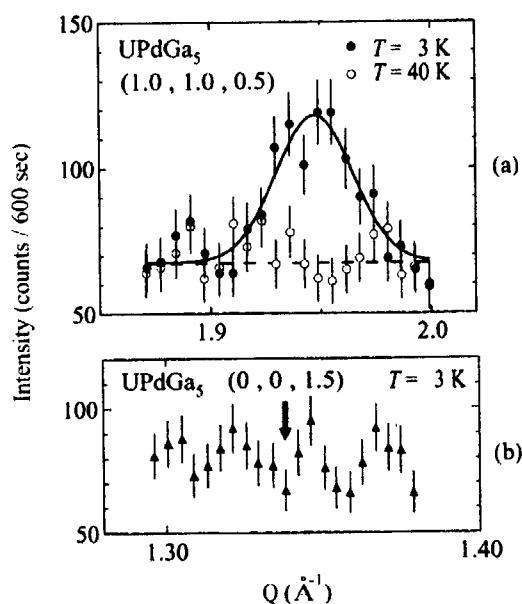


Figure 2: Neutron diffraction profiles at (a) (1 1 0.5) and (b) (0 0 1.5) in UPdGa₅ measured at 3.0 K ($< T_N$) and 40 K ($> T_N$) shown by open and closed circles, respectively.

lattice constant⁹). Their prediction of the magnetic structure for UPdGa₅ is consistent with the one determined from the present neutron diffraction experiment. The magnetic structure of UNiGa₅ and UPtGa₅ has been studied¹⁰. UNiGa₅ has a Néel-type ordering, namely, the adjacent uranium moments are aligned in opposite directions. On the other hand, the uranium moments in UPtGa₅ order ferromagnetically in the basal *c*-plane and couple antiferromagnetically along the *c*-axis. This difference implies a sign change of the nearest neighbor interaction. This is not understood from the results of band calculation, because these compounds have almost the same topology of the Fermi surface in the paramagnetic state^{11,12}. Tokiwa *et al.* discussed about it from a viewpoint that the orbital contribution of 5*f* electrons would be essential in the magnetic structure¹⁰. Kaneko *et al.* revealed that the local stress in the UGa₃ block in their crystal structure exhibits the systematic change, which would be related to the change of the magnetic structure⁹.

Recently Hotta reported theoretical calculation of the magnetic phase diagram based on *j-j* coupling scheme¹³. It is pointed out that the narrow region with the $q=(0\ 0\ 1/2)$ antiferromagnetic structure realized in UPdGa₅ and UPtGa₅ appears in the phase diagram with introducing a splitting of the Γ_8 level. This is consistent with a recovery of the magnetic anisotropy with increasing the uniaxial stress on UGa₃ layer observed in UPdGa₅ and UPtGa₅. In contrast, there is a wide stable region for the magnetic structure with $q=(1/2\ 1/2\ 1/2)$ realized in UNiGa₅. Further

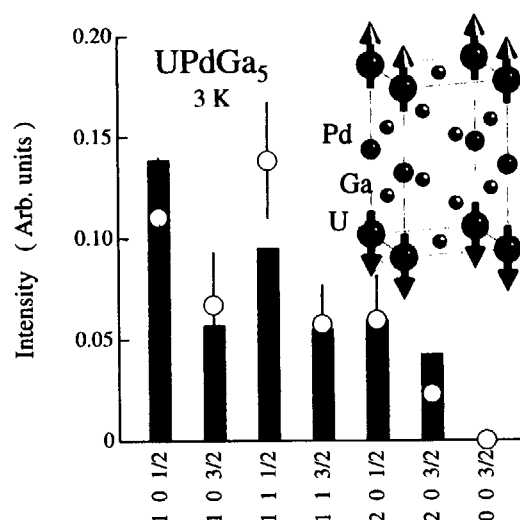


Figure 3: Integrated intensity of antiferromagnetic reflection of UPdGa₅. Open circles represent the experimental result and the bars denote the calculated one assuming the magnetic structure shown in the inset. The magnetic moment of uranium is deduced to be 0.33 μ_B .

studies should be expanded into Np or Pu compounds with multiple 5*f* electron systems.

References

- 1) J. L. Sarrao, L. A. Morales, J. D. Thompson, B. L. Scott, G. R. Stewart, F. Wastin, J. Rebizant, P. Boulet, E. Colineau and G. H. Lander, *Nature* **420** (2002) 297.
- 2) F. Wastin, P. Boulet, J. Rebizant, E. Colineau and G. H. Lander, *J. Phys. Condens. Matter* **15** (2003) S2279.
- 3) Yu. N. Grin, P. Rogl and K. Hiebl, *J. Less-Common Met.* **121** (1986) 497.
- 4) Y. Tokiwa, Y. Haga, E. Yamamoto, D. Aoki, N. Watanabe, R. Settai, T. Inoue, K. Kindo, H. Harima and Y. Ōnuki, *J. Phys. Soc. Jpn.* **70** (2001) 1744.
- 5) V. Sechovský, L. Havela, G. Schaudy, G. Hilsher, N. Pillmayr, P. Rogl and P. Fischer, *J. Mag. Mag. Mater.* **104-107** (1992) 11.
- 6) S. Ikeda, N. Metoki, Y. Haga, K. Kaneko, T. D. Matsuda, A. Galatanu and Y. Ōnuki, *J. Phys. Soc. Jpn.* **72** (2003) 2622.
- 7) Y. Tokiwa, S. Ikeda, Y. Haga, T. Ōkubo, T. Iizuka, K. Sugiyama, A. Nakamura and Y. Ōnuki, *J. Phys. Soc. Jpn.* **71** (2002) 845.
- 8) S. Ikeda, Y. Tokiwa, Y. Haga, E. Yamamoto, T. Ōkubo, M. Yamada, N. Nakamura, K. Sugiyama, K. Kindo, Y. Inada, H. Yamagami and Y. Ōnuki, *J. Phys. Soc. Jpn.* **72** (2003) 576.
- 9) K. Kaneko, N. Metoki, G. H. Lander, N. Bernhoeft, Y. Ishii, S. Ikeda, Y. Tokiwa, Y. Haga and Y. Ōnuki, *Phys. Rev. B* **68** (2003) 214419.
- 10) Y. Tokiwa, Y. Haga, N. Metoki, Y. Ishii and Y. Ōnuki, *J. Phys. Soc. Jpn.* **71** (2002) 725.
- 11) H. Yamagami, *Acta Phys. Pol. B* **34** (2003) 1201.
- 12) H. Yamagami, *Physica B* **312-313** (2002) 297.
- 13) T. Hotta, *Phys. Rev. B* **70** (2004) 054405.

2.3.9 Magnetic Excitations in Heavy-Fermion Superconductor $\text{PrOs}_4\text{Sb}_{12}$

K. Kuwahara, K. Iwasa*, M. Kohgi, K. Kaneko¹, S. Araki^{1,**}, N. Metoki^{1,2},
H. Sugawara***, Y. Aoki and H. Sato

Department of Physics, Tokyo Metropolitan University, Tokyo 192-0397

¹*Advanced Science Research Center, JAERI, Ibaraki 319-1195*

²*Department of Physics, Tohoku University, Sendai 980-8578*

The filled skutterudite compound $\text{PrOs}_4\text{Sb}_{12}$ is the first Pr-based heavy-fermion (HF) superconductor with the superconducting transition temperature $T_c = 1.85$ K.^{1,2)} The large specific heat jump $\Delta C/T_c \sim 500$ mJ/K²mol at T_c suggests that heavy quasiparticles are formed at low temperatures and participate in a superconducting transition. Considering the occurrence of the field-induced antiferro-quadrupolar (AFQ) ordering above ~ 5 T below ~ 1 K,^{3,4)} interestingly, the HF superconductivity of $\text{PrOs}_4\text{Sb}_{12}$ seems to be mediated by a nonmagnetic quadrupolar interaction.

We have studied magnetic excitations in a single crystal of this material by inelastic neutron scattering (INS) at low temperatures under high magnetic fields. The single crystal sample (about 4 g) used in the present experiment is the same as that used in a previous elastic neutron experiment.⁴⁾ The sample was mounted at the mixing chamber of a ^3He - ^4He dilution refrigerator with a superconducting magnet. INS experiments were performed on the cold neutron triple axis spectrometer LTAS at the JAERI.

Figure 1 shows the energy spectra of excitations with different Q vectors along $[1,0,0]$ and $[1,1,0]$ directions at the lowest temperature in a zero magnetic field. The well-defined crystal field (CF) excitations at 0.7 meV are observed at $(1.6,1.6,0)$, $(1.9,1.9,0)$ and $(2.1,0,0)$, as reported in the previous INS experiment of the polycrystal sample¹⁾. The widths of the INS peaks at $(1.6,1.6,0)$ and $(1.9,1.9,0)$ are about 0.3 meV (FWHM), slightly larger than the instrumental resolution. At $(2.8,0,0)$, on the other hand, the energy of the INS peak is about 0.5 meV and the peak becomes very broad and asymmetrical. These results show that the magnetic excitations at 0.7 meV soften at the zone boundary along the $[1,0,0]$ direction. The observed softening may originate from the intersite interaction between Pr ions. Taking into account the fact that $(1,0,0)$ is the modulation vector of the field-induced AFQ phase⁴⁾, the observed softening may be ascribed to quadrupolar instability with the same wave vector. Such dispersive modes are well known as magnetic excitons in singlet ground-state systems. The observed behavior might be due to the exciton caused by a nonmagnetic quadrupolar interaction.

Under magnetic fields, the observed field depen-

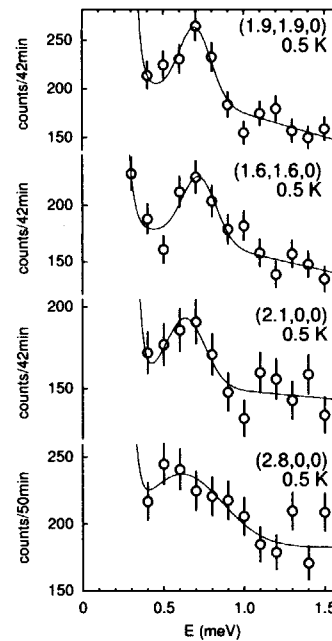


Figure 1: Energy spectra of excitations in $\text{PrOs}_4\text{Sb}_{12}$ with different Q vectors at the lowest temperature in a zero magnetic field. Lines are guides to the eyes.

dence of excitations is better reproduced by a CF level scheme with a singlet ground-state⁴⁾. In a high resolution experiment, furthermore, the change of the excitation spectra at $(1,0,0)$ was observed on passing through the superconducting transition temperature, suggesting some correlation between the magnetic response and the superconductivity.

References

- 1) M. B. Maple *et al.*: J. Phys. Soc. Jpn. **71** (2002) Suppl. 23.
- 2) E. D. Bauer *et al.*: Phys. Rev. B **65** (2002) 100506(R).
- 3) Y. Aoki *et al.*: J. Phys. Soc. Jpn. **71** (2002) 2098.
- 4) M. Kohgi *et al.*: J. Phys. Soc. Jpn. **72** (2003) 1002.

* Present address: Department of Physics, Tohoku University, Sendai 980-8578.

** Present address: Graduate School of Science, Osaka University, Osaka 560-0043.

*** Present address: Department of Mathematical and Natural Sciences, Faculty of Integrated Arts and Sciences, Tokushima University, Tokushima 770-8592.

2.3.10 Effect of magnetic field on static spin correlation in electron-doped system

M. Fujita, M. Matsuda¹, S. Katano¹ and K. Yamada

Institute for Materials Research, Tohoku University, Katahira, Sendai 980-8577

¹*Advanced Science Research Center, Japan Atomic Energy Research Institute, Tokai, Ibaraki 319-1195*

1 Introduction

Mechanism of high- T_c superconductivity mediated by spin fluctuations is one of the central topics in highly correlated electron systems. Studies of spin correlations in the hole-doped high- T_c cuprates such as $\text{La}_{2-x}\text{Sr}_x\text{CuO}_4$ (LSCO) have intensively been carried out by neutron scattering experiments, and show an intimate relation between spin correlations and superconductivity¹⁾. Recent neutron-scattering measurements on the LSCO with x around 1/8 revealed a large enhancement of the long-ranged incommensurate (IC) magnetic order under the field²⁾. Lake *et al.*, furthermore, found a tendency of the stabilization in the magnetic ordering in the vortex state of the optimally doped LSCO and discussed that the IC antiferromagnetic (AF) insulator is a possible ground state after suppressing the superconductivity by magnetic fields³⁾.

In order to test the universality of the field-effect on the spin correlations, that is, the relation between magnetism and superconductivity in the cuprates superconductors, comprehensive study on the electron-doped system is indispensable. Quite recently, Kang *et al.* performed neutron-scattering measurement on well-known electron-doped system of $\text{Nd}_{2-x}\text{Ce}_x\text{CuO}_4$ (NCCO) with $x=0.15$ ($T_c=25$ K) and reported a huge enhancement of magnetic order under the field⁴⁾. However, in that system, a field-effect on Nd^{2+} magnetic moment is expected to be predominant, and therefore, the results may conceal the inherent nature of Cu^{2+} spins that would play an important role for superconductivity. Thus, experiments using samples with negligible effects from large rare-earth magnetic moments are required. We hence performed neutron scattering measurements under the magnetic fields up to 9 T on a single crystal of superconducting $\text{Pr}_{0.89}\text{LaCe}_{0.11}\text{CuO}_4$, in which the effect of rare-earth moments is negligible compared with that in NCCO⁵⁾.

2 Results and Discussion

In this sample, a fairly small intensity from the magnetic order was observed in the zero-field at the tetragonal (0.5 1.5 0) reciprocal position, where corresponds to AF zone center in the as-grown non-superconducting samples⁶⁾. In Fig. 1, we show the temperature-dependence of the magnetic peak inten-

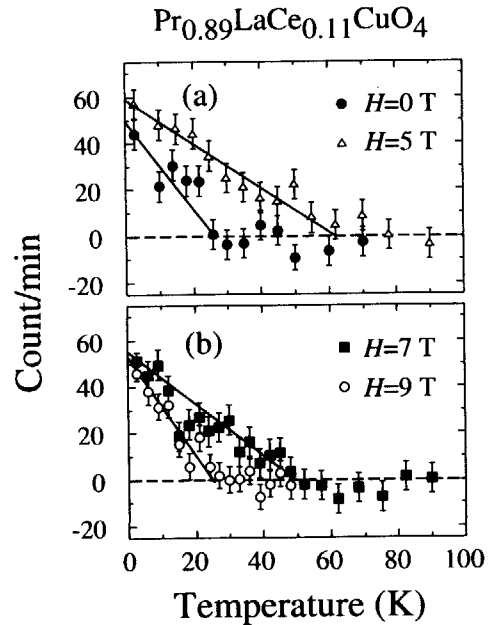


Figure 1: Temperature dependence of the peak-intensity measured under the magnetic field of (a) 0 and 5 T, and (b) 7 and 9 T at the tetragonal (0.5 1.5 0) position after subtracting the background at high temperature. Solid lines are guides to the eyes.

sity after subtracting background estimated at high temperatures. In zero-field, the intensity at 3 K normalized with the sample volume is $\sim 5\%$ of that in the as-grown sample, and T_N of 27 ± 4 K is much lower than that of 200 ± 5 K in the as-grown non-superconducting sample⁶⁾. (T_N is the onset temperature for the appearance of magnetic intensity upon cooling.) These results suggest that a competitive relation between the AF order, and superconductivity and show that the AF order is dramatically degraded in the present SC sample by the oxygen reduction.

Applying the field of 5 T, T_N increases up to ~ 60 K and the low-temperature peak-intensity at 5 T is also enhanced with the rate of $\sim 20\%$ of that at 0 T. In the hole-doped LSCO, on the other hand, T_N does not change even though the peak-intensity increases under the field with the factor of 2. The enhancement of T_N , therefore, indicates a different field-dependence of the enhanced antiferromagnetism between the electron- and hole-doped systems.

Further increasing the field, the peak-intensity at

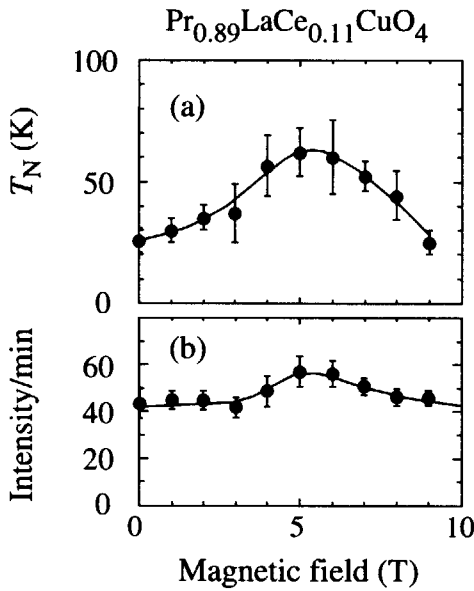


Figure 2: Field-dependence of (a) the onset temperature for the magnetic ordering temperature and (b) the peak-intensity at 3 K.

low temperature decreases possibly owing to a cant of spins from the CuO_2 planes. More importantly, T_N decreases in connection with the reduction of the peak-intensity, suggesting that the enhancement (the degradation) of the AF order in the electron-doped system is characterized by the simultaneous increase (decrease) in T_N and the intensity. In Fig. 2, we present the field-dependence of T_N and intensity measured at 3 K.

The field dependence of the intensity at $(0.5\ 0\ 0)/(1.5\ 0\ 0)$ shows no observable enhancement. At this reciprocal lattice point, however, Kang *et al.*, observed a huge increase in the intensity⁴). This discrepancy may be attributed to the difference of sample preparation, and the ordering of the magnetic moments on

the Nd atoms. We just note here that this point is not the AF zone center of the as-grown sample. Our results show that the enhancement of the AF ordering under magnetic field is a common feature of the cuprate high- T_c superconductors, and the ground state when the superconductivity is suppressed is the antiferromagnetic insulator.

Finally, we discuss the difference in the spin correlations in the electron- and hole-doped systems. At each field, temperature-dependence of the peak-intensity shows a linear change, which is typical for the defect-induced magnetism in correlated Fermi systems. Recent μSR results for the PLCCO system showing the reduction of both volume fraction of magnetically ordered region and staggered moment upon electron-doping near the AF and SC phase boundary. These results suggest the existence of antiferromagnetically ordered islands on the SC background in the present sample, and that the magnetic property in the AF island itself changes by electron-doping. On the other hand, in the LSCO system, evidence for the stripe formation of doped-hole was found. In this case, magnetic property in the AF region separated by charge-riever would persist upon hole-doping. Therefore, the character of doped antiferromagnetism between hole- and electron-doped systems associated with the charge distribution is somewhat different. This may be related with the different field-dependence of spin correlations in two systems. In order to clarify the common high- T_c mechanism, further study on magnetism is needed.

References

- 1) K. Yamada *et al.*: Phys. Rev. B. **57**, 6165 (1998).
- 2) S. Katano *et al.*: Phys. Rev. B. **62**, R14677 (2000), B. Lake *et al.*: Nature (London), **417**, 299 (2002).
- 3) B. Lake *et al.*: Science, **291**, 1759 (2001).
- 4) H.J. Kang *et al.*: Nature (London), **423**, 522 (2003).
- 5) M. Fujita *et al.*: Phys. Rev. B. **67**, 014514 (2003).
- 6) M. Fujita *et al.*: Physica C **392-396**, 130 (2003).

2.4 Magnetism and Low Temperature Physics

**- Low Dimension, Frustration, Magnetic Transitions and
Quantum Liquids -**

This is a blank page.

2.4.1 Phonon Measurements in the Spin Gap System TiCuCl_3

A. Oosawa, K. Kakurai and H. Tanaka¹

Advanced Science Research Center, JAERI, Tokai, Ibaraki 319-1195

¹ Res. Cent. for Low Temperature Physics, Tokyo Institute of Technology, Oh-okayama, Meguro-ku, Tokyo 152-8551

TiCuCl_3 is a spin gap system with the excitation gap $\Delta = 7.5$ K. This system shows the various quantum phase transitions, such as field-induced, impurity-induced and pressure-induced magnetic orderings, so that has been attracting considerable attentions both theoretically and experimentally. Besides, the importance of the spin-phonon coupling has been suggested from some experiments in this system recently. For instance, in the polarized neutron scattering study under the high-pressure, the pressure-induced successive magnetic phase transitions indicative of the reorientation of the ordered moments were observed and discussed in terms of the spin-phonon coupling¹⁾. From the NMR²⁾ and sound attenuation³⁾ studies in the field-induced magnetic ordering, the hysteresis behavior of the phase transition indicative of the weakly first order was observed. Also, the unusual temperature dependence of the broadened two-magnon continuum and Fano lines have been observed in the Raman scattering study⁴⁾. In order to investigate the lattice properties in this system, we carried out the phonon measurements in TiCuCl_3 by means of the neutron inelastic scattering experiments.

The preparation of the single crystal of TiCuCl_3 has been reported in ref. 5. Neutron inelastic scattering measurements were performed using the JAERI-TAS1. The constant- k_f mode was taken with a fixed final neutron energy E_f of 14.7 meV and collimations were set as open-80'-80'-80'. Sapphire and pyrolytic graphite filters were placed to suppress the background by high energy neutrons and higher order contaminations, respectively. We used a sample with a volume of approximately 2.5 cm³. The sample was mounted in the cryostat with its a^* - and c^* -axes in the scattering plane. The crystallographic parameters were determined as $a^* = 1.5885 \text{ \AA}^{-1}$, $c^* = 0.71195 \text{ \AA}^{-1}$ and $\cos \beta^* = 0.1106$ at room temperature.

First, we measured the constant- Q energy scan profile in TiCuCl_3 for $T = 297$ K and observed six phonon excitations up to $E = 20$ meV. From the dispersion relations of the six excitations, it was found that one of these excitations is the acoustic mode, while the other modes are the optic modes, in which the excitation energies of the five optic modes are 1.7, 4.3, 7.5, 11.1 and 15.0 meV at the zone center, respectively. The result, in which five optic modes exist, is consistent with that obtained from the Raman scattering experiments⁴⁾.

Figure 1 shows the temperature dependence of inte-

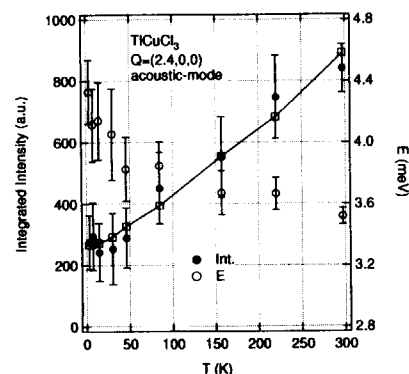


Figure 1: Temperature dependence of the integrated intensity I and the excitation energy E of the acoustic mode at $Q = (2.4, 0, 0)$ in TiCuCl_3 . The solid line with open squares denote the fitting result of temperature dependence of the integrated intensity by eq. (1).

grated intensity I and the excitation energy E of the acoustic mode at $Q = (2.4, 0, 0)$ in TiCuCl_3 . The temperature dependence of the integrated intensities can be well described by the phonon temperature factor,

$$I \propto \frac{1}{E} \times \left(\frac{1}{\exp\left(\frac{E}{k_B T}\right) - 1} + 1 \right) \quad (1)$$

as shown in the solid line with open squares of Fig. 1. As shown in Fig. 1, the temperature dependence of the excitation energy E looks unusual. Namely, with decreasing temperature from $T = 300$ K, the excitation energy E gradually increases, and then shows a rapid increase below $T = 50$ K. From the magnetic susceptibility measurements⁵⁾, it has been found that the magnetic susceptibility has a broad maximum at $T = 38$ K, and then decreases steeply toward zero with decreasing temperature to $T = 0$ K. This results obtained from the magnetic susceptibility measurements indicate that the antiferromagnetic short range correlations begin to develop below $T = 38$ K. Hence, we infer that the rapid phonon energy increase below $T = 50$ K obtained from the present measurements is related to the development of the antiferromagnetic short range correlations, namely the formation of the spin singlet.

References

- 1) A. Oosawa *et al.*: J. Phys. Soc. Jpn. **73** (2004) 1446.
- 2) O. Vyaselev *et al.*: Phys. Rev. Lett. **92** (2004) 207202.
- 3) E. Ya. Sherman *et al.*: Phys. Rev. Lett. **91** (2003) 057201.
- 4) K.-Y. Choi *et al.*: Phys. Rev. B **68** (2003) 174412.
- 5) A. Oosawa *et al.*: J. Phys.:Condens.Matter **11** (1999) 265.

2.4.2 Magnetic Excitations from the Linear Heisenberg Antiferromagnetic Spin Trimer System $A_3Cu_3(PO_4)_4$ with $A=Ca, Sr$, and Pb

M. Matsuda, K. Kakurai, A. A. Belik¹, M. Azuma¹, M. Takano¹, and M. Fujita²

Advanced Science Research Center, JAERI, Tokai, Ibaraki 319-1195

¹*Institute for Chemical Research, Kyoto University, Gokasho, Uji 610-0011*

²*Institute for Materials Research, Tohoku University, Katahira, Sendai 980-8577*

$A_3Cu_3(PO_4)_4$ ($A=Ca, Sr$, and Pb) is an candidate to study the spin trimer antiferromagnetism.¹⁻⁵⁾ A schematic view of the magnetic interactions in the copper chains is shown in Fig. 1. In the isolated Heisenberg antiferromagnetic $S = \frac{1}{2}$ trimer in a line the energy level scheme is described as follows. The ground state is a doublet with $E(0)=-J_1$ and $S_T = \frac{1}{2}$, where J_1 is the intra-trimer interaction and S_T is the total spins of a trimer. The first and second excited states are a doublet with $E(1)=0$ and $S_T = \frac{1}{2}$ and a quartet with $E(2)=\frac{1}{2}J_1$ and $S_T = \frac{3}{2}$, respectively. The neutron scattering technique is an ideal tool to directly investigate the energy level scheme of the spin trimer system as mentioned above. We have performed inelastic neutron scattering experiments on the polycrystalline samples of $A_3Cu_3(PO_4)_4$ ($A=Ca, Sr$, and Pb) on TAS2.

Temperature dependence of the inelastic neutron spectra in constant- Q scans in $Pb_3Cu_3(PO_4)_4$ is shown in Fig. 2(a). Figure 2(b) shows the Q -dependence of the peak intensities at 9 meV and 13.5 meV measured at 8 K. Since a cluster of the linear spin trimer is well isolated, almost dispersionless and sharp excitation peaks are observed even in the powder measurements. With increasing temperature intensities at 9.00 meV and 13.69 meV decrease, whereas a new excitation peak develops at 4.9 meV. The excitation energies of 4.9 meV, 9.00 meV, and 13.69 meV correspond to $E(2) - E(1)$, $E(1) - E(0)$, and $E(2) - E(0)$, respectively. Our analysis of the temperature and Q dependencies on the scattering intensities indicates that $Pb_3Cu_3(PO_4)_4$ is well described by the isolated Heisenberg antiferromagnetic spin trimer model without any adjustable parameters except the overall scale factor. This result indicates that the anisotropy in the exchange interaction is considered to be very small in this compound.

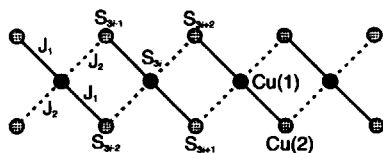


Figure 1: Schematic view of the major magnetic interactions J_1 and J_2 in the one-dimensional array of copper spin trimers.

We also performed inelastic neutron scattering experiments on the polycrystalline samples of $Sr_3Cu_3(PO_4)_4$ and $Ca_3Cu_3(PO_4)_4$ and obtained the results similar to those in $Pb_3Cu_3(PO_4)_4$. Only the exchange parameters are slightly changed. In this study the intra-trimer coupling constants are determined to be 9.45(3), 10.04(3), and 9.13(2) meV for $A_3Cu_3(PO_4)_4$ with $A=Ca, Sr$, and Pb , respectively.

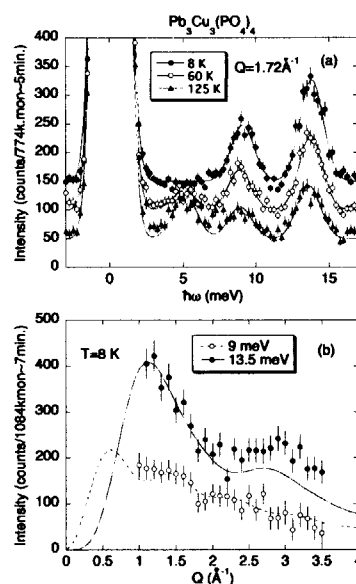


Figure 2: (a) Constant- Q scans at various temperatures in $Pb_3Cu_3(PO_4)_4$. 50 counts are added at each successive temperature so that the scans are compared on one graph. (b) Q dependence of neutron scattering intensity at 9 meV and 13.5 meV. Background intensity measured at a different energy is subtracted from the raw data.

References

- 1) J. B. Anderson, E. Kostiner and F. A. Ruszala: *J. Solid State Chem.* **39** (1981) 29.
- 2) M. Drillon, E. Coronado, M. Belaiche and R. L. Carlin: *J. Appl. Phys.* **63** (1988) 3551.
- 3) H. Effenberger: *J. Solid State Chem.* **142** (1999) 6.
- 4) A. A. Belik, A. P. Malakho, B. I. Lazoryak and S. S. Khasanov: *J. Solid State Chem.* **163** (2002) 121.
- 5) Y. Ajiro, T. Asano, K. Nakaya, M. Mekata, K. Ohya, Y. Yamaguchi, Y. Koike, Y. Morii, K. Kamishima, H. Aruga-Katori and T. Goto: *J. Phys. Soc. Jpn.* **70** Suppl. A (2001) 186.

2.4.3 Crystal and Magnetic Structures of Triple Perovskite $\text{Ba}_3\text{Fe}_2\text{ReO}_9$

M. Wakeshima, K. Yamamura, Y. Hinatsu, N. Igawa¹, and Y. Ishii¹

Division of Chemistry, Graduate School of Science, Hokkaido University, Sapporo 060-0810

¹NSRC, JAERI, Tokai, Ibaraki 319-1195

The crystal structure and magnetic properties of the triple-perovskite type compound $\text{Ba}_3\text{Fe}_2\text{ReO}_9$ were investigated. Through magnetic susceptibility measurements, this compound showed complicated magnetic behavior below 450 K. The Mössbauer spectrum measurements indicated that a half of the Fe ions showed the magnetic ordering below 450 K and the other half of Fe ions did below 320 K. In order to elucidate these behaviors, powder neutron measurements were performed at 10 K and 300 K with a High Resolution Powder Diffractometer (HRPD) in the JRR-3M reactor with a neutron incident wave length ($\lambda = 1.82268 \text{ \AA}$).

Neutron diffraction profile measured at 300 K shows that $\text{Ba}_3\text{Fe}_2\text{ReO}_9$ crystalizes in the 6H-perovskite type structure (stacking sequence hcchcc) with space group $P6_3/mmc$. Figure 1(a) is illustrated the crystal structure of $\text{Ba}_3\text{Fe}_2\text{ReO}_9$. The structure consists of dimers of face-sharing octahedra separated by single corner sharing octahedra. By the Rietveld analysis, it was revealed that the Fe ions occupy the single corner site, and that the Re and Fe ions occupy the dimer sites randomly in the ratio of 1:1.

In the data collected at 10 K (Fig. 2), no additional peaks are observed and the clear enhancement of peak intensities is recognized. This result means that the magnetic unit cell is equal to the nuclear unit cell. The magnetic structure of $\text{Ba}_3\text{Fe}_2\text{ReO}_9$ was determined by the Rietveld analysis. The two octahedral transition metal sites (single corner and dimer sites) were allowed to have different magnetic moments.

The magnetic structure at 10 K is illustrated in Fig. 1(b). In this figure, only the magnetic moment of the Fe^{3+} ion is extracted. In the dimer sites, the magnetic moments of Fe^{3+} are coupled antiferromagnetically. The magnetic coupling between the single corner and dimer sites is also antiferromagnetic. The direction of the magnetic moments is along the c axis. The ordered magnetic moments are listed in Table 1. These magnetic ordered moments are considerably smaller than theoretical one ($gS = 5\mu_B$) of the Fe^{3+} ions. From this result, it is suggested that the randomness of the Fe and Re ions in the dimer sites leads to the frustrations between the magnetic couplings such as a spin-glass.

Table 1: Ordered magnetic moments (μ_B) of $\text{Ba}_3\text{Fe}_2\text{ReO}_9$.

	dimer	corner
10 K	2.88(4)	2.67(7)
300 K	2.82(5)	2.53(8)

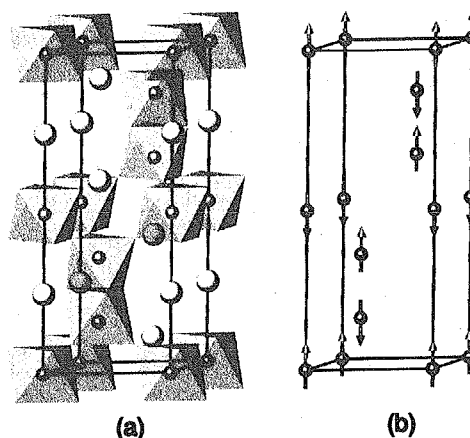


Figure 1: (a) Crystal structure of $\text{Ba}_3\text{Fe}_2\text{ReO}_9$; (b) Magnetic structure of $\text{Ba}_3\text{Fe}_2\text{ReO}_9$ at 10 K.

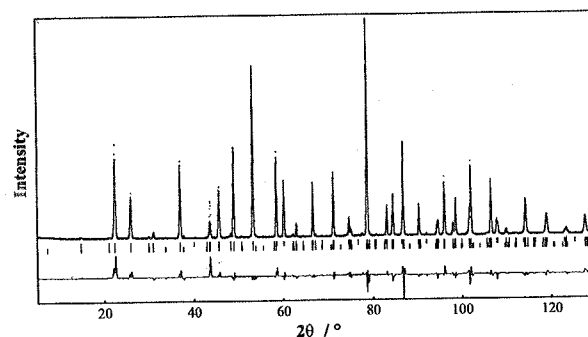


Figure 2: Neutron diffraction profile at 10 K of $\text{Ba}_3\text{Fe}_2\text{ReO}_9$.

2.4.4 Neutron Powder Diffraction Study for $S = 1/2$ Quantum Antiferromagnet NH_4CuCl_3 M. Fujisawa, A. Oosawa¹, Y. Ishii¹, H. Tanaka² and K. Kakurai¹*Department of Physics, Tokyo Institute of Technology, Meguro, Tokyo 152-8551*¹*Advanced Science Research Center, JAERI, Tokai, Ibaraki 319-1195*²*Low Temperature Center, Tokyo Institute of Technology, Tokyo 152-8551*

The space group of NH_4CuCl_3 has been reported to be $P2_1/c$ at room temperature¹⁾, which is isomorphous to the related antiferromagnetic dimer systems TiCuCl_3 and KCuCl_3 which have a gapped singlet ground state. NH_4CuCl_3 has a magnetic ground state with no gap and shows magnetization plateaus at 1/4 and 3/4 of the saturation magnetization²⁾. The origin of the 1/4 and 3/4 plateaus is still unclear. In order to understand the unusual magnetic properties in NH_4CuCl_3 , it may be important to consider the freezing process of the reorientational dynamics of the NH_4^+ ions at low temperature. For instance, Matsumoto recently suggested that the inequivalent dimer model, in which the ground state consists of the inequivalent three Cu^{2+} dimers, can explain the 1/4 and 3/4 plateaus³⁾. The inequivalent dimer sites may be induced by the freezing of the dynamics of the NH_4^+ ions, of course, by the structural phase transition to lower symmetries at low temperature. In order to investigate the freezing process of NH_4^+ ions or the existence of the structural phase transition at low temperature, it is important to determine precise crystal structures, so that we performed a neutron diffraction investigation in fully deuterated ND_4CuCl_3 at low temperature.

Powder neutron diffraction measurements were carried out using a high resolution powder diffractometer (HRPD) at $T = 296$ K, 48 K and 2.8 K in JAERI, Tokai, Japan. The wavelength of neutrons is 1.823 Å. Rietveld refinements of the neutron diffraction data were carried out by using the RIETAN-2000 program⁴⁾. It is noted that we have already confirmed that ND_4CuCl_3 has the same magnetic properties as NH_4CuCl_3 .

The experimental results are shown in Fig.1. No remarkable changes of the diffraction pattern between 296 K, and low temperatures 48 K and 2.8 K can be seen. Namely, no super lattice reflections appear and only the peak position of the reflections, as denoted by the arrows in Fig.1 (b), has a slight shift for 48 K and 2.8 K. This means that we could observe no structural phase transitions and only the changes of the lattice parameters to lower temperature in the present measurements. We also analyzed this diffraction pattern in the viewpoints of the freezing of the reorientation of NH_4^+ ions, however we could not obtain the good fitting results.

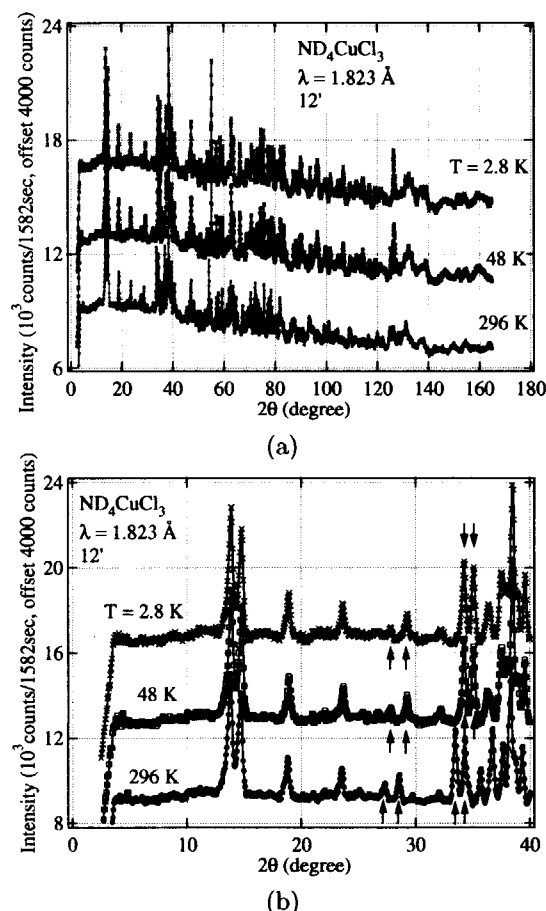


Figure 1: Neutron powder diffraction patterns of ND_4CuCl_3 at $T = 296$ K, 48 K and 2.8 K obtained on HRPD ((a) for all 2θ and (b) for low 2θ).

In the present analysis, we assumed that no ND_4^+ tetrahedrons are distorted. We will try to reanalyze the diffraction data in consideration of the distorted those for the future.

References

- 1) R. D. Willett *et al.*: J. Chem. Phys. **38** (1963) 2429.
- 2) W. Shiramura *et al.*: J. Phys. Soc. Jpn. **67** (1998) 1548.
- 3) M. Matsumoto: Phys. Rev. B **68** (2003) 180403.
- 4) F. Izumi and T. Ikeda: Mater. Sci. Forum **321-324** (2000) 198.

2.4.5 Estimation of temperature dependence of magnetic structure of Z-type barium ferrite $\text{Ba}_3\text{Co}_{1.8}\text{Fe}_{24.2}\text{O}_{41}$ by powder neutron diffraction

Y. Takada, T. Nakagawa, Y. Fukuta, T. A. Yamamoto, T. Tachibana¹, T. Shimada¹, Y. Ishii², N. Igawa²

Graduate School of Engineering, Osaka University, 2-1 Yamadaoka, Suita, Osaka 565-0871

¹NEOMAX Co. Ltd., 2-15-17 Egawa, Shimamoto-cho, Mishima-gun, Osaka 618-0003

²Neutron Scattering Research Group, JAERI, 2-4 Shirane, Tokai-mura, Naka-gun, Ibaraki-ken 319-1195

1 Introduction

Co_2Z -type hexaferrite $\text{Ba}_3\text{Co}_2\text{Fe}_{24}\text{O}_{41}$ keeps high permeability even in UHF region (300 MHz - 3 GHz), because it has the easy-magnetization direction parallel to its basal plane (*ferroxplana*) and larger magnetic anisotropy. Thus, it is expected as one of promising candidate materials for commercial use in GHz components such as mobile phone, wireless LAN, inductor cores and electromagnetic absorbent materials¹⁻³⁾.

In our previous works, we found that substitution of cobalt for iron improved permeability of the Z-type ferrites. The magnetization curve of $\text{Ba}_3\text{Co}_{1.8}\text{Fe}_{24.2}\text{O}_{41}$ measured by VSM indicated there are two transformation points at 540 and 680 K¹⁾. However, no crystal structure changes were observed in high-temperature XRD profiles. These facts mean that two magnetic changes occur in this temperature range.

The aim of this study is investigation of the temperature dependence of magnetic structure of $\text{Ba}_3\text{Co}_{1.8}\text{Fe}_{24.2}\text{O}_{41}$ with neutron diffraction.

2 Experimental

Powder sample of $\text{Ba}_3\text{Co}_{1.8}\text{Fe}_{24.2}\text{O}_{41}$ was prepared at 1573 K in oxygen atmosphere by the ceramic method.

High-temperature neutron diffraction patterns of the samples were obtained using HRPD installed at JRR-3 in JAERI. Neutron wavelength was 1.823 Å, monochromized by the Ge(331) reflection. The powder sample was cast in a vanadium folder with 15 mm in diameter. Diffraction patterns in the range of 2θ

= 2.5 - 162.5° were measured at various temperatures lower than 773 K in vacuum. Angle step was 0.05° and duration time at each step was 500 sec.

3 Results and discussion

Figure 1 is the closeup of neutron diffraction peaks of $2\theta = 19 - 26^\circ$ at 294 K, 523 K, 573 K and 773 K. These diffraction peaks are mainly attributed to magnetic scattering. The diffraction pattern at 773 K is completely due to nuclear scattering because measurement temperature is higher than its Curie temperature (about 683 K) and magnetic order completely disappears. Comparing peak intensities at 523 K with those at 573 K, peaks due to the reflections from (0010) and (0012) planes rapidly vanish. On the other hand, the peak due to (100) increases. This means that magnetic structure changes in this temperature region. Figure 2 shows the temperature dependence of angles of magnetic moments against c-axis determined from the Rietveld analyses for the neutron diffraction patterns. The angle of magnetic moments turns rapidly from the direction parallel to c-plane to c-axis in the temperature region from 523 K to 573 K. The property of $\text{Ba}_3\text{Co}_{1.8}\text{Fe}_{24.2}\text{O}_{41}$ as *ferroxplana* loses above 523 K.

References

- 1) T. Tachibana et al., Proceedings of ICF-8, Kyoto and Tokyo, Japan; JSPPM (2000) 888-890.
- 2) T. Tachibana et al., J. Magn. Mater. 262 (2003) 248-257.
- 3) T. Nakagawa et al., J. Am. Ceram. Soc. Jpn. (Submitted).

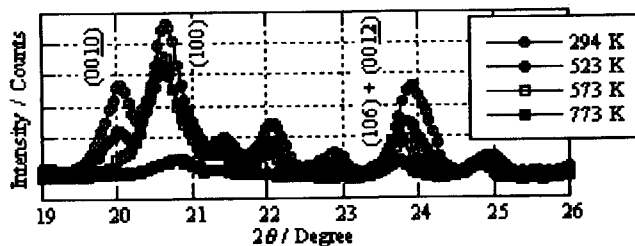


Figure 1: Neutron diffraction patterns of $\text{Ba}_3\text{Co}_{1.8}\text{Fe}_{24.2}\text{O}_{41}$ at $2\theta = 19 - 26^\circ$ at 294 K, 523 K, 573 K and 773 K.

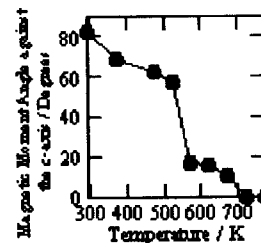


Figure 2: Temperature dependence of angles of magnetic moments against c-axis.

2.4.6 Crystal Structure of the Spin Gap System TiCuCl_3 A. Oosawa, Y. Ishii, K. Kakurai and H. Tanaka¹

Advanced Science Research Center, JAERI, Tokai, Ibaraki 319-1195

¹Res. Cent. for Low Temperature Physics, Tokyo Institute of Technology, Oh-okayama, Meguro-ku, Tokyo 152-8551

Spin gap system TiCuCl_3 has been attracting much interest because this system shows the various quantum phase transitions. It has been reported that this system crystallizes in a monoclinic structure which belongs to the space group $P2_1/c$ ¹⁾. However, in the recent neutron diffraction experiments for single crystal TiCuCl_3 , the very weak nuclear reflections were observed for $Q = (h, 0, l)$ with odd l at low temperature, which should be forbidden in the space group $P2_1/c$ ²⁾. This means that this system may undergo a structural phase transition to lower symmetry at low temperature. In order to investigate the crystal structures at low temperature, we carried out the neutron powder diffraction experiments.

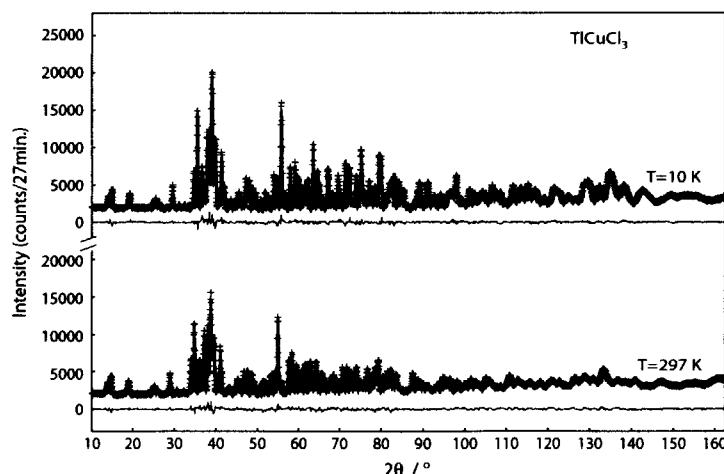
The preparation of single crystals of TiCuCl_3 has been reported in ref. 3. TiCuCl_3 powder was obtained by grinding up the single crystals using the agate mortar with pestle in atmosphere for approximately ten minutes. The neutron powder diffraction patterns were measured on HRPD installed at JRR-3 in JAERI. The obtained diffraction patterns were analyzed by Rietveld method using RIETAN-2000⁴⁾.

The obtained neutron powder diffraction patterns of TiCuCl_3 for $T = 10$ and 297 K are shown in the figure. From the Rietveld refinements, it was found that the obtained patterns for $T = 10$ and 297 K can be reproduced by the crystallographic parameters, as

shown in the table, with the space group $P2_1/c$, as denoted by the thick lines in the figure. This means that TiCuCl_3 has no structural phase transition, thus we infer that the observed nuclear peaks for odd l in the single crystal neutron diffraction experiments was not due to the intrinsic structural phase transitions to lower symmetries, but due to the extrinsic effects, such as impurities and lattice defects. It was also found that the obtained patterns include the lines of a little amount of $\text{CuCl}_2 \cdot 2\text{H}_2\text{O}$ and CuCl_2 , which may be due to the deliquescence by the grinding in atmosphere. It is noted that the isotropic displacement parameters B have large values for $T = 297$ K, which is consistent with the X-ray powder diffraction experiments in related system KCuCl_3 ⁵⁾. It is unusual and may be related to the anomalous spin-lattice correlations in this system⁶⁾.

References

- 1) K. Takatsu, W. Shiramura and H. Tanaka: J. Phys. Soc. Jpn. **66** (1997) 1611.
- 2) H. Tanaka, A. Oosawa, T. Kato, H. Uekusa, Y. Ohashi, K. Kakurai and A. Hoser: J. Phys. Soc. Jpn. **70** (2001) 939.
- 3) A. Oosawa, M. Ishii and H. Tanaka: J. Phys.: Condens. Matter **11** (1999) 265.
- 4) F. Izumi and T. Ikeda: Mater. Sci. Forum **321-324** (2001) 538.
- 5) M. Hanawa, Y. Ohishi and Y. Moritomo: private communications.
- 6) A. Oosawa, K. Kakurai and H. Tanaka: see in this JAERI-Review.



Upper figure: Neutron powder diffraction patterns of TiCuCl_3 for $T = 10$ K and 297 K. The thick and thin lines denote the calculated pattern and the difference between the observed pattern and the calculated that, respectively. Right table: Crystallographic parameters of TiCuCl_3 obtained by Rietveld refinements.

• $T = 10$ K

$$\begin{cases} a = 3.9207\text{\AA}, b = 14.050\text{\AA}, c = 8.7907\text{\AA} \\ \alpha = 90^\circ, \beta = 95.608^\circ, \gamma = 90^\circ \end{cases}$$

	x	y	z	$B(\text{\AA}^2)$
Ti	0.779	0.170	0.554	0.308
Cu	0.236	0.050	0.158	0.359
Cl(1)	0.272	0.195	0.262	0.389
Cl(2)	0.679	-0.006	0.319	0.458
Cl(3)	-0.181	0.097	-0.036	0.334

• $T = 297$ K

$$\begin{cases} a = 3.9755\text{\AA}, b = 14.137\text{\AA}, c = 8.8656\text{\AA} \\ \alpha = 90^\circ, \beta = 96.399^\circ, \gamma = 90^\circ \end{cases}$$

	x	y	z	$B(\text{\AA}^2)$
Ti	0.776	0.170	0.553	2.194
Cu	0.241	0.051	0.150	1.254
Cl(1)	0.265	0.194	0.263	1.561
Cl(2)	0.678	-0.007	0.318	1.253
Cl(3)	-0.179	0.097	-0.035	1.350

2.4.7 Study of Ferromagnetism of CeP under High Pressure

D. Kawana, T. Osakabe¹, A. Hannan, M. Kohgi

Department of Physics, Tokyo Metropolitan University, Hachioji, Tokyo 192-0397

¹Advanced Science Research Center, JAERI, Tokai, Ibaraki 319-1195

CeP shows unusual properties due to its very low carrier density ($0.01/\text{f.u.}$)¹⁾. Its magnetic properties under high pressures are especially interesting. Above about 0.5 GPa it shows complex magnetic structures composed of double layers of ferromagnetic Ce(001)-plane with a large moment value of about $2 \mu_B$ sandwiching the type-I antiferromagnetic structure of Γ_7 Ce ions at low temperatures²⁾. Above about 10 K (T_{C1}) the Γ_7 Ce layers become paramagnetic, while the ferromagnetic double layers keep ordering up to the upper critical temperature T_{C2} . The period of the structure decreases from 9 to 4 Ce-layers with increasing pressure up to about 1.7 GPa. The magnetic structures around 2 GPa are similar to those of CeSb and CeBi at ambient pressure. The resistivity measurement³⁾ indicates that T_{C2} becomes maximum (~ 50 K) at about 3 GPa. Above the pressure, T_{C2} decrease with increasing pressure and disappears at about 6 GPa. The above facts indicate that the 4f electron state of CeP shows a drastic change from a localized state to a non-magnetic itinerant one in the pressure range 0 - 6 GPa. In order to investigate this process from the microscopic point of view, we study the compound by means of neutron diffraction technique under high pressures. From the previous experimental results, it was revealed that, in the pressure range between 2.5 and 2.8 GPa, a ferromagnetic phase appears at low temperatures below around 30 K, while another phase, 3^* ($\uparrow\uparrow \circ \downarrow\downarrow \circ$), appears above this temperature⁴⁾. It was also revealed that only a ferromagnetic phase exists at low temperatures under a pressure above about 3.2 GPa.⁵⁾ In order to extend the study of the pressure dependence of the ferromagnetic state of CeP at higher pressures, we performed an experiment at the triple-axis-spectrometer TAS-1(2G) installed at JRR-3 reactor, JAERI. To apply a pressure on the sample, we used a sapphire anvil cell. The sample of $0.3 \times 0.2 \times 0.08 \text{ mm}^3$ was set in a hole of phosphorous bronze gasket, with a little amount of ruby powder for pressure calibration and Daphne7373 as pressure transmitting medium. We observed a temperature dependence of the peak intensity of 200 Bragg peak, where a ferromagnetic component is superimposed on the nuclear Bragg scattering, at 3.9 GPa. With decreasing temperature, the peak intensity increases at about 40 K. However, due to low counting statistics, an accurate determination of the transition temperature is difficult as shown in Fig.

1. However, the saturation moment of the ferromagnetic state at the lowest temperature is estimated to be $1.3 \pm 0.3 \mu_B$ by comparing the integrated intensity of the peak at 1.5 K with that at 55 K. This value is rather small compared to the magnetic moment of a fully polarized Ce^{3+} ion ($2.14 \mu_B$). The present results is consistent with the view point that the the 4f electron state of CeP approaches to a delocalized state at pressures above 3 GPa. However, more accurate estimation of T_{C2} and saturation moment is required for the detailed discussion of the interesting phenomena of CeP though the experimental limitation is quite severe for a neutron diffraction experiment in such a high pressure region.

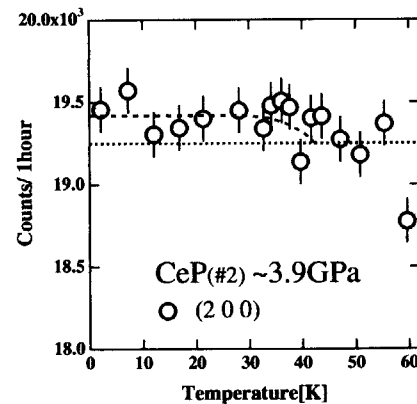


Figure 1: Temperature dependence of peak intensity of 200 peak of CeP at 3.9 GPa.

References

- 1) T. Suzuki *et al.*: Physica B, **186-188** (1993) 347.
- 2) M. Kohgi *et al.*: Physica B, **281-282** (2000) 417.
- 3) N. Mōri *et al.*: Physical Properties of Actinide and Rare Earth Compounds JJAP Series **8** (1993) 182.
- 4) A. Hannan *et al.*: Applied Phys A, **74** (2002) S565.
- 5) D. Kawana, Master Thesis (2004, Tokyo Metropolitan University)

2.4.8 Neutron powder diffraction study of RB_{12} T. Osakabe, F. Iga¹

Advanced Science Research Center, JAERI, Tokai, Ibaraki 319-1195

¹ Graduate School of Advanced Sciences of Matter, Hiroshima Univ., Higashi-Hiroshima, Hiroshima 739-8530

Rare-earth dodecaborides RB_{12} ($\text{R}=\text{Tb}, \text{Dy}, \text{Ho}, \text{Er}, \text{Tm}, \text{Yb}, \text{Lu}$) series has NaCl-type crystal structures consisting of R and B_{12} cubooctahedrons. It has shown clearly from the recent single-crystal neutron diffraction experiments on $\text{R} = \text{Ho}, \text{Er}$, and Tm that these compounds show the same antipahse domain type antiferromagnetic structures with the propagation vector $\mathbf{Q} = (1/2 - \delta, 1/2 - \delta, 1/2 - \delta)$, $\delta \approx 1/26$ ¹⁾. On the other hand, $\text{R}=\text{Yb}$ is well known as a mixed-valence compound and a Kondo-semiconductor with the gap of about 200 K at Fermi level. The gap develops below about 100 K. A lot of studies on this compound has been done in order to solve the mechanism of the gap formation. Recently, Iga *et al.* carried out neutron inelastic scattering experiments on this compound using the single crystal sample²⁾. They found that, although the compound did not undergo the long-range magnetic order, the compound showed the $(1/2, 1/2, 1/2)$ antiferromagnetic correlation in the excitation energy of about 160 K at low temperature. They claimed the correspondence between the magnetic behavior of YbB_{12} and that of the other compounds which show the long-range magnetic order. In this report, we show a part of the result of the neutron powder diffraction study on $\text{R}^{11}\text{B}_{12}$ series. The purpose of the study is investigating the relation between the magnetic behavior and the crystal parameter of these compounds.

The crystal lattices of these compounds are very hard, because the lattice constant changes only 0.1 % or less by changing the temperature from 300 K to 4 K. Fortunately, neutrons are not absorbed so strongly by ^{11}B atoms and have almost same sensitivity to ^{11}B atoms as those of other elements. Thus, we could detect the temperature dependence of the atomic positions of ^{11}B atoms of these compounds, although the errors were large. Figure 1(a) and (b) show the temperature dependence of the lattice constant and interatomic distance of YbB_{12} obtained by the Rietveld analysis (RIETAN-2000). With decreasing temperature, the lattice constant stops decreasing at about 100 K, at which the gap starts to develop. Furthermore, as clearly shown in Fig. 1(b), the size of the B_{12} cluster enlarges and consequently interatomic distance between Yb atom and B atom rapidly decreases. On the other hand, in HoB_{12} which shows the long-range antiferromagnetic order, B_{12} cluster suddenly diminishes at magnetically ordering temperature, $T_N=7.2$

K and consequently the Ho-B distance is lengthened. These results indicate that the gap formation or the long-range magnetic order of RB_{12} are closely connected with the interatomic distance between rare-earth atom and boron atom.

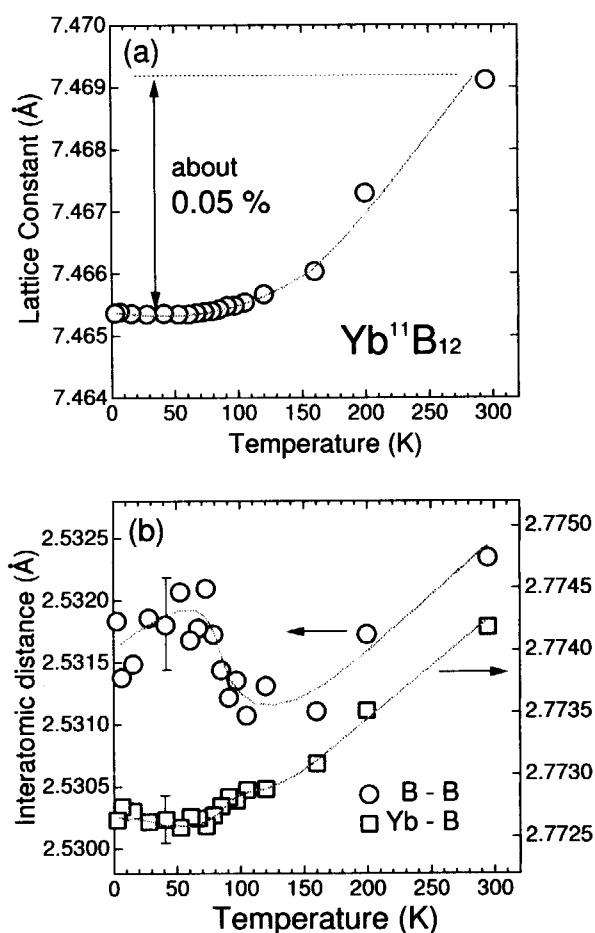


Figure 1: (a) Temperature dependence of the lattice constant and (b) temperature dependence of the interatomic distance of YbB_{12} obtained by RIETAN-2000 analysis.

References

- 1) T. Osakabe *et al.*: to be published.
- 2) F. Iga, T. Takabatake, J.-M. Mignot, P. A. Alekseev, L.-P. Regnault: JPSJ meeting, 2003 autumn, 20pPSA-40

2.4.9 Magnetic field effects on the diffuse scattering of a spin-frustrated spinel ferrite ZnFe_2O_4 single crystal

K. Kamazawa, K. Katano¹ and Y. Tsunoda²

Advanced Research Institute for Science and Engineering, Waseda Univ., 3-4-1 Ohkubo, Shinjuku-ku, Tokyo 169-8555, Japan

¹Neutron Scattering Group, Advanced Science Research Center, Japan Atomic Energy Research Institute, Tokai, Ibaraki 319-1195, Japan

²Department of Applied Physics, School of Science and Engineering, Waseda University, 3-4-1 Ohkubo, Shinjuku-ku, Tokyo 169-8555, Japan

In the previous paper we reported that magnetic diffuse scattering of neutrons is located along and slightly inside of the first Brillouin zone boundary (BZB) of the FCC structure for a frustrated spinel ferrite ZnFe_2O_4 ¹⁾. The intensity distribution of these diffuse scattering was well reproduced by an RPA calculation²⁾ using a weak ferromagnetic coupling for the nearest neighbor spins and the antiferromagnetic coupling for the third neighbor spins. However, we also found another type of diffuse scattering located around the (4 0 0) and (4 4 0) nuclear Bragg peak positions which are explained by the structure factor of the B-site atoms. These diffuse scatterings indicate the ferromagnetic short range order of the spins at the B-site. We refer to this diffuse scattering as the ferromagnetic diffuse scattering. In order to clarify the details of this ferromagnetic diffuse scattering, we performed neutron scattering measurements on a ZnFe_2O_4 single crystal under applied magnetic fields.

In the neutron scattering measurements, we used TAS-2 triple-axis spectrometer installed at the T2 thermal guide of JRR-3M, Tokai, Japan. The incident neutron wave vector was $k_i = 2.66 \text{ \AA}^{-1}$. A pyrolytic graphite (PG) analyzer and a thick PG filter were used. The full-width at the half-maximum (FWHM) of the energy resolution was about 0.8 meV.

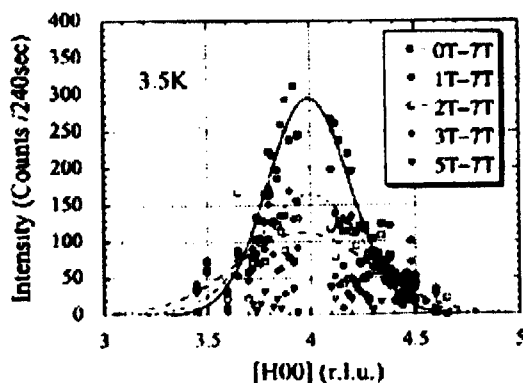


Figure 1: Magnetic field dependences of the elastic diffuse scattering obtained by scanning along the [1 0 0] axes at 3.5 K.

Since diffuse scattering data were taken through the analyzer, the spin fluctuations with characteristic time shorter than 10^{-11} s were discarded. Neutron scattering experiments were performed in the cubic (HK0) zone, and magnetic fields were applied in the [0 0 1] direction. Figure 1 shows the line profiles obtained by scanning along the [H 0 0] direction at 3.5 K under the magnetic field of 0, 1, 2, 3, 5, and 7 T. The intensity of the diffuse peak located around the (4 0 0) nuclear Bragg peak decreases dramatically with increasing magnetic field. On the other hand, the strong diffuse peak around the (3 0 0) RLP, which is an equivalent one to that distributed along the first BZB, does not show appreciable field dependence. This point was confirmed in the measurements of the diffuse peak around the equivalent (1 0 0) RLP. In order to check the localization of this diffuse scattering to a Bragg peak position under the magnetic field, the (4 0 0) Bragg peak intensity was carefully examined under the various fields. However, no evidence of the ferromagnetic longrange order was observed even in the field of 7 T. This result is consistent with the DC magnetic susceptibility data which just decrease with increasing magnetic field and shows no anomaly.

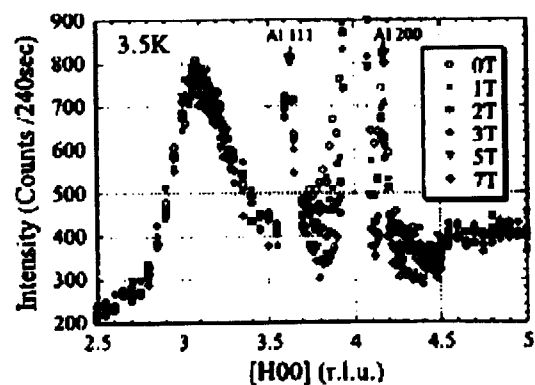


Figure 2: Magnetic diffuse scattering obtained by subtraction of the scan in 7 T from that in each magnetic field at 3.5 K.

Magnetic diffuse scattering intensities obtained by subtraction of the scan in 7T from that in each magnetic field at 3.5K are shown in Fig. 2. It indicates that with increasing the magnetic field the FWHM of the diffuse peak increases with decreasing intensity, suggesting that the ferromagnetic clusters are subdivided into small clusters. These experimental results therefore suggest that the ferromagnetic correlations in ZnFe_2O_4 are weakened rather than are strengthened in the magnetic field though it seems to be contrary to the expected sense.

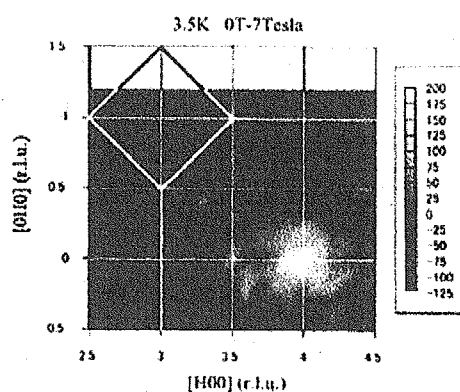


Figure 3: Subtracted contour map around the (4 0 0) Bragg peak position studied at 3.5 K. The solid lines indicate the Brillouin zone boundaries of the FCC structure.

Figure 3 shows the subtracted data ($I(H=0T) - I(H=7T)$) in an elastic contour map around the (4 0 0) Bragg peak position studied at 3.5 K. Ferromagnetic diffuse scattering distributes almost spherically, indicating that the ferromagnetic spin correlation is isotropic. As described before, the magnetic diffuse scattering around (4 0 0) decreases in magnetic field, however, the scattering around (3 0 0) and along the BZB does not change appreciably in the field. One effect that might be expected under the magnetic field is a change in inelastic scattering which shows very low-frequency dispersion relations in zero magnetic field. We hence studied inelastic scattering energy spectra at the (1.8 0 0) and (3.8 0 0) RLPs under the various magnetic fields at 3.5 K.

The data obtained at the (1.8 0 0) RLP are given in Fig. 4. No appreciable change in the energy spectrum was observed even at 7T. Similar results were obtained at the (3.8 0 0) RLP where the field sensitive ferromagnetic diffuse scattering was observed as an elastic component as shown before. Previously we studied magnetic diffuse scattering of the same normal spinel ferrite CdFe_2O_4 , using a single crystal specimen. Although the atomic configuration of Fe^{3+} ions in CdFe_2O_4 is just the same as that of ZnFe_2O_4 , the location of the magnetic diffuse peak was completely different³⁾. The diffuse peak intensity in the former distributes in the second zone of the FCC Brillouin

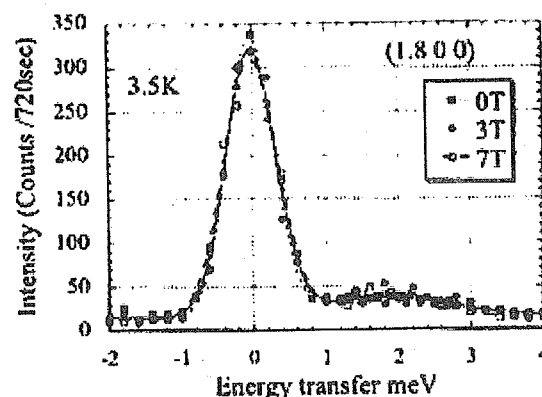


Figure 4: Magnetic field dependences of the energy spectra studied at the (1.8 0 0) RLP at 3.5 K.

zone boundary (BZB), while that in the latter is in the first zone of the FCC BZB as mentioned before. Furthermore, in CdFe_2O_4 , ferromagnetic diffuse scattering located around the (4 0 0) nuclear Bragg peak position was not observed. Thus, the spin correlations in these systems are entirely different. The ferromagnetic diffuse scattering which is very sensitive to the applied magnetic field observed here is a characteristic of ZnFe_2O_4 . Further measurements over a wider region in the reciprocal lattice space are desired to clarify these distinctive features of the field-sensitive diffuse scattering in the ZnFe_2O_4 system.

References

- 1) K. Kamazawa, *et al.*, Phys. Rev. B 68 (2003) 024412.
- 2) Y. Yamada, *et al.*, Phys. Rev. B 66 (2002) 064401.
- 3) K. Kamazawa, *et al.*, Phys. Rev. B 70 (2004) 024418.

2.4.10 Antiferromagnetic Ordering in a Ternary Uranium Compound $\text{U}_3\text{Ni}_5\text{Al}_{19}$ Y. Haga¹, N. Metoki¹, K. Kaneko¹ and Y. Ōnuki^{1,2}¹Advanced Science Research Center, JAERI, Tokai, Ibaraki 319-1195²Graduate School of Science, Osaka University, 560-0043

$\text{U}_3\text{Ni}_5\text{Al}_{19}$ crystallize in a peculiar flat orthorhombic structure (space group Cmcm) with the lattice parameters $a = 4.092$, $b = 15.947$ and $c = 26.974$ Å. Uranium atoms align along the a -axis with the same spacing 4.092 Å. Twelve uranium atoms in the unit cell occupy two crystallographic $4c$ and $8f$ sites of very similar local environments. Magnetic susceptibility $\chi(T)$ with field along the c -axis shows a sharp cusp at 23 K, implying an antiferromagnetic ordering. These antiferromagnetic moments are aligned ferromagnetically by a relatively weak magnetic field of 7 T at low temperature. Such a ferromagnetic moment is not observed when the field is applied along a or b directions, suggesting strong magnetic anisotropy along the c -axis.¹⁾

In order to clarify the antiferromagnetic state we have performed neutron scattering experiments. Single crystals of a typical dimension of $1 \times 1 \times 5$ mm² were grown from an aluminum flux with the starting composition $\text{UNi}_2\text{Al}_{20}$. Neutron scattering experiments were performed at the triple-axis spectrometer TAS-2 with an incident neutron energy of 14.7 meV monochromatized by a vertically bent PG monochromator. Higher order contamination was removed by 8 cm thick PG filter. The $(h\ 0\ l)$ and $(0\ k\ l)$ scattering planes were measured in order to study the magnetic structure.

Figure 1 shows an example of the scattering profile of the (044) Bragg peak above and below the transition temperature 23 K. We found a strong temperature dependence of the intensity across 23 K. Such temperature dependence was observed also on other Bragg peaks. This result indicates that the magnetic scattering is always superimposed on the nuclear Bragg peaks. Figure 2 is the temperature dependence of the (205) Bragg intensity measured with the fixed counter position at the peak maximum. We observed clear increase of the peak intensity due to the magnetic ordering below 23 K. The peak intensity above 23 K corresponds to the scattering intensity of (205) nuclear reflection. The background is denoted by dashed line in Fig. 2. The observed magnetic scattering can be attributed to the antiferromagnetic (AFM) ordering, since the absence of the ferromagnetic moment is shown by the $\chi(T)$ measurements. The AFM Bragg peaks with integer reflection indices indicate that the size of the magnetic unit cell is the same as the structural one. Furthermore no antifer-

romagnetic peak was observed at super lattice positions; the magnetic reflections appear at the nuclear Bragg positions. Within our experimental sensitivity, no (h00) magnetic peak was observed. The absence of the (h00) magnetic reflection could be explained from the direction of the magnetic moment, which would be parallel to the a -axis. This is consistent with the susceptibility data and the metamagnetic behavior.

In summary, we have investigated the antiferromagnetic state of a new uranium compound $\text{U}_3\text{Ni}_5\text{Al}_{19}$. The magnetic Bragg peaks were superimposed on the nuclear reflections, indicating that the magnetic unit cell is the same as the chemical one.

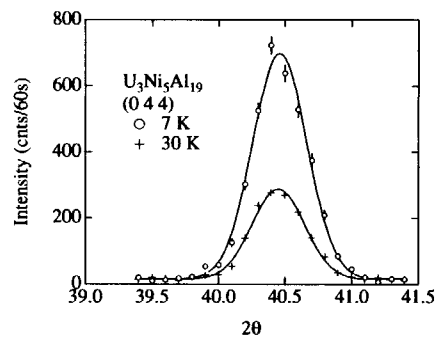


Figure 1: Neutron scattering profile of (440) reflection for $\text{U}_3\text{Ni}_5\text{Al}_{19}$ above and below 23 K

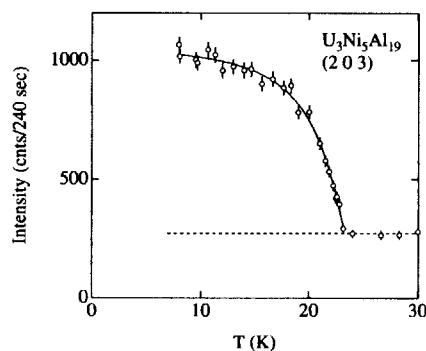


Figure 2: Temperature dependence of the (502) reflection intensity of $\text{U}_3\text{Ni}_5\text{Al}_{19}$.

References

- 1) Y. Haga *et al.*, to be published in the proceedings of SCES04.

This is a blank page.

2.5 Structural Physics

- Ionic Conductivity, Phase Transition, Dynamics -

This is a blank page.

2.5.1 Momentum Dependence of Low Energy Modes of Methane Hydrate

T. Kamiyama, S. Ohonuma, D. Nio, Y. Kiyanagi, T. Uchida¹, T. Ebinuma¹, H. Narita¹, N. Igawa², Y. Ishii²

Graduate School of Engineering, Hokkaido University, Sapporo 060-8628

¹*Institute for Energy Utilization, National Institute of Advanced Industrial Science and Technology, Sapporo 062-8517*

²*Advanced Science Research Center, JAERI, Tokai, Ibaraki 319-1195*

Clathrate hydrates have many properties that are interesting not only for scientific reasons but also in the fields of geology and nuclear engineering. Gas clathrate hydrates are a non-stoichiometric inclusion of elements or molecules within a host framework or "cage" composed of water molecules. There are many elements and molecules that are able to act as guest molecules, including: Ar, O₂, N₂, CH₄, and CO₂, but in this study we are specifically interested in methane hydrate (MH).

There has recently been a surge of interest in MH due to its potential use as an energy source, and for geo-scientific or environmental reasons. However, our interest is in its potential use as a moderator on a pulsed neutron source. A good moderator material should have a high hydrogen density and a large density-of-states in and around the thermal region (1-100 meV) in order to produce a well-defined Maxwellian. Pure solid methane is already used in various pulsed sources around the world and is excellent for producing a high flux of cold neutrons. In contrast water ice lacks low energy vibrational modes and is much better at producing thermal neutrons. Because of its high content of methane, MH potentially combines the properties of ice and methane to produce a moderator with a high performance over a wide energy range.

Until now the several inelastic neutron scattering measurements of MH have already been undertaken by our group. For lower energy (E) and momentum (Q) transfer region, we have measured the dynamical structure factor $S(Q, E)$ map and found the discrete feature of the dispersive peak which is in proportion to Q^2 . The main discrete peaks can be explained as the rotational peaks of methane free-rotation, but there still remain the excess intensities of the cross-section around 4.5 meV and over 7 meV (figure 1). It is said that in the low E - Q region there exist the translational modes of methane in the water cage¹⁾. In this study we have measured these unknown peaks in detail and made clear the features of them.

Figure 2 shows the E -constant spectra of $S(Q, E)$ around $E = 6.5$ meV and 8 meV, respectively. The points with error bars correspond to the data taken by MARI at ISIS, UK. The TAS-1 data show good agreements with the MARI data on tendencies. The TAS-1 data, which have better statistics and wider Q

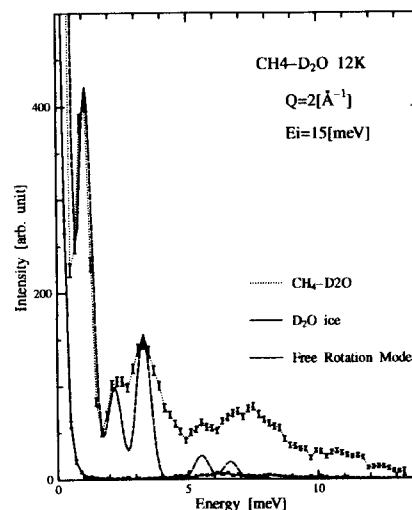


Figure 1: Comparison between experimental $S(Q, E)$ of methane hydrate (MARI at ISIS) and methane free rotation model at 12 K.

region, can be recognized the peak shapes and positions. Now we are trying to subtract the influences of rotational peaks from the $S(Q, E)$ and analysing the excess intensities on the $S(Q, E)$. Next, we will discuss about the origin of them.

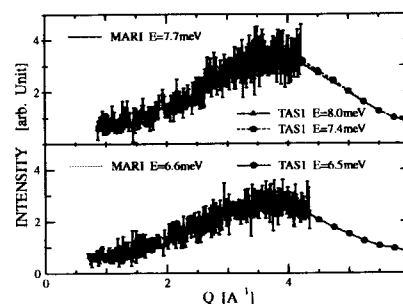


Figure 2: Constant energy spectra of methane hydrate.

References

- 1) J. S. Tse, C. I. Ratcliffe, B. M. Powell, V. F. Sears and Y. P. Handa, *J. Phys. Chem. A*, 101 (1997) 4491.

2.5.2 Thermal Vibration of Superionic Conducting Glass (AgI)_{0.8}-(Ag₂MoO₄)_{0.2}D. Hosaka, A. Thazin, T. Shimoyama, T. Sakuma, H. Takahashi¹, M. Arai² and Y. Ishii²*Faculty of Science, Ibaraki University, Mito, Ibaraki 310-8512*¹*Faculty of Engineering, Ibaraki University, Hitachi, Ibaraki 316-8511*²*Advanced Science Research Center, JAERI, Tokai, Ibaraki 319-1195*

AgI-Ag₂MoO₄ is a good model system to understand the relationship among structure and transport properties in disordered materials. The glasses with composition AgI-Ag₂MoO₄ belong to fast ion conducting (FIC) glasses which can be used as electrolytes in solid state electrochemical devices¹⁾.

It was observed that the structure features of AgI-doped glasses are as follows; (1) the glass network structure is unaffected by the addition of AgI; (2) the neutron structure, $S(Q)$, exhibits a prepeak at low $Q \sim 0.6 - 0.9 \text{ \AA}^{-1}$ and (3) a strong Ag-I correlation is observed in the radial distribution function around 2.8 Å. At previous work, we utilized X-ray diffraction for studying of thermal vibration of AgI doped glasses and present work we employed neutron scattering in order to perform the structural analysis of (AgI)_{0.8}-(Ag₂MoO₄)_{0.2} glass.

AgI and Ag₂MoO₄ were mixed and melted in a pyrex bottle at 600 °C. The sample was poured on a stainless-steel block and pressed by another block.

The neutron scattering experiments were performed at TAS-1 in JRR-3M reactor of JAERI. The measured Q -range is from 0.9 \AA^{-1} to 10.5 \AA^{-1} which corresponds to the scattering angle from 5° to 120° with the neutron wavelength of 1.0 Å. For low temperature experiments aluminium cans are used with heat exchange gas and the GM-type cryostat was used in this work. The measurements were performed at 10, 150 and 300 K and the intensity data were obtained with every 0.05 \AA^{-1} .

The data were corrected for absorption, multiple scattering, container and background effects using Placzek correction method resulting in the total differential cross section. After the incoherent scattering intensity was subtracted from the corrected intensity, the coherent intensity which is related to the structure was obtained. The coherent intensity was normalized at large- Q range, then the structure $S(Q)$ was derived as shown in Fig.1.

The absolute value of $S(Q) - 1$ for these glasses increases slightly with the increase of temperature. The differences of the structure factors $S_{10K}(Q) - S_T(Q)$ were obtained from the observation values of these glasses at 150 and 290 K. There can be noticed that the deviations of the differences from zero increase as the temperature increases. The maximums of the differences appear at $Q=2.05, 3.16, 5.12, 7.11 \text{ \AA}^{-1}$ and

the minimums are at $Q=2.58, 3.9, 6.02, 8.03 \text{ \AA}^{-1}$ in this glass. The positions of Q of the maximums and minimums almost correspond to those in Fig.1 at 10, 150 and 290 K.

The results of analysis, it was obtained that Debye-Waller temperature parameter B increases with the increase of temperature. The values of $B_T - B_{10K}$ are 0.5 and 0.9 \AA^2 at $T=150$ and 290 K , respectively. This tendency of the temperature dependence is similar to that of the crystalline superionic conductors $n\text{AgI} \cdot 3\text{Ag}_2\text{O} \cdot 2\text{V}_2\text{O}_5$ and $\text{AgI} \cdot \text{AgPO}_3$ ²⁾. The relation between the Debye-Waller temperature parameter B and the mean-square displacement of atoms $\langle u^2 \rangle$ is shown as the equation $B=8\pi^2\langle u^2 \rangle$. The calculated values of the effective mean-square displacement $\langle u^2 \rangle_T - \langle u^2 \rangle_{10K}$ are 0.019 and 0.0342 \AA^2 at $T=150$ and 290 K respectively. It was found that the value of Debye-Waller temperature parameter and mean square displacement of these glasses increase with the temperature.

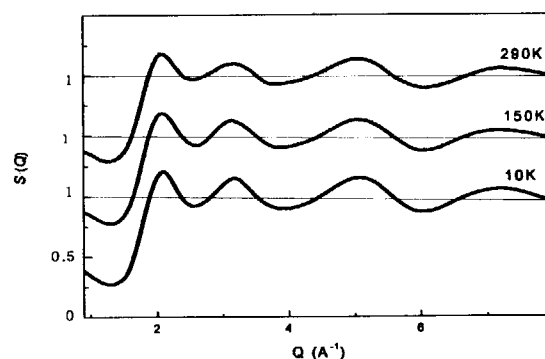


Figure 1: Structure factor $S(Q)$ of (AgI)_{0.8}-(Ag₂MoO₄)_{0.2} glasses at 10, 150 and 290 K.

References

- 1) T. Minami and M. Tanaka : *J. Solid. State. Chem.* **32** (1980) 289.
- 2) A. Thazin, M. Arai, T. Sakuma and H. Takahashi : *Solid State Ionics* **150** (2002) 291.

2.5.3 Phonon study on high performance thermoelectric material "skutterudite"

C. H. Lee, M. Matsuda¹ and H. Sugawara²

National Institute of Advanced Industrial Science and Technology, 1-1-1 Umezono, Tsukuba, Ibaraki 305-8568, Japan

¹Advanced Science Research Center, Japan Atomic Energy Research Institute, Tokai, Ibaraki 319-1195, Japan

²Graduate School of Science, Tokyo Metropolitan University, Minami-Ohsawa, Hachioji, Tokyo 192-0397, Japan

Filled skutterudite compounds RM_4X_{12} (R = rare-earth; M = Fe, Ru or Os; X = P, As or Sb) have attracted great attention due to their potential as thermoelectric devices. In particular, their low lattice thermal conductivity is advantageous to achieve high thermoelectric performance. For further improvement in their performance, the origin of their low lattice thermal conductivity needs to be investigated. Previous studies suggest that the suppression of thermal conductivity is a consequence of free vibration of rare-earth atoms in a large lattice cage, which is so called rattling effect¹⁾. To confirm the hypothesis, phonon behavior should be studied. In this work, we have studied phonon of $CeRu_4Sb_{12}$ by neutron scattering using single crystal samples. Note that all previous neutron scattering studies of phonons were restricted to powder samples and this is the first report on a phonon study using single crystals.

The measurements were conducted using the 3-axis spectrometer, TAS-1, at JRR-3M reactor of Japan Atomic Energy Research Institute in Tokai. The incident (final) neutron energy was fixed at E_i (E_f) = 14.7 meV or 13.7 meV using the (002) reflection of a pyrolytic graphite monochromator and an analyzer. In order to increase the sample volume, five single crystals were assembled and mounted in an Al container filled with He thermal exchange gas. Total volume of the samples is about 0.2 cc.

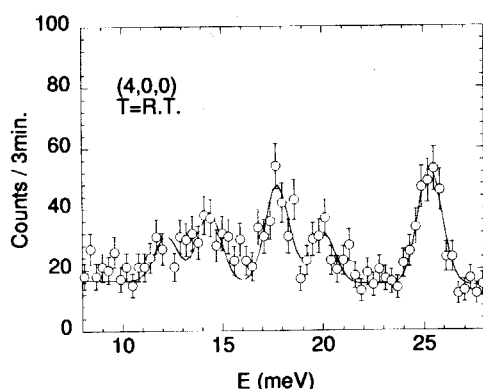


Figure 1: Energy spectrum of phonons at (4,0,0) for $CeRu_4Sb_{12}$.

Figures 1 and 2 depict energy spectra of phonon at Γ point in the energy range of $8\text{ meV} \leq E \leq 50\text{ meV}$ at room temperature. Solid lines depict a fit using gaussian function. Many branches are observed in the measurements. According to V. Keppens *et al.*¹⁾, there is a broad peak around $E = 15\text{ meV}$ for $LaFe_4Sb_{12}$ measured by inelastic powder neutron technique. They discussed that the broadening is an effect of hybridization with acoustic phonons. The present results, however, indicate that their observation of broad peak is not due to such hybridization but rather due to the emergence of many phonon branches. Feldman *et al.* has calculated phonon energies of $LaFe_4Sb_{12}$ and show that their maximum energy is $E = 32\text{ meV}$ ²⁾. Although sample composition is different, our observation of phonons around $E = 40\text{ meV}$, higher than the prediction, requires recalculating using more suitable parameters. Further studies should be carried out to clarify the rattling effect.

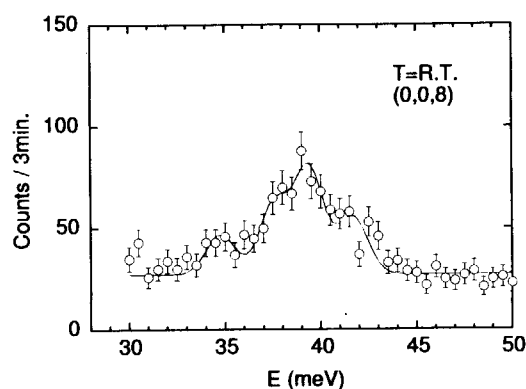


Figure 2: Energy spectrum of phonons at (0,0,8) for $CeRu_4Sb_{12}$.

References

- 1) V. Keppens *et al.* : Nature 395, 876 (1998).
- 2) J. L. Feldman *et al.* : Phys. Rev. B 68, 94301 (2003).

2.5.4 Origin of FSDP for Superionic Silver Vanadate Glasses

H. Takahashi, Y. Sanao, T. Sakuma¹ and Y. Ishii²*Faculty of Engineering, Ibaraki University, Hitachi 316-8511*¹*Faculty of Science, Ibaraki University, Mito 310-8512*²*Advanced Science Research Center, JAERI, Tokai, Ibaraki 319-1195*

We have investigated the medium range order in AgI containing superionic glasses in terms of the diffraction peak in low q region. Small peak observed around 5 to 10 nm^{-1} in q space is often called the first sharp diffraction peak (FSDP). FSDP was observed in silver vanadate glasses with and without AgI addition by X-ray diffraction. No FSDP was found by neutron diffraction. So it is considered that FSDP arises from the density fluctuation of vanadium oxide glass network. Another FSDP was found in $0.67(\text{AgI})\text{-}0.33(3\text{Ag}_2\text{O}\cdot 2\text{V}_2\text{O}_5)$ glass by the elastic neutron scattering experiment¹⁾. In the present investigation, detailed FSDP measurements using triple-axis spectrometer were performed for several glasses with different AgI content in order to obtain information about the origin of FSDP.

Powder glass sample filled into a cylindrical vanadium container of 10 mm in diameter was used as a specimen. Elastic and total neutron scattering experiments for $x(\text{AgI})\text{-(}1\text{-}x)(3\text{Ag}_2\text{O}\cdot 2\text{V}_2\text{O}_5)$ glasses, where $x = 0.3, 0.5, 0.6$ and 0.67 , were performed by LTAS at JRR-3. The incident neutron wavelength of 0.483 nm is employed. The scattering data was recorded in the range $1.0 \leq Q \leq 10.0\text{ nm}^{-1}$ at room temperature.

Figure 1 shows the elastic neutron scattering profiles for $x(\text{AgI})\text{-(}1\text{-}x)(3\text{Ag}_2\text{O}\cdot 2\text{V}_2\text{O}_5)$ glasses. The diffraction profile for $x = 0.67$ glass is essentially the same as the previous one obtained by TAS-2. The separation of FSDP from the tail of non-scattered beam is improved by using the longer wavelength of neutron in the present investigation. It is reconfirmed that FSDP could not be detected from the total scattering experiments as before. FSDP is observed above $x = 0.5$ by elastic neutron scattering. Sub-figure indicates the composition dependence of FSDP position. FSDP position extrapolated to $x = 0.3$ falls around $q = 0.8$ in this sub-figure. It is clear that no FSDP is found at $x = 0.3$. Therefore the critical AgI concentration for the formation of FSDP, in other words medium range structure, lies between $x = 0.3$ and 0.5 . Composition dependence of the molar volume also suggests the structure change in the same AgI concentration. Structure change assumed by FSDP measurement is consistent with the results of the molar volume. FSDP observed by neutron scattering originates from the correlation between Ag, I and/or O based on the coherent scattering length of

the elements. Since doped AgI concentration strongly affects the appearance of FSDP, it is natural to conclude that AgI microdomain is formed above critical AgI concentration. Domain size is considered to increase with AgI concentration as shown in the figure. It is verified that AgI containing silver vanadate system precipitates AgI crystal beyond $x = 0.7$. So AgI microdomain is assumed to act as a nuclear of AgI microcrystal. The fact that FSDP could not be detected by neutron diffraction suggests that inelastic and quasielastic scatterings due to the low-energy diffusive motion of Ag ion obscure the structural information in the medium range order.

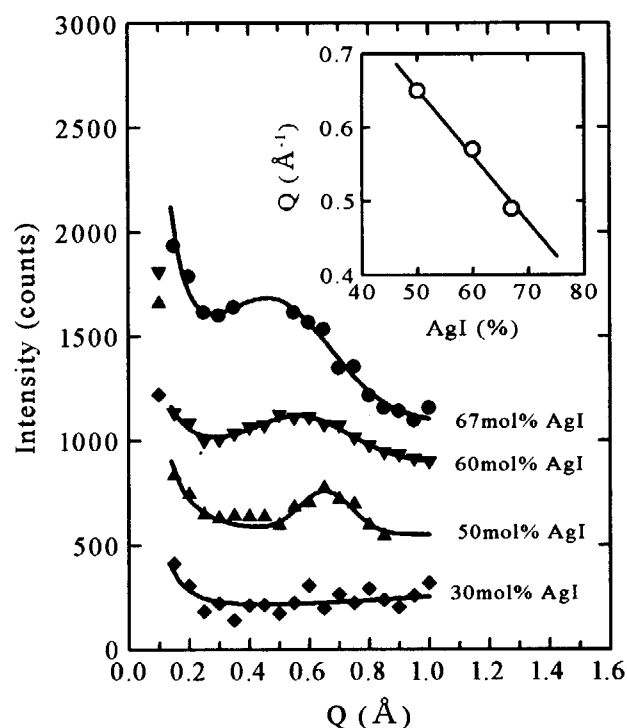


Figure 1: AgI Concentration dependence of FSDP for silver vanadate glasses.

References

- 1) H. Takahashi, N. Rikitake, T. Sakuma and Y. Ishii : Solid State Ionics, **168** (2004) 93.

2.5.5 Lattice dynamics of PbTiO_3 I. Tomeno, Y. Ishii¹ Y. Tsunoda² K. Oka³ and H. Unoki³*Faculty of Education and Human Studies, Akita University, Akita 010-8502*¹*Neutron Science Research Center, JAERI, Tokai, Ibaraki 319-1195*²*School of Science and Engineering, Waseda University, Shinjuku-ku, Tokyo 169-8555*³*Nanoelectronics Research Institute, AIST, Tsukuba, Ibaraki 305-8568*

PbTiO_3 has attracted much attention from the scientific and engineering viewpoints. Unlike BaTiO_3 , PbTiO_3 undergoes only a single phase transition from a cubic to tetragonal phase at $T_c=763$ K. PbTiO_3 is also the end member of relaxor ferroelectrics $(1-x)\text{Pb}(\text{Zn}_{1/3}\text{Nb}_{2/3})\text{O}_3-x\text{PbTiO}_3$ (PZN-PT). The inelastic neutron-scattering experiments were carried out using the triple-axis spectrometer, TAS-1 at JRR-3M.

The TA phonon dispersion relations for tetragonal PbTiO_3 are compared in Fig.1 with those for tetragonal KNbO_3 , ¹⁾ tetragonal BaTiO_3 ²⁾ and cubic PZN. ³⁾ Both PbTiO_3 and PZN possess two common features. First, the ZB TA phonon energies for Pb-based crystals are considerably lower than those for the other perovskites. The ZB TA phonon energies for cubic PZN are lower than the corresponding energies for tetragonal PbTiO_3 . The mass and charge randomness at the B site appears to weaken the effective force-constants in PZN. Second, the TA phonon dispersion relations are isotropic with respect to the high-symmetry directions. The isotropic TA phonon dispersion relations are also found for tetragonal BaTiO_3 . ²⁾ The ZB TA phonon energies for PbTiO_3 are approximately half of those for BaTiO_3 . ²⁾ The Pb atom plays a major role in the ZB acoustic phonons. In contrast, the extremely anisotropic TA phonon curves are found for tetragonal KNbO_3 . ¹⁾

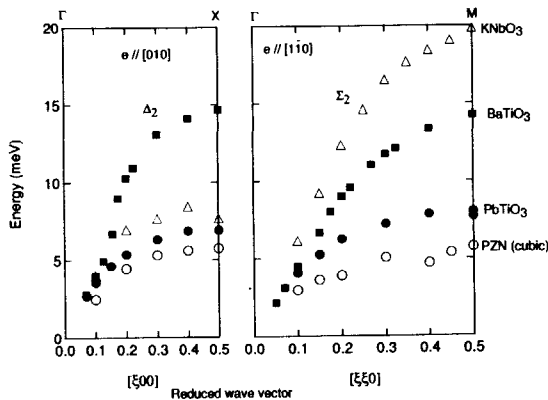


Figure 1: The TA phonon dispersion relations for typical perovskites.

Figure 2 depicts the temperature dependence of phonon dispersion relations along the $[110]$ and $[001]$ directions. The energy of the zone-center TO- A_1 mode is significantly higher than that for the TO-E mode at room temperature. In view of the LST relationship, the dielectric-constant relation $\epsilon_{11} > \epsilon_{33}$ mainly originates from the fact that the low-lying zone-center TO- A_1 mode is well stiffened at room temperature.

The energy of the zone-center TO- A_1 mode decreases to 12.7 meV at 643 K ($0.84T_c$). On the other hand, the energy of the zone-center TO-E mode practically remains constant up to 643 K. The softening of the TO- A_1 mode up to 643 K is rather moderate compared to the behavior of the TO- F_{1u} mode in the cubic phase. ⁴⁾ The distinctive behavior of the TO modes in both sides is consistent with the fact that the temperature dependence of ϵ_{33} is characterized by a first-order phase transition.

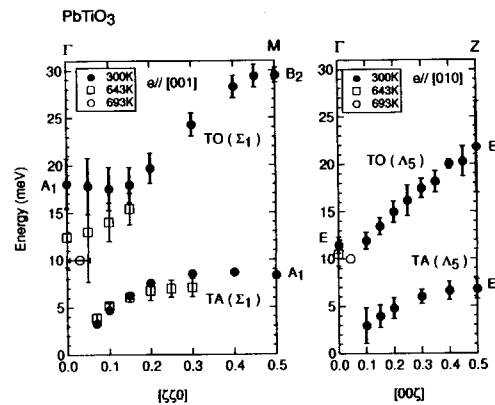


Figure 2: Temperature dependence of phonon dispersion relations for PbTiO_3 .

References

- 1) M. D. Fontana, G. Dolling, G. E. Kugel, and C. Carabatos, Phys. Rev. B20 (1979) 3850.
- 2) G. Shirane, J. D. Axe, J. Harada, and A. Linz, Phys. Rev. B2 (1970) 3651.
- 3) I. Tomeno, S. Shimanuki, Y. Tsunoda, and Y. Ishii, J. Phys. Soc. Jpn. 70 (2001) 1444.
- 4) G. Shirane, J. D. Axe, J. Harada and J. P. Remeika : Phys. Rev. B2 (1970) 155.

2.5.6 Structural study of $\text{Ca}_3\text{Ru}_2\text{O}_7$ by powder neutron diffractionY. Yoshida, S. I. Ikeda, N. Shirakawa, N. Aso¹, M. Nishi¹, Y. Uwatoko¹ and S. Katano²

Nanoelectronics Research Institute, AIST, Tsukuba, Ibaraki 305-8568

¹ISSP, the university of Tokyo, Kashiwa, Chiba 277-8581²Advanced Science Research Center, JAERI, Tokai, Ibaraki 319-1195

The Ruddlesden-Popper (R-P) type ruthenates ($\text{Sr}, \text{Ca})_{n+1}\text{Ru}_n\text{O}_{3n+1}$ attract many researchers since the discovery of the spin-triplet superconductor, Sr_2RuO_4 ($n=1$).¹⁾ The double-layered $\text{Sr}_3\text{Ru}_2\text{O}_7$ ($n=2$) shows the Fermi-liquid behavior and ferromagnetic instability in the ground state, which has been lately discussed a quantum criticality tuned by a magnetic field.^{2,3)} The recent report revealed that substantial ferromagnetic ordering emerged under the uniaxial pressure up to 1 GPa.⁵⁾ The crystal structure is a distorted R-P type structure with the orthorhombic space group $Bbcb$ ⁴⁾, which have rotations of RuO_6 octahedra around c -axis. Such a distortion may play an important role in magnetic properties of $\text{Sr}_3\text{Ru}_2\text{O}_7$. It is interesting to investigate how the structural distortion relates to the physical properties.

$\text{Ca}_3\text{Ru}_2\text{O}_7$ has a more distorted crystal structure than $\text{Sr}_3\text{Ru}_2\text{O}_7$ owing to the smaller ionic radius of Ca^{2+} than of Sr^{2+} . The crystal structure shows the orthorhombic symmetry with $Bb2_1m$ space group, accompanying both the rotation and tilting of RuO_6 octahedra.⁶⁾ $\text{Ca}_3\text{Ru}_2\text{O}_7$ shows a quasi-two-dimensional metallic ground state with antiferromagnetic ordering ($T_N = 56$ K) and have a first-order metal-to-nonmetal transition at $T_{\text{MI}} = 48$ K.^{7,8)} Recently, the jump of the lattice parameters was observed at the first-order transition temperature from x-ray diffraction and a thermal contraction measurement.^{9,10)} To clarify the temperature dependence of the structural parameters, we carried out neutron powder diffraction measurements for $\text{Ca}_3\text{Ru}_2\text{O}_7$.

Powdered sample was prepared from crushed single crystals of $\text{Ca}_3\text{Ru}_2\text{O}_7$ grown by a floating zone method. Neutron-diffraction measurements were performed at the JRR-3M reactor, Tokai, JAERI. The powder diffractometer HRPD was used in the measurements from 10 K to room temperature (RT).

Nuclear structure refinements were made for $\text{Ca}_3\text{Ru}_2\text{O}_7$ measured at 10 K and RT using a Rietveld refinement program RIETAN.¹¹⁾ In the nuclear structure refinements, the obtained R values for each temperatures are in the range from 7.56 to 9.86%. The final structural parameters at RT are consistent with those in the previous report.⁶⁾ From the result of Rietveld analysis, the temperature dependences of the structural parameters are obtained. For example,

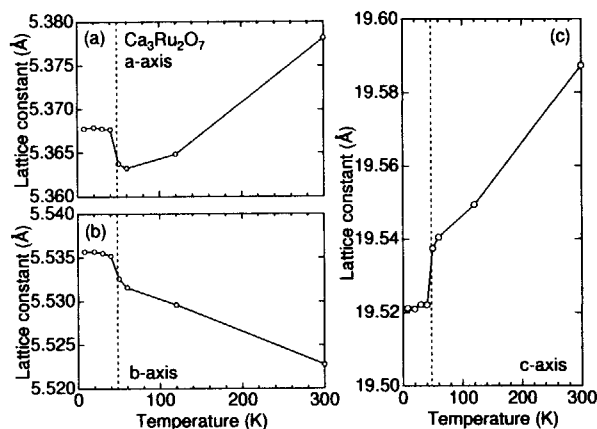


Figure 1: Temperature dependences of lattice constants (a) a, (b) b and (c) c.

Figs. 1(a), (b) and (c) show the temperature dependences of the lattice constants a , b and c of $\text{Ca}_3\text{Ru}_2\text{O}_7$, respectively. The lattice constants a and c shorten on cooling from RT , while b elongates with decreasing temperature. As mentioned in the previous report, the lattice parameters jump at the first-order transition temperature, denoted as broken lines in the figure, where c shortens about 0.1%, while a and b lengthen both about 0.07%. The lattice volume increases at this transition.

On cooling below T_N , an additional reflection emerges and can be observed at 10 K, which can be indexed in the $Bb2_1m$ lattice with (100). This peak corresponds to an antiferromagnetic ordering. To discuss magnetic structure, it needs further neutron-diffraction study using single crystals.

References

- 1) Y. Maeno *et al.*, *Physics Today* **54**, (2001) 42.
- 2) S. I. Ikeda *et al.*, *Phys. Rev. B* **62**, (2000) R6089.
- 3) S. A. Grigera *et al.*, *Science* **294**, (2001) 329.
- 4) H. Shaked *et al.*, *J. Solid State Chem.* **154**, (2000) 361.
- 5) S. I. Ikeda *et al.*, *J. Phys. Soc. Jpn.* **73**, (2004) 1322.
- 6) G. Cao *et al.*, *Phys. Rev. B* **62**, (2000) 998.
- 7) G. Cao *et al.*, *Phys. Rev. Lett.* **78**, (1997) 1751.
- 8) Y. Yoshida *et al.*, *Phys. Rev. B* **69**, (2004) 220411.
- 9) G. Cao *et al.*, *Phys. Rev. B* **67**, (2003) 184405.
- 10) E. Ohmichi *et al.*, to be published in *Phys. Rev. B*.
- 11) F. Izumi and T. Ikeda, *Mater. Sci. Forum*, **321-324** (2000) 198.

2.5.7 Defect structure of oxygen-excess pyrochlore-type $\text{Ce}_2\text{Zr}_2\text{O}_8$ elucidated using neutron powder diffraction

H. Otobe, N. Igawa¹, Y. Ishii¹

Department of Material Science, JAERI, Tokai, Ibaraki 319-1195

¹Neutron Science Research Center, JAERI, Tokai, Ibaraki 319-1195

The neutron diffraction studies have been performed on oxygen-excess pyrochlore-type (P-type) $\text{Ce}_2\text{Zr}_2\text{O}_8$ in order to elucidate the defect structure of this material.

P-type $\text{An}_2\text{Zr}_2\text{O}_{7+x}$ (An = Pu, Am, Cm etc.) has attracted significant research interest as radioactive waste-forms and targets for actinide transmutation in nuclear engineering field.^{1,2)} It is important to clarify the thermodynamic and defect properties of these systems for such applications. However, it is difficult to handle the transuranium materials for their high radiotoxicity. It is convenient to study the thermodynamic and defect properties of P-type $\text{Ce}_2\text{Zr}_2\text{O}_{7+x}$, a rare earth analogue of P-type $\text{An}_2\text{Zr}_2\text{O}_{7+x}$ (An = Pu, Am, Cm etc.) and apply the study to that of transuranium materials.

Thomson *et al.* studied the structure of P-type $\text{Ce}_2\text{Zr}_2\text{O}_{7.97}$ by neutron and X-ray powder diffraction methods.³⁾ P-type $\text{Ce}_2\text{Zr}_2\text{O}_8$ is the first example of oxygen-excess pyrochlores with fluorite-dioxide composition (O/M=2) among a variety of pyrochlores already synthesized. Their neutron diffraction data were different from that of stoichiometric fluorite dioxide and P-type $\text{Ce}_2\text{Zr}_2\text{O}_7$. The peaks seen over $2.1 < d\text{-spacing} < 2.6 \text{ \AA}$ could not be attributed to those of the stoichiometric materials. They proposed a defect model that excess oxygen sites are composed of two types: One is a tetrahedrally coordinated anion site as in the fluorite-type zirconia, the other is a trigonal anion site surrounded by three cerium ions, although the cations are ordered in the usual pyrochlore arrangements. Their data and model are very impressive, but their samples

had the impurities as written in their papers. Therefore, we have prepared the P-type $\text{Ce}_2\text{Zr}_2\text{O}_8$ sample without impurities.

Figure 1 shows the neutron diffraction pattern of pyrochlore $\text{Ce}_2\text{Zr}_2\text{O}_8$ obtained by using HRPD ($\lambda=1.823 \text{ \AA}$). This pattern exhibited the same peaks as those of Thomson *et al.* The result indicates the peaks over $40^\circ < 2\theta < 50^\circ$ are intrinsic to P-type $\text{Ce}_2\text{Zr}_2\text{O}_8$, oxygen-excess pyrochlore. Figure 1 also shows the calculated pattern of stoichiometric P-type $\text{Ce}_2\text{Zr}_2\text{O}_7$ by a program RIETAN-2000.⁴⁾ The Rietveld analysis is in progress.

References

- 1) W.L. Gong, W. Lutze, R.C. Ewing; J.Nucl. Mater.277, 239 (2000).
- 2) P.E. Raison, R.G. Haire, T. Sato and T. Ogawa; Mat. Res. Soc. Symp. Proc, Materials Research Society 556, 1 (1999).
- 3) J. B. Thomson, A. R. Armstrong, P. G. Bruce; J. Solid State Chem.148, 56 (1999).
- 4) F. Izumi and T. Ikeda; Mater. Sci. Forum 321-324, 198 (2000).

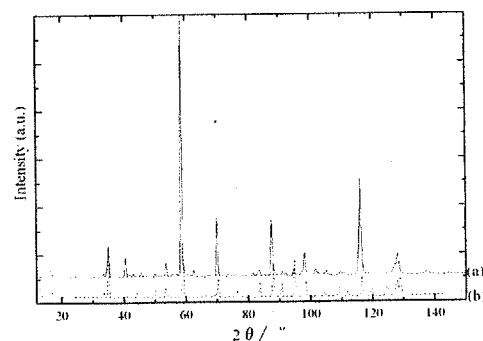


Figure 1: (a) the observed pattern of P-type $\text{Ce}_2\text{Zr}_2\text{O}_8$
(b) the calculated pattern of stoichiometric P-type $\text{Ce}_2\text{Zr}_2\text{O}_7$.

2.5.8 Modulated Structure of Bi-substituted Misfit Layered Cobaltite $[\text{Ca}_2\text{CoO}_3]_p\text{CoO}_2$ Y. MIYAZAKI, Y. SUZUKI, M. ONODA¹, N. IGAWA², Y. ISHII², Y. MORII² and T. KAJITANI*Department of Applied Physics, Tohoku University, Sendai 980-8579*¹*Advanced Materials Laboratory, NIMS, Tsukuba, Ibaraki 305-0044*²*Neutron Science Research Center, JAERI, Tokai, Ibaraki 319-1195*

Misfit-layered cobalt oxides have recently attracted much attention as potential candidates for thermoelectric (TE) materials. Among the compounds, partly Bi-substituted $[\text{Ca}_2\text{CoO}_3]_p\text{CoO}_2$ samples are known to exhibit excellent TE properties at higher temperatures. We have employed a high-resolution neutron powder diffraction technique to investigate the modulated crystal structure of the Bi-substituted compound, in particular the site preference of Bi and the substitution effect on the positional modulation of atomic sites.

Neutron powder diffraction (ND) data were collected at 293 K by means of HRPD diffractometer installed at the JRR-3M reactor in JAERI. The ND data were analyzed using a Rietveld refinement program PREMOS 91. The superspace group of $C2/m(1p0)s0$ was appropriately adopted.

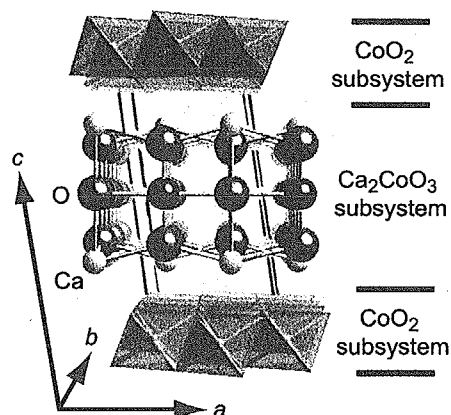


Figure 1: Fundamental crystal structure of $[\text{Ca}_2\text{CoO}_3]_p\text{CoO}_2$.

Figure 1 shows the fundamental structure viewed in perspective from the b -axis. The structure consists of a CoO_2 sheet and an ordered three-layered rock salt (RS)-type Ca_2CoO_3 block, stacked parallel to the c -axis. The CoO_2 sheet is composed of a triangular lattice as seen in the CdI_2 -type structure. Bismuth atoms are found to substitute both for Ca and Co atoms in the RS-type $[\text{Ca}_2\text{CoO}_3]$ subsystem. The resulting structural formula is expressed as $[(\text{Ca}_{0.90}\text{Bi}_{0.10})_2(\text{Co}_{0.95}\text{Bi}_{0.05})\text{O}_3]_{0.6183}\text{CoO}_2$. Upon Bi-substitution, the a - and c -axis lengths markedly increased while the b_{CoO_2} - and b_{RS} -axes showed only

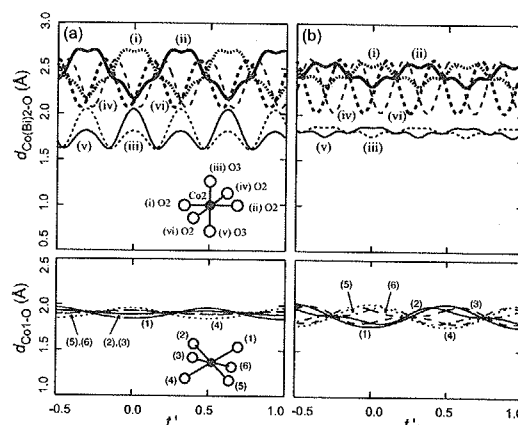


Figure 2: Co-O distances plotted against a complementary coordinate, t' , for (a) the Bi-free and (b) Bi-substituted samples.

slight expansion. The variation of the atomic positional modulation can be further understood by plotting against t' , a complementary coordinate in the (3+1)-dimensional superspace. Figure 2 shows the Co-O distances of Bi-free (a) and Bi-substituted (b) samples. The upper left panel shows the $\text{Co}_2\text{-O}$ distances in the RS-type subsystem of Bi-free $[\text{Ca}_2\text{CoO}_3]_p\text{CoO}_2$ sample, plotted against t' . The $\text{Co}_2\text{-O}$ distances are periodically altered with the interval of $t' = 0.6181$. A Co atom at $z = 1/2$ has six oxygen neighbors, with four equatorial O2 and two apical O3 atoms. Among these bonds, two apical bonds (iii and v) are fairly shorter than the other four equatorial bonds.

When a small amount (5%) of Bi is substituted for the Co_2 site, the modulation amplitudes of the two apical $\text{Co(Bi)}_2\text{-O}_3$ bonds (iii and v) are remarkably reduced as illustrated in the upper right panel. In contrast to the $\text{Co(Bi)}_2\text{-O}$ bonds, the six $\text{Co}_1\text{-O}_1$ bonds illustrated in the lower panels show an opposite substitution effect. The $\text{Co}_1\text{-O}_1$ bonds of the Bi-free phase (lower left panel) show small modulation amplitudes from 1.8 to 1.95 Å, relative to the Bi-substituted phase of 1.75 to 2.0 Å.

The observed increase in Seebeck coefficient and electrical resistivity of the Bi-substituted phase can be explained in terms of the decrease of hole concentration in the CoO_2 sheets, as well as the significant modulation of the conduction paths.

2.5.9 DIRECT OBSERVATION OF THE HYDROGEN TRANSFER IN THE SOLID-STATE ORGANIC PHOTOREACTION BY NEUTRON DIFFRACTION METHOD

T. Hosoya, H. Uekusa, T. Ozeki, Y. Ohashi, T. Ohhara¹, I. Tanaka¹ and N. Niimura²

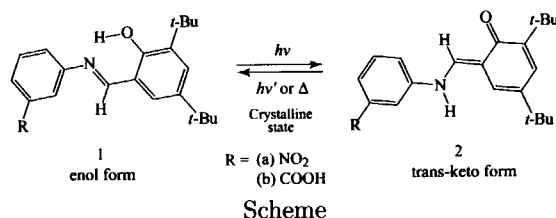
Department of Chemistry and Materials Science, Tokyo Institute of Technology, Tokyo 152-8550

¹Institute of Materials Structure Science, HEARO (KEK), Tsukuba, Ibaraki 305-0801

²Department of System Engineering, Ibaraki University, Hitachi, Ibaraki 316-8511

Hydrogen/proton transfer is one of the most elemental chemical reaction, and often observed in many organic and enzymatic reactions. In many cases, the hydrogen/proton transfer is key point of reaction process. Though many spectroscopic methods, e.g., ¹H-NMR, FT-IR, and theoretical calculations have been carried out to track the hydrogen/proton, more accurate and direct positional information is needed in order to clarify transfer process by using neutron diffraction method.

Light-induced reversible color change of substances is known as photochromism and has attracted attention due to their potential applications such as optical data storage etc. Salicylideneaniline derivatives show photochromism or thermochromism, which is reversible color change with variation of temperature. The color change from stable yellow to unstable red is brought about by the change of molecular conformation. This reaction involves a proton transfer in the keto-enol tautomerization. Previously, photo-irradiated trans-keto form of N-3,5-di-tert-butylsalicylidene-3-nitroaniline **1b** were observed by X-rays (Fig., R=NO₂)¹⁾.



Photoirradiation was carried out with two photon absorption method by laser, and the population of trans-keto **1b** form was about 10%. Therefore, the transferred proton was not observed. We try to observe the transferred proton of trans-keto form with neutron diffraction method. Crystals of **1a** and N-3,5-di-tert-butylsalicylidene-3-carboxyaniline **1b** were prepared and photo-irradiated with ultra high pressure Hg lamp.

Trans-keto form of **1a** has long lifetime enough for neutron diffraction measurement at room temperature (~ 4 days), but population of trans-keto form was only 10% with laser. On the other hand, corresponding form of **1b** has short lifetime at room temperature (~ 1 hour), but population of trans-keto form was more than 15% with Hg lamp. So the diffraction measure-

ment of **1b** was carried out at 173 K.

Soon after the irradiation with Hg lamp (410 nm) for 2 hours from four direction, crystals were mounted on the BIX-III (1G) neutron imaging plate diffractometer set up at the JRR-3M reactor in JAERI. Neutron diffraction data were collected for total 5 days at 173 K (**1b**) and 293 K (**1a**) and peak integration by *DENZO* created a *SHELX*-format *hkl* file.

Table 1: Experimental/Refinement details

	<i>m</i> -COOH	<i>m</i> -NO ₂
Crystal system	Monoclinic	Triclinic
Space group	P2 ₁ /n	P-1
a / Å	14.734(2)	6.02(3)
b / Å	6.004(2)	10.31(4)
c / Å	21.997(3)	16.75(5)
α / °	-	101.19(5)
β / °	91.26(1)	92.12(7)
γ / °	-	101.50(8)
V / Å ³	1945.4(7)	996(7)
Z	4	4
θ range / °	7.89–70.39	9.76–70.73
Temp. / K	173	173
Refs. collected / unique	864 / 864	246 / 246
Completeness to θ / %	21.3	6.1
R _{int}	0.0482	0.0603
R ₁ , wR(F ²)	0.262, 0.594	0.298, 0.610
Goodness-of-Fit	3.26	5.64
Data / params.	846 / 112	246 / 33

After structure analysis, enol form were clearly observed both **1a** and **1b**. However, the reactions were not proceeded. 410 nm light did not reach inside the thick crystals (but 0.3 mm is too thin for single-crystal neutron diffraction measurement) because the light-induced trans-keto form highly absorbs this light. Initial structures was well refined in spite of small number of reflections (**1a**: 246, **1b**: 864). So it is practical to carry out this measurement using thin crystal if more diffraction data are collected for longer exposure time. And further refinement of light-irradiation condition will be needed in order to increase the population of trans-keto form in a crystal.

References

- 1) Harada, J., Uekusa, H., and Ohashi, Y., *J. Am. Chem. Soc.*, **121**, 5809 (1999).

2.5.10 Small-angle neutron scattering study on the precipitation of 6000 Al alloys

M. Ohnuma, J. Suzuki¹, T. Honma² and K. Hono*National Institute for Materials Science, Tsukuba, Ibaraki 305-0047*¹*Advanced Science Research Center, JAERI, Tokai, Ibaraki 319-1195*²*University of Tsukuba, Tsukuba, Ibaraki 305-0047*

Because of the strong demand on weight reduction of automotive bodies for better fuel efficiency and lower exhaust emission, there is a strong drive to replace the current steel sheet to aluminum alloy sheet for automotive body applications. Due to its excellent formability and medium strength after age hardening, Al-Mg-Si based 6000 series alloys are considered to be the best candidate for automotive body sheet material. In addition, the alloys can be strengthened during an automotive paint bake cycle, i.e. aging treatment at 170-175°C for approximately 20 - 30 min. This bake hardening (BH) effect is known to be degraded by aging at room temperature (RT). For preventing this problem, alloys are heated to 250°C which is called reversion treatment, before BH heat treatment. It is also known that the Cu addition to Al-Mg-Si based 6000 alloys can help reversion treatment. Although the microstructure of the alloy are extensively studied by transmission electron microscope (TEM), positron annihilation lifetime (PAL) and three dimensional atom probe (3DAP)¹, the relation between the mechanical properties and the microstructure and the effect of Cu addition are not clear yet. Most important information at this stage is an average information of the precipitates, i.e. the size and volume fraction of the precipitates. A small-angle scattering is most suitable technique for this purpose, however, because of the small difference of electron density among these three constituent elements, small-angle X-ray scattering can not be applied for this alloy. Thus, small-angle neutron scattering (SANS) is only the way to get average information of precipitates. In this paper, we studied SANS for Al-0.7Mg-1.0Si and Al-0.6Mg-1.0Si-0.3Cu (at%) alloys with different annealing processes.

Figure 1 shows the SANS profiles of the Al-0.7Mg-1.0Si and Al-0.6Mg-1.0Si-0.3Cu alloys before and after BH treatment accompanied with aging at RT. No detectable difference between the alloys with and without BH treatment in both alloys indicating no additional precipitates form by BH treatment. Consequently, no strengthening occurs by this process. In contrast, the SANS profiles of these alloys before and after BH treatment accompanied with reversion treatment after aging at RT show some difference in high- q region as shown in Fig.2. The excess scattering corresponds to the formation of β'' phase. The differ-

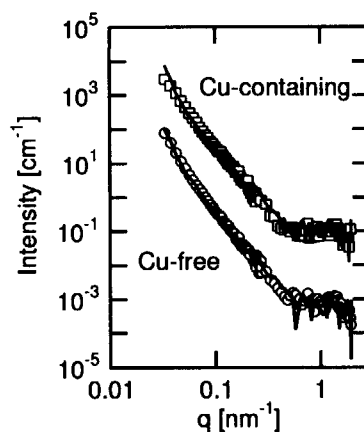


Figure 1: SANS profiles of the alloy aged at RT. Markers and lines are the profiles before and after BH treatments, respectively. The profiles of Cu containing alloys are shifted by factor of 100.

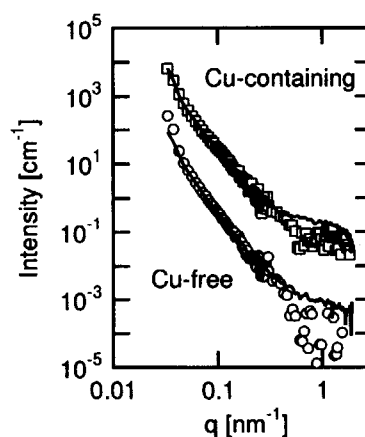


Figure 2: SANS profiles of the alloy after reversion treatment. Markers and lines are the profiles before and after BH treatments, respectively. The profiles of Cu containing alloys are shifted by factor of 100.

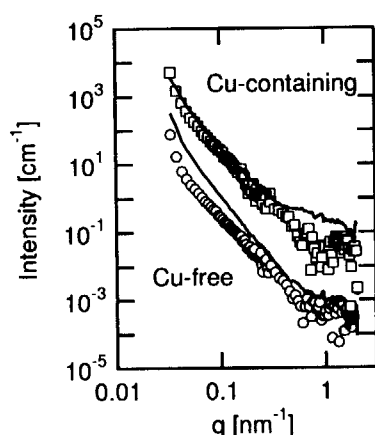


Figure 3: SANS profiles of the as-quenched alloy. Markers and lines are the profiles before and after BH treatments, respectively. The profiles of Cu containing alloys are shifted by factor of 100.

ence before and after BH treatment is larger in the alloy with Cu than the one in Cu-free alloys, suggesting that the addition of Cu increase the volume fraction of β'' phase. For confirming the enhancement of β'' formation by adding Cu, SANS profiles of the sample without room temperature aging were also observed and show in Fig.3. Again, the profile of Cu-containing alloy shows excess scattering due to the formation of β'' phase in high- q region. In contrast, the difference in this q -region is not clear in the profiles for Cu-free alloy before and after BH treatment, suggesting that the amount of β'' precipitate is relatively small. Instead, there is clear difference in low- q region which indicates the change in larger scale unit (≥ 100 nm) is prominent in Cu-free alloy. It is known that 6000-alloys include a certain amount of large precipitates (≥ 100 nm) which are believed to give no effects to mechanical properties. The change in low- q region seems to be attributed to the contrast change between large precipitate and matrix due to the formation of GP zone. Unfortunately, the formation of GP zone cannot be detected by SANS because of the small difference in concentration. However combined with TEM and 3DAP results²⁾, we can summarize the relation between mechanical property and precipitation as follows. In as-quenched state from solid solution treatment, solute elements are in highly super saturated state. Therefore, GP zones are formed by RT aging and Vickers hardness increase from about 60Hv in as-quenched state up to about 90Hv after RT aging. Because the formation of GP zone consume solute element, driving force for the formation of β'' which can occur at 170C, decrease prominently. Thus the amounts of β'' precipitates is less than the detectable level by SANS (Fig.1) and no clear difference in Vickers hardness value in the alloy aged at RT and

then BH. Since the GP zone formed during RT aging is resolved by reversion treatment (at 250C), the driving force for formation of β'' is high after reversion treatment. Therefore, the β'' can be obtained by BH treatment after reversion if the formation of GP zone during BH treatment can be suppressed. This condition is actually obtained in Cu-containing alloy and clear contribution from β'' phase is observed in SANS (Fig.2). TEM results also shows no indication of GP zone formation. The hardness increase from 70Hv to 97Hv due which is attributed to the β'' precipitates. In the Cu-free alloy, however, the formation of GP zone occurs together with β'' formation. Therefore the scattering from β'' in SANS profiles is weaker than that of Cu-containing alloy (Fig.2). The hardness increase from 66 to 93Hv which is higher than the value of the alloy aged at RT (85Hv) indicating some contribution of β'' precipitates. The effect of Cu is much clearer in the alloy without aging at RT (Fig.3). Because highly saturated solute elements is used for the formation of β'' phase efficiently in Cu-containing alloy, the amount of β'' reach maximum value among the measured alloys and the hardness also reach maximum value, 117Hv. In contrast, high super saturation of solute element is mostly consumed for the formation of GP zone in Cu-free alloy. Therefore, the amount of β'' is very small after BH treatment and increment of Hv is same value with the one after RT aging which can be explained by the formation of GP zone. Because of the concentration change in matrix due to the formation of the large amount of GP zone, the scattering contrast between large precipitate and matrix become large and cause the increasing of scattering in low- q region. Instead, the scattering from β'' is unclear due to the their small volume (Fig.3). As summary, the relation of mechanical property and microstructure in 6000 alloy become clear using SANS. Especially, it is confirmed that addition of Cu suppress or delay the GP zone formation at 170C and enhance the formation of β'' .

References

- 1) Y.Nagai, M. Murayama, Z. Tang, T. Nonaka, K. Hono and M.Hasegawa, *Acta mater.* 49(2001), 913-920.
- 2) T.Honma, K.Matsumoto, K.Hono, Y. Nagai, and M. Hasegawa, to be published.

This is a blank page.

2.6 Materials Science and Industrial Applications

- Microstructure and Residual Stress -

This is a blank page.

2.6.1 Elastic Constants Measurement of NCF600 by Neutron Diffraction - Evaluation on residual stress of weld joint in nuclear core internal structure-

R. Mizuno, A. Moriai¹, H. Suzuki¹ and Y. Morii¹

NDE Center, Japan Power Engineering and Inspection Corporation, Yokohama 230-0044

¹Neutron Science Research Center, JAERI, Tokai, Ibaraki 319-1195

Stress corrosion cracking (SCC) has occurred at weld joints with NCF600 material, which is Ni-based alloy, in nuclear core internal structures. Table 1 shows chemical composition of NCF600. It is important to determine the residual stress distributions inside the weld joint in order to evaluate the crack propagation by SCC. It is possible to measure the stress distributions inside bulk by neutron diffraction. Neutrons are scattered from the incident beam direction through angles 2θ , according to Bragg's law,

$$\lambda = 2d \sin \theta, \quad (1)$$

where λ is the wavelength of neutron, d is the spacing between lattice planes. Lattice strain is determined by neutron diffraction, which measures the spacing between lattice planes, according to equation (2),

$$\varepsilon = (d - d_0)/d_0, \quad (2)$$

where d_0 is the spacing between lattice planes without strain. By measured strains of three directions, stresses are determined by equation (3),

$$\begin{aligned} \sigma_x &= \frac{E}{(1+\nu)(1-2\nu)} ((1-\nu)\varepsilon_x + \nu(\varepsilon_y + \varepsilon_z)), \\ \sigma_y &= \frac{E}{(1+\nu)(1-2\nu)} ((1-\nu)\varepsilon_y + \nu(\varepsilon_x + \varepsilon_z)), \\ \sigma_z &= \frac{E}{(1+\nu)(1-2\nu)} ((1-\nu)\varepsilon_z + \nu(\varepsilon_x + \varepsilon_y)) \end{aligned} \quad (3)$$

where E is Young's modulus, ν is Poisson's ratio and σ_x , σ_y and σ_z are components of stress of each directions.

Hence, the elastic constants are necessary to calculate stress from measured strains. They have dependency on diffraction plane. Ni(111), Ni(200) and Ni(220) in NCF600 are available to measure the diffraction patterns because of high diffraction intensities. So the elastic constants for three lattice planes were measured by neutron diffraction. Tensile specimen of NCF600 was set and applied tensile stresses from 50 to 200MPa in steps of 30MPa. Then, the applied load was recorded by a load cell and the diffraction patterns were measured with each lattice plane for two directions; axial direction and radial direction.

Relative strains to the lattice spacing of the applied stress of 50MPa were determined from equations (1) and (2) using wavelength of neutron of 0.20868nm; d_0 is the lattice spacing on applied stress of 50MPa. Figure 1 shows the relative stress-strain diagram to 50MPa applied stress for each lattice planes. Young's modulus and Poisson's ratio for Ni(100), Ni(200) and Ni(220), respectively, are 246GPa, 0.094, 162GPa, 0.163 and 213MPa, 0.378 as shown Table 2.

Table 1: Chemical composition of NCF600 (wt%)

	C	Si	Mn	P
NCF600	≤0.15	≤0.50	≤1.00	≤0.030
	Cr	Fe	Cu	Ni
≤0.015	14.00-17.00	6.00-10.00	≤0.50	Bal.

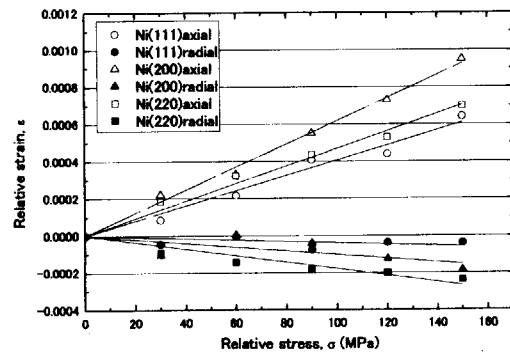


Figure 1: Stress-strain diagram for Ni(111), (200) and (220).

Table 2: Results of elastic constants measurement

	Young's modulus	Poisson's ratio
Ni(111)	246GPa	0.094
Ni(200)	162GPa	0.163
Ni(220)	213GPa	0.378

2.6.2 Development of New Stress Measurement Method Using Neutron Diffraction

H. Suzuki, A. Moriai, N. Minakawa¹ and Y. Morii

Neutron Science Research Center, JAERI, Tokai, Ibaraki 319-1195

¹Advanced Machine Factory Ltd., Hitach, Ibaraki 319-1231

Neutron stress measurement method can determine the stress states by measuring the lattice strains in three orthogonal directions. In the conventional method, it is required to measure the lattice strains of the same diffraction family in all three directions. However, it is possibly difficult to measure the lattice strains of the same diffraction family in all three directions on the textured materials, and it is also possibly difficult to measure the lattice strains in all three orthogonal directions due to some reasons such as the size and the shape of the samples, etc. Furthermore, it is required to obtain the stress free lattice spacing d_0 in order to determine the residual stresses, so that the accuracy of the stress measurement depends on the accuracy of d_0 measured using the powder sample or the annealed sample. Therefore, it is very important to establish the high-versatility stress measurement method which can measure the stress states accurately under the various conditions or for the various objects.

Equation (1) shows the general formula for calculating the residual stress states in neutron diffraction technique. In conventional method, measured lattice strains in three orthogonal directions are submitted to eq.(1) and the residual stress states can be obtained by making a least square method. However, if we use this conventional principle, the tri-axial stress states can be obtained by observing the lattice strains of two or more kinds of diffraction family in only two orthogonal directions.

$$\varepsilon_{ii} = \frac{1}{E_{hkl}} \{ (1 + \nu_{hkl}) \sigma_{ii} - \nu_{hkl} (\sigma_{11} + \sigma_{22} + \sigma_{33}) \} \quad (1)$$

This proposed method was applied to evaluate the stress states of the Ni-base alloy NCF600 loaded in-situ. Measured diffraction planes were three kinds of diffraction family such as Ni{111}, Ni{200}, and Ni{220}. Changes in measured stresses almost agreed with theoretical changes within 10 MPa error. Therefore, this proposed method can determine the relative stress states accurately by observing the lattice strains in two orthogonal directions. However, if we measure the residual stress states using this method, it is required to know the stress-free lattice parameter. Therefore, stress measurement accuracy was affected by the accuracy of d_0 measured using reference samples.

Equation (2) shows the principle of the stress measurement method without using measured stress-free

lattice constant a . It is possible to obtain the lattice constant and the tri-axial residual stresses by observing the lattice spacings of two or more kinds of diffraction family in two or three orthogonal directions.

$$d_{ii} \sqrt{h^2 + k^2 + l^2} = \frac{a}{E_{hkl}} \{ (1 + \nu_{hkl}) \sigma_{ii} - \nu_{hkl} (\sigma_{11} + \sigma_{22} + \sigma_{33}) \} + a \quad (2)$$

We tried to apply this new method, which can determine the residual stress states without using measured d_0 , to uniaxial applied stress measurement of NCF600. Figure 1 shows the changes in lattice constant and stress states related to the applied stresses. The lattice constant a was almost constant without dependent of applied stresses, and the average value of it was about $3.5639 \pm 0.0001 \text{ \AA}$ which almost agreed with the lattice constant ($3.5623 \pm 0.0003 \text{ \AA}$) of annealed sample with 0.0016 \AA error. On the other hand, the tendency of changes in stress states evaluated using proposed method coincided with theoretical change. Therefore, it is expected that this proposed method will be one of the method which can solve the problems in conventional method.

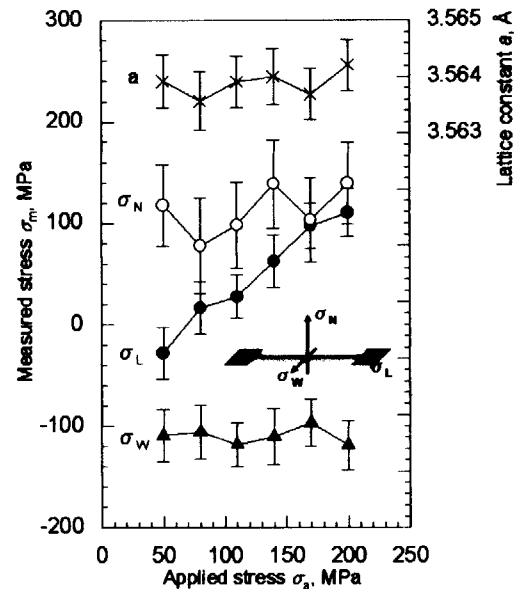


Figure 1: Changes in each stress component and lattice constant.

2.6.3 Strain Measurement of $\text{Al}_2\text{O}_3/\text{YAG}$ binary MGC by Neutron diffraction

H. Suzuki, Y. Waku¹, A. Moriai, N. Minakawa² and Y. Morii

Neutron Science Research Center, JAERI, Tokai, Ibaraki 319-1195

¹UBE Industries, Ltd., Ube, Yamaguchi, 755-8633

²Advanced Machine Factory Ltd., Hitach, Ibaraki 319-1231

Engines or turbines are required the operation at higher temperature to improve thermal efficiency. For this purpose, it is necessary to develop a material which remains stable at very high temperature such as more than 1973 K. An $\text{Al}_2\text{O}_3\text{-Y}_3\text{Al}_5\text{O}_{12}$ (YAG) eutectic material has been recently fabricated by melting and unidirectional solidification of raw material oxides using a eutectic reaction to control precisely the crystal growth.¹⁾ Such kind of composite material is called melt growth composite (MGC). $\text{Al}_2\text{O}_3/\text{YAG}$ -MGC consists of single crystal of both Al_2O_3 and YAG, and they are continuously connected and finely entangled in three-dimensions without grain boundaries. However, since thermal expansion coefficient differs in both phases, residual stresses are generated by mismatch between two phases, and it may affect the fracture mechanism and mechanical properties of the MGCs. In the present study, residual stresses in each phase of $\text{Al}_2\text{O}_3/\text{YAG}$ -MGC were measured by using neutron diffraction.

Powder diffraction of $\text{Al}_2\text{O}_3/\text{YAG}$ -MGC was measured using REsidual Stress Analysis (RESA) at JRR-3 in order to obtain a lattice constant in stress-free condition and to confirm the consisted phases. Figure 1 shows the result of the peak fitting of powder diffraction using REITAN-2000.²⁾ It was confirmed that the measured diffraction pattern was fitted well with the calculated pattern, and that this MGC was consisted of two phases of Al_2O_3 and YAG. The lattice constants of each phase were shown as below.

Al_2O_3 : $a=4.7587\pm0.0002$ Å, $c=12.9923\pm0.0005$ Å.

YAG: $a=12.0055\pm0.0003$ Å.

The lattice strains were measured in each phase of the MGC specimen with the size of 4 mm width, 3 mm thickness, and 40 mm length. Before measuring the lattice strains, the pole figure and the rocking curve were measured in some diffraction. As a result of pole figure measurement, it was confirmed that all phases were single crystal. On the other hand, the full wide half maximum of the rocking curve was approximately 1 deg to 2 deg, so that the crystallinity of MGC was comparatively low.

Table 1 shows the lattice strains in each phase of MGC. Lattice strains of some kinds of diffraction family such as YAG{532}, YAG{611}, YAG{400}, and $\text{Al}_2\text{O}_3\{113\}$ were measured. Negative and positive strains correspond to compressive and tensile strains,

respectively. As a result of strain measurement, it was confirmed that both of the tensile and compressive residual strains were observed in YAG phase, and the compressive residual strains existed in Al_2O_3 phase. In this study, Cd slit with aperture of 10mm width and 15mm height was utilized, so that measured lattice strains were average strain in the whole sample. Since the stress distributions in the composite materials are complex, it is very important to evaluate accurate stress distributions in MGC. Therefore, it is required to measure the lattice strains using the slit with small aperture of 1 mm \times 1 mm in order to clarify the residual stress distributions in $\text{Al}_2\text{O}_3/\text{YAG}$ -MGC.

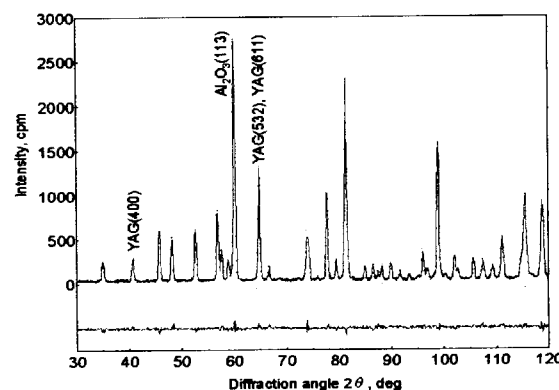


Figure 1: Diffraction pattern of $\text{Al}_2\text{O}_3/\text{YAG}$ -MGC, and the result of fitting between measured and calculated patterns using REITAN-2000.

Table 1: Lattice strains of each phase in $\text{Al}_2\text{O}_3/\text{YAG}$ -MGC

	Lattice strain
YAG(352)	0.00007 ± 0.00004
YAG(253)	-0.00031 ± 0.00004
YAG(611)	0.00020 ± 0.00004
YAG(400)	-0.00033 ± 0.00005
$\text{Al}_2\text{O}_3(2\bar{1}3)$	-0.00046 ± 0.00006
$\text{Al}_2\text{O}_3(113)$	-0.00048 ± 0.00007

References

- 1) Y. Waku *et al.*, Nature, Vol. 389, No.6646, Sep. (1997) 49.
- 2) F. Izumi and T. Ikeda, Mater. Sci. Forum, 321-324 (2000) 198.

2.6.4 Phase Transformation at Crack Tip of Shape Memory Alloy TiNi

Y. AKINIWA, H. KIMURA, K. TANAKA, N. MINAKAWA¹ and Y. MORII¹

Department of Mechanical Science and Engineering, Nagoya University, Nagoya 464-8306

¹*Advanced Science Research Center, JAERI, Tokai, Ibaraki 319-1195*

1. Introduction

The equiatomic TiNi alloy is an intermetallic compound that shows not only excellent resistance against corrosion and wear but also shape memory effect with large recovery strain and superelasticity. Though TiNi has been used for pipe couplings and the frames of glasses utilizing the shape memory effect and superelastic property¹⁾, the practical application is limited because the fatigue properties of TiNi has not been fully clarified. In addition to the conventional use, TiNi has attracted attention as an actuator of intelligent structure in recent years and the fatigue reliability over long-term use has been recognized as an important subject in the utilization²⁾. In order to evaluate the fatigue properties, it is necessary to understand the martensitic transformation at a crack tip because the stress-induced martensitic phase plays an important role to improve the fatigue property. Judging from the past experiments by the authors, the distribution of the stress-induced martensitic transformation at a crack tip differs depending on whether the area is plane stress or plane strain. This implies that the stress condition, as well as the stress intensity factor, must be considered for the fatigue design of this material. Neutron diffraction measurement is believed to be the most suitable method to measure the martensitic transformation in plane strain condition. In this study, stress-induced martensitic transformation at a crack tip was investigated in shape memory TiNi. The cracked specimen was utilized for the measurement by neutron diffraction in order to clarify the martensitic transformation at a crack tip.

2. Material and measurement

Shape memory TiNi was heated to 450 degrees Celsius in order to introduce shape memory effect at room temperature before the neutron diffraction measurement. It is mainly composed of austenitic phase at room temperature of approximately 25 degrees Celsius without loading. A specimen in the dimension of 10 x 70 x 6 mm³ were prepared by electrical discharge machining followed by electrolytic polishing. Due to the thickness, most of neutron diffraction is considered to be obtained from the inner part in plane strain condition. A fatigue crack was introduced from a notch in the middle of the specimen. The neutron facility of JAERI (RESA) was used for the neutron diffraction measurement. The width of the incident beam was

0.5 mm with the preset time of 1800 sec. The wave length of the beam was 0.21009 nm. The diffraction plane of (102) was employed for the measurement of the stress-induced martensitic phase at the crack tip. The measurement was conducted under the uniaxial load of 35 N.

3. Martensitic Transformation at Crack Tip

The results of the neutron diffraction at $x = -500, 0, 500, 1000, 1500, 2000, 2500, 3000, 4000, 5500$ micrometer, where crack tip is at $x = 0$ and crack propagation direction is along x axis, show that the diffraction intensity drops at $x = 1500$. Therefore, the distribution of the stress-induced martensitic transformation is expected to stretch about 1200 micrometer ahead of the crack tip under the applied stress intensity factor. The residual martensitic phase was also observed at the crack wake, which is believed to affect the crack closure. The results of the nano-indentation on the surface in plane stress show that the martensitic phase stretches several times larger than the present result. The suppression of the stretch of the martensitic phase at the crack tip is expected to result from the triaxiality of the stress at crack tip and the negative volume change from the austenitic to martensitic phase in TiNi.

4. Conclusion

The distribution of martensitic phase at a crack tip was measured in plane strain condition by neutron diffraction measurement. The area of the martensitic phase was found to be smaller than that in plane stress condition. However, the existence of the martensitic phase was confirmed in plane strain condition in contrast to some expectation by other researchers that it rarely exists. The results show that the stress conditions such as the thickness of a structural component must be taken into account for the fatigue design of shape memory TiNi in addition to the stress intensity factor. Further investigation is necessary for the quantitative analysis by the combination of neutron diffraction measurement for plane strain condition and atomic force microscopy on the surface for plane stress condition.

References

- 1) H. Sakamoto: Trans. Jpn. Inst. Met. **24** (1983) p. 665.
- 2) H. Tobushi: J. of JSTP **35-403** (1994) p. 910.

2.6.5 Estimation of change in texture by restoration of a ferrite steel after large strain deformation

T. Suzuki, Y. Tomota, M. Uno, A. Moriai¹, T. Kamiyama², H. Tashiro³*Faculty of eng, Ibaraki Univ., Hitachi, Ibaraki 316-8511*¹*JAERI, Tokai, Ibaraki 319-1195*²*KEK, Tsukuba, Ibaraki 305-0801*³*Nippon Steel Co. Kamaishi, Iwate 026-8567***1. Introduction**

When a ferrite steel is subjected to extremely heavy drawing, microstructure becomes nano-sized. It has been proposed that "continuous recrystallization" occurs by heavy plastic deformation¹⁾. Here, texture change by annealing was investigated in order to estimate the restoration process of drawn ferrite steels.

2. Experimental Procedures

A ferrite steel with the chemical compositions of 0.008C, 0.01Si and 0.13Mn was hot-forged to a bar with 5.5 mm diameter and then drawn by true strains of 2.0(2.0mm) to 6.6 (0.2mm) at the Kamaishi work of Nippon Steel Co.. The specimens were annealed at several temperatures between 373 and 1073K for 3.6 ks in vacuum. Neutron diffraction was performed at JAERI to measure the texture.

3. Results and Discussion

Figure 1 shows the texture change with annealing. The intensity of pole density at the center of 110 pole figure changes by the annealing temperature in the specimen drawn by 2.0 mm. This result suggests the change in crystal orientation occurred by recrystallization. On the other hand, the maximum intensity of pole figure hardly changed by annealing temperature in the case of the specimen drawn by 0.2 mm. It is considered that the texture evolved by sever drawing is succeeded to the annealed structure.

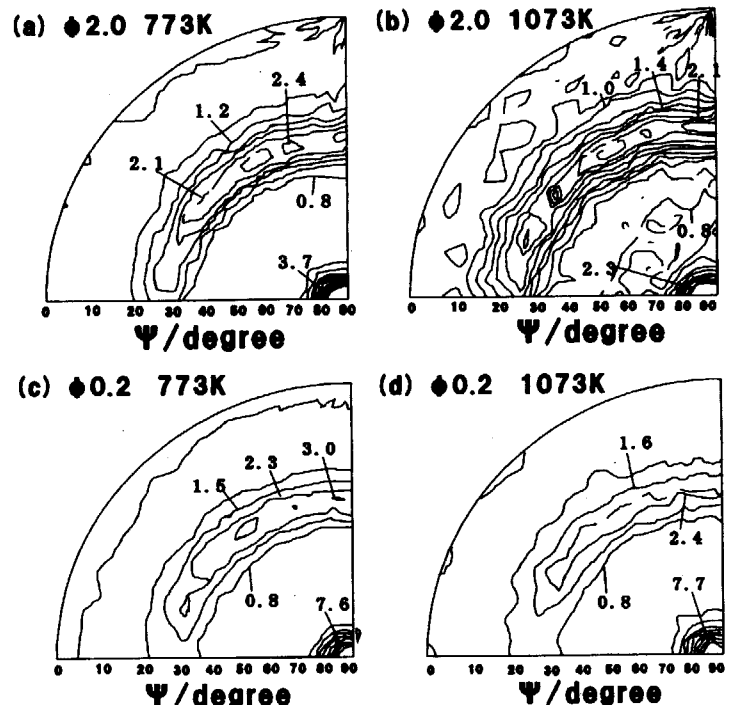


Figure 1: (110) pole figures of drawn ferrite steel annealed at (a), (c) 773K and (b), (d) 1073K for 3.6ks measured by neutron diffraction.

References

- 1) N. R. Tao, Z. B. Wang, W. P. Tong, M. L. Sui, J. Lu and K. Lu: *Acta mater.*, 50(2002), pp. 4603-4616.

2.6.6 Residual stress measurement using neutron diffraction for a quenched steel bar with induction heating

H. Tokuda^{*1}, Y. Tomota^{*2}, T. Suzuki^{*3}, K. Kawasaki^{*4}, A. Moriai^{*5}, N. Minakawa^{*5} and Y. Morii^{*5}

^{*1} Graduate student of Ibaraki University, Hitachi, Ibaraki 316-8511

^{*2} Graduate School of Science and Engineering, Ibaraki University, Hitachi, Ibaraki 316-8511

^{*3} Faculty of Engineering, Ibaraki University, Hitachi, Ibaraki 316-8511

^{*4} Neturen Co. Ltd., Hiratsuka, Kanagawa 254-0013

^{*5} Neutron Science Research Center, JAERI, Tokai, Ibaraki 319-1195

1. Introduction

Neutron diffraction enables us to know the stress condition inside a bulky specimen, which cannot do it by other alternative method. However, several problems were found to be improved. In this study, the residual stress of a quenched SCM440 steel bar with induction heating was examined by neutron diffraction.

2. Experimental procedures

A commercially available low alloyed steel with the chemical compositions of 0.42C, 0.20Si, 0.78Mn, 0.020P, 0.011S, 0.05Ni, 1.05Cr, 0.04Cu, 0.16Mo, 0.005V in mass % was used. A round bar shown in Fig. 1 was prepared and rapidly induction-heated followed by water quenching. Then, the elastic strains remained were measured by a conventional X-ray method and neutron diffraction using a diffractometer for residual stress measurement (RESA) at JAERI, where the stress free lattice spacing was determined by the measurements for tiny coupons.

3. Results

A good agreement was found between the results obtained by the present method and those by the conventional X-ray $\sin^2\Psi$ method with a serial polishing technique where three dimensional stresses were estimated from the plane-stress data obtained. There are however several improvements for the neutron stress measurement. In particular, the measurement for a specimen with gradient microstructure change like the present material requires the preparation of small coupons and small gauge measuring volume.

The full paper of this study will appear in the journal of ISIJ (Tetsu to Hagane: accepted for publication).

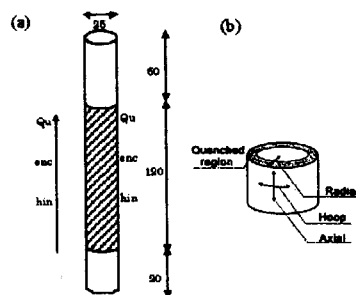


Figure 1: Geometry of a specimen quenched after induction heating (a) and definition of stress directions (b).

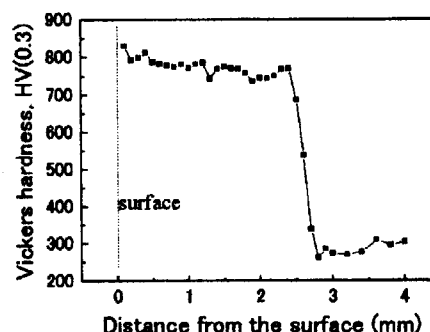


Figure 2: Hardness distribution in the cross section of the round bar specimen.

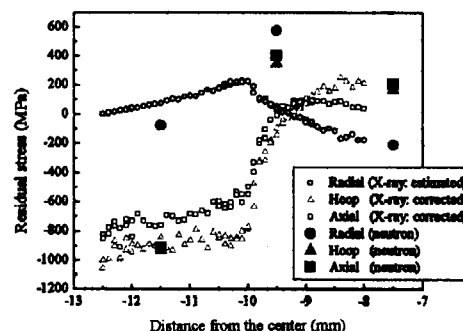


Figure 3: Residual stresses measured by the neutron and X-ray methods as a function of distance from the center of the specimen.

2.6.7 Distribution of the martensite of induction hardened S45C round bar observed by small angle neutron scattering

K. Inoue, K. Aizawa¹, A. Moriai¹ and F. Ikuta²

Faculty of Science and Technology, Ryukoku University, Seta, Otsu 520-2194

¹Neutron Scattering Research Group, JAERI, Tokai, Ibaraki 319-1195

²Neturen Co., Ltd., Tamura, Hiratsuka 254-0013, Japan

Induction hardening at the surface of carbon steel is usually used for industrial purpose because it extremely improves the mechanical properties of the surface, such as the wear resistance and the fatigue resistance. The hardening is accompanied by a martensitic transformation at the surface.¹⁾ The photographs of the induction hardened round bar and of the sliced specimen cut from the center of the bar are shown in Fig. 1. For sliced specimen, we can distinguish the martensitic region from the coexistent region of pearlite and ferrite as a contrast.

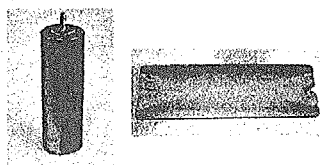


Figure 1: Photographs of the induction hardened round bar and the sliced specimen cut from the round bar.

The SEM images at each position along the central line of the sliced specimen, which corresponds to radial position on the central sectional plane of round bar, are shown in Fig. 2. We obviously see the change of the image as moving from the surface to the center. This change shows that martensite at the surface gradually change to the coexistent state of pearlite and ferrite as approaching to the center.

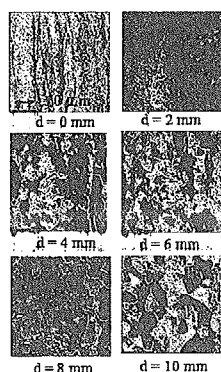


Figure 2: SEM image of the induction hardened S45C at each radial position on the central sectional plane of round bar. "d" means the distance from the surface.

To investigate the volume fraction of the martensite at each position on the center line parallel to the short side of the sliced specimen, we observed a small angle neutron scattering. SANS-J at JRR-3M was used. We covered q -range from 0.03 to 1.9 (nm^{-1}), by using the length, L , of 10 m and 1.5 m, where L means the length from the sample to the detector. The wavelength of the beam was 0.679 nm, and the resolution (FWHM) was 10.33 %. The transmitted beam was very weak. This is partly because the sliced specimen has a thickness of 1mm, and partly because there exist the void, impurity and so on in the sample as it is one of the industrial utility goods. Q -dependence of the scattered beam is shown in Fig. 3.

We see that the intensity changes abruptly at around the position of 6 mm from the surface. The fact is consistent with the change of the contrast in the photograph of the sliced specimen. We have a plan to make a measurement with more thin plate, to avoid the multiple scattering. By using the Guinie plot, we will get the information about the size and the form of the martensite.

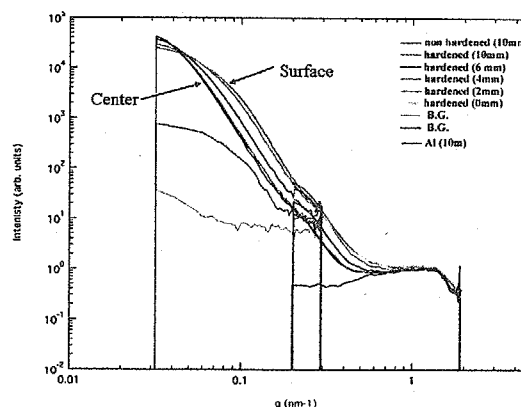


Figure 3: Q -dependence of the intensity of small angle scattered neutron beam.

References

- 1) K. Inoue, M. Sugimoto, N. Minakawa, A. Moriai, et al.: *Proceedings of International Conference on Advanced Technology in Experimental Mechanics, Nagoya, 2003*, published by The Japan Society of Mechanical Engineers. Paper No. OS04W0182. (CD edition, 6 pages).

2.6.8 A Challenge to d_0 -Disused Neutron Stress Measurement Using Area Detector

T. Sasaki¹, Y. Morii², N. Minakawa², N. Niimura² and Y. Hirose¹

¹Department of Materials Science and Engineering, Kanazawa University, Kanazawa, Ishikawa 920-1192

²Advanced Science Research Center, JAERI, Tokai, Ibaraki 319-1195

The aim of our study is to improve a method for determining stress inside materials with an area detector. The use of an area detector for the stress measurement can bring about an efficient use of diffraction data from the irradiated material. For example, we can obtain 360 strains from one measurement with our present measurement technique. Though the direction of each strain is limited by the diffraction condition, there is a lot of merits in the use of an area detector. What is particularly important is the fact that we do not need a precise value of the lattice spacing in stress free state (d_0) at the process that stress and strain are converted from the diffraction data. This strong point owes to the adoption of the principle of the stress analysis which is called the $\cos\alpha$ method.

Since the $\cos\alpha$ method has been firstly developed as only for the X-ray diffraction method, it is fundamentally not adequate to use it for the neutron diffraction data. However, the result of the application of the $\cos\alpha$ method to the neutron diffraction data performed by us showed a simple relation, that is to say, a one-to-one correspondence to the mechanical condition of the material such as the applied stresses. Moreover, the $\cos\alpha$ method can provide precise stresses through a simple data correction in which the raw diffraction data are subtracted by those that were obtained from the material treated by the stress-relief process.

All what mentioned above are the conclusions found from our first experiment¹⁾, in which the thickness of the specimen was 5 mm. In order to increase the degree of the practical usefulness of the method, it should also be valid to wider range of the thickness of the materials. Therefore, we planned the second experiment to examine the relation between the stresses that are output by the $\cos\alpha$ method and those that exist in the material when the thickness of the material varies. The range of the specimen's thickness adopted in this experiment was from 1 mm to 20 mm. This report describes about its outline. The similar experimental conditions were adopted in the present experiment. Figure 1 shows the schematic of the optics which was used in the experiment.

Figure 2 shows the misfit stresses, which were calculated using the $\cos\alpha$ method, with respect to the thickness of the specimen. The applied stress in each sample was 0 MPa. Though the residual stress might be one of the causes which contribute to the misfit

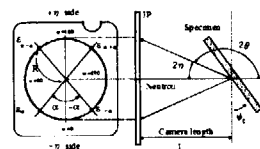


Figure 1: Experimental optics used in the experiment.

stress, the possibility would be low considering the heat treatment for the stress relief as well as the deep sampling volume due to the large penetration depth of the neutron beam. Based on our computer simulation, the misfit stresses are generated by the dependency of the shapes of the diffraction profiles on the position of the Debye-Scherrer ring. The dotted line in the figure 2 indicates the result of the computer simulation. The true line denotes the relation in case of the use of the centroid method. They are in good agreement to the experimental data. It was also found from the computer simulation that the stresses of the $\cos\alpha$ method show one-to-one relation to the applied stresses in the material with the slope of 1.0 for every thickness that we examined. This means that the $\cos\alpha$ method is valid for determining the mean stress in the gauge volume in the material even for the neutron diffraction data. The most valuable advantage of the $\cos\alpha$ method in the neutron stress measurement is that the stress can be obtained without a high accuracy. It will contribute greatly to the promotion of the neutron experiment in industry.

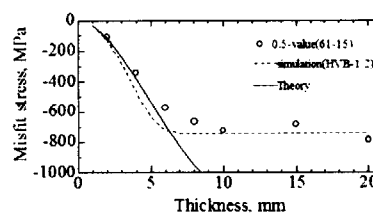


Figure 2: Experimental result on misfit stress.

References

- 1) T. Sasaki, N. Minakawa, Y. Morii, N. Niimura and Y. Hirose, Transactions of The Japan Society of Mechanical Engineers, vol.69, No.688, pp.1711-1716, 2003.

2.6.9 Evaluation of strength in overlaid materials by neutron diffraction

T. Ishikawa, K. Miyata, H. Yano, R. Ishikawa, Y. Morii¹, A. Moriai¹ and N. Minakawa¹

Hitachi-Engineering Co., Ltd. Hitachi, Ibaraki 317-0073

¹*Advanced Science Research Center, JAERI, Tokai, Ibaraki 319-1195*

Residual stress measurement inside a machine structure is important when evaluating crack progress etc. In a welding material, the stress near the welding boundary and the strength evaluation are important. We measured the residual stress by neutron diffraction, about a boundary of overlaid Nickel base alloy and Low alloy steel. The technical problem with this measurement is that diffraction might become irregular, because the Nickel base alloy of the weld metal has texture. Also, diffraction might become an interference at the boundary of a different metal. Therefore, another purpose of this measurement was to confirm this.

Figure 1 shows the form of a specimen. This specimen was Heat-treated at 621 °C for 24 hours at the size of 200 × 200 × 60 mm, and cut into the shown size after that. The release stress from cutting was 50 MPa or less, as a result of measuring with a strain gauge.

The RESA neutron wavelength used was 0.20858 nm. The slit width and height used was 3mm. The measurement of Young's modulus and Poisson's ratio were (111)(200) of Nickel base alloy, and (110) (200) of Low alloy steel. But, the (111) diffraction of the Nickel base alloy became irregular due to its texture. And the (200) diffraction intensity of the Low alloy steel was weak, because the neutron pass length was long. Consequently in the stress analysis the Nickel base alloy was measured at(200), and the Low alloy steel was measured at (110).

Figure 2 shows the residual stress distribution around the boundary of an overlaid weld and base metal. The residual stress of the overlaid boundary was tension from 200 to 300 MPa in the X and Y direction.

This data will be used as fundamental evaluation data of crack progress and strength.

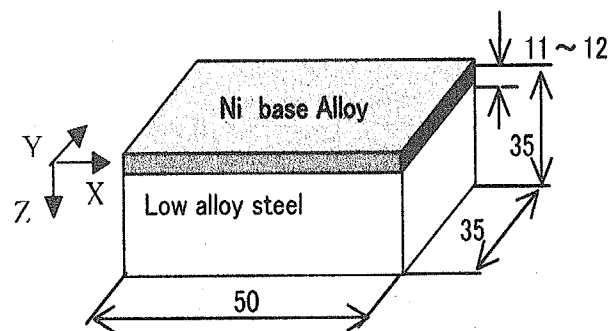


Figure 1: Geometry and dimensions of Overlaid Material specimen.

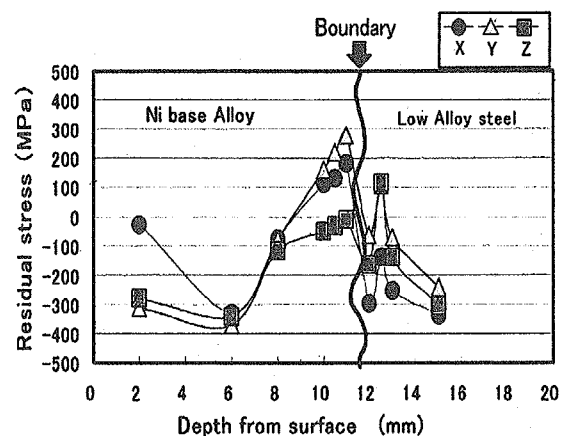


Figure 2: Residual stress distribution around the boundary of Overlaid weld and base metal.

2.6.10 Residual Strain Measurements in 3-axial Directions for 2-dimensional Cylindrical Carbon-Carbon Composite by Neutron Diffraction Method

S. Baba, N. Minakawa¹, A. Moriai¹, M. Yamaji and M. Ishihara

Department of Advanced Nuclear Heat Technology, JAERI, Oarai, Ibaraki 311-1394

¹*Department of Advanced Science Research Center, JAERI, Tokai, Ibaraki 319-1195*

The carbon fiber reinforced carbon matrix composite (c/c composite) is thought to be one of the advanced heat resistant materials in the nuclear engineering field. However, a lot of cracks are observed in manufacturing process of the ring type c/c composite due to the delamination between the fiber and the matrix by the residual stress. This is because of the different shrinkage between the fiber and the matrix during carbonization and graphitization heat treatment. The aim of the present study is to clarify the residual strain occurring in the c/c composite to improve the manufacturing process. The residual strain was measured by neutron diffraction method using the RESA (Residual Stress Analysis for neutron diffraction) in the JRR-3M (Japan Research Reactor-No.3 Modified) of JAERI. Cylindrical c/c composite after the first baking process was used in the experiment. First, the precise wavelength of neutron diffraction was determined using the standard silicon (Si) powder, National Bureau of Standards (NBS). Moreover, the most suitable line for lattice spacing of strain-free materials (d_0) was determined by grinding c/c composite powder. The measured d_{002} diffraction intensity of the c/c composite sample showed the peak with the shoulder in the low angle site, and the intensity of the peak appears respectively at higher position with narrow width for well-graphitized parts and at lower position with wide width for not well-graphitized parts. The residual strain in 3-axes directions (radial (Fig.1), hoop and axial) was measured by changed 002 diffraction angles. The 3-axes strains were also analyzed by FEM (Finite Element Method)(Fig.2). The results of analysis by FEM that supposed the complete connection condition of the fiber and matrix are not agree with the value of measurement the strains by neutron diffraction method. Future study has necessary to carry out the analysis with precise conditions.

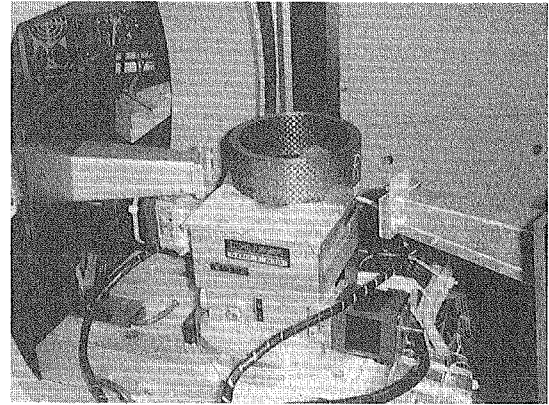


Figure 1: Set up sample on goniometer for r-direction.

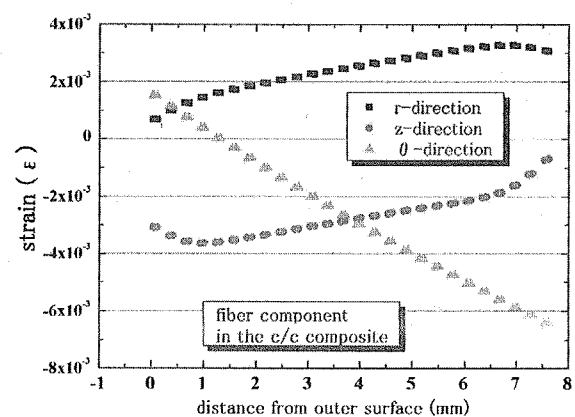


Figure 2: Estimation of 3-axial strains by FEM.

2.6.11 Distribution of the martensite of induction hardened S45C round bar observed by very small angle neutron scattering apparatus PNO

K. Inoue, T. Hirayama, K. Aizawa¹, A. Moriai¹ and F. Ikuta²

Faculty of Science and Technology, Ryukoku University, Seta, Otsu 520-2194

¹Neutron Scattering Research Group, JAERI, Tokai, Ibaraki 319-1195

²Neturen Co., Ltd., Tamura, Hiratsuka 254-0013, Japan

To improve the mechanical properties, such as the wear resistance and the fatigue resistance of the industrial carbon steel, we usually make an induction hardening at the surface of the material. The hardening is accompanied by a martensitic transformation. The volume fractions of martensitic phase alter gradually according to the depth from the surface.¹⁾

To get the information about the size and the form of the martensite at each position of an induction hardened S45C round bar, we have made a very small angle neutron scattering using PNO at JRR-3M. The wave length was 0.2 nm. It covered the q -range from -0.07 to 0.07 nm^{-1} .

The diameter of the round bar was 20 mm and the height was 40 mm. For the present experiment, we prepared the 1 mm thick sliced specimen cut from the center of the bar. The detail about the sample and the experiment done by SANS-J are written in another paper written by the same authors in this Progress Report.

The q -dependence of the transmitted beam at each position of the sliced specimen is shown in Fig.1. The

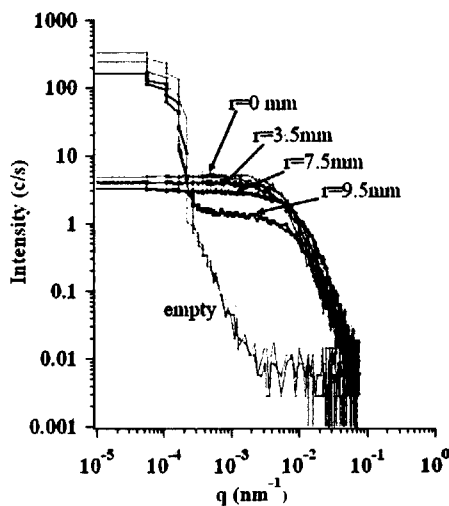


Figure 1: Q -dependence of the intensity of the transmitted beam. The letter, r , means the position on the sliced specimen, corresponding to the radius of the central sectional plane of the round bar.

transmitted beams from the center of the sliced spec-

imen of the hardened round bar and of the non hardened round bar are shown in Fig. 2. In Fig. 2 the difference between two cases is not observed. This suggests that induction hardening does not reach to the center.

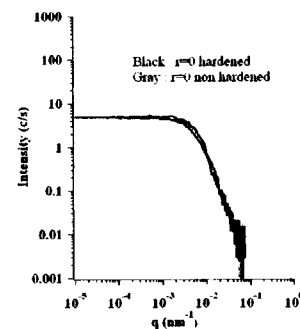


Figure 2: Q -dependence of the intensity of the transmitted beam from the center of hardened round bar and from that of non hardened one.

In Fig. 1, at $r=9.5 \text{ mm}$, the abrupt increase of the intensity below $q=3 \times 10^{-4} \text{ nm}^{-1}$ is observed. This fact indicates that the beam was slightly off from the edge of the sample. When we neglect this abrupt increase, we see that the intensity at the plateau becomes relatively low in case of $r=9.5 \text{ mm}$. This will be due to the existence of the martensite at the surface of the round bar. The intensity of this plateau gradually increases as we leave from the surface of the round bar. In every case, the intensity begins to decrease above $q=10^{-2} \text{ nm}^{-1}$. The slope of the curve is nearly q^{-4} at the center ($r=0$). It becomes closer to q^{-3} as we approach to the surface ($r=9.5 \text{ mm}$).

We have a plan to connect the data obtained by PNO to the data obtained by SANS-J. Because SANS-J covers the q range from 0.03 to 1.9, we will obtain the data with wide q -range from $q=0$ to $q=1.9$. By fitting to the Guinier plot, we will get the information about the size and the form of the martensite.

References

- 1) K. Inoue, M. Sugimoto, N. Minakawa, A. Moriai, et al.: *Proceedings of International Conference on Advanced Technology in Experimental Mechanics, Nagoya, 2003*, published by The Japan Society of Mechanical Engineers. Paper No. OS04W0182. (CD edition, 6 pages).

2.6.12 Non-destructive Measurement of Residual Stress Beneath the Surface of Laser Peened Steel

K. Akita, Y. Sano¹, T. Kubo¹, S. Ohya, H. Suzuki² and A. Moriai²

Department of Mechanical Systems Engineering, Musashi Institute of Technology, Tokyo 158-8557

¹ *Power and Industrial Systems Research and Development Center, Toshiba Corporation, Yokohama 235-8523*

² *Neutron Science Research Center, JAERI, Tokai, Ibaraki 319-1195*

Laser peening process is one kind of surface treatment technology using a mechanical interaction between the surface of a metallic material and the plasma induced by the irradiation of a nanoseconds-order laser pulse. The laser peening introduces compressive residual stress in surface layer, and it is effective for the improvement of fatigue strength, the corrosion resistance[1], and the prevention of stress corrosion cracking (SCC)[2]. The laser peening, therefore, has been applied to reactor core shrouds of nuclear power plants to prevent SCC.

Non-destructive measurement of the residual stress near the laser peened surface is important to understand the generation mechanism of the residual stress on laser peening. And the residual stress on inside wall of pipe welds is important to evaluate the integrity of components in nuclear reactors. However the both experiments have not been performed.

As the first stage of this study, non-destructive measurements of depth profile of residual stress near the laser peened surface was performed using neutron diffraction.

The material used for this study was a high tensile strength steel, HT1000. The size of the specimen was 40mm×40mm with the thickness of 15 mm. The HT1000 specimen was annealed by furnace cooling after keeping at 973 K for 3 hours for removing residual stress caused by machining. The fundamental wave of a Q-switched Nd: YAG laser is frequency-doubled to a water penetrable wave ($\lambda=532$ nm) by a second harmonic generator with a nonlinear optical crystal. The pulse duration

is 8 ns in FWHM and the pulse frequency is 10 Hz. The specimen was driven to x- and y-directions in a water jacket during laser irradiation. The coverage C_v is defined as:

$$C_v = (\pi D^2/4) \times N_d, \quad (1)$$

where D is the diameter of laser spot ($\simeq 1$ mm), N_d is the irradiation density which is the average number of laser pulses irradiated in unit area. C_v for the specimen was 2827 %. Our laser peening process in this study did not use any coating materials such as black paint. The neutron diffractometer for residual stress measurements, RESA, in JRR-3M was used to measure the residual stresses. The measured diffraction plane was α -Fe 110. The wavelength was 2.086 Å. The diffraction angle 2θ was 62 deg. The gage volume was $0.5 \times 0.5 \times 15$ mm³. The acquisition time was 90 seconds.

It was found non-destructively that the compressive residual stress reached about 1 mm in depth from the specimen surface. The detailed distribution of residual stress beneath the surface will be measured in the next stage.

References

- 1) R. Fabbro, et al., J. Laser Applications, 10, 265 (1988)
- 2) Y. Sano, et al., Proc. 8th Int. Conf. on Nuclear Engineering (ICONE-8), Baltimore, Paper No. 8441 (2000)

2.6.13 Residual Stress Analysis of Metal/Ceramic Functionally Graded Materials

Mitsuhiro Hataya, Makoto Nakagawa, Takao Hanabusa, Kazuya Kusaka, Toshio Matsubara¹, Yukio Morii², Nobuaki Minakawa², Atsushi Moriai² and Hiroshi Suzuki²

Department of Mechanical Engineering, Tokushima University, Tokushima 770-8506

¹*Tokushima Prefectural Industrial Technology Center, Tokushima 770-8021*

²*JAERI, Tokai, Ibaraki 319-1195*

It is very difficult to join a metal and a ceramic film directly, because the difference in their coefficients of thermal expansion is so large that cracks may occur in the film or a delamination may occur in an interface. A functionally graded material (FGM) is usual to relax an abrupt change in mechanical and/or physical properties at an interface of joining.

We prepared the Fe/Al₂O₃ FGM consisting five layers from iron to Al₂O₃ by spark plasma sintering (SPS). Residual stresses in each layer of FGM were measured by RESA in order to investigate the best production condition of FGM.

Table 1 shows measurement condition of residual stress. Figure 1 shows residual stress distribution in FGM. Figure 2 shows an average internal residual stress distribution.

The following results were obtained from the residual stress measurement in FGM.

- Residual stresses in all parts of Fe were tensile and increased with decreasing the volume fraction of Fe.
- Residual stresses in all parts of Al₂O₃ were compression and increased with decreasing the volume fraction of Al₂O₃.
- The difference in an average internal stress was large in the part of Fe 20%- Al₂O₃ 80%.

Table 1: Conditions of residual stress measurement

Slit size (mm ²)	15(Width) × 2(Height)
Distance from sample to slits (mm)	50
Wave length (nm)	0.208022
Diffraction plane	Fe (110) Al ₂ O ₃ (116)

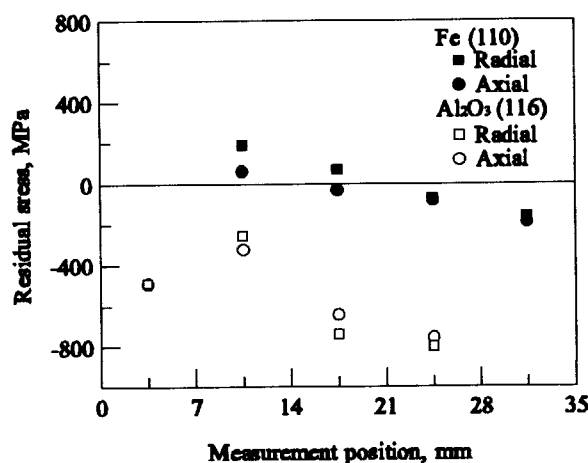


Figure 1: Residual stress distribution in FGM.

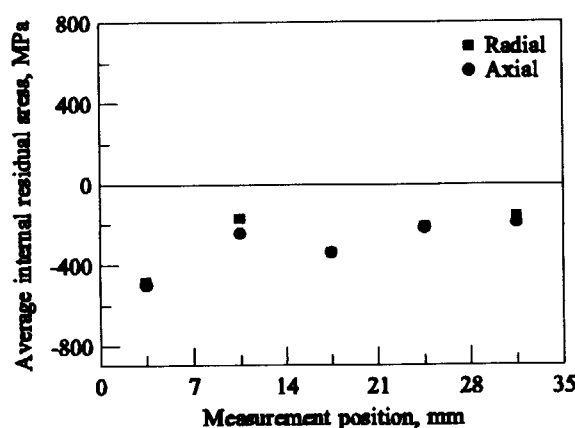


Figure 2: Average internal residual stresses (MPa).

2.6.14 Quality Estimation of Aluminum Die-casting by Neutron Diffraction

Mitsuhiro Hataya¹, Atsushi Moriai², Hiroshi Suzuki², Yukio Morii², Takao Hanabusa¹
and Nobuaki Minakawa³

¹Department of Mechanical Engineering, Tokushima University, Tokushima 770-8506

²JAERI, Tsukuba, Ibaraki 319-1195

³Advanced Machine Factory Ltd., Hitachi, Ibaraki 319-1222

In this research, we estimated quality of aluminum die-casting as a part of the application of neutron diffraction method to the industrial world. We measured residual strain in aluminum die-casting by using RESA in JRR-3. We prepared two kind of aluminum die-castings, good one and no-good one, were made by manufacturing cooperation. Their differences were distinguished with bending caused by differences of product conditions.

Figure 1 is diagram and measured positions of aluminum die-casting. Table 1 shows measurement condition of residual strain. Figure 2 shows residual strain distribution in aluminum die-casting.

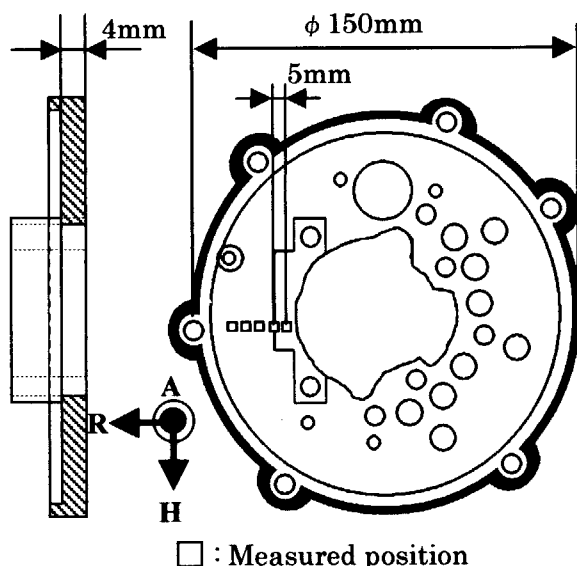


Figure 1: Diagram of aluminum die-casting.

Table 1: Conditions of strain distribution measurement

Slit size (mm)	15 (Width) × 2 (Height)
Distance from sample and slit (mm)	50
Wave length (nm)	0.2087459
Diffraction plane	Al (111), (220), (311)

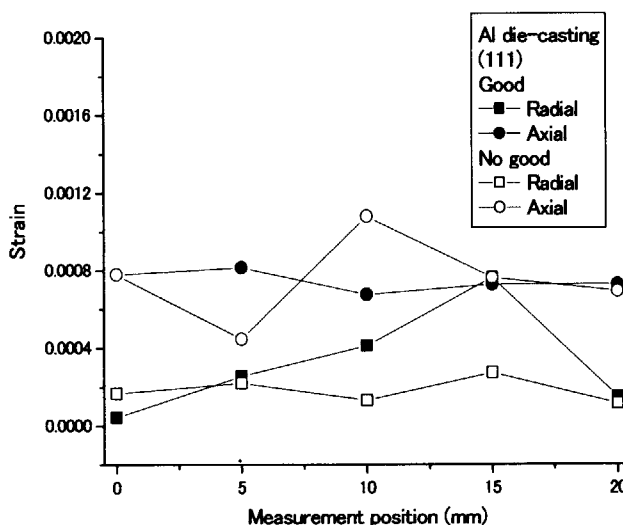


Figure 2: Strain distribution in Al die-casting.

We can see clearly difference of residual strain in aluminum die-casting between good one and no-good one from Fig.2. So, we could prove that we can estimate quality of industrial product by using neutron diffraction.

We can say from these results that neutron diffraction method is very useful for the industrial world.

2.6.15 Investigation of the residual stress measurement by the neutron scattering of an amorphous metal

Nobuaki Minakawa¹, Atushi Moriai², Hiroshi Suzuki², and Yukio Morii²

¹Advanced Machine Factory Ltd., Hitachi, Ibaraki 319-1222

²JAERI, Tokai, Ibaraki 319-1195

Outline

The tensile strength of an amorphous metal is the mighty value over 1000MPa, which attracts attention from industrial utilization. In order that to evaluate the soundness and life of parts and manufactured goods; these are indispensable to measure an internal stress. Amorphous material must expect performing a stress measurement on the basis of the waves by scattering, in order that a diffraction line is not obtained unlike general material (material with a crystal structure). Many amorphous researches were advanced, the key was expected on the basis of the structure, which an atomic density group makes, and the test measurement was performed in that there are many tentative theories. At first trial, the relation between a diffraction line when an amorphous metal alloy crystallizes, and the scattering wave of an amorphous metal was measured.

Measurement

We used the transition metal system four components alloy as an amorphous metal specimen.

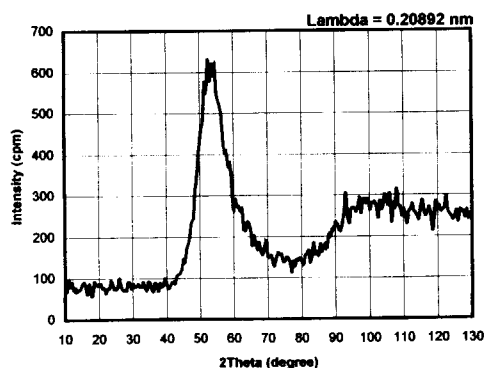


Figure 1: Neutron scattering of Amorphous.

The scattering measurement used by 0.20892nm, rotating phi axis using the neutron diffractometer for the residual stress analysis (RESA) installed in JRR-3. As a result is shown in Fig. 1. In order that temperature gradients are different, as for the terminal section of the same specimen, crystallization grows up. The scattering measurement was performed, rotating phi axis using the terminal section specimen. As a result is shown in Fig. 2.

Result

From the specimen in which crystallization proceeded, as shown in Fig. 2, diffraction lines were measured in the scattering waves. It understands that the crystallized specimen is BCC structure from the diffraction lines. The crystal lattice plane, which grows from the first wave, is (110) plane, and this result is congruous with the tentative theory relation for the atomic high density is generated from the first wave.

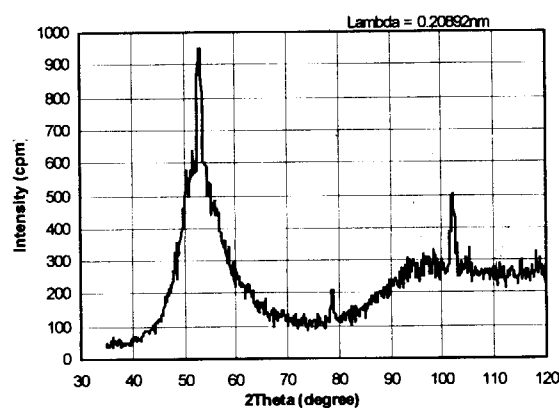


Figure 2: Neutron Diffraction of Amorphous.

This is a blank page.

2.7 Fundamental Physics

- Interferometry -

This is a blank page.

2.7.1 Development of high intensity ultracold neutron production with ortho-deuterium

M. Utsuro, M. Tanaka¹, K. Mishima², Y. Nagai, T. Shima, Y. Fukuda³, T. Kohmoto³, T. Momose⁴, A. Moriai⁵, K. Okumura⁶, H. Yoshino⁶

Research Center for Nuclear Physics, Osaka University

¹*Department of Sanitary Technology, Kobe Tokiwa College*

²*Graduate Course of Science, Osaka University*

³*Department of Physics, Faculty of Science, Kobe University*

⁴*Graduate Course of Science, Kyoto University*

⁵*Division of Research Reactor, Japan Atomic Energy Research Institute*

⁶*Research Reactor Institute, Kyoto University*

Ultracold neutrons (UCN) with the velocity of about 6 m/s are utilized in various kinds of fundamental physics experiments on neutrons. Ortho-deuterium molecules have much attractive properties as the UCN converter material¹⁾ lying in the rotational ground state at the low temperature below about 20 K. All of the solid deuterium (SD2)-UCN sources such as LANL and PSI projects are supposed as the SD2 converter to be inserted into high radiation fields directly coupled to pre-moderators. We have proposed²⁾ a new concept studied here of a single crystal UCN converter of ortho-deuterium at the exit of a cold neutron guide from a pulsed source, making us rid of the high radiation load problems.

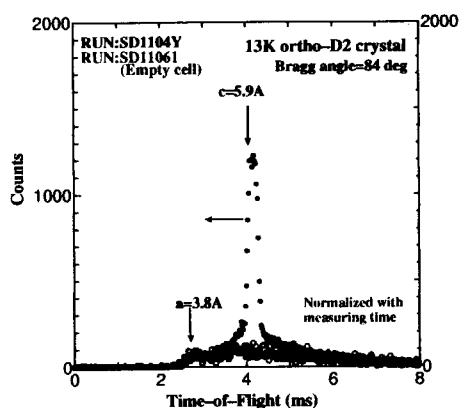


Figure 1: The measured results of the Bragg scattering experiment.

The high purity ortho-deuterium gas was prepared with the magnetic catalyser contained in an aluminum cartridge at the top of a two-stage helium refrigerator, then ortho-concentration of about 98% was attained³⁾. Our UCN converter of ortho-deuterium single crystal was prepared in the $2\text{cm}^W \times 6\text{cm}^H \times 3\text{cm}^D$ crystallizing cell in the refrigerator. The crystal orientation prepared was clearly identified with the Bragg scattering as shown in Fig.1, with the time-of-flight of the chopper-pulsed cold neutron beam at the exit of C2 guide tube, JRR-3M reactor, JAERI. Further, a pre-

liminary result of UCN production experiment is also shown in Fig.2, where the countrate in the UCN time region is in reasonable agreement with our expectation.

The present scheme applied to a high intensity pulsed neutron facility now under construction should provide the most intense UCN beam for possible joint uses of UCN.

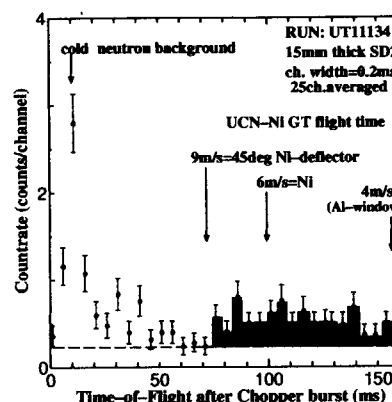


Figure 2: The measured results of the UCN production.

The present work was partially supported by the consigned research from JAERI as the "Reimei" research program in the fiscal year 2003. We especially thank to the experimental helps by Dr. Y. Aratono and Mr. K. Nakamura at the Tokai Research Establishment, JAERI.

The present refrigerator was kindly offered by the Iwatani Gas Company Ltd..

References

- 1) M. Utsuro and M. Hetzelt, Proc. of Internat. Con. on Inelastic Neutron Scattering (IAEA, Vienna, 1978) Vol.I, pp.67-75.
- 2) M. Utsuro et al., Internat. Con. on Precision Measurements with Slow Neutrons, held at the Nat. Inst. Science and Technol., Gaithersburg USA, April 2004.
- 3) K. Mishima, "Irradiation effect of ortho deuterium for UCN source", Doctoral dissertation, Osaka Univ.(2004).

This is a blank page.

2.8 Instrumentation and Methods

- Extreme Conditions, Beam Handling, Detectors and Data Treatments -

This is a blank page.

2.8.1 Development of the thermal neutron focusing device

T. Osakabe and K. Soyama¹*Advanced Science Research Center, JAERI, Tokai, Ibaraki 319-1195*¹*Neutron Science Research Center, JAERI, Tokai, Ibaraki 319-1195*

The neutron focusing is an indispensable technical element in the experiments under extreme condition, such as high pressure or high magnetic field with tiny samples. The best method for compensating weak signals from tiny samples is focusing the incident neutron beam on a sample position by supermirror reflection. We have developed the thermal neutron focusing device with a lot of curved supermirrors according to the proposal of D.F.R. Mildner¹⁾.

Figure 1 shows the photograph of the device installed in the triple-axis spectrometer TAS-1 (2G). The device is 400 mm long and has 18 sheets of 3Qc NiC/Ti neutron supermirrors with the shape of circle. The extension of the end of each mirror meets at a focal point, which is located in 150 mm from the end of the device. Neutrons are repeatedly reflected with the same angle by the inner side of the mirror and arrive at a focal point (sample position).

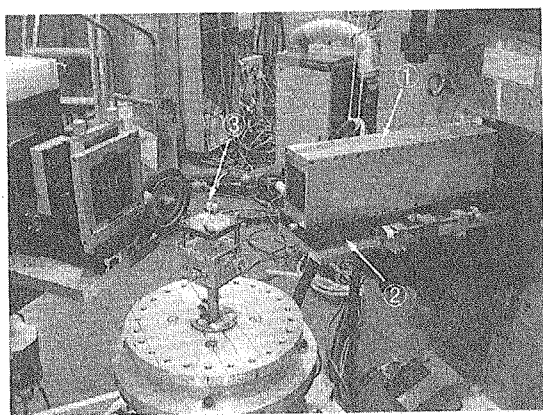


Figure 1: Photograph of the focusing device installed in the TAS-1 (2G) spectrometer. 1:focusing device, 2:adjustable stage (placed on the optical bench, 3:sample).

Figure 2(a), (b) and (c) show the neutron intensity distributions at focal length detected by the neutron IP. The intensity gains at a focal point are about 4.2, 2.7 and 2.0 for incident neutron energy of 4.9 meV, 13.7 meV and 30.5 meV respectively. Figure 2 also show the results of Monte Carlo ray-tracing simulation for the neutron intensity distributions. The each result of the measurement almost agrees with the result of simulation. This indicates that the device demonstrates the expected performance.

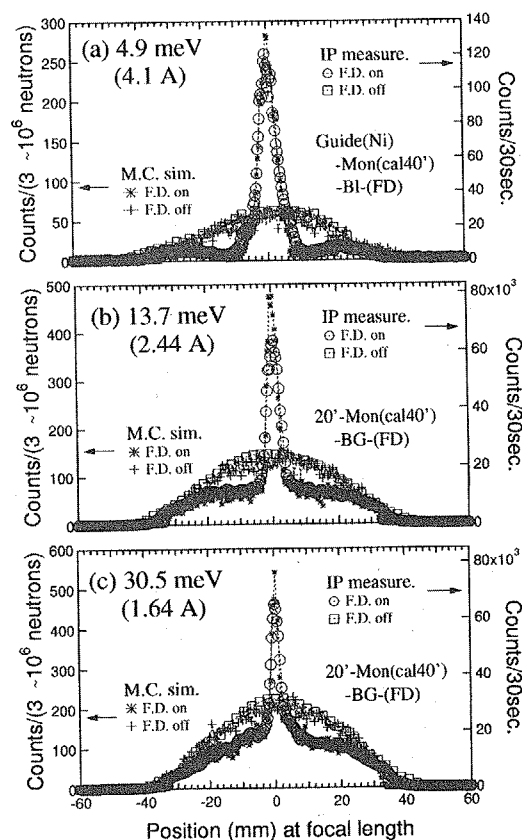


Figure 2: The neutron intensity distributions obtained by the neutron IP with or without the focusing device for the incident neutron energy of (a) 4.9 meV, (b) 13.7 meV and (c) 30.5 meV. The results of the M.C. simulation are also shown in the figures.

References

- 1) D.F.R. Mildner: Nucl. Instr. And Meth. A299 (1990) 416.

2.8.2 Development of Electrostatic Levitation Furnace for Neutron Scattering Experiments of High Temperature Liquids

T. Masaki, T. Ishikawa, P. -F Paradis, Y. Arai, N. Igawa¹, Y. Ishii¹, and S. Yoda

Japan Aerospace Exploration Agency, 2-1-1, Sengen, Tsukuba, Ibaragi 305-8505

¹*Neutron Science Research Center, JAERI, Tokai, Ibaraki 319-1195*

In recent years, many attentions have been focused on the containerless techniques for the experimental research of high temperature melts or deeply undercooling liquids, especially for the structure analysis by neutron or X-ray scattering method ¹⁾. Recently, JAXA has been developing levitation droplet technique due to the electro-static force either for the microgravity experiments in the International Space Station (ISS) or for the normal gravity experiment in laboratory on ground. Since this technique has merits for neutron scattering experiments, JAXA and JAERI are developing an electrostatic levitation furnace (ESL) for neutron scattering experiments of extremely high temperature melts and deeply undercooling liquids. This ESL has been developed since 2002 and the neutron diffraction of levitated sintered alumina was successfully performed at the room temperature ²⁾. Last year, the neutron scattering experiments was performed to study the structure of levitated liquid zirconium at 2500K with the ESL. The liquid zirconium was levitated in the ELS and kept contactless condition for eight hours. However, the diffraction data could not be taken with sufficient accuracy because the sample position was unstable due to a serious trouble on the electrical isolation of the high voltage line in the ESL.

In this year, the neutron diffraction experiment was tried again for the levitated liquid zirconium. The insulation of voltage line was improved and some of metallic parts nearby the voltage line were replaced by the ceramic parts. The experiment was successfully performed and the levitated molten zirconium at the temperature of 2100 K could be kept for twenty four hours in total. Figure 1 shows the levitated liquid zirconium in the ESL. The results of neutron diffraction experiments of liquid zirconium are shown in figure 2. The diffracted neutron from the ESL chamber and back ground intensity are subtracted. Two sharp peaks are remained on the diffraction of zirconium, which are derived from diffraction peaks of copper electrodes. The shape of scattering intensity can be regarded as a typical diffraction pattern of liquid sample. More detailed analysis of diffraction data is quite difficult because the scatter of data is rather large.

Near future, the new facility for the high intensity of neutron beam can be applicable to these kinds of ex-

periments. At that time, the accuracy of data will be remarkably improved and the detailed analysis of undercooled liquids will be possible by using the present apparatus.

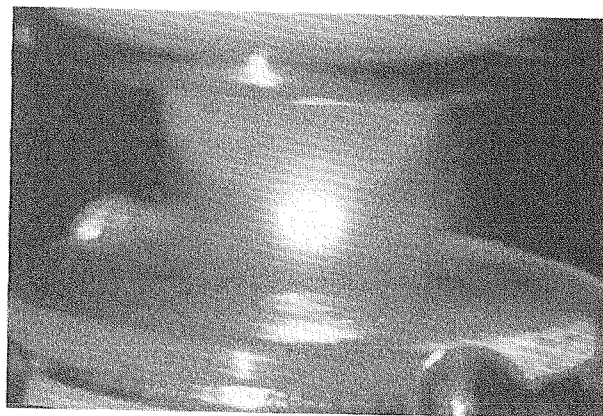


Figure 1: Levitated liquid Zr at 2100K
The bright sphere is the levitated sample. The upper and lower disks are electrodes for controlling the electrostatic field.

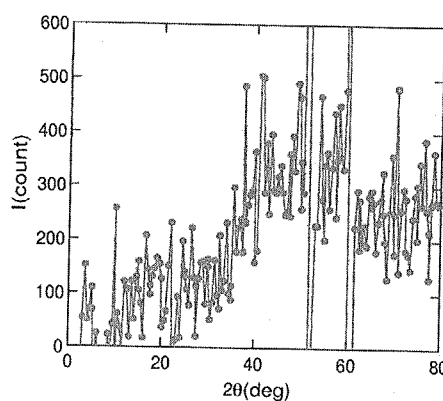


Figure 2: Neutron scattering pattern of levitated liquid Zr.

References

- 1) T. Schenk, D. Holland-Moritz, V. Simonet, R. Bellissent and D.M. Herlach : *Phys. Rev. Lett.* **89** (2002) 075507.
- 2) H.Aoki, P.-F. Paradis, T. Ishikawa, T. Aoyama, T. Masaki, S. Yoda, Y. Ishii and T. Itami : *Rev. Sci. Instr.* **74** (2003) 1147.

2.8.3 Neutron Imaging Characteristics of $\text{CaBPO}_5\text{:Ce}^{3+}$ Based Photostimulable Phosphors

K. Sakasai, M. Katagiri, M. Matsubayashi, T. Nakamura and Y. Kondo¹

Neutron Science Research Center, JAERI, Tokai, Ibaraki 319-1195

¹ Department of Applied Physics, Tohoku University, Sendai, Miyagi 980-8579

The neutron imaging plate (NIP) has made a great success¹⁾ in the field of neutron scattering study but the NIP is sensitive to not only neutron but also gamma ray. Therefore, it is difficult to discriminate neutron signal from gamma ray one when the NIP is read out. To overcome the problem, the authors have been studying a $\text{CaBPO}_5\text{:Ce}^{3+}$ based material as a new neutron storage phosphor consisting of light materials.

The $\text{CaBPO}_5\text{:Ce}^{3+}$ based powder sample was prepared by firing raw materials (CaCO_3 , H_3BO_3 , $(\text{NH}_4)_2\text{HPO}_3$, and $\text{CeCl}_3 \cdot 7\text{H}_2\text{O}$) in a muffle furnace in a nitrogen atmosphere at 600°C for 2 hours and at 800°C for 2 hours. A disk-like sample with a diameter of 12 mm and a thickness of 1 mm was prepared for 2D image measurement. This sample was made by the Spark Plasma Sintering (SPS) method. In the SPS method, the powder was set in a carbon vessel and then fired for 10 minutes at 800°C . The powder sample was pressed with a stress of 5 kN in a vacuum atmosphere throughout the firing.

Although the $\text{CaBPO}_5\text{:Ce}^{3+}$ sample showed Photo-stimulated Luminescence (PSL) after neutron irradiation, the PSL yields were not so high compared to those of $\text{SrBPO}_5\text{:Eu}^{2+}$ samples²⁾. Therefore, the authors have made $\text{CaBPO}_5\text{:Ce}^{3+} + \text{CaF}_2$ samples (molar ratio was 1:1) and measured the PSL decay characteristics. It was confirmed that PSL yields of the $\text{CaBPO}_5\text{:Ce}^{3+}$ are significantly increased by adding CaF_2 and the ratio of $\text{PSL}_{\text{CBP and CaF}_2} / \text{PSL}_{\text{CBP}}$ was 26.7, where $\text{PSL}_{\text{CBP and CaF}_2}$ and PSL_{CBP} are the total PSL outputs of $\text{CaBPO}_5\text{:Ce}^{3+} + \text{CaF}_2$ and $\text{CaBPO}_5\text{:Ce}^{3+}$ samples, respectively.

Figure 1 shows PSL yields per neutron fluence of the $\text{CaBPO}_5\text{:Ce}^{3+} + \text{CaF}_2$ sample as a function of neutron energy. The neutron irradiation was carried out at the SANS-J Facility. As seen in the figure, the PSL yields were proportional to $E^{-0.5}$, where E is neutron energy. This is a clear evidence that the samples are sensitive to neutrons and the PSL output is proportional to the number of nuclear reactions of ^{10}B atoms with neutrons because the neutron cross section of $^{10}\text{B}(n,\alpha)\text{Li}$ is proportional to $E^{-0.5}$.

After the sample was irradiated with a collimated neutron beam with a diameter of 1.5 mm, its surface was scanned with focused laser light by using an X-Y stage controller. The neutron flux and neutron irradiation time were $2.4 \times 10^4 \text{ n/cm}^2/\text{s}$ at 0.65 nm and

30 minutes, respectively. The scanning was carried out every 0.25 mm on the sample surface. The results are shown in Fig.2. The beam intensity image can be clearly obtained.

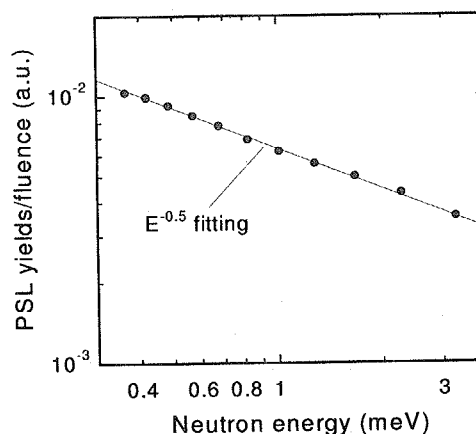


Figure 1: The PSL yields per neutron fluence of the $\text{CaBPO}_5\text{:Ce}^{3+} + \text{CaF}_2$ sample as a function of neutron energy.

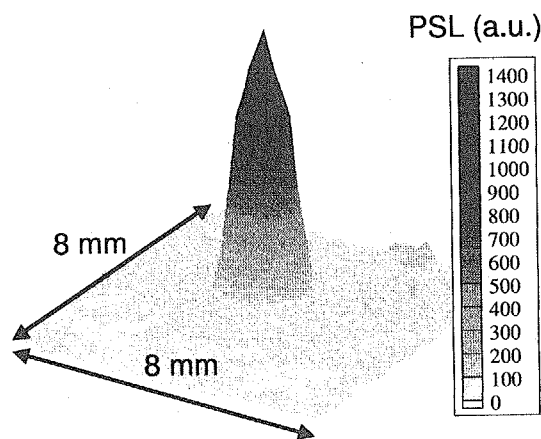


Figure 2: A collimated neutron beam image obtained with the sample. The beam size was 1.5 mm ϕ .

References

- 1) Y. Karasawa *et al.* : Physics B, **241-243** (1998) 139.
- 2) K. Sakasai *et al.* : Applied Physics A, **74** (2002) S1589.

2.8.4 CRYOPAD on the Triple-axis Spectrometer TAS-1 for Spherical Polarimetry

M. Takeda, M. Nakamura, Y. Shimojo, K. Kakurai, E. Lelièvre-Berna¹, F. Tasset¹ and L. -P. Regnault²

Advanced Science Research Center, Japan Atomic Energy Research Institute, 2-4 Shirakata Shirane, Tokai, Naka, Ibaraki, 319-1195 Japan

¹*Institut Laue-Langevin, 6 rue Jules Horowitz BP 156 - 38042 Grenoble Cedex 9, France*

²*CEA-Grenoble, Département de Recherche Fondamentale sur la Matière Condensée, SPSMS-MDN, F-38054 Grenoble Cedex 9, France*

CRYOPAD (CRYOgenic Polarization Analysis Device) is a novel instrument which makes it possible to measure the spherical changes of neutron-spin polarization in the scattering processes of magnetic materials¹⁻³. ILL and CEA-Grenoble, in the framework of EC/ENPI, and JAERI, in the framework of the MoU between ILL and ASRC JAERI, have designed and assembled three third generation CRYOPADs at ILL (CRYOPADUM project), optimized both for elastic and inelastic neutron scattering. One is installed on the ILL instrument D3 (Millennium Project) and the other on the CEA-Grenoble instrument IN22. The JAERI CRYOPAD has been successfully installed on the triple-axis spectrometer TAS-1 at JRR-3 in this fiscal year.

CRYOPAD consists of a couple of Nb Meissner screens and a hybrid precession torus (HPT) which has two independent hybrid precession coils: HPC_{in} and HPC_{out}. In order to cool the Nb screens into the superconducting state the screens are attached to the bottom of liquid He bath of cryostat as a concentric circle. In a normal operation on TAS-1 typical liquid-He-consumption rate is 12 % (= 2 ℓ) a day. Autonomy is more than one week. The two Nb magnetic shields screen the stray fields of the HPT and an earth-magnetic-field. The residual magnetic fields are less than 0.3 (nT) inside the sample chamber where the measurements of spin rotation can be performed with the accuracy of 0.5 deg for 14.7 meV neutrons.

HPC_{in} controls rotation of the incident beam polarisation vector around the horizontal axis, perpendicular to the wave vector, \vec{k}_i , and HPC_{out} that of scattered neutrons around the axis perpendicular to \vec{k}_f . The fields produced by the two coils are decoupled by the Nb screens and a Nb frame surrounding the yoke of HPC_{in} coil to control the spin rotation of incident and scattered neutrons independently. In addition to the HPT, nutators at just outside the outer Nb screen control the direction of polarization vector in the plane perpendicular to \vec{k}_i and \vec{k}_f . The combination of the HPT and nutators enables to perform spherical polarization analysis.

The neutron-spin control has been checked by using PG(004) Bragg reflection, whose scattering angle is almost equal to 90.0 deg for 14.7 meV neutrons as shown in Fig. 1. The results are summarized in Table 1 as

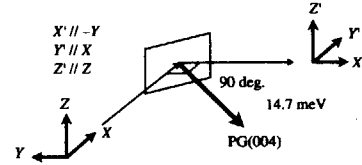


Figure 1: Experimental set-up for checking spin handling by combination of the nutators and HPCs (HPC_{in} and HPC_{out}).

sociated with expected values of the final polarization. The deviation from 1 or 0 stems from the instrumental imperfection such as incomplete polarization and uncontrolled rotation due to the residual field. Anyway the off-diagonal terms are negligibly small. This indicates that we can spherically control the neutron spin as desired and that the door to a new world of research on magnetism is now open at JAERI.

Table 1: Directions of polarization of incident beam (In), direction to be analyzed (Detection), measured final polarization (P_f), and expected final polarization.

In	Detection	P_f	
		(measured)	(expected)
Z	Y' (// +X)	-0.031 ± 0.010	0.0
Z	X' (// -Y)	-0.021 ± 0.012	0.0
Z	Z' (// +Z)	0.910 ± 0.003	1.0
Y	Y' (// +X)	0.003 ± 0.002	0.0
Y	X' (// -Y)	-0.915 ± 0.003	-1.0
Y	Z' (// +Z)	0.021 ± 0.010	0.0
X	Y' (// +X)	0.919 ± 0.003	1.0
X	X' (// -Y)	-0.008 ± 0.006	0.0
X	Z' (// +Z)	0.017 ± 0.012	0.0

We are much indebted to N. Kernavans, E. Bourgeat-Lami, S. Pujol and X. Tonon for their assistance in assembling CRYOPAD at ILL.

References

- 1) F. Tasset, Physica B 156-157 (1989) 627.
- 2) F. Tasset, P. J. Brown, E. Lelièvre-Berna, T. Roberts, S. Pujol, J. Allibon, E. Bourgeat-Lami, Physica B 267-268 (1999) 69.
- 3) L. P. Regnault, B. Geffray, P. Fouilloux, B. Longuet, F. Mantegazza, F. Tasset, E. Lelièvre-Berna, E. Bourgeat-Lami, M. Thomas, Y. Gibert, Physica B 335 (2003) 255.

2.8.5 Development of cold neutron imaging detector

H. Sakurai¹, F. Tokanai¹, S. Gunji¹, S. Motegi¹, M. Kaneko¹, S. Kikuchi¹, J. Suzuki², T. Oku²

¹Department of Physics, Yamagata University, 1-4-12 Kojirakawa, Yamagata 990-8560, Japan

²Japan Atomic Energy Research Institute (JAERI), 2-4 Shirane Shirakawa, Tokai, Ibaraki 319-1195, Japan

For the detection of thermal neutrons, a gas proportional counter with the fill gas of ^3He is frequently employed because the absorption cross section are significant for thermal neutrons. The optical capillary gas proportional counter is available to the neutron imaging with gas mixtures of ^3He . The nuclear reaction between a neutron and ^3He produces a proton with energy of 570 keV and a triton with the energy of 190 keV. For a cold neutron, these two particles are ejected to opposite sides of each other and hence the image of their tracks should be straight line in gas. Using cold neutrons at JRR-3 in JAERI, we have tested the imaging of tracks using the optical CGPC filled with a gas mixture of ^3He .

Figure 1 is a schematic view of the optical imaging CGPC setup on the beam line of cold neutrons C3-1-2-1 at JRR-3 in JAERI. The CGPC is filled with the gas mixture $^3\text{He} + 8\%\text{CH}_4 + 2\%\text{TMA}$ at 1.1 atm. The energy of cold neutrons is adjusted to 0.45 meV by a velocity selector before reaching the setup. Incoming cold neutrons were confined to the centre area of the CGPC by a slit with a size of 5 mm \times 5 mm made of cadmium to control the counting rate to approximately 66 cps.

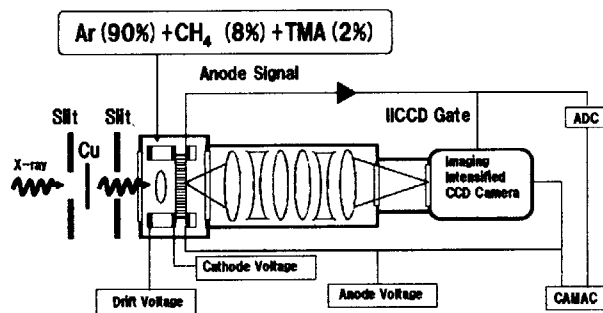


Figure 1: Schematic of the optical imaging CGPC setup on the beam line for cold neutrons at JRR-3 in JAERI. The CGPC is filled with the Penning gas mixture $^3\text{He} + 8\%\text{CH}_4 + 2\%\text{TMA}$ at 1.1 atm. The absorption region for cold neutron is 10 mm. The CGPC is viewed through a lens system by an ICCD.

A track image produced from the cold neutron is shown in Fig 2a. Also, Fig 2b shows the brightness distribution of the track image projected to the x -coordinate and the distribution indicates the be-

haviour of energy depositions along the track. The whole track length is approximately 15.2 mm on the image and there is a brighter portion with the length of 1.8 mm in the vicinity of the track end compared with the other.

Since this track image is a projection of the track to the capillary plate, the maximum lengths are estimated to 18.2 mm for the whole length and 2.2 mm for the bright portion, respectively, taking account of the gas depth. As the ranges of the triton and the proton are approximately 3.6 and 23 mm for this gas mixture from a calculation of dE/dx , the track image shows a part of track in the absorption region. Moreover, the rate of dE/dx of the triton is greater than that of the proton. These result in due to the triton and the other due to proton. Therefore, we conclude that the absorption point of neutron is in the vicinity of (430, 370) at the graph of track image in Fig 2a with ambiguity of 0.5 mm.

These results indicate that the neutron absorption point can precisely determine with the the track image.

Publication: "A test of imaging by cold neutron using optical capillary gas proportional counter", NIMA(2004) in press

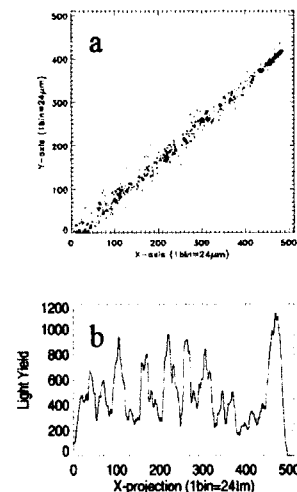


Figure 2: (a) A track image produced by absorption of a cold neutron in ^3He . The trace consists of a triton and a proton. (b) Light yields of the CCD for the track image which shows a projected profile of energy deposition.

2.8.6 A Study on Application of a Magnetic Neutron Lens to Focusing Geometry SANS Experiments

T. Oku, J. Suzuki, H. Sasao, T. Adachi¹, T. Shinohara¹, K. Ikeda¹, T. Morishima¹, K. Sakai¹, H.M. Shimizu¹

Advanced Science Research Center, JAERI, Tokai, Ibaraki 319-1195

¹*RIKEN, 2-1 Hirosawa, Wako, Saitama 351-0198*

A sextupole magnetic field functions as an ideal focusing and defocusing lens for neutrons when the neutron has positive and negative spin polarity to the local field, respectively. So far, the neutron focusing effect of sextupole magnets has been investigated experimentally and numerically^{1,2)}. For practical use of the lens function of a sextupole magnet in neutron scattering experiments, a sextupole magnet with a sufficiently large aperture accompanied with strong focusing power is demanded. Recently, we have developed a superconducting sextupole magnet (SSM) with an aperture of 46.8 mm in diameter which generates the sextupole magnetic field $B = (G/2)r^2$ with $G=12,800$ T/m², where r is the distance from the magnet axis³⁾.

Its neutron focusing effect has been investigated using unpolarized cold neutrons⁴⁾. We have proposed to apply the sextupole magnet to small-angle neutron scattering experiments with focusing geometry (FSANS) to improve the q -resolution and/or measuring efficiency by focusing neutrons on the detector⁵⁻⁷⁾. To get the advantage in the practical FSANS measurement over a conventional pinhole-geometry SANS experiment, it is necessary to employ a neutron focusing device with little scattering and absorption of the neutrons. The sextupole magnet is considered to be a suitable focusing device, because of its neutron focusing property which is free from the scattering and absorption of the neutrons. However, if neutrons with negative spin polarity are included in the incident beam, they are defocused by the sextupole magnet and, then raise the background level. Therefore, the incident beam should be well polarized in case of the FSANS experiment with the sextupole magnet. In this paper, we investigated the neutron focusing effect of the SSM using unpolarized and polarized neutrons, and discussed the feasibility of the SSM on the application to the FSANS experiments.

The SSM has a 2 m-long sextupole coil which is composed of six saddle-shaped coils. There exists non-adiabatic regions where the neutron spin is flipped; 1) around the center axis of the magnet where the sextupole magnetic field is weak, 2) around both ends of the sextupole coil where the magnetic field distribution deviates from the sextupole magnetic field distribution. We then removed these non-adiabatic regions by applying a dipole field along the beam axis

using solenoid coils equipped in the SSM⁸⁾. The detailed specifications of the SSM are described in Ref. 3). The SSM was installed at the beamline C3-1-2-1 of JRR-3 in Japan Atomic Energy Research Institute (JAERI). The experimental setup is shown in Fig. 1. The neutrons are monochromatized by the mechanical velocity selector. The neutron wavelength is $\lambda = 13.44$ Å with $\Delta\lambda/\lambda = 0.177$. The polarizer is the FeSi magnetic supermirror. We used the transmitted neutrons through the polarizer, which have negative spin polarity. The spin polarization efficiency is ~ 0.96 . The transmission of the polarized neutrons with $\lambda = 13.44$ Å through the polarizer is ~ 0.66 . The spin flipper (SF) is a radio-frequency gradient spin flipper which was designed to be effective for the neutron beam with wavelengths longer than 4 Å and a beam size of 50 mm in diameter⁹⁾. The neutrons with positive and negative spin polarity are incident in the SSM when the SF is on and off, respectively.

We measured 2d neutron intensity distribution using a neutron imaging plate (BAS-ND) with position resolution of 0.2 mm under several conditions as follows:

case1 SSM on, polarizer off:

The incident beam to the SSM is unpolarized.

case2 SSM on, polarizer on, SF on:

The incident beam to the SSM is polarized with positive spin polarity.

case3 SSM on, polarizer on, SF off:

The incident beam to the SSM is polarized with negative spin polarity.

case4 SSM off, polarizer on:

SSM is off.

case5 Beam shutter closed:

The incident beam to the SSM is shut out for the background measurement.

Each measuring time is 11 hours. When the SSM is on, current in the sextupole coil is $I_{ssm} = 210$ A, which corresponds to the current to produce the magnetic field gradient of $G = 8,235.6$ T/m². In this condition, the neutrons with positive spin polarity are focused on the detector (Fig. 1). When the SSM is off, $G = 0$ and the neutrons are not accelerated by the SSM. When

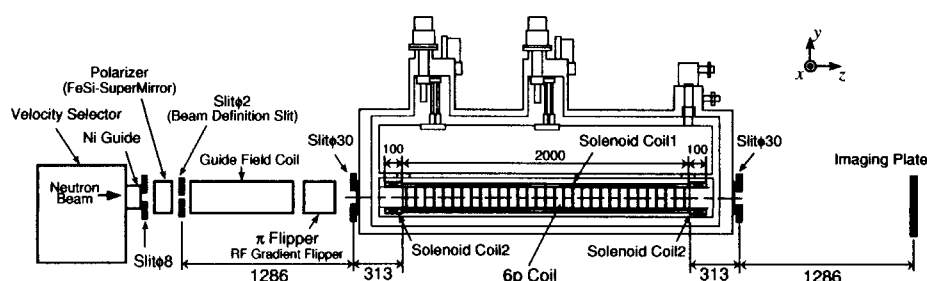


Figure 1: Experimental setup.

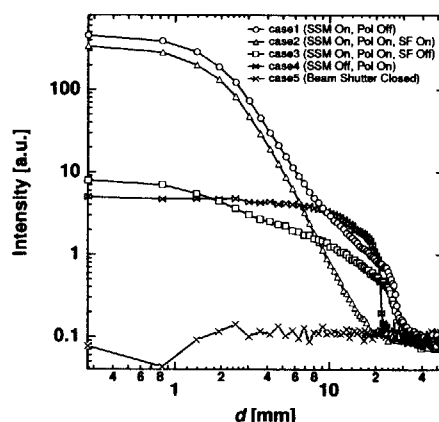
the polarizer is on, solenoid coils are also excited to remove the non-adiabatic regions.

The radially averaged intensity is plotted as a function of d , where d is the distance from the peak position of the 2d intensity distributions (Fig. 2). In cases 1 and 3, a shoulder was observed around $d \sim 23$ mm, but not in case 2 (Fig. 2). Thus, the shoulder should be produced by the neutrons defocused by the SSM. The ratio of the focused to defocused neutrons by the SSM in case 2 is estimated to be 50 times larger than that in case 1, based on the polarization of ~ 0.96 of the incident beam. In case 2, therefore, such a shoulder should be unobservable, because the contribution of the defocused neutrons to the intensity distribution is buried under the background level. The differences of the peak values between cases 1 and 2 and the shoulder values between cases 1 and 3 are considered to result from the neutron transmission of the polarizer.

The ratio R of the peak value to the background level of the intensity distribution of a direct beam is one of measures which are often used to evaluate SANS instruments. In general, R is desired to be larger than $\sim 10^4$. Here, we define R_{mag} as the ratio of the peak value to the level of defocused neutrons for the SANS instrument with focusing geometry using the sextupole magnet. $R_{mag} \sim 8,000$ can be achieved even in the experimental condition of case 2 which is not optimized for a high R_{mag} value. Around the experimental condition of this study, R_{mag} is approximately proportional to $(\Delta\lambda/\lambda)^{-1}$. By optimizing the experimental condition, R_{mag} is expected to be increased by several times. The details of the optimization of the experimental condition will be discussed elsewhere. Therefore, the level of the defocused neutrons by the SSM can be sufficiently reduced by the same way as in this study, and $R_{mag} > \sim 10^4$ can be achieved in the FSANS experiment with the sextupole magnet.

In conclusion, we have investigated the neutron focusing effect of the SSM using unpolarized and polarized cold neutrons to discuss the feasibility of the application of the sextupole magnet to FSANS experiments. The experimental setup, which consisted of the polarizer, the spin flipper, the SSM, etc., worked

as expected. By utilization of the polarizer with efficiency of ~ 0.96 , the level of the defocused neutrons could be reduced to be $\sim 1/8000$ of the peak value of the direct beam. The level is expected to be further decreased by optimizing the experimental condition. Thus, we conclude that the sextupole magnet can be employed as a focusing device for FSANS experiments.

Figure 2: Radially averaged intensity. d is the distance from the intensity peak position.

References

- 1) H.M. Shimizu et al., NIM-A 430 (1999) 423.
- 2) J. Füzi et al., Appl. Phys. A 74 (2002) S210.
- 3) J. Suzuki et al., J. Appl. Cryst. 36 (2003) 795.
- 4) H.M. Shimizu et al., Nucl. Instr. and Meth. A 529 (2004) 5.
- 5) B. Alefeld et al., NIM-A 274 (1989) 210.
- 6) B. Alefeld et al., Physica B 234-236 (1997) 1052.
- 7) S.-M. Choi et al., J. Appl. Cryst. 33 (2000) 793.
- 8) M. Furusaka et al., NIM-A 529 (2004) 223.
- 9) T. Oku et al., Physica B 335 (2003) 226.

2.8.7 Development of optical devices and detectors for cold neutrons

H. M. Shimizu, T. Adachi, K. Ikeda, T. Shinohara, K. Hirota, H. Sato, Y. Takizawa, S. Morita, H. Ohmori, K. Sakai¹, T. Oku², J. Suzuki², S. Satoh³ and M. Furusaka³

RIKEN, Wako, Saitama 351-0198

¹Department of Physics, Tokyo Institute of Technology, Ohokayama, Meguro 152-8551

²Advanced Science Research Center, JAERI, Tokai, Ibaraki 319-1195

³Institute of Material Structure Science, KEK, Tsukuba, Ibaraki 305-0801

We have developed optical devices for cold neutrons, focusing lens using MgF_2 especially.¹⁾ Fresnel type lens has wide caliber and better transmission.^{2,3)} The detailed design was described before.²⁾ We have reported the 25 times higher performance with Focusing geometry Small Angle Neutron Scattering (F-SANS)⁴⁾ compared to Pinhole geometry Small Angle Neutron Scattering (P-SANS) last year.¹⁾ In this report, development of fundamental nature of neutron focusing lens is described.

The performance of the compound lens was investigated using a cold neutron beam from the SANS-J instrument at the JRR-3 reactor of JAERI. A collimated neutron beam entered the lens, and the transmitted and refracted intensities were measured by a two-dimensional position sensitive detector (PSD) located at 10 m downstream from the center of the lens. The PSD has 128×128 position channels over a 640-mm in diameter sensitive area. The position resolution of the PSD was specified to be 5 mm.

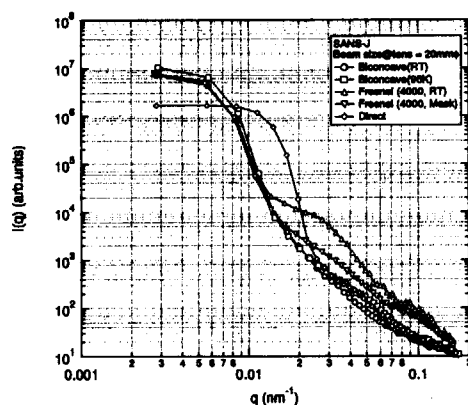


Figure 1: Measurement of the focused beam profiles comparing biconcave lens at Room Temperature (\circ), at 95 K (\square), Fresnel lens without mask (\triangle), with mask (∇) and no lens (\diamond).

Major problem of the Fresnel lens performance is undesirable refraction or reflection around back-cut region of the Fresnel structure. Those refracted or reflected neutron makes hump around direct beam. In order to solve this problem, neutron absorbing mask made by Gd. The detailed design was described before.³⁾ As a result, the hump around direct beam becomes 80% less by using this Gd absorbing mask.³⁾ This means 90% noise is reduced by Gd absorbing mask. The comparison of the beam profiles at 1.1 nm wavelength and 20 mm in diameter neutrons with/without Gd absorbing mask is shown in Fig. 1.

Meanwhile, major problem of the biconcave lens performance is less transmission with wide caliber. In order to solve this problem, the lenses were cooled at 95 K. Transmission of 27 lenses was 0.59 with 1.1 nm in wavelength and 20 mm in diameter neutron beam at room temperature. That was improved up to 0.85 at 95 K. These two profiles were also shown in Fig. 1. We also have developed two dimensional position-sensitive neutron detector (PSND) with high spatial resolution and portability. Coupling of $^6\text{LiF}+\text{ZnS}(\text{Ag})$ scintillator in 0.3 mm thickness and 3 inches resistance dividing type photo multiplier tube (RPMT) made 30 mm \times 30 mm sensitive area and 0.5-0.7 mm spatial resolution possible. In Fig. 2, full width half maximum (FWHM) of fifth peak from left side was 1.6 ch. The position resolution of the PSND was specified to be 0.5 mm. Then, FWHM for neutron beam in 0.5 mm width should be 0.8 mm. The spatial resolution is expected to be 0.63 mm by deconvolution of beam width.

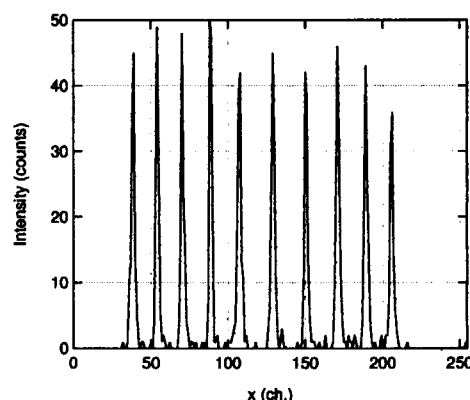


Figure 2: A typical line profile of 10 times multi shot using Cd slit in 0.5 mm width with 10 mm position shifting.

References

- 1) S. Koizumi, M. Matsuda and K. Kurihara: *Progress report on neutron scattering research*, (JAERI-Review 2004-005, Tokai, 2004) p. 142.
- 2) T. Oku, S. Morita, S. Moriyasu, Y. Yamagata, H. Ohmori, Y. Takizawa, H. M. Shimizu, T. Hirota, Y. Kiyonagi and J. Suzuki, *Nucl. Instrum. Methods A* **462** (2001) 435.
- 3) T. Adachi, K. Ikeda, T. Shinohara, K. Hirota, T. Oku, J. Suzuki, H. Sato, K. Hoshino, J. Guo, W. Lin, H. Ohmori, H. M. Shimizu, K. Sakai, C.-K. Loong and K. C. Littrell, *Nucl. Instrum. Methods A* **529** (2004) 112.
- 4) S.-M. Choi, J. G. Barker, C. J. Glinka, Y. T. Cheng and P. L. Gammel, *J. Appl. Cryst.*, **33** (2000) 793.

2.8.8 Development of a high-performance microstrip gas chamber with a capability of track discrimination for neutron detection

T. Nakamura, S. Masaoka, H. Yamagishi, K. Soyama and K. Aizawa

Neutron Science Research Center, JAERI, Tokai, Ibaraki 319-1195

We have been developing microstrip gas chamber (MSGC) using helium-3 gas as neutron converter. The specifications expected to the MSGC detector are high detection efficiency ($>60\%$ for thermal neutrons), high spatial resolution ($< 1\text{mm}$), high neutron-gamma-ray discrimination ratio ($> 10^7$), high counting rate ($> 10^6\text{cps/detector}$), and a moderate area. It is common that large amount of heavy gas such as CF_4 has to be filled to achieve a high spatial resolution in a conventional positioning scheme, such as charge-division or delay-line chain. However, achieving a gas gain of more than ten in such a gas condition would require an electric field strength of $\sim 10^4\text{V/mm}$ between the microstrip electrodes, thereby, making the detector unstable due to the dielectric breakdown at the surface of the substrate.

To solve these problems and achieve the specifications, we developed the MSGC system, in which all the signal channels are read-out individually, and the incident positions of the neutrons are determined by the instrument system with a capability of secondary particle discrimination (InSPaD)¹⁾. The InSPaD identifies the particles - proton and triton - created in the nuclear reaction ${}^3\text{He} + n \rightarrow p + T$ on the basis of the track length, and determines the incident position of neutron accurately, not determined as the center of gravity. The simulation result showed a high spatial resolution less than 1 mm regardless of the gas condition using the InSPaD. Full description of the InSPaD can be found in ²⁾. With this system, one can use "light" gas condition without a loss of a spatial resolution, thereby, stability of the detector should be further increased.

The MSGC was manufactured by TOSHIBA Co. and can deal with charge-up at high counting rate by appropriately adjusting the resistivity of the polyimide substrate using a organic titanium coatings. Figure 1 shows the proto-type of the microstrip substrate, which measures $50 \times 50\text{mm}^2$ mounted on the PCB socket board for individual read-out. We have made two of high pressure gas chambers; one is for the test (Figure 2) and the other is for the prototype compact chambers. For both chambers, signal channels of 160 and 561 can be fed through so that to read-out all the signals lines individually. The gas chamber withstands up to 8 atm. The windows of the chambers were made of aluminum with a thickness of 3 mm. At each channels of read-out, the signal

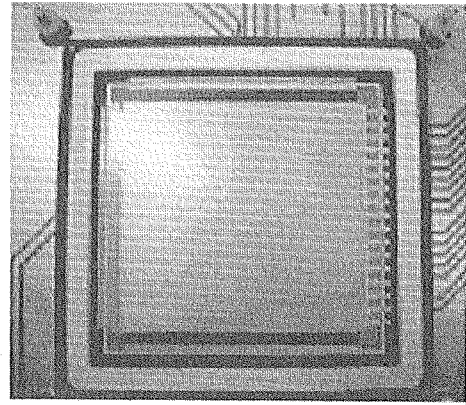


Figure 1: Microstrip substrate mounted on the PCB socket board for individual readout.

pulse were amplified, shaped and discriminated individually. We do not measure the pulse height, but only check the numbers of the fired channels (i.e. hit-detection) to ensure high count rate. The feasibility of the hit-detection method is well confirmed in x-ray ³⁾ and in neutron detection ⁴⁾. In the InSPaD, the voltage levels of the discriminators for each channels were set identical but appropriately so that the numbers of suprathreshold channels should become different for a proton and a triton. The identification of the proton and a triton can be done using the numbers of suprathreshold channels, and the incident position of neutron can be determined by the simple logical calculation. The InSPaD realizes the identification of the particles with a simple, fast and cost-effective method, thus, ensuring high count rate, and moreover increases the signal to noise ratio of the detector system, which is attributable to the relatively high discrimination levels to differentiate a proton and a triton.

The operational principle including feasibility test of the InSPaD and the basic characteristics were confirmed using a test detector system ⁵⁾. Figure 3 shows the signal height of the event when the projected track on the plane of the anodes is at an angle to the anodes, which was estimated at $\sim 40^\circ [\sin^{-1}(4.8/7.5)]$ using a projected track length of 4.8 mm and a track length of 7.5 mm. If we set the threshold level to $10 \times 10^{-15}\text{C}$ for this event, the numbers of suprathreshold signals are two and five for the triton and proton, respectively, and the InSPaD can be used to determine the incident

position of the neutron as strip 4. This result demonstrates the feasibility of the InSPaD; in the future we will establish a full read-out system using an InSPaD.



Figure 2: Test gas chamber for individually read-out, which withstands up to 8 atm.

References

- 1) H. Yamagishi, *et al.*: Japanese patent pending, P2000-253967.
- 2) H. Yamagishi, *et al.*: Rev. Sci. Instrum. **75** (2004) 2340.
- 3) T. Tanimori, *et al.*: Nucl. Instr. and Meth. A **436** (1999) 188.
- 4) T. Nakamura, *et al.*: Proc. 16th Int. Conf. Advanced Neutron Sources (ICANS XVI), Dusseldorf, 2003, p. 441.
- 5) T. Nakamura, *et al.*: Nucl. Instr. and Meth. A **529** (2004) 336.

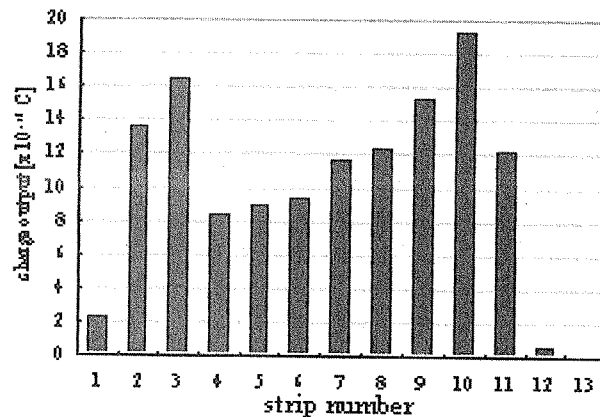


Figure 3: Signal-height distribution along the track measured event to event in a mixture of 15% C_2H_6 with helium-3 at 4 atm when the projected track in the plane of the anodes was angled about 40deg to the anodes.

2.9 Neutron Radiography

This is a blank page.

2.9.1 Neutron Irradiation Characteristics of $\text{CaBPO}_5\text{:Ce}^{3+}$ Based Photostimulable Phosphors

K. Sakasai, M. Katagiri, M. Matsubayashi, T. Nakamura and Y. Kondo¹

Neutron Science Research Center, JAERI, Tokai, Ibaraki 319-1195

¹ Department of Applied Physics, Tohoku University, Sendai, Miyagi 980-8579

The neutron imaging plate (NIP) has made a great success¹⁾ in the field of neutron scattering study but the NIP is sensitive to not only neutron but also gamma ray. Therefore, it is difficult to discriminate neutron signal from gamma ray one when the NIP is read out. To overcome the problem, the authors have been studying a $\text{CaBPO}_5\text{:Ce}^{3+}$ based material as a new neutron storage phosphor consisting of light materials.

The preparation of $\text{CaBPO}_5\text{:Ce}^{3+}$ based powder sample was described elsewhere²⁾. To increase the Photostimulated Luminescence (PSL) after neutron irradiation, the authors have made $\text{CaBPO}_5\text{:Ce}^{3+} + \text{CaF}_2$ samples (molar ratio was 1:1) and measured the PSL decay characteristics. The results are depicted in Fig.1, where the results of $\text{CaBPO}_5\text{:Ce}^{3+}$ was also shown for comparison. The neutron irradiation was carried out for 9.6 s at JAERI CNRF facility. One can see that PSL yields of the $\text{CaBPO}_5\text{:Ce}^{3+}$ are significantly increased by adding CaF_2 .

Figure 2 shows a PSL output decay curve of luminescence of the neutron-irradiated $\text{CaBPO}_5\text{:Ce}^{3+} + \text{CaF}_2$ sample. The neutron irradiation time was 100s at the TNRF. In the figure, results with a Li block (1-cm thickness) are also shown, where the block was set in front of the sample to shield it from the neutron irradiation. The ratio of $\text{PSL}_{\text{with}}/\text{PSL}_{\text{without}}$ was less than 0.09, where PSL_{with} and $\text{PSL}_{\text{without}}$ were total PSL signals in cases with and without the Li block, respectively. Since 97 % of incident neutrons were absorbed in the Li block, the influence of such intense gamma ray on the signal was less than 6 %. The figure indicates that the $\text{CaBPO}_5\text{:Ce}^{3+} + \text{CaF}_2$ sample may be usable in such a high gamma-ray field of 2 Sv/hr.

Figure 3 shows the PSL output of the $\text{CaBPO}_5\text{:Ce}^{3+} + \text{CaF}_2$ sample as a function of neutron fluence measured at TNRF and SANS. The $\text{CaBPO}_5\text{:Ce}^{3+} + \text{CaF}_2$ sample has good output linearity for neutron fluence over three decades.

References

- 1) Y. Karasawa *et al.* : Physics B, **241-243** (1998) 139.
- 2) K. Sakasai *et al.* : IEEE2003 Conference Record (CD-ROM).

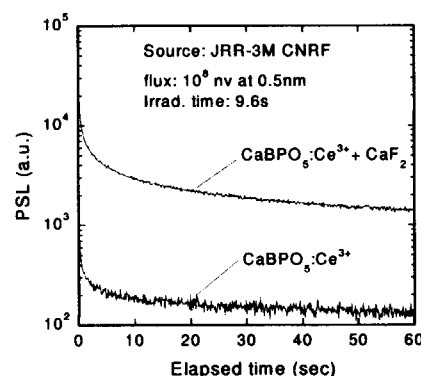


Figure 1: The PSL decay curves of $\text{CaBPO}_5\text{:Ce}^{3+} + \text{CaF}_2$ and $\text{CaBPO}_5\text{:Ce}^{3+}$ samples.

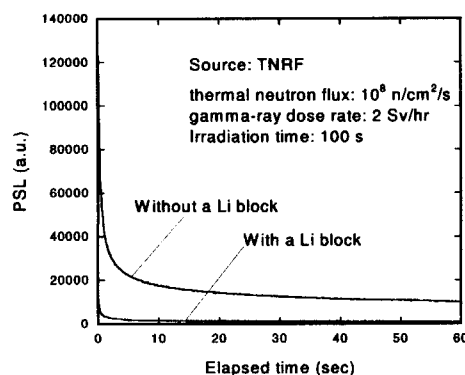


Figure 2: The PSL output decay curve of luminescence of the $\text{CaBPO}_5\text{:Ce}^{3+} + \text{CaF}_2$ sample after neutron irradiation at TNRF.

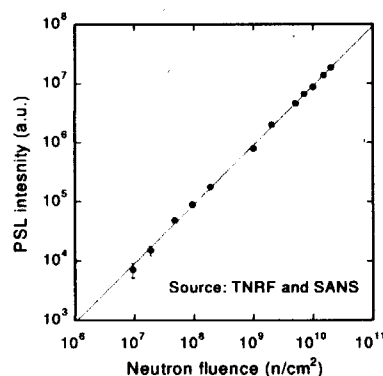


Figure 3: The PSL output of $\text{CaBPO}_5\text{:Ce}^{3+} + \text{CaF}_2$ sample as a function of neutron fluence measured at TNRF and SANS.

2.9.2 Development and Application of Neutron Radiography Techniques with High Temporal Resolution

K. Mishima, Y. Saito and M. Matsubayashi¹

Research Reactor Institute, Kyoto University, Osaka 590-0494

¹Neutron Science Research Center, JAERI, Tokai, Ibaraki 319-1195

Introduction To make clear rapid transient phenomena, such as boiling bubbles and molten-metal-water interaction by using high frame-rate neutron radiography (HFR-NR), an imaging system requires high temporal and spatial resolutions. The limitation of resolution of the HFR-NR has restricted its applications. To overcome this limitation, it is important to seek the best combination of imaging devices such as a fluorescent converter, high-speed video camera, and image intensifier¹⁾. In this study, to achieve high temporal and high spatial resolution for HFR-NR, various combinations of imaging devices have been tested.

Fluorescent Converter High resolution, high sensitivity and rapid decay of scintillation are required for the fluorescent converter in the HFR-NR system. Addition of the killer material into the ZnS type scintillator causes a drop of the scintillation intensity but has potential capability of reducing scintillation decay time²⁾. ⁶LiF:ZnS(Ag, Ni) fluorescent converters of which specification are shown in Table 1, were examined to confirm the effect of killer materials by using thermal neutrons in JRR-3M in this study.

Table 1: Specification of fluorescent converters

	Ni (ppm)	Particle size (μm)	Coating weight (mg/cm^2)
JN1	0.0	10.0/ZnS(Ag):3.8	43.5
JN2	0.5	10.0/ZnS(Ag):3.8	43.5
JN3	1.0	10.0/ZnS(Ag):3.8	43.5
JN4	2.0	10.0/ZnS(Ag):3.8	43.5

Table 2: Specification of image intensifier

Image Intensifier	GIB-M2P	C6598-50MOD
Company	nac	Hamamatsu
Micro Channel Plate	Double	Single
Photo Cathode	Multialkali	GaAsP
Resolution [lp/mm]	25	35

Image intensifier The I.I. used in this study are shown in Table 2. The effects of photocathode material and the number of micro channel plates on the image quality were investigated.

High speed video camera In this study, three kinds of high-speed video cameras were tested (FAST-CAM ultima-UVS, FASTCAM Super10K, and HG-100K) in this study. In the HFR-NR system, the internal shutter of the camera is disabled but the gating operation of the I.I. makes exposure time control possible to suppress moving effect for slower recording.

Experiments Experiments were performed using a rotating stainless steel disc and a rotating cadmium disc, which has several holes of various diameters to study the temporal resolution of the imaging system. Original images of the rotating cadmium disc were shown in Fig.1 a),b). As shown in these figures, the effect of killer materials could be investigated.

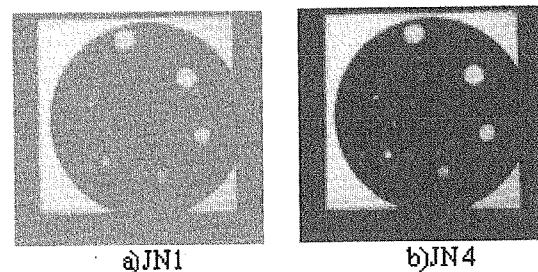


Figure 1: Original images of the rotating Cd disc.

Summary To achieve high temporal and high spatial resolution for high frame-rate NR, various combinations of imaging devices have been tested. The development of fluorescent converters to realize fast scintillation decay with killer materials has performed.

References

- 1) T. Hibiki, K. Mishima, K. Yoneda, S. Fujine, A. Tsuruno and M. Matsubayashi: Nucl. Instrum. Methods Phys. Res. A, **351** (1994) 423.
- 2) M. Matsubayashi, T. Hibiki, and K. Mishima: Nonstr. Test. Evalu., **16** (2001) 267.

2.9.3 Very Low Energy Neutron Radiography with Neutron Energy Selection System for Variable Image Contrast

Y.Kawabata, T.Nakano¹, M.Hino, T.Oku², J.Suzuki² and U.Matsushima³

Research Reactor Institute, Kyoto University, Kumatori, Osaka 590-0494

¹*Faculty of Engineering, Kyoto University, Kyoto 606-8501*

²*Japan Atomic Energy research Institute, Tokai, Ibaraki 319-1195*

³*University of the Ryukyus, Nishihara, Okinawa 903-0213*

Neutron radiography is widely used in nondestructive tests and basic researches, for instance, mechanics, biology and so on. Many techniques for high quality images are progressing and the control of neutron energy is one of the important methods. There are two ways for this purpose. One is to use white beam and another is to use monochromatic beam.

Usually, white beam is used in neutron radiography. It gives high flux and a short exposure time. When a sample is thick, faster neutrons are used because they have higher penetration power into samples. Low energy neutrons are used when the high resolution is required.

Monochromatic neutron radiography is usually performed with a velocity selector or a monochromator. As polycrystal materials have the Bragg cut-off wavelength of about 0.4nm, the neutron total cross section changes drastically at this wavelength. The typical technique of the monochromatic neutron radiography is the comparison of the difference in the images with the neutrons of wavelength longer or shorter than the Bragg cut off. It makes clear image of some polycrystal samples.

When the characteristic wavelength of a cold neutron guide tube is longer than the Bragg cut-off, it is impossible to use this effect. Though it does not have a drastic change, the change of the absorption cross-section according to the neutron wavelength gives us the chance to guess the materials in the sample. The cross-sections of elements are well known but the sample and measurement geometry affects an image because of the neutron scattering. It is difficult to estimate the quantity of materials from an image directly when the geometry is complicated. So it is necessary to measure the neutron transmission with a simple geometry to estimate quantitatively. This is a reason to measure neutron transmission of typical step samples with the neutron radiography measurement system.

The wavelength dependence of the neutron transmission was measured for typical samples by a neutron radiography system. It is performed at NOP(C3-1-2), JRR-3M, using a velocity selector. As the geometry should be simple, a converter is set close to a plate type sample of 1cm width. The images are taken by using a monochromated beam of which the wavelength resolution is 82%. Samples were Al, Pb, Sn, Zn, Cu,

Fe, Ni, polyethylene resin, stainless steel, acrylic resin, Ag, brass and Ti. Some results of attenuation coefficient are shown in Fig.1 and 2. The results would be a basic data to identify materials in a sample from a neutron radiography images ¹⁾.

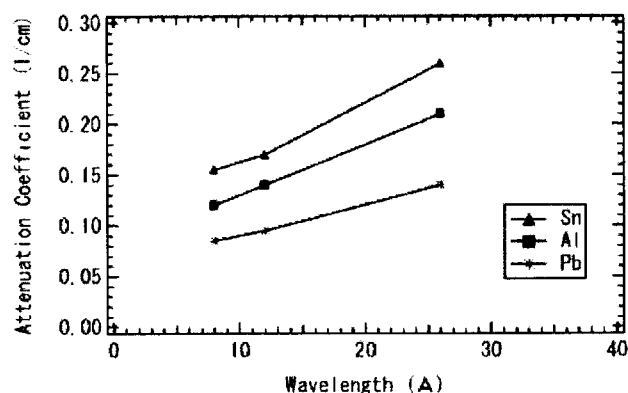


Figure 1: Attenuation Coefficient of Sn, Al and Pb.

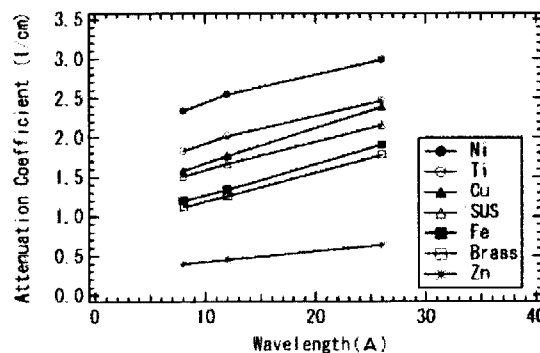


Figure 2: Attenuation Coefficient of Ni, Ti, Cu, stainless steel, Fe, brass and Zn.

References

- 1) Y.Kawabata, T.Nakano, M.Hino, T.Oku, J.Suzuki, U.Matsushima, Proc. 11th Asia-Pacific Conference on Non-Destructive Testing, Jeju, Korea, 2003.

2.9.4 Preliminary Bone Imaging Study Using Neutron Computed Tomography

T. Takeda, Y. Tsuchiya, M. Matsubayashi¹, Jin Wu, Thet Thet Lwin and A. Yoneyama²

Graduate School of Comprehensive Human Sciences, University of Tsukuba, Tsukuba, Ibaraki 305-8575

¹*Tokai Establishment, JAERI, Tokai, Ibaraki 319-1195*

²*Advanced Research Laboratory, Hitachi, Ltd., Hatoyama, Saitama 350-0395*

The osteoporosis is a risk factor for fracture in older person. Since bone strength depends on quantity and quality of trabecular bone, non-destructive inner observation of bone provides a useful information for investigation of osteoporosis. Inner trabecular bone has been observed by an micro X-ray CT using synchrotron radiation, although, the inner soft tissue was not visible. Neutron radiography can sensitively detect minute changes of water content in tissues due to the large neutron attenuation for water¹⁾. Therefore, there is a possibility to detect the inner soft tissue structure of bone by neutron radiography. In this study, neutron computed tomography (CT) was applied to observe the inner bone structures for the basic medical research.

Neutron CT was performed at the thermal neutron radiography facility (TNRF-2). The sample was a rabbit's thighbone that was fixed by 10% formalin solution. A cooled CCD camera (C4880, Hamamatsu photonics. K. K.) with a fluorescence neutron converter of ⁶LiF-ZnS(Ag) was used for taking projection images. The operation temperature of the CCD was 223K. The pixel number of the CCD was 1000 × 1080 and the area of the visual view was set about 50mm × 50mm by an optical lens. Thus, the spatial resolution was 50 × 50 μm per pixel. The distance between the center of the sample stage and the fluorescence neutron converter was set at 20 mm. The projection images were taken for one degree step up to 180 degrees. Exposure time was 3 seconds for every projection. The CT images were reconstructed using filtered back projection (FBP) method with Shepp and Logan filter.

Figure 1 shows a projection image of the rabbit's thighbone. Neutron transmission was more acquired in the bone than in the inner bone marrow area. The reconstructed CT images are shown in Fig. 2. The bone and bone marrow were depicted in different CT value. The projection and CT images seemed to reflect the different moisture for bone structure.

This study showed that neutron CT has an ability to depict the different soft tissue density, and it might be possible to estimate the amount of moisture in the bone.

[Figure]

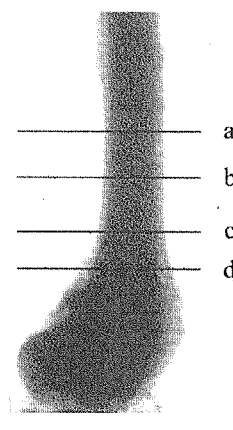


Figure 1: Projection image of the rabbit's thighbone. Bar = 5 mm.

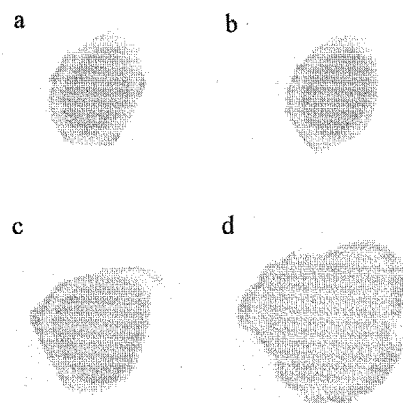


Figure 2: Neutron CT images of rabbit's thighbone.

References

- 1) Y. Tsuchiya, M. Matsubayashi, T. Takeda, Thet Thet Lwin, Jin Wu, A. Yoneyama, A. Matsumura, T. Hori and Y. Itai: *Jpn. J. Appl. Phys.* **42** (2003) 7151.

2.9.5 3D Measurement of Void Distribution of Boiling Flow in a Tight-Lattice Rod Bundle by Neutron Tomography

Masatoshi Kureta, Hidesada Tamai

Dept. of Nuclear Energy System, Japan Atomic Energy Research Institute, Japan

1. Purpose of the Experimental Study

Study on void fraction in tight-lattice rod bundles is indispensable for R&D of the Reduced-Moderation Water Reactor (RMWR)⁽¹⁾. 3D void distribution of boiling flow in a seven-rod tight-lattice bundle was measured by neutron tomography in order to investigate the boiling transition and to verify the numerical analysis codes.

2. Neutron Tomography Experiment

2.1 Neutron tomography (Neutron radiography 3D CT)

Neutron tomography system for measurement of void distribution was developed based on the neutron radiography (NR) and computed tomography (CT) techniques⁽²⁾. The experimental system was installed into the research reactor, JRR-3. Void fraction was calculated using parallel processing technique. CT value was reconstructed by the FBP method with Shepp&Logan filter. Spatial resolution was 0.1–0.2mm. Measurement error was estimated within $\pm 5\%$.

2.2 Experiment

Void measurement experiment was conducted using a seven-rod bundle test section with diameter of 12mm, gap between tubes of 1mm and heated length of 0.89m. Pure water flowed between stainless tubes which were uniformly heated by the DC power supply. Experimental condition is shown in Table 1. NR images were recorded by 180 steps (1°) in the radial direction.

2.3 Result

Figure 1 shows the measured void distribution with the tubes and flow shroud. White and dark areas between tubes indicate high and low void fraction regions, respectively. It was found from the experiments that water tends to remain between tubes and vapor tends to gather from the peripheral to the center.

3. Discussion

To evaluate the extensibility of the subchannel analysis code, COBRA-TF, to the tight-lattice rod bundle, prediction by the code was compared with the measured data. Figure 2 shows the prediction by the code. It was found from the comparison between Fig.1 and Fig. 2 that trend of the void distribution calculation was similar but the code was overestimated the void fraction.

It is because the effect of the narrow gap is not taken into account in the code. That is, applicability of the constitutive models in the code which is originally developed for a tube becomes low for a tight triangular configuration.

4. Summary

Void distribution of boiling flow in a tight-lattice bundle was measured by neutron tomography.

Followings were made clear:

(1) Water remains between tubes and vapor gathers into

Table 1: Experimental condition

Flow	Uniformly Heated, Vertical Upward, Boiling
Pressure	In: Max.0.33MPa, Exit: Atmospheric Pressure
Temperature	Inlet Temperature = 85-90 °C
Mass Velocity	139 - 462 kg/m ² s
Elevation	0.86 m
Heat Flux	19.6 - 117.6 kW/m ²

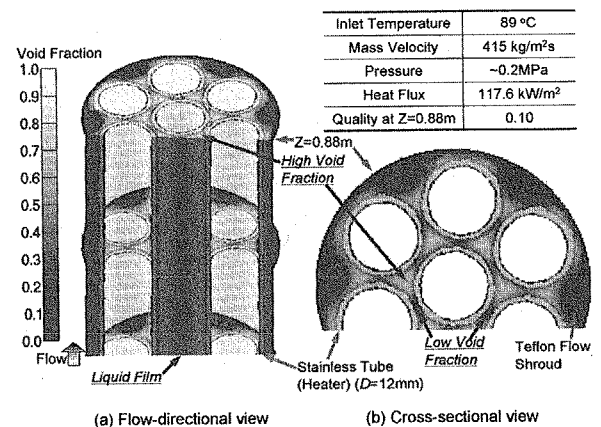


Figure 1 : Void distribution of boiling flow measured by neutron tomography.

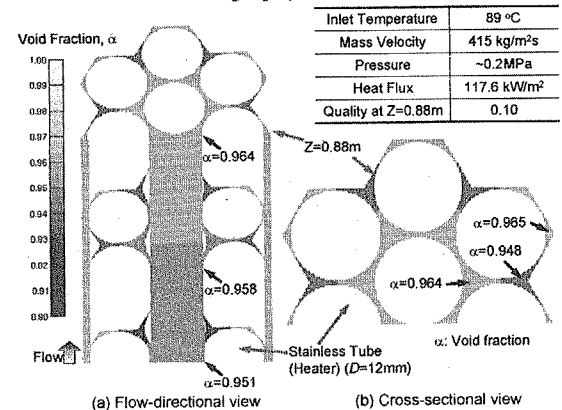


Figure 2 : Subchannel analysis of the experiment by the COBRA-TF code.

the center.

- (2) Subchannel analysis code, COBRA-TF, overestimates the void fraction in the tight-lattice bundle.

References

1. T. Okubo, *et al.*, CD-ROM of GENES4/ANP2003, No. 1145, Kyoto, Japan, 2003.
2. M. Kureta, *J. of Jet Flow Eng.*, Vol.20, 2, pp. 24-31, 2003 (in Japanese).

2.9.6 Experimental Study on Void Fraction in Tight-Lattice Rod Bundles

Masatoshi Kureta, Hiroyuki Yoshida, Akira Ohnuki* and Hajime Akimoto

*Japan Atomic Energy Research Institute, Tokai Research Establishment,
Department of Nuclear Energy System, Tokai, Naka, Ibaraki, 319-1195, Japan*

Japan Atomic Energy Research Institute (JAERI) is carrying a design study on the Reduced-Moderation light Water Reactor (RMWR) in cooperation with power companies, reactor makers and university.

The RMWR adopts a triangular tight-lattice fuel rod configuration with the gap width of about 1mm between rods, and is based on the BWR technology. The database for void fraction in such a tight bundle is indispensable to verify the numerical analysis codes in the design study.

In this paper, void fraction characteristics in the tight-lattice rod bundles are experimentally investigated. Void fraction was measured by neutron radiography (NR) technique and quick-response area-averaged void fraction meters.

Experiments were performed using two test sections ([A] 7-rod bundle with 12mm in rod diameter and 1mm gap between rods, [B] 19-rod bundle with 12mm in rod diameter and 1.3mm gap). Void fraction experiments were carried out under atmospheric pressure condition. Void fraction of air/water two-phase flow and boiling flow in [A] was measured using high-frame-rate neutron radiography (HFR-NR) and high-resolution neutron radiography (HR-NR) at the reactor room of the research reactor JRR-3M. Since neutron has a high sensitivity to thin water layer, we can not only observe but also measure the void fraction distribution in the tight rod bundle by using the neutron radiography technique. In the experiment by the NR, high void fraction of 0.5 ~ 0.92 under high gas velocity of ~max. 200m/s was measured, and behavior of two-dimensional void fraction distribution was also observed. Void fraction of air/water two-phase flow in [B] was measured by (1)

conductance-type and (2) capacitance-type area-averaged void fraction measurement techniques (void fraction meter). Void probe is metallic films which were fixed at inside of the flow channel.

In the experiment by the void fraction meter, void fraction was measured under wide range of 0.07 ~ 0.9. All measurement systems have been newly developed by the JAERI and the error estimation methods of each technique were already established.

Time-averaged flow-directional or area-averaged void fraction was evaluated with the quality or superficial velocities of gas and liquid phases. It was found from the observation by the HFR-NR that water lumps flows at the corner of the channel in case of air/water two-phase flow, on the other hand, water lumps disappeared at the corner in case of uniformly heated boiling condition. Fluctuation of the void fraction is about ± 0.1 in case of RMWR simulation condition (= void fraction is about 0.8). Void fraction map was made by the present database in order to verify the numerical analysis code.

2.9.7 Measurement of Vapor Behavior in Tight-lattice Bundles by Neutron Radiography

Masatoshi Kureta and Hajime Akimoto

Japan Atomic Energy Research Institute, Tokai, Ibaraki, JAPAN 319-1195

Three-dimensional (3D) and instantaneous void fraction distributions in tight-lattice bundles were measured by neutron radiography (NR) in order to make clear the flow behavior and to verify the advanced fine-mesh numerical analysis codes for the R&D of the Reduced-Moderation Water Reactors (RMWR) which are water-cooled breeder reactors.

Void fraction is calculated using two neutron radiography measurement systems, (1) neutron radiography 3D computed tomography (neutron tomography) and (2) high-frame-rate neutron radiography (HFR-NR) which were developed by authors. 3D time-averaged void fraction distribution is evaluated with the spatial resolution of 0.1-0.2mm using neutron tomography and consecutive changing of 2D vapor behavior is observed quantitatively with time step of 1ms using HFR-NR. Experiments were conducted in the research reactor JRR-3. 7-rod bundle test section with heated length of 0.89m ("7-rod test section") and 14-rod bundle test section with heated length of 0.24m ("14-rod test section") were used. Schematic view of the test sections were shown in Fig. 1. Void fraction is measured under atmospheric pressure and similar

inlet condition to the designed RMWR core. Rods (tubes) are fixed with gap of 1.0mm/1.3mm, and are uniformly heated. Water flows upward between rods in the flow shroud.

In this paper, void fraction and vapor behavior in tight-lattice bundles is focused and discussed based on the results obtained by the NR experiments. Figures 2 and 3 show the half-cut view of 3D void distribution and consecutive images of instantaneous void fraction in a 14-rod test section, respectively. It was found from the result of Fig. 2 that "Void drift phenomenon", vapor accumulates to the central or wide space, and high void fraction spots are appeared between rods at low quality region. And, it was observed by the HFR-NR experiments as shown in Fig. 3 that big vapor bubbles flow upward frequently not only in central flow space but in peripheral space of the channel.

The present study was conducted with the governmental funding from Publicly Invited Research Projects for Development of Innovative Nuclear Technologies by the Ministry of Education, Culture, Sports, Science and Technology (MEXT).

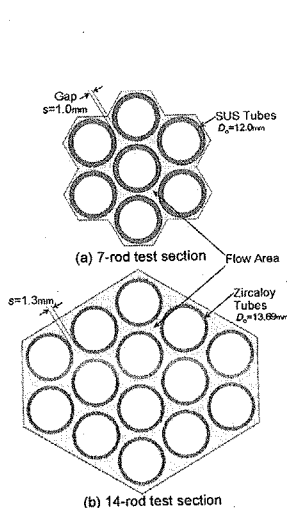


Figure 1: Test sections.

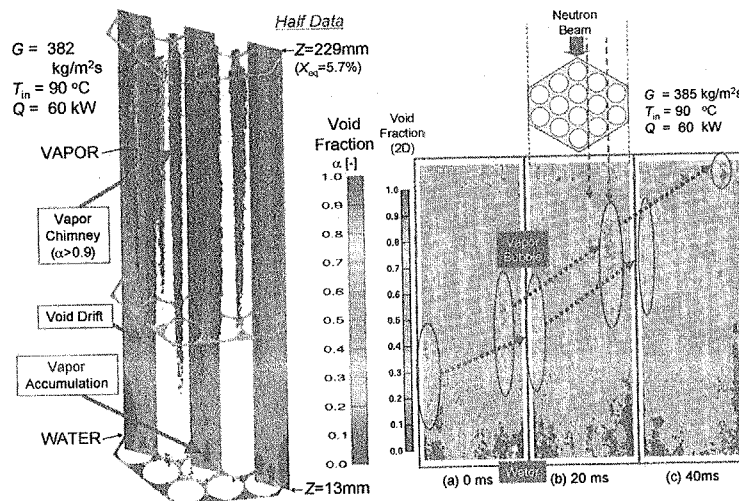


Figure 2: 3D void distribution.

Figure 3: Consecutive images of void fraction.

2.9.8 Observation of Simulated Mixed OXide Fuel Rod by Neutron Radiography

R. Yasuda, M. Nakata, M. Matsubayashi¹, A. Harada, K. Harada, Y. Nishino

JAERI, Dept. of Hot Laboratories

¹ JAERI, Neutron Science Research Center

1. Introduction

In Mixed OXide (MOX) fuels, high concentrated Pu particles in fuel pellets cause issue, which is inhomogeneous distribution of thermal stress in the fuel pellets and cladding tubes due to difference in burn up between the particles and matrix. Hence, information about the number, size, and distribution of the particles are required to evaluate integrity and reliability of the fuels. Neutron radiography (NRG) is good tool for obtaining the information about the particles because the neutron cross-section of the particle is very larger than that of the matrix. We have investigated the feasibility of advanced NRG techniques such as the neutron imaging plate (NIP) and neutron computed tomography (NCT) methods for evaluation of the Pu particle size and distribution. However, because Pu included in the MOX fuel is a fissile and poison material, usage of the MOX fuel is difficult and complicated. Hence, simulated fuel pellets controlled with neutron cross-section using ZrO_2 and Dy_2O_3 were prepared to obtain the basic data for evaluating the availability of those techniques to MOX fuels. This paper describes the outline results of examinations of the NIP and NCT techniques using the simulated fuel rod.

2. Experimental

ZrO_2 and Dy_2O_3 powders were prepared for making the simulated pellets. Those powders were ground and refined by a ball mill, and mixed with the weight percent of Dy_2O_3 to ZrO_2 , 10.0, 5.0, 3.0, 2.0, 1.0, 0.5, 0.2, 0.1 wt.% cylinder type green pellets. The mixed powder was compression-molded with loading 1.5 ton to a pellet. The pellets were sintered under air atmosphere at 1500°C for 4 hours. The sintered pellets were installed into a Zircaloy cladding tube with hydrides formed to simulate the irradiate one.

The NIP and NCT methods on the simulated fuel rod were performed using at the 2nd thermal neutron radiography facility in JRR-3. In the NIP method, the rod is fixed on a cassette with Al tapes and exposed with neutron beam for 4sec. In the NCT method, the 180 pieces of projections of the rod were obtained by a cooled type CCD camera in every

1° from $0 \sim 180^\circ$. The projections were reconstructed to tomographies by image analyses.

3. Results and Discussion

Figure 1① shows a NIP image of the simulated fuel rod. The image of the pellets becomes black with increasing the amount of adding Dy_2O_3 with the large neutron cross-section. The several black particles are observed in some pellets and are Dy_2O_3 clusters, which have not dissolved in ZrO_2 matrix at the sintering process. Fig.1② shows the Photo Stimulated Luminescence (PSL) distribution along a white dotted line A on the Fig.1①. Each plateau region on the plotted line corresponds to a position of the pellet on the Fig.1①. The difference in the concentration of the Dy_2O_3 can be numerically observed among the pellets from 0.5 to 10.0 wt.% Dy_2O_3 , although cannot be confirmed from 0.1 to 0.5 wt.%.

Figure 2 shows a CT image on a white dotted line in Fig.1①. In the CT image, the Dy_2O_3 particle distribution on the cross section can be observed. Little black areas on the image show that of less Dy_2O_3 concentration.

By the NCT and NIP method, thus, the 3d-distribution of the Dy_2O_3 particles can be non-distractively obtained.

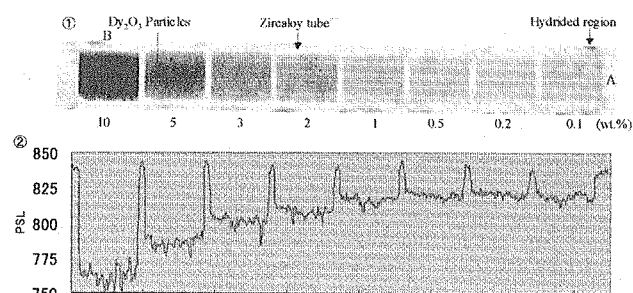
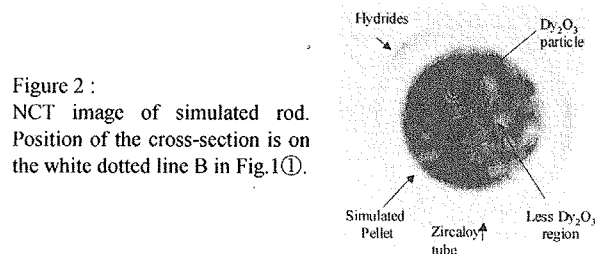


Figure 1 : ①:NIP image of simulated rod.

②:PSL distribution on the white dotted line A on the NIP image.

Figure 2 :
NCT image of simulated rod.
Position of the cross-section is on the white dotted line B in Fig.1①.

2.9.9 Observation of hydrogen distribution in hydrogen-absorbing-alloys by using neutron-radiography technique

M. Matsubayashi, T. Ebisawa¹⁾, K. Kubo²⁾, H. Arashima²⁾, and H. Itoh²⁾

Neutron Science Research Center, JAERI, Tokai, Ibaraki 319-1195

¹⁾Machinery Research Laboratory Yokohama branch, The Japan Steel Works, Ltd., Yokohama, Kanagawa 236-0004

²⁾Muroran Research Laboratory, The Japan Steel Works, Ltd., Muroran, Hokkaido 051-8505

Introduction

Recently, research and development of fuel cells is actively conducted because fuel cells are regarded as one of promising clean energies. To avoid degradation of the performance of fuel cells, hydrogen gas of a high degree of purity should be utilized. As resources of hydrogen of a high degree of purity to fuel cells, hydrogen-absorbing alloys which can store hydrogen gas in high concentration and under low pressure, are proposed. In this study, hydrogen distribution in hydrogen-absorbing alloys and alloy particles with which are filled ultra-slim hydrogen-absorbing-alloy tanks were obtained by using neutron computed tomography (CT) technique. The high-resolution-static neutron radiography system¹⁾ in JRR-3M was utilized for capturing projection images.

Hydrogen storing alloy

Even in the case that low concentration of hydrogen such as 500 ~ 600 ppm was injected into TiCrV alloy and TiCrMo alloy unlike with Mg-based alloys²⁾, hydrogen was observed to distribute homogeneously in the alloys, and to be diffused in the alloys relatively quickly.

Ultra-slim hydrogen storing alloy tank

As for ultra-slim hydrogen-absorbing-alloy tanks filled with alloy particles, the once-hydrogenated sample and the 30-times-hydrogenation-repeated sample were compared with each other. In the vicinity of the hydrogen-gas-injection hole, comparatively homogeneous distribution was observed for the once-hydrogenated sample as shown in Fig. 1. The darker portion in the image indicates higher concentration of hydrogen gas. Meanwhile, hydrogen distribution in low concentration was observed for the 30-times-hydrogenation-repeated sample in the vicinity of the hydrogen-gas-injection hole and at the bottom of the

tank, due to the repetition of hydrogen injection-and-discharge, or due to the swelling-and-shrinkage of alloy particles, or movement of alloy particles. In addition, it was confirmed that outer wall was bulged after hydrogenation by the actual measurement and that the distribution of bulge correlated well with the hydrogen distribution.

The experimental results are expected to be fed back to the manufacturing technique of tank. In the future, mechanism of hydrogen process for this alloy series and design technique of tank would be established.

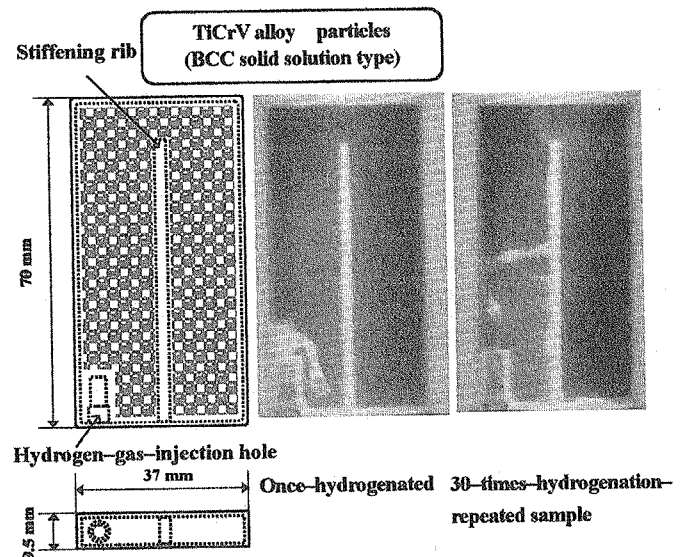


Figure 1: Schematic drawing of the Ultra-slim hydrogen absorbing alloy tank and projection images.

References:

- 1) M. Matsubayashi, *et al.*, :Nuclear Technology 132 (2000) 309-324.
- 2) H. Sakaguchi, *et al.*, :J. Alloys and Compounds 354 (2003) 208-215.

This is a blank page.

2.10 Prompt γ —ray Analysis

This is a blank page.

2.10.1 Cadmium Analysis in Rice by Multiple Gamma-ray Detection Method

Y. Toh, M. Oshima, M. Koizumi, A. Osa, A. Kimura, J. Goto, Y. Hatsukawa

Department of Material Science, JAERI, Tokai, Ibaraki 319-1195

Maximum level for cadmium of the rice in Japan is specified to 1.0 ppm. Based on the risk assessment of cadmium in Joint FAO/WHO Expert Committee on Food Additives (JECFA), the provisional tolerable weekly intake for cadmium 0.7ug/kg.bw was set up provisionally in 1988. The discussion based on the provisional tolerable 0.4ppm has been performed in Codex Committee on Food Additives and Contaminants (CCFAC)¹⁻³⁾.

The issue on cadmium concerns all foods, and especially, rice is the most important staple food in Japan and is the major crop in the Japanese agriculture. The dietary intake of rice accounts for a quarter of total daily food intake on an energy basis; and rice represents 30% of total agricultural production. Since about 50% of this is brought about from rice, the amount of ingestion will be greatly dependent on the cadmium concentration of rice. Therefore, the measurement of cadmium concentration is important for the Japanese health.

Instrumental Neutron Activation Analysis (INAA) cannot be used for the determination and quantification of cadmium. Therefore, Prompt Gamma Neutron Activation Analysis (PGA) is suitable for measurement of cadmium. When cadmium is measured by PGA, Hydrogen is the disturbance element. Since the prompt gamma ray of hydrogen is 2223keV, the prompt gamma ray of cadmium are covered by low-energy tail due to the Compton scattering and a detection limit is reduced. Although the influence from hydrogen can be reduced by using ashed samples, this procedure needs the long time and effort. Cadmium mainly emits the prompt gamma ray of 558 and 651 keV. By applying the multiple gamma ray detection method to PGA, the influence from nuclei which emits only one prompt gamma ray coincidentally can be reduced. The detection limit of cadmium contained in the rice by Prompt Gamma Neutron Activation Analysis using the Multiple Gamma ray detection method (MPGA) was estimated⁴⁾. The quantification of Cd contained in rice performed by MPGA at the C-2 port of Japan Research Reactor No.3 Modified (JRR-3M) in Japan Atomic Energy Research Institute (see Fig.1).

Taking account of Compton gamma rays of hydrogen, it is presumed that one can quantify cadmium contents in rice to 0.05 ppm or less by the MPGA measurement for 10 minutes if the detector system have about 10% absolute efficiency for prompt gamma

rays of cadmium. About 10^4 samples of the rice may be measured for three months, and the more detailed pollution inspection may be attained.

This study is supported by Industrial Technology Research Grant Program in 03A52003c from New Energy and Industrial Technology Development Organization (NEDO) of Japan.

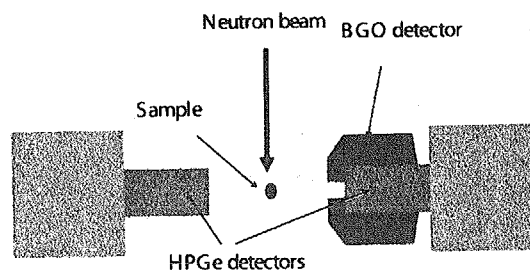


Figure 1: A schematic drawing of gamma ray detectors used in the measurement for cadmium in rice.

References

- 1) Report of the 36th session of the CODEX committee on food additives and contaminants, (Rotterdam, The Netherlands 22 - 26 March 2004).
- 2) Thirty-third Report of the Joint FAO/WHO Expert Committee on Food Additives World Health Organization Technical Report Series, (1989) p. 776.
- 3) Report of the 35th session of the CODEX committee on food additives and contaminants, (Arusha, Tanzania 17-21 March 2003).
- 4) Y.Toh, M. Oshima, Y. Hatsukawa, M. Koizumi, A. Osa, A. Kimura, J. Goto: J. of Nucl. Radiochem. Sci, Vol4 (2003) p. 197.

2.10.2 Development of Neutron In-beam Mössbauer Spectrometer

M. K. Kubo, Y. Kobayashi¹, Y. Yamada², Y. Sakai³, H. Shoji⁴, C. Yonezawa⁵, H. Matsue⁵

Department of Chemistry, International Christian University, Tokyo 181-8585

¹*Applied Nuclear Physics Laboratory, RIKEN, Wako, Saitama 351-1098*

²*Department of Chemistry, Science University of Tokyo, Shinjuku, Tokyo 162-8061*

³*Daido Institute of Technology, Minami-ku, Nagoya 457-8530*

⁴*Graduate School of Science, Tokyo Metropolitan University, Hachioji, Tokyo 192-0039*

⁵*Japan Atomic Energy Research Institute, Tokai, Ibaraki 319-1195*

Emission Mössbauer spectroscopy is a sensitive tool for investigation of trace amount of chemical species formed after radioactive decay and nuclear reactions. Among various nuclear excitation methods, thermal neutron capture has its uniqueness in the aspect that the neutron has no charge and gives less radiation damage to the material along its passage compared with charged particles especially when only γ -rays are emitted during de-excitation after the nuclear reaction. Chemical form change following a neutron capture reaction had attracted a lot of interest, but there have been a few works¹⁾ utilizing the advantage of the emission Mössbauer spectroscopy. We have been investigating the chemical and physical behaviors of implanted radioactive nuclei in various materials, e.g., ^{57}Mn in graphite and KMnO_4 ²⁾ by using a parallel plate avalanche counter (PPAC)³⁾. The high efficiency and signal-to-noise ratio (S/N) of the PPAC prompted us to start a new emission Mössbauer study aiming at the detailed *in situ* spectroscopic study on chemical and physical behaviors of the trace species produced via neutron capture reactions. Our first goal is to establish a stable system for emission Mössbauer spectroscopy of ^{57}Fe arising from the neutron capture reaction $^{56}\text{Fe}(n,\gamma)^{57}\text{Fe}$.

After a preliminary feasibility study, electrons originating from prompt γ -rays were suspected to be the main part of the noise. The PPAC is an electron detector which detects the conversion electrons after Mössbauer excitation and also Compton scattered electrons of prompt γ -rays after nuclear reactions hitting the inside of the detector, since the detector has not been equipped with an electron energy discriminator. In order to obtain good S/N we treated the inner part of the PPAC with enamel coating. After this treatment and the change of the counter gas from 2-methylpropane to perfluoropropane lead to an improvement of S/N about 50% in an off-line radioisotope source experiment.

At the PGA sample station we installed a detection setup. A stainless foil sample of 25 μm thick was placed at the target position of the PGA system facing to the neutron beam with 45 degrees and also to the PPAC. The measurement was conducted at room temperature. The spectrum (Fig. 1) showed one sin-

glet peak similar to the normal absorption one and no significant changes were observed in physical or chemical state of iron in stainless steel caused by the nuclear reaction. A metallic iron was also examined (Fig. 2).

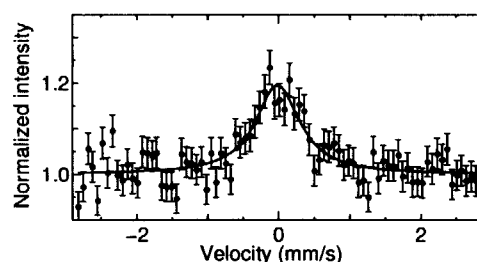


Figure 1: A neutron in-beam Mössbauer spectrum of stainless steel.

Although the only large four peaks were clearly seen due to insufficient statistics, the spectrum consisted of a sextet line as seen in normal absorption spectroscopy. In this study the first step of construction of a neutron in-beam Mössbauer spectrometer has been achieved. Temperature variation in measurement will be the next stage.

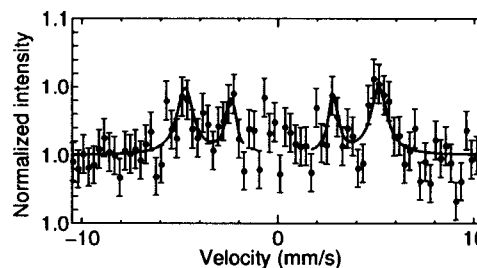


Figure 2: A neutron in-beam Mössbauer spectrum of metallic iron.

References

- 1) W. G. Berger *et al.*, *Phys. Lett.*, **24A**, 466 (1967). W. G. Berger, *Z. Phys.*, **225**, 139 (1969). G. Czjzek and W. G. Berger, *Phys. Rev.*, **B1**, 957 (1970).
- 2) Y. Kobayashi *et al.*, *Eur. Phys. J. A* **13**, 243 (2002). Y. Kobayashi *et al.*, *J. Radioanal. Nucl. Chem.*, **255**, 403 (2003).
- 3) T. Saito *et al.*, *J. Radioanal. Nucl. Chem.*, **255**, 519 (2003).

2.10.3 A Research on Boron in Soybean Plants using Doppler Broadening of Prompt γ -RayY. Sakai, M. K. Kubo¹, H. Matsue² and C. Yonezawa²*Daido Institute of Technology, Nagoya 457-8530, Japan*¹*International Christian University, Tokyo 181-8585, Japan*²*Japan Atomic Energy Research Institute, Ibaraki 319-1195, Japan*

We revealed that the prompt γ -ray analysis (PGA) can be applied to physico-chemical characterization of materials containing and/or surrounding boron species by probing the Doppler broadened line shape of 478-keV γ -ray emitted from ^7Li which is produced in the $^{10}\text{B}(n,\alpha)^7\text{Li}$ reaction¹⁾. The energetic ^7Li ion loses the kinetic energy through the interaction with atoms which the moving ion encounters in medium. It was proved experimentally and theoretically that the velocity $v(t)$ decreases with time t ;

$$v(t) = v_0 \exp(-Dt),$$

where v_0 is the initial velocity ($4.8 \times 10^6 \text{ ms}^{-1}$) and D is called "degradation constant". At the first approximation, the degradation constant D for a compound or a mixture is obtained from a weighted sum of degradation constants of the constituent elements. From analytical-scientific viewpoints, D is expected to reflect the elemental composition and the average density of a material where ^7Li ions move and lose their kinetic energy.

It is well known that boron is one of the essential micronutrients for plants. However, the biochemical function of boron in plant life has not been yet understood sufficiently, although a number of investigations have been done so far. In most of such researches, physiological and/or biochemical changes occurring when plants are deprived of boron have been experimentally studied, which should, however, be indirect functions but not those for normal "live" plants.

In the present article, we report on the boron dynamics in soybeans at the various stages of growing by applying the Doppler broadening method. It should be emphasized that by this non-destructive method boron species in "live" soybeans were examined in-situ, resulting in an important clue to clarify the biological functions in plants.

Commercially available soybean seeds were

purchased. Prompt γ -ray measurement was carried out for the dry seed with no treatment (Sample A). The seeds were germinated on sheets of wetted tissue paper after immersing in water overnight. One of the swelling seeds with a bourgeon after 3 days (Sample B) was submitted to the measurement. Another one was grown to a greenish sprout after 7 days and used as a target sample (Sample C). Another swelling seed was transferred onto a pot of soil. It grew up to a young plant of ca. 30 cm height with many green leaves after 40 days, one of which was taken as Sample D. All the samples were picked up and sealed in a polyethylene bag immediately before the measurements. Harvested seeds (Sample E), which were obtained after air-drying the mature soybean plant with crops inside a room for about two months, were also submitted to the measurement.

The measurements were performed for several hours using the PGA system installed at the neutron-beam guide of JRR-3M by Yonezawa et al.²⁾. The line shapes of the Doppler broadened spectra depend greatly on the degradation constant D , from which we evaluated the D values by a fitting procedure proposed by Kubo and Sakai³⁾ previously. The measured prompt γ -ray spectra at 478 keV of ^7Li for the soybean samples are shown in Figure 1. The degradation constants D obtained from the line-shape analysis are 1.46, 1.26, 1.27, 1.74, and 1.47 in a unit of 10^{12} s^{-1} for the samples of A, B, C, D, and E, respectively. For a comparison, it had better cite the D values reported in our previous paper¹⁾; 1.48 and 1.22 in a unit of 10^{12} s^{-1} for polycrystalline boric acid (H_3BO_3) and aqueous solution of H_3BO_3 , respectively.

The D values for both the dry seeds for planting (Sample A) and the dry seeds harvested (Sample E) are close to each other, implying that the boron species in the harvested soybean seeds

was recycled to that of the starting seeds. These values are also very close to that for polycrystalline boric acid. This result suggests that boron in dry soybean seeds is in the physicochemical form of solid H_3BO_3 or that close to it.

As been obviously distinguished in Figure 1, the line shapes of the swelling seed (Sample B) and the sprout (Sample C) are substantially different from those of the dry seeds (Sample A and E). The fitted D values for both the samples are found to be close to each other and close to that of an aqueous solution of boric acid, leading to that the boron species in the swelling seed and the sprout should be dissolved in water.

The D value obtained for the fresh green leaves of young soybean plant (Sample D) was relatively high as described above. It is, however, very difficult or almost impossible to ascribe such a high D value of $1.74 \times 10^{12} \text{ s}^{-1}$ to boron in some organic medium or polycrystalline boric acid, because the high value forces us to speculate that boron might be surrounded with atoms having high atomic-numbers and/or with a high density. This finding seems mysterious but very interesting, which stimulates our academic and practical curiosity greatly and leads us to furthermore research.

Our work does not provide information on sufficient biological functions of boron. However, it is safely mentioned that the Doppler broadening method should be a new and powerful tool for non-destructive characterization of boron species in biological samples.

Details of the present report will be soon published elsewhere⁴⁾.

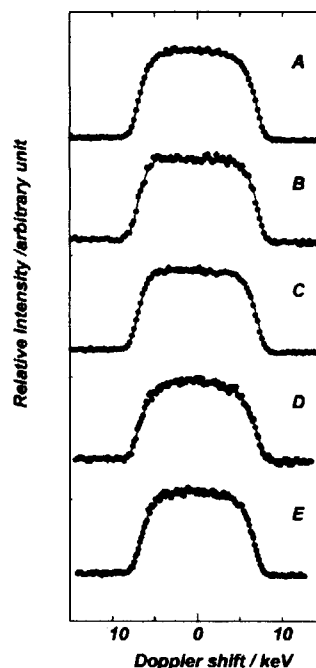


Figure 1: Spectral line-shapes of prompt γ -ray of 478 keV of ^7Li measured for the following samples of soy-bean plant: A; Dry seeds (no treatment after purchased) (0 day, i.e., before planting), B; Swelling seeds with a small bourgeon (3 days), C; Sprout (7 days), D; Leaves of the young plant (40 days), E; Dry seeds (153 days, harvested)

References

- 1) Y. Sakai, C. Yonezawa, M. Magara, H. Sawahata, Y. Ito : Nuclear Instrum. Methods, Phys. Res. **A353** (1994) 699.
- 2) C. Yonezawa, A. K. Haji Wood, M. Hoshi, Y. Ito, E. Tachikawa : Nuclear Instrum. Methods, Phys. Res. **A329** (1993) 207.
- 3) M. K. Kubo, Y. Sakai : J. Nucl. Radiochem. Sci. **1** (2000) 83.
- 4) Y. Sakai, M. K. Kubo, H. Matsue, C. Yonezawa : J. Radioanal. Nucl. Chem.: in press (2004).

Appendix

This is a blank page.

Appendix A

Program Committee for Neutron Beam Utilization in the JFY 2003 of the Advisory Council for JAERI'S Research Facilities

(Chairman)	Hideki	Yoshizawa	Professor, The Institute for Solid State Physics, The University of Tokyo
(Vice-Chairman)	Mitsuru	Ebihara	Professor, Graduate School of Science, Tokyo Metropolitan University
	Susumu	Ikeda	Professor, High Energy Accelerator Research Organization
	Toshiji	Kanaya	Professor, Institute for Chemical Research, Kyoto University
	Kenya	Kubo	Associate Professor, Division of Natural Sciences, International Christian University
	Masafumi	Kohgi	Professor, Graduate School of Science, Tokyo Metropolitan University
	Mamoru	Sato	Professor, Graduate School of Integrated Science, Yokohama City University
	Hirohiko	Shimizu	Research Unit Leader, Image Information Research Unit, RIKEN
	Masayoshi	Tamaki	Associate Professor, Department of Nuclear Engineering, Nagoya University
	Takeji	Hashimoto	Professor, Graduate School of Engineering, Kyoto University
	Makoto	Hayashi	Head, Div Power, Laboratory, Hitachi Ltd.
	Kazuma	Hirota	Associate Professor, Graduate School of Science, Tohoku University
	Kazuyoshi	Yamada	Professor, Institute for Materials Research, Tohoku University
	Yukio	Oyama	Director, Center for Proton Accelerator Facilities, JAERI
	Kazuhisa	Kakurai	Principal Scientist, Advanced Science Research Center, JAERI
	Masaki	Katagiri	Principal Scientist, Neutron Science Research Center, JAERI
	Takemasa	Shibata	Deputy Director, Advanced Science Research Center, JAERI
	Nobuo	Niimura	Professor, Department of Systems Engineering, Ibaraki University
	Yasuhiko	Fujii	Director, Neutron Science Research Center, JAERI
	Yoshiro	Funayama	Deputy Director, Department of Research Reactor, JAERI
	Kazuo	Watanabe	Deputy Director, Department of Environmental Sciences, JAERI
(Secretary)	Yukio	Morii	Deputy Director, Neutron Science Research Center, JAERI
(Secretary)	Hisashi	Sagawa	General Manager, Department of Research Reactor, JAERI
(Observer)	Teruo	Inabe	Head, Division of Collaborative Activities, Office of Planning, JAERI
(Observer)	Hiromasa	Watanabe	Head, Office of Planning
(Observer)	Masahito	Matsubayashi	Senior Scientist, Neutron Science Research Center, JAERI
(Observer)	Chushiro	Yonezawa	Senior Scientist, Department of Environmental Sciences, JAERI
(Observer)	Naohiko	Hori	Chief, Department of Research Reactor, JAERI

Appendix B**Themes of Cooperative Research Projects with Universities in the JFY 2003**

N-01	Evaluation of Residual Stress and Material Properties under Loading in Structural Materials	Y. Akiniwa	Nagoya Univ.
N-02	The First Challenge to Refined Structural Analysis of Synthetic Polymer Crystals by Neutron Imaging Plate System	K. Tashiro	Osaka Univ.
N-03	Structural Analysis of a Functional Reaction Field Formed by Chemical Complexes in Supercritical Carbon Dioxide	Y. Enokida	Nagoya Univ.
N-04	Crystal Structures of Polymers	Y. Takahashi	Osaka Univ.
N-05	Disorder in Superionic Conductors	T. Sakuma	Ibaraki Univ.
N-06	Exotic Magnetic Phases of Ce-compound-strongly-correlated-electron-systems under High Pressure and Low Temperatures	M. Kohgi	Tokyo Metro. Univ.
N-07	Study of the New Type of Heavy Fermion Super Conductor $\text{PrOs}_4\text{Sb}_{12}$	M. Kohgi	Tokyo Metro. Univ.
N-08	A High Resolution Neutron Structure Analysis of FMN-binding Protein	Y. Morimoto	Kyoto Univ.(KURRI)
N-09	Mechanism Analysis of a Salicylate Hydroxylase by a Neutron Structural Analysis	Y. Morimoto	Kyoto Univ.(KURRI)
N-10	Supercritical Carbon Dioxide / Metallic Colloids Composition and its Structural Change at the Emulsion Place which Water Forms	M. Harada	Nara Women's Univ.
N-11	Study on the Mechanism of Residual Stress of Steel Caused by Heat Treatment	K. Inoue	Ryukoku Univ.
N-12	Magnetic and Chemical Structures of Semi Magnetic Conductors, II	T. Kajitani	Tohoku Univ.
N-13	Spin Dynamics of Hole-doped $(\text{Nd}, \text{Y}, \text{Ca})_2\text{BaNiO}_5$	J. Akimitsu	Aoyama Gakuin Univ.
N-14	Neutron Scattering Study of Spin Fluctuations in the High- T_c Cuprates under Extreme Conditions	K. Yamada	Tohoku Univ.

- | | | | |
|------|--|---------------|------------------------|
| N-15 | Development of Cold Neutron Imaging Detector | H. Sakurai | Yamagata Univ. |
| N-16 | Development of the Method for Determining Residual Stress using Whole Part of Neutron Debye-scherrer Pattern Detected with Neutron Image Plate | T. Sasaki | Kanazawa Univ. |
| N-17 | Investigation of Magnetic Structure of Z-type Ba Ferrite and its Temperature Dependence | T. Yamamoto | Osaka Univ. |
| N-18 | Elementary Excitations in the Quantum Spin System TiCuCl_3 and Related Compounds | H. Tanaka | Tokyo Inst. of Tech. |
| N-19 | Magnetic-field-induced Structures in Organic Organized Materials | S. Ozeki | Shinshu Univ. |
| N-20 | Search for Chiral Glass Phase in Ceramic Superconductor by Polarized Neutrons | S. Kawarazaki | Osaka Univ. |
| N-21 | Magnetic Structure of Perovskite Oxides Containing Lanthanide and Iridium | Y. Hinatsu | Hokkaido Univ. |
| N-22 | Green Chemistry in Nano-structure of Self-assembled Molecules | M. Annaka | Kyushu Univ. |
| N-23 | Missing Number | | |
| N-24 | Three-dimensional Structure Analysis of Endopolygalacturonase I from <i>Stereum Purpureum</i> by Neutron Diffraction | Mamoru Sato | Yokohama City Univ. |
| N-25 | Geometrical Spin Frustration System under the High Pressure | Y. Tsunoda | Waseda Univ. |
| N-26 | Measurement of Residual Stress Distribution on Laser Peened Inner Surface of Pipe | K. Akita | Musashi Inst. of Tech. |
| N-27 | Analysis of Hydrogen Transfer Process in the Formation of Lactams from Amides | Y. Ohashi | Tokyo Inst. of Tech. |
| N-28 | Missing Number | | |
| N-29 | Antiferromagnetism in the Lightly Hole-doped $\text{La}_{2-x}\text{SrCuO}_4$ with Ni-substitution | K. Yamada | Tohoku Univ. |
| N-30 | Studies on Reactive Block Copolymer Systems | T. Hashimoto | Kyoto Univ. |
| N-31 | Observation of Quadrupolar Orderings in RB_2C_2 by Neutron Diffraction under High Magnetic Fields | H. Onodera | Tohoku Univ. |

N-32	Successive Phase Transitions of $\text{RBaCo}_2\text{O}_{5.5}$ (R=Tb, Ho and Y)	Masatoshi Sato	Nagoya Univ.
N-33	Pressure-induced Metal-insulator Transition of $\text{Pr}_{1-x}\text{A}_x\text{CoO}_3$ (A=Ca, Sr and Ba)	Masatoshi Sato	Nagoya Univ.
N-34	Dynamical Study on Clathrate Hydrates	T. Kamiyama	Hokkaido Univ.
N-35	Functional Mechanism of Proteins Based on Their Hydrogen-atom Positions	K. Fukuyama	Osaka Univ.
N-36	Relation between Nano-scale Structural Distortions and Meta-magnetic Transition in $\text{Sr}_3\text{Ru}_2\text{O}_7$	Y. Uwatoko	The Univ. of Tokyo
N-37	Observation of Aspect Structure Change in Polymer Mixture System According to Progress of Polymerization Reaction	Y. Matsushita	Nagoya Univ.
N-38	Relationship between Dynamic Heterogeneities and Concentration Fluctuations in Miscible Polymer Blends 3	M. Naoki	Gunma Univ.
N-39	Crystallization of Block Copolymers and Their Blends with Corresponding Homopolymers	T. Shiomi	Nagaoka Univ. of Tech.
N-40	Lattice Dynamics of PbTiO_3 and RVO_4	I. Tomeno	Akita Univ.
N-41	Flux Line Study on Heavy Fermion Superconductor $\text{PrOsO}_4\text{Sb}_{12}$	H. Sato	Tokyo Metro. Univ.
N-42	Measurement of Internal Stresses in Structure-graded Materials	T. Hanabusa	Tokushima Univ.
N-43	Nano-structure Formation of Surfactant-polymer Complex under Shear	Y. Soejima	Kyushu Univ.
N-44	Study on the Relation between Unusual Formation of High-ordered Protein Structures and Abnormal Apoptosis	M. Furusaka	KEK
G-01	Study of Chemical Behaviors of Swift Charged Particles Using Neutron Beam Guides	Y. Sakai	Daido Inst. of Tech.
G-02	Study of Chemical Behaviors of Swift Charged Particles Using	K. Kubo	ICU
R-01	Image Analysis of Biological Objects by Neutron Radiography	T. Takeda	Tsukuba Univ.
R-02	Development and Application Radiography Techniques with High Temporal Resolution	K. Mishima	Kyoto Univ.(KURRI)

Appendix C**Themes of Cooperative Research Projects with Private Enterprises
and National Laboratories in the JFY 2003**

NK-01 Application with drawal

NK-02 Investigation for the Construction of Tannin Gels Adsorbing with Metal Elements	K. Hamaguchi	Mitsubishi Nucler Fuel Co. Ltd.
NK-03 In Situ Observation of Deformation of Polymer Chain by Small-angle Neutron Scattering	T. Kasahara	Sumitomo Chemical Co. Ltd.
NK-04 Refractive Optics and Detector for Cold Neutron	H. M. Shimizu	RIKEN
NK-05 Evaluation of Strength in Overlaying Materials by Neutron Diffraction	R. Ishikawa	Hitachi Engineering Co. Ltd.
NK-06 Missing Number		
NK-07 Evaluation on Residual Stress of Weld Joint in Nuclear Core Internal Structure	I. Komura	JAPEIC
NK-08 Development of the Residual Strain Measurement Technique of Automobile Engine Parts by the Neutron Diffraction Method	T. Hamamoto	Toyota Co. Ltd.
NK-09 Study of Liquid Structures in the High Temperature/under Cooling State Due to Electrostatic Levitation Furnace	S. Yoda	JAXA

Appendix D

Publication List in the Period of the JFY 2003

1. Beam Enhancement with a HOPG Pre-crystal in the Precise Neutron Optics
H. Tomimitsu, Y. Hasegawa, K. Aizawa
Phys. Lett. A (2003) 183-188
2. Evidence for Magnetic-field-induced Quadrupolar Ordering in the Heavy-fermion Superconductor $\text{PrOs}_4\text{Sb}_{12}$
M. Kohgi, K. Iwasa, M. Nakajima, N. Metoki, S. Araki, N. Bernhoeft, J.-M. Mignot,
A. Gukasov, H. Sato, Y. Aoki, H. Sugawara
J. Phys. Soc. Jpn. **72** No.5 (2003) 1002-1005
3. Neutron Diffraction Study of the Pressure-Induced Magnetic Ordering in the Spin Gap System TiCuCl_3
A. Oosawa, S. Fujisawa, T. Osakabe, K. Kakurai, H. Tanaka
J. Phys. Soc. Jpn. **72** No.5 (2003) 1026-1029
4. Neutron Diffraction Study of $5f$ Itinerant Antiferromagnet UPtGa , and UNiGa ,
K. Kaneko, N. Metoki, G. H. Lander, N. Bernhoeft, Y. Tokiwa, Y. Haga, Y. Onuki, Y. Ishii
Physica B **329-333** (2003) 510-511
5. Polarized Neutron Scattering Study of the CuO_2 Chains in $\text{Ca}_2\text{Y}_2\text{Cu}_2\text{O}_{10}$
M. Matsuda, M. Nakamura, M. Takeda, K. Kakurai, H. Yamaguchi, T. Ito, K. Oka
Physica B **329-333** (2003) 711-712
6. Neutron Scattering Study of Magnetic Ordering and Excitations in the Doped Spin Gap System $\text{Ti}(\text{Cu}_{1-x}\text{Mg}_x)\text{Cl}_3$
A. Oosawa, M. Fujisawa, K. Kakurai, H. Tanaka
Phys. Rev. B **67** (2003) 184424 1-8
7. Specific Heat of the Tetragonal Antiferromagnet TbB_2C_2
K. Kaneko, H. Onodera, Y. Yamaguchi
Acta Physica Polonica B **34** (2003) 1007-1010
8. Neutron Scattering Study on Magnetic Order and Magnetic Excitations of a Localized Uranium Compound $\text{U}_3\text{Pd}_8\text{Si}_6$
K. Koike, N. Metoki, Y. Haga, K. A. McEwen, M. Kohgi, R. Yamamoto, N. Aso,
T. Komatsubara, N. Kimura, H. Aoki
Acta Physica Polonica B **34** (2003) 1121-1124
9. Superconductivity in CeRh_2Si_2 under Pressure
S. Araki, M. Nakashima, R. Settai, T. C. Kobayashi, A. Onuki
Acta Phys. Polonica B **34** (2003) 439-442
10. Crystal Structure, Magnetic Ordering, and Magnetic Excitation in the $4f$ -localized Ferromagnet CeAgSb_2
S. Araki, N. Metoki, A. Galatanu, E. Yamamoto, A. Thamizhavel, Y. Onuki
Phys. Rev. B **68** (2003) 024408-1~9
11. The Inside Evaluation of Material Contributes to Product Development
Y. Morii
The Science News (2003.8.8) 6 (Japanese)
12. Polarization Dependence of Spin Excitations in $\text{BaCu}_2\text{Si}_2\text{O}_7$
A. Zheludev, S. Raymond, L.-P. Regnault, F. H. L. Essler, K. Kakurai, T. Masuda, K. Uchinokura
Phys. Rev. B **67** (2003) 134406-1~10

13. Higher-order Collinear Interaction and Magnetic Excitation in the $5f$ Localized System $U_3Pd_{10}Si_4$
N. Metoki, Y. Koike, Y. Haga, K. Kaneko, S. Araki, K. A. McEwen, M. Kohgi, N. Aso,
G. H. Lander, T. Komatsubara, N. Kimura, H. Aoki, Y. Onuki
J. Phys.: Condens. Matter **15** (2003) S1957-S1963
14. Cold Neutron Beam Focusing by a Superconducting Sextupole Magnet
J. Suzuki, T. Oku, T. Adachi, H. M. Shimizu, T. Hiramachi, T. Tsuchihashi, I. Watanabe
J. Appl. Cryst **36** (2003) 795-799
15. Magnetic Order of UGa_3 Investigated by Means Neutron Scattering under Uniaxial Pressure
M. Nakamura, T. D. Matsuda, K. Kakurai, G. H. Lander, S. Kawarazaki, Y. Onuki
J. Phys.: Condens. Matter **15** (2003) S1997-S2000
16. Crystalline Electric Field Excitations in $CeAgSb_2$
S. Araki, N. Metoki, A. Thamizhavel, Y. Onuki
J. Phys.: Condens. Matter **15** (2003) S2179-S2182
17. Magnetic Structures of High Temperature Phases of $TbBaCo_2O_{5.5}$
M. Soda, Y. Yasui, T. Fujita, T. Miyashita, M. Sato, K. Kakurai
J. Phys. Soc. Jpn. **72** No.7 (2003) 1729-1734
18. Effects of "Stripes" on the Magnetic Excitation Spectra of $La_{1-x}Nd_xSr_{0.12}CuO_4$
M. Ito, Y. Yasui, S. Iikubo, M. Soda, M. Sato, A. Kobayashi, K. Kakurai
J. Phys. Soc. Jpn. **72** No.7 (2003) 1627-1630
19. Crystal and Magnetic Structure in the Itinerant $5f$ Antiferromagnet UCr_2Si_2
T. D. Matsuda, N. Metoki, Y. Haga, S. Ikeda, K. Kaneko, E. Yamamoto, Y. Onuki
J. Phys.: Condens. Matter **15** (2003) S2023-S2027
20. Magnetic Properties of U_2RhGa_8 and U_2FeGa_8
S. Ikeda, T. Okubo, Y. Inada, Y. Tokiwa, K. Kaneko, T. D. Matsuda, E. Yamamoto, Y. Haga, Y. Onuki
J. Phys.: Condens. Matter **15** (2003) S2015-S2018
21. Magnetic P-T Phase Diagrams of $CeSb$ and $CeBi$
T. Osakabe, A. Hannan, D. Kawana, M. Kohgi, H. Kitazawa
Acta Physica Polonica B **34** (2003) 1469-1472
22. Magnetic Excitations in an Itinerant $5f$ Antiferromagnet UPt_2Si_2
N. Metoki, Y. Koike, Y. Haga, N. Bernhoeft, G. H. Lander, Y. Tokiwa, Y. Onuki
Acta Physica Polonica B **34** (2003) 979-982
23. Development of a Spin Flipper for an Application of a Neutron Magnetic Device
T. Oku, K. Sakai, T. Adachi, K. Ikeda, H.M. Shimizu, R. Maruyama, M. Hino, S. Tasaki, Y. Kiyonagi,
T. Kamiyama, H. Iwasa, K. Sasaki, T. Ino, M. Furusaka, D. Yamazaki, J. Suzuki, T. Ebisawa
Physica B **335** (2003) 226-229
24. Magnetic Phase Diagrams with Possible Field-induced Antiferroquadrupolar order in TbB_2C_2
K. Kaneko, H. Onodera, H. Yamauchi, T. Sakon, M. Motokawa, Y. Yamaguchi
Phys. Rev. B **68** (2003) 012401-1~4
25. Small-angle Scattering on Soft Matter with Dynamical Asymmetry
S. Koizumi
J. Appl. Cryst. **36** (2003) 381-388

26. Single Crystal Growth and Magnetic Properties of 5f-itinerant Antiferromagnet UPdGa_3
S. Ikeda, N. Metoki, Y. Haga, K. Kaneko, T. D. Matsuda, A. Galatanu, Y. Onuki
J. Phys. Soc. Jpn. **72** No.10 (2003) 2622-2626
27. Frustrating Interactions and Broadened Magnetic Excitations in the Edge-sharing CuO_2 Chains in $\text{La}_5\text{Ca}_4\text{Cu}_{14}\text{O}_{41}$
M. Matsuda, K. Kakurai, J. E. Lorenzo, L. P. Regnault, A. Hiess, G. Shirane
Phys. Rev. B **68** (2003) 06406-1~4
28. Electrical and Magnetic Properties of Pseudo-One-Dimensional Calcium Iridium Oxide $\text{Ca}_2\text{Ir}_2\text{O}_{12}$
M. Wakeshima, N. Taira, Y. Hinatsu, Y. Ishii
Solid State Commun. **125** (2003) 311-315
29. Magnetic Studies on Quaternary Iron Sulfides $\text{BaLn}_2\text{FeS}_6$ ($\text{Ln}=\text{Ce}, \text{Pr}, \text{Nd}, \text{Sm}$) by Magnetic Susceptibility, Specific Heat, ^{57}Fe Mossbauer Spectrum and Neutron Diffraction Measurements
M. Wakeshima, K. Ino, Y. Hinatsu, Y. Ishii
Bull. Chem. Soc. Jpn. **76** (2003) 1519-1525
30. Development of a High-resolution Scintillator-based Area Detector for Neutrons
N. Sakamoto, Y. Kiyonagi, S. Sato, H. Sagehashi, M. Furusaka, J. Suzuki, K. C. Littrell, C. K. Loong, A. Gorin, I. Manuilov, A. Ryazantsev, K. Kuroda, K. Sakai, F. Tokanai, T. Adachi, T. Oku, K. Ikeda, H. Miyasaka, S. Suzuki, K. Morimoto, H. M. Shimizu
J. Appl. Cryst. **36** (2003) 820-825
31. Recent Progress in the Development of Concave Fresnel lenses for Neutrons
T. Adachi, K. Ikeda, T. Oku, K. Sakai, S. Suzuki, J. Suzuki, H. M. Shimizu, K. C. Littrell, C.-K. Loong, W. Lin, J. Guo, N. Mitsuishi, S. Morita, H. Ohmori
J. Appl. Cryst. **36** (2003) 806-808
32. Structure and Thermal Expansivity of Tetrahydrofuran Deuterate Determined by Neutron Powder Diffraction
C. Y. Jones, S. L. Marshall, B. C. Chakoumakos, C. J. Rawn, Y. Ishii
J. Phys. Chem. B **107** (2003) 6026-6031
33. Neutron Diffraction Study of Structure I and Structure II Trimethylene Oxide Clathrate Deuterate
A. J. Rondinone, B. C. Chakoumakos, C. J. Rawn, Y. Ishii
J. Phys. Chem. B **107** (2003) 6046-6050
34. CO_2 Hydrate: Synthesis, Composition, Structure, Dissociation Behavior, and a Comparison to Structure I CH_4 Hydrate
S. Circone, L. A. Stern, S. H. Kirby, W. B. Durham, B. C. Chakoumakos, C. J. Rawn, A. J. Rondinone, Y. Ishii
J. Phys. Chem. B **107** (2003) 5529-5539
35. Development of an Electrostatic Levitator for Neutron Diffraction Experiments
Y. Ishii, T. Masaki
Hamon **13** No.3 (2003) 177-178 (Japanese)
36. Complimentary Use of Neutron and X-ray Reflection in Study on a Giant Magnetoresistance (GMR) Effect of Magnetic Multilayers
M. Takeda, Y. Endoh, A. Kamijo, S. Langridge, R. Dalglish, J. H. Her, K. B. Lee
Trans. MRS-J **28** (2003) 23-26
37. Thermal Vibration in Superionic Conducting Glasses by Neutron Elastic Scattering
H. Takahashi, T. Sakuma, Y. Ishii
Solid State Ionics **160** (2003) 103-107

38. Long Periodic Magnetic Structure in CeB_2C_2
K. Ohoyama, K. Kaneko, T. Onimaru, A. Tobo, K. Ishimoto, H. Onodera, Y. Yamaguchi
J. Phys. Soc. Jpn. **72** No.12 (2003) 3303-3304
39. Magnetic Properties of Tetragonal $\text{Ce}_{1-x}\text{Lu}_x\text{B}_2\text{C}_2$ ($0 \leq x \leq 0.31$) Compounds
A. Tobo, K. Ishimoto, J. Konno, K. Ohoyama, K. Kaneko, Y. Yamaguchi, H. Onodera
J. Phys. Soc. Jpn. **72** No.12 (2003) 3231-3236
40. Large Orbital Magnetic Moment and Its Quenching in Itinerant Uranium Intermetallic Compounds
 UT Ga_5 (T: Ni, Pd, Pt)
K. Kaneko, N. Metoki, N. Bernhoeft[†], G. H. Lander, Y. Ishii, S. Ikeda, Y. Tokiwa, Y. Haga, Y. Omuki
Phys. Rev. B **68**(2003)214419 1-9
41. Comparative Study on the Magnetic Excitation Spectra of Y123 and La214 High-T_c Systems
— Are the Dynamical Stripes Important?
M. Sato, M. Ito, H. Harashina, Y. Yasui, S. Iikubo, A. Kobayashi, K. Kakurai
Physica B **329-333** (2003) 683-684
42. Magnetic Structure and the Anomalous Hall Effect of $\text{Cu}_{1-x}\text{Zn}_x\text{Cr}_2\text{Se}_4$
S. Iikubo, Y. Ohno, Y. Yasui, T. Fukamachi, K. Oda, M. Sato, K. Kakurai
Physica B **329-333** (2003) 707-708
43. Phonon Anomaly in the Inorganic Spin-Peierls Compound CuGeO_3
M. Nishi, Y. Fujii, H. Kadowaki, S. Katano, K. Kakurai, J. Akimitsu
Physica B **329-333** (2003) 872-873
44. Field-induced Magnetic ordering in TiCuCl_3 : Lattice Deformation and Features of First-order Transition
O. Vyaselev, M. Takigawa, A. Vasiliev, A. Oosawa, H. Tanaka
Physica B **329-333** (2003) 892-893
45. Detailed Studies on the Anomalous Hall Effect of Pyrochlore Molybdates
Y. Yasui, T. Kageyama, S. Iikubo, K. Oda, M. Sato, K. Kakurai
Physica B **329-333** (2003) 1036-1037
46. Doppler Shift Neutron Spin Echo at Bragg Reflection of Magnetite Particle in Ferrofluid
N. Achiwa, H. Nishioka, T. Ebisawa, M. Nishi, K. Nakajima, K. Kakurai
Physica B **335** (2003) 104-108
47. Neutron Scattering Studies on In-plane Longitudinal Phonons of $\text{YBa}_2\text{Cu}_3\text{O}_y$
M. Ito, H. Harashina, Y. Yasui, M. Sato, K. Kakurai
Physica C **388-389** (2003) 363-364
48. Spin Dynamics of the Spin Dimer System TiCuCl_3 Probed by Raman Spectroscopy
K. -Y. Choi, G. Guntherodt, A. Oosawa, H. Tanaka, P. Lemmens
Phys. Rev. B **68** (2003) 174412 1-6
49. Sound Attenuation Study on the Bose-einstein Condensation of Magnons in TiCuCl_3
E. Ya. Sherman, P. Lemmens, B. Busse, A. Oosawa, H. Tanaka
Phys. Rev. Lett. **91** (2003) 057201-1-4
50. Ferromagnetic Transition of Pyrochlore Compound $\text{Yb}_2\text{Ti}_2\text{O}_7$
Y. Yasui, M. Soda, S. Iikubo, M. Ito, M. Sato, N. Hamaguchi, T. Matsushita, N. Wada,
T. Takeuchi, N. Aso, K. Kakurai
J. Phys. Soc. Jpn. **72** No.11 (2003) 3014-3015

51. Higher-order-filter Velocity Selector for Thermal Neutrons
K. Kakurai, H. Okumura, K. Nukui, N. Aso, K. Nakajima, M. Nishi, K. Suzuki, S. Watanebe,
Y. Kawamura, B. Betzold, M. Sato
Hamon 13 No.4 (2003) 223-225 (Japanese)
52. Recent Activities and Progress on PORE Reflectometer
M. Takeda, N. Torikai, T. Ino, S. Tasaki
KENS Report-XIV 2001-2002 (2003) 205-206
53. Neutron Structural Biology, Complementarity between Neutron and X-ray
N. Niimura, T. Chatake
Hamon 13 No.1 (2003) 47-50 (Japanese)
54. Hydration in Proteins Observed by High-resolution Neutron Crystallography
T. Chatake, A. Ostermann, K. Kurihara, Fritz G. Parak, N. Niimura
Journal Proteins 50 (2003) 516-523
55. High Resolution Neutron Protein Crystallography. Hydrogen Andhydration in Proteins
N. Niimura, T. Chatake, A. Ostermann, K. Kurihara, I. Tanaka
Journal Z.Kristallogr. 218 (2003) 96-107
56. Hydrogen and Hydration Structure of Protein
N. Niimura
Japanese Society of Enzyme Engineering News 49 (2003) 26-37
57. Characterization of Protein Crystals for Protein Crystallization under Microgravity
N. Niimura, S. Arai
JASMA journals 20 No.2 (2003)111-117
58. A Rational Single Crystal Growth Method of the Protein • DNA on the Crystallization Map
Y. Ohnishi, S. Arai, N. Niimura
Kiso Kagaku Note 10 No.18 (2003) 10-13 (Japanses)
59. Crystallization and Preliminary Neutron Analysis of DsrD Protein from the Sulfate-reducing Desulfovibrio Vulgaris
T. Chatake, N. Mizuno, G. Voordouw, Y. Higuchi, S. Arai, I. Tanaka, N. Niimura
Acta Crystallographica Section D 59 (2003) 2306-2309
60. Effects of Salt Concentration on Association of the Amyloid Protofilaments of Hen Egg White Lysozyme Studied by Time-resolved Neutron Scattering
S. Fujiwara, F. Matsumoto, Y. Yonezawa
J. Mol. Biol. 331 (2003) 21-28
61. Magnetic Field Effects on the Diffuse Scattering of a Spin-frustrated Spinel Ferrite $ZnFe_2O_4$ Single Crystal
K. Kamazawa, S. Katano, Y. Tsunoda
Physica B 345 (2004) 96-98
62. Unusual Antiferromagnetic Properties Affected by Antiferroquadrupolar Interaction in TbB_2C_2
K. Kaneko, N. Metoki, K. Ohoyama, H. Onodera, Y. Yamaguchi
J. Magn. Magn. Mater. 272-276 (2004) e375-e376
63. Neutron Scattering Study on the Field-Induced Antiferro-quadrupolar Ordering in the Heavy Fermion Superconductor $PrOs_4Sb_{12}$
N. Metoki, K. Kaneko, S. Araki, M. Kohgi, K. Iwasa, K. Kuwahara, N. Bernhoeft, J. M. Mignont,
A. Gukasov, H. Sato, Y. Aoki, H. Sugawara
J. Magn. Magn. Mater. 272-276 (2004) e91-e92

64. Percolation Fractal Dimension in Scattering Line Shapes of the Random-field Ising Model
F. Ye, M. Matsuda, S. Katano, H. Yoshizawa, D. P. Belanger, E. T. Seppala, J. A. Fernandez-Baca,
M. J. Alava
Physica B **272-276** (2004) 1298-1299
65. Development of Thermal Neutron Focusing Device Using Supermirrors
T. Osakabe, K. Soyama, K. Suzuki, T. Miyo
Hamon **14 No.1** (2004) 84-87 (Japanese)
66. Static Antiferromagnetic Correlations under Magnetic Field in Electron-doped High-Tc Cuprate Superconductor
 $\text{Pr}_{0.89}\text{LaCe}_{0.11}\text{CuO}_4$
M. Fujita, M. Matsuda, K. Katano, K. Yamada
Physica B **345** (2004) 19-22
67. How to Use Neutron in Development of Magnetic and Devices
M. Takeda
Hamon **14 No.1** (2004) 48-49 (Japanese)
68. Spin Dependent Quantum Renormalization Factor in the One-dimensional Heisenberg Antiferromagnetic
Systems Determined by Inelastic Neutron Scattering Experiments
S. Itoh, Y. Endoh, K. Kakurai, H. Tanaka
J. Phys. Soc. Jpn **73** (2004) 269-274
69. Magnetic Structures and Spin States of $\text{NdBaCo}_2\text{O}_7$
M. Soda, Y. Yasui, M. Ito, S. Ikubo, M. Sato, K. Kakurai
J. Phys. Soc. Jpn **73** (2004) 464-468
70. Magnetization Plateaux of the $S=1/2$ Two-dimensional Frustrated Antiferromagnet Cs_2CuBr_4
T. Ono, H. Tanaka, O. Kolomyats, H. Mitamura, T. Goto,
K. Nakajima, A. Oosawa, Y. Koike, K. Kakurai, J. Klenke, P. Smeibidle, H. Meibner
J. Phys.: Condens. Matter **16** (2004) S773-S778
71. A New Neutron Single Crystal Diffractometer Dedicated for Biological Macromolecules (BIX-4)
K. Kurihara, I. Tanaka, Refai, A. Ostermann, N. Niimura
Journal of Synchrotron Radiation **11** (2004) 68-71
72. Hydration Structures in Proteins and Neutron Diffraction Experiment on Dissimilatory Sul-fate reductase D (DsrD)
T. Chatake, A. Ostermann, K. Kurihara, FritzParak, N. Mizuno, Y. Higuchi, I. Tanaka, N. Niimura
Journal of Synchrotron Radiation **11** (2004) 72-75
73. Hydrogen and Hydration in Proteins
N. Niimura, T. Chatake, K. Kurihara, M. Maeda
Cell Biochemistry and Biophysics **40 No.3** (2004) 1-20
74. The Neutron Diffractometer which is Proud of Worldwide Highest Performance
N. Niimura, K. Kurihara, I. Tanaka
Kagaku **59 No.2** (2004) 46-47 (Japanese)
75. Crystallization of a Large Single Crystal of Cubic Insulin for Neutron Protein Crystallography
M. Maeda, T. Chatake, I. Tanaka, A. Ostermann, N. Niimura
Journal of Synchrotron Radiation **11** (2004) 41-44

This is a blank page.

国際単位系 (SI) と換算表

表1 SI基本単位および補助単位

量	名称	記号
長さ	メートル	m
質量	キログラム	kg
時間	秒	s
電流	アンペア	A
熱力学温度	ケルビン	K
物質の量	モル	mol
光度	カンデラ	cd
平面角	ラジアン	rad
立体角	ステラジアン	sr

表3 固有の名称をもつSI組立単位

量	名称	記号	他のSI単位 による表現
周波数	ヘルツ	Hz	s ⁻¹
力	ニュートン	N	m·kg/s ²
圧力, 応力	パスカル	Pa	N/m ²
エネルギー, 仕事, 熱量	ジュール	J	N·m
工率, 放射束	ワット	W	J/s
電気量, 電荷	クーロン	C	A·s
電位, 電圧, 起電力	ボルト	V	W/A
静電容量	ファラド	F	C/V
電気抵抗	オーム	Ω	V/A
コンダクタンス	ジーメン	S	A/V
磁束	ウェーバ	Wb	V·s
磁束密度	テスラ	T	Wb/m ²
インダクタンス	ヘンリー	H	Wb/A
セルシウス温度	セルシウス度	°C	
光束	ルーメン	lm	cd·sr
照度	ルクス	lx	lm/m ²
放射能	ベクレル	Bq	s ⁻¹
吸収線量	グレイ	Gy	J/kg
線量当量	シーベルト	Sv	J/kg

表2 SIと併用される単位

名称	記号
分, 時, 日	min, h, d
度, 分, 秒	°, ', "
リットル	l, L
トン	t
電子ボルト	eV
原子質量単位	u

$$1 \text{ eV} = 1.60218 \times 10^{-19} \text{ J}$$

$$1 \text{ u} = 1.66054 \times 10^{-27} \text{ kg}$$

表4 SIと共に暫定的に維持される単位

名称	記号
オングストローム	Å
バ	b
バ	bar
ガ	Gal
キュリー	Ci
レントゲン	R
ラ	rad
レ	rem

$$1 \text{ Å} = 0.1 \text{ nm} = 10^{-10} \text{ m}$$

$$1 \text{ b} = 100 \text{ fm} = 10^{-28} \text{ m}^2$$

$$1 \text{ bar} = 0.1 \text{ MPa} = 10^5 \text{ Pa}$$

$$1 \text{ Gal} = 1 \text{ cm/s}^2 = 10^{-2} \text{ m/s}^2$$

$$1 \text{ Ci} = 3.7 \times 10^{10} \text{ Bq}$$

$$1 \text{ R} = 2.58 \times 10^{-4} \text{ C/kg}$$

$$1 \text{ rad} = 1 \text{ cGy} = 10^{-2} \text{ Gy}$$

$$1 \text{ rem} = 1 \text{ cSv} = 10^{-2} \text{ Sv}$$

表5 SI接頭語

倍数	接頭語	記号
10 ¹⁸	エクサ	E
10 ¹⁵	ペタ	P
10 ¹²	テラ	T
10 ⁹	ギガ	G
10 ⁶	メガ	M
10 ³	キロ	k
10 ²	ヘクト	h
10 ¹	デカ	da
10 ⁻¹	デシ	d
10 ⁻²	センチ	c
10 ⁻³	ミリ	m
10 ⁻⁶	マイクロ	μ
10 ⁻⁹	ナノ	n
10 ⁻¹²	ピコ	p
10 ⁻¹⁵	フェムト	f
10 ⁻¹⁸	アト	a

(注)

- 表1～5は「国際単位系」第5版, 国際度量衡局 1985年刊行による。ただし, 1 eV および 1 uの値はCODATAの1986年推奨値によった。
- 表4には海里, ノット, アール, ヘクタールも含まれているが日常の単位なのでここでは省略した。
- barは, JISでは流体の圧力を表す場合に限り表2のカテゴリーに分類されている。
- EC閣僚理事会指令ではbar, barnおよび「血圧の単位」mmHgを表2のカテゴリーに入れている。

換算表

力	N (=10 ⁵ dyn)	kgf	lbf
	1	0.101972	0.224809
	9.80665	1	2.20462
	4.44822	0.453592	1

粘度 1 Pa·s (N·s/m²) = 10 P (ポアズ) (g/(cm·s))

動粘度 1 m²/s = 10⁴ St (ストークス) (cm²/s)

圧	MPa (=10 bar)	kgf/cm ²	atm	mmHg (Torr)	lbf/in ² (psi)
	1	10.1972	9.86923	7.50062 × 10 ³	145.038
力	0.0980665	1	0.967841	735.559	14.2233
	0.101325	1.03323	1	760	14.6959
	1.33322 × 10 ⁻⁴	1.35951 × 10 ⁻³	1.31579 × 10 ⁻³	1	1.93368 × 10 ⁻²
	6.89476 × 10 ⁻³	7.03070 × 10 ⁻²	6.80460 × 10 ⁻²	51.7149	1

エネルギー・仕事・熱量	J (=10 ⁷ erg)	kgf·m	kW·h	cal (計量法)	Btu	ft·lbf	eV
	1	0.101972	2.77778 × 10 ⁻⁷	0.238889	9.47813 × 10 ⁻⁴	0.737562	6.24150 × 10 ¹⁸
	9.80665	1	2.72407 × 10 ⁻⁶	2.34270	9.29487 × 10 ⁻³	7.23301	6.12082 × 10 ¹⁹
	3.6 × 10 ⁶	3.67098 × 10 ⁵	1	8.59999 × 10 ⁵	3412.13	2.65522 × 10 ⁶	2.24694 × 10 ²⁵
	4.18605	0.426858	1.16279 × 10 ⁻⁶	1	3.96759 × 10 ⁻³	3.08747	2.61272 × 10 ¹⁹
	1055.06	107.586	2.93072 × 10 ⁻⁴	252.042	1	778.172	6.58515 × 10 ²¹
	1.35582	0.138255	3.76616 × 10 ⁻⁷	0.323890	1.28506 × 10 ⁻³	1	8.46233 × 10 ¹⁸
	1.60218 × 10 ⁻¹⁹	1.63377 × 10 ⁻²⁰	4.45050 × 10 ⁻²⁶	3.82743 × 10 ⁻²⁰	1.51857 × 10 ⁻²²	1.18171 × 10 ⁻¹⁹	1

1 cal = 4.18605 J (計量法)
 = 4.184 J (熱化学)
 = 4.1855 J (15 °C)
 = 4.1868 J (国際蒸気表)
 仕事率 1 PS (仏馬力)
 = 75 kgf·m/s
 = 735.499 W

放射能	Bq	Ci
	1	2.70270 × 10 ⁻¹¹
	3.7 × 10 ¹⁰	1

吸収線量	Gy	rad
	1	100
	0.01	1

照射線量	C/kg	R
	1	3876
	2.58 × 10 ⁻⁴	1

線量当量	Sv	rem
	1	100
	0.01	1

(86年12月26日現在)

